Ambient Noise in an Urbanized Tidal Channel

Christopher Bassett

A dissertation
submitted in partial fulfillment of the
requirements for the degree of

Doctor of Philosophy

University of Washington

2013

Reading Committee:

Jim Thomson, Chair

Brian Polagye, Chair

Peter Dahl

Program Authorized to Offer Degree:
Mechanical Engineering

University of Washington

Abstract

Ambient Noise in an Urbanized Tidal Channel

Christopher Bassett

Co-Chairs of the Supervisory Committee:
Jim Thomson
Applied Physics Laboratory/Civil and Environmental Engineering

Brian Polagye
Mechanical Engineering

In coastal environments, when topographic and bathymetric constrictions are combined with large tidal amplitudes, strong currents (> 2 m/s) can occur. Because such environments are relatively rare and difficult to study, until recently, they have received little attention from the scientific community. However, in recent years, interest in developing tidal hydrokinetic power projects in these environments has motivated studies to improve this understanding. In order to support an analysis of the acoustic effects of tidal power generation, a multi-year study was conducted at a proposed project site in Puget Sound (WA) are analyzed at a site where peak currents exceeded 3.5 m/s. From these analyses, three noise sources are shown to dominate the observed variability in ambient noise between 0.02-30 kHz: anthropogenic noise from vessel traffic, sediment-generated noise during periods of strong currents, and flow-noise resulting from turbulence advected over the hydrophones.

To assess the contribution of vessel traffic noise, one calendar year of Automatic Identification System (AIS) ship-traffic data was paired with hydrophone recordings. The study region included inland waters of the Salish Sea within a 20 km radius of the hydrophone deployment site in northern Admiralty Inlet. The variability in spectra and hourly, daily, and monthly ambient noise statistics for unweighted broadband and M-weighted sound pressure levels is driven largely by vessel traffic. Within the one-year study period, at least one AIS transmitting vessel is present in the study area 90% of the time and over 1,363 unique

vessels are recorded. A noise budget for vessels equipped with AIS transponders identifies cargo ships, tugs, and passenger vessels as the largest contributors to noise levels. A simple model to predict received levels at the site based on an incoherent summation of noise from different vessel types yields a cumulative probability density function of broadband sound pressure levels that shows good agreement with 85% of the temporal data.

Bed stresses associated with currents can produce propagating ambient noise by mobilizing sediments. The strength of the tidal currents in northern Admiralty Inlet produces bed stresses in excess of 20 Pa. Significant increases in noise levels at frequencies from 4-30 kHz, with more modest increases noted from 1-4 kHz, are attributed to mobilized sediments. Sediment-generated noise during strong currents masks background noise from other sources, including vessel traffic. Inversions of the acoustic spectra for equivalent grain sizes are consistent with qualitative observations of the seabed composition. Bed stress calculations using log layer, Reynolds stress, and inertial dissipation techniques generally agree well and are used to estimate the shear stresses at which noise levels increase for different grain sizes. Ambient noise levels in one-third octave bands with center frequencies from 1 kHz to 25 kHz are dominated by sediment-generated noise and can be accurately predicted using the near-bed current velocity above a critical threshold.

When turbulence is advected over a pressure sensitive transducer, the turbulent pressure fluctuations can be measured as noise, though these pressure fluctuations are not propagating sound and should not be interpreted as ambient noise. Based on measurements in both Admiralty Inlet, Puget Sound and the Chacao Channel, Chile, two models are developed for flow-noise. The first model combined measurements of mean current velocities and turbulence and agrees well with data from both sites. The second model uses scaling arguments to model the flow-noise based solely on the mean current velocity. This model agrees well with the data from the Chacao Channel but performs poorly in Admiralty Inlet, a difference attributed to differences turbulence production mechanisms. At both sites, the spectral slope of flow noise follows a $f^{-3.2}$ dependence, suggesting partial cancellation of the pressure fluctuations when the turbulent scales are on order of, or smaller than, the

characteristic size of the hydrophone. At both sites, flow-noise levels can exceed ambient noise levels during slack currents by more than 50 dB at 20 Hz and flow-noise is measured at frequencies greater than 500 Hz. In Admiralty Inlet, the use of a compact flow shield is shown to reduce flow-noise levels by up to 30 dB.

Below 1 kHz, the dominant source of ambient noise is vessel traffic, though during periods of strong currents, the propagating noise from vessels can be difficult to identify because of flow-noise. At frequencies above 1 kHz, during periods of strong currents, the dominant source of ambient noise is bedload transport. Observation of this higher frequency sound is not affected by flow-noise, which is limited to lower frequencies in northern Admiralty Inlet.

These results are combined with marine species hearing thresholds, a turbine source spectrum, and a simple propagation model to roughly quantify the probability of marine animals detecting the sound of operating turbines against ambient noise. The results suggest that the likely detection range of operating turbines is limited to less than 1 km under most conditions. The sound produced by operating tidal turbines at the proposed demonstration-scale tidal power project is not likely to have any significant behavioral effect at greater range.

Finally, the ambient statistics at the site are also combined with a sound propagation model and vocalization characteristics of Southern Resident killer whales to determine the effective range for passive acoustic monitoring techniques at the proposed project location. Due to the frequency overlap between sediment-generated noise and killer whale vocalizations, during peak currents the detection range for vocalizations is reduced by up to 90% when compared to slack current noise levels. Although the reduction in detection range is significant, this analysis suggests that passive acoustic monitoring will still be effective at ranges greater than the typical range at which killer whales can detect the turbines. These results of these two detection studies will inform the design of post-installation monitoring plans to quantify noise production by operating turbines and the associated environmental changes.

This dissertation provides a comprehensive analysis of ambient noise measurements in

an energetic coastal environment and advances the understanding of noise sources unique to these environments, such as sediment-generated noise and flow-noise. The improved understanding of these noise sources will aid in the interpretation of acoustic measurements in other energetic environments. Furthermore, as uncertainties in sound produced by tidal turbines and marine animal behavioral responses to this sound are reduced, the foundation laid by this research will allow the acoustic impacts of tidal hydrokinetic power projects to be quantified.

TABLE OF CONTENTS

Page

LIST OF FIGURES

LIST OF TABLES

ACKNOWLEDGMENTS

The experiences that I have had through my own work and supporting that of my colleagues have been transformative to say the least. Prior to starting the research discussed in this document, I had never considered ocean studies of any kind. In fact, my involvement in this project was entirely circumstantial. Nonetheless, it has changed my trajectory and I can't thank Jim Thomson enough for providing me with the opportunity to begin down this path. Alberto Aliseda initially put me in contact with Jim Thomson. For this, I cannot thank him enough. Since beginning the project countless people have been involved, either directly or indirectly, or provided encouragement. As a result, I will inevitable fail to acknowledge someone's contribution. To anyone I fail to acknowledge, I sincerely apologize.

I would like to extend my sincere gratitude of all of the members of my committee, all of whom it has been a pleasure to work with. Perhaps the best part of working with my committee was that each member was especially interested or engaged in different aspects of my work. As a result, I had the chance to work closely with and learn from all of my committee at different stages of this work. Jim Thomson and Brian Polagye, as co-chairs, were most involved with all of the work discussed in this thesis. Throughout this process they have both provided me with the perfect balance of independence and guidance, which has allowed me to both pursue interesting results and make important mistakes. Peter Dahl's guidance was critical to the development of Chapter 6 while Marla Holt's input was crucial to the work discussed in Chapter 4. Finally, I would thank Terrie Klinger for agreeing to serve on my committee as the Graduate School Representative.

Without support from various funding agencies and interested partners my research would not have been possible. The Snohomish Public Utility District No. 1 not only funded my Masters work but also provided critical support for this research and other related work at the same site. The US Department of Energy provided key support for the field

operations. Critically, the National Science Foundation Graduate Research Fellowship Program (Award No. DGE-0718124) provided three years of financial support. This funding gave me the permission to pursue the data sets and results and I found most compelling. Steve Burges was especially supportive of my GRFP application, despite not having met me previously. I would express my gratitude for this generous gesture.

Throughout the past four years I have been involved with research related to tidal energy at the Northwest National Marine Renewable Energy Center (NNMREC). The scope of this project forced me to interact with researchers at many institutions with regarding a variety of topics. Along the way Alex Horner-Devine, Andrea Ogston, Sarah Giddings, Dom Tollitt, Jason Wood, and Heather Dillon have all provided some sort of support ranging from data processing techniques to general support relating to graduate school. Not only were many of these interactions a critical part of the learning process, I always left discussions with the aforementioned scientists with new ideas and enthusiasm.

A large number of other students have provided constant support for my work. I hope that I have reciprocated this throughout the past few years. In particular, I would like to thank Dan Nowacki, J. Paul Rinehimer, Colin Bateson, and Teymour Javaherchi. Colin, Teymour, and I started this process together, had similar class schedules, and generally worked through different obstacles together. Dan and J. Paul have both provided critical technical support, mostly quick and effective solutions to coding questions, on countless occasions.

Field work at the site on which this research focuses is particularly challenging. The difficulties arise from the highly energetic conditions that make such sites suitable for tidal energy development. I can't thank Joe Talbert and Alex de Klerk (field engineers) enough for their hard work. I've been constantly impressed by their ability to provide solutions for the constantly changing plans that this project entailed. To this end, Captains Andy Reay-Ellers and Mark Anderson were instrumental throughout the demanding deployments and recoveries of the instrumentation packages. James Joslin, Rob Cavagnaro, Sam Gooch, Jeff Epler, Mike Palodichuck, Walt Deppe, and Dave Sutherland also participated in the

deployment/recovery of instrumentation packages.

My family has provided a tremendous amount of support during my years at UW. Of course, this has also been the case throughout my life. I'm certain that without their support, especially the financial support of my paternal grandparents during my undergraduate years, I would never have attended the University of Washington. I would also like to thank my sister (Stephanie) and parents (Karen and Steve) for their support and encouragement. When I mentioned that I had decided to go back to school, the response from my parents of them was something like "I didn't see that coming." The truth is, I didn't either. What I expected even less was deciding to stay beyond the Masters program. Ever since I informed my parents (and grandparents) of my intentions to go back to school they have been my biggest cheerleaders.

There are two particular people that have had a notable impact of my life. Without these two individuals, I might not have pursued a career in engineering/science. My paternal grandfather's brother, Charles Bassett III, was an engineer, test pilot, and astronaut in the Gemini project. His life was cut short by a plane crash in 1966, just before his first space flight. While I never knew him, stories of his life have provided a constant source of inspiration to me. I would also like to thank Dana Goodman-Geller, my high school calculus teacher. At the time she taught my calculus course, she was a young and relatively inexperienced; however, she was a phenomenal teacher. Without her class I might not have developed the interest in math required to succeed in an engineering discipline.

I couldn't possibly finish this document without acknowledging the support of my partner, Paula Alonso. We met during the Friday Harbor Bioacoustics course. In this years since, she has been tremendously supportive of my work and, even more importantly, the ideal partner when I was struggling. I can't thank her enough for all of this and for putting up with the uncertainties associated with everything from my post-graduation plans to not knowing when we would be able to talk again while I was in the field.

Chapter 1

INTRODUCTION

Concerns about climate change, environmental degradation, the consumption of natural resources, and national energy security have been driving investments in renewable energy technologies. At a regional level, the recent adoption of renewable portfolio standards, such as Washington's Initiative 937, which requires utilities to obtain 15% of their electricity from renewable sources (excluding conventional hydropower) by 2020, has reinforced this movement. In the Salish Sea, strong tidally-driven currents are an unexplored source of predictable, renewable energy. Public Utility District No. 1 of Snohomish County (the District), Washington received permits from the Federal Energy Regulatory Commission (FERC) to study seven sites for a demonstration-scale tidal power project in Puget Sound, Washington. The District subsequently chose to pursue a project in northern Admiralty Inlet. Pending the completion of project licensing, the District plans to deploy two 6-meter OpenHydro Open-Centre turbines in 2015. In combination, these units will have a peak power production of approximately 250 kW and an average power production of 30 kW. Once installed, the project will be the first project of its kind operating in the waters of the Pacific Northwest and the first grid-connected array in the world.

Tidal hydrokinetic energy is a nascent approach to renewable energy generation in the United States. To date, demonstration projects have operated in the East River in New York and in Cobscook Bay, Marine. While commercial prototypes have been tested in Europe, information about the environmental consequences of large scale deployment remain limited. In March, 2010 a scientific workshop on the environmental effects of tidal energy development was held at the University of Washington. The purpose was to identify key environmental stressors, receptors, and research priorities. The results of the workshop identified the acoustic effects of installation, operation, routine maintenance, and decommissioning as a key knowledge gap [*Polagye et al.*, 2011]. Operational turbines will produce

sound, but the characteristics of this sound in comparison to characteristics of ambient noise is unknown. As such, it is not yet possible to draw conclusions about the potential impact of sound produced by demonstration-scale or commercial-scale tidal power projects. Future work to quantify these impacts requires quantifying the time-varying sound produced by turbines, the temporal and spatial variations in ambient noise, and the effect of sound exposure on different taxonomic groups. This thesis develops basic knowledge about the characteristics of ambient noise in an energetic tidal environment and then applies this knowledge to assess the extent to which turbine sound might be detectable by different taxonomic groups, as well the effectiveness of passive acoustic monitoring of marine mammals during periods of strong currents.

By necessity, field studies at sites suitable for tidal power production involves working in highly energetic environments. Perhaps the best summary of why such energetic sites do not appear often in the literature was made by one of the anonymous reviewers of the initial manuscript on sediment-generated noise, the final version of which is included in this document (Chapter 5). The reviewer stated "...most sane experimenters avoid regions of the ocean with 1-3 m/s currents!" The reviewer may be correct. But in spite of these challenges, responsible development of tidal energy projects makes such studies a necessity. This provides a unique opportunity to study questions of interest to the oceanographic and underwater acoustic community that also have direct applications to the development of marine renewable energy technology.

In concept, the objective of this thesis is simple: to quantify ambient noise levels. With few prior measurements from highly energetic sites available, it was unclear, at the start of this thesis, what scientific questions would emerge in the study of such sites. *Bassett* [2010] describes the initial investigations that motivate further studies of vessel noise, sediment-generated noise, and flow-noise that are presented here.

Chapter 2 provides a more detailed introduction to tidal power, the proposed project, and site details. The following chapters focus specifically on one of the identified noise sources or the application of the results from those chapters. With the exception of a site description, each chapter includes critical background and methodology that are relevant to the chapter. These chapters all assume a working knowledge of the basic principles of acoustics, acoustic

signal processing and a familiarity with tidal hydrokinetic power. Therefore, Chapter 3 includes an introduction to the principles of underwater sound including the basic physics, measurement approaches, and signal processing.

Chapter 4 describes a study of vessel noise in Admiralty Inlet, Puget Sound. Due to the near-constant presence of vessel traffic; especially shipping vessels, tugs, and passenger vessels; ambient noise levels are driven in large part by anthropogenic noise. In addition to presenting ambient noise statistics, this chapter combines ship traffic data obtained by an Automatic Identification System (AIS) receiver and vessel source levels to develop a noise level model and an energy budget for vessel noise. The chapter, as it appears here (with the exception of formatting changes and the removal of site information), was published in the *Journal of the Acoustical Society of America* and as cited as:

> Bassett, C., B. Polagye, M. Holt, and J. Thomson, A vessel noise budget for Admiralty Inlet, Puget Sound, Washington (USA), *J. Acoust. Soc. Am., 132(6)*, 3706-3719, 2012.

Chapter 5 describes a study that determined that the frequencies at which noise level increases occur are consistent with the sound produced by colliding sediment grains of sizes known to be present at the site. During periods when near-bed currents exceed 0.85 m/s, significant increases in ambient noise levels at frequencies greater than 1 kHz are recorded at the project site in Admiralty Inlet. This analysis combines information about the seabed composition, bed stresses, and acoustic data to demonstrate that the strong currents that make a site suitable for tidal energy development can also lead to noisy conditions when the bed is mobilized. Chapter 5, as it appears (with the exception of formatting changes and the removal of site information), was published in the *Journal of Geophysical Research – Oceans* and is cited as:

> Bassett, C., J. Thomson, and B. Polagye, Sediment-generated noise and bed stress in a tidal channel, *J. Geophys. Res. – Oceans, 118*, 1-17, 2013.

Chapter 6 describes a study of flow-noise. In *Bassett* [2010] it was recognized that there was a strong correlation between low-frequency ($<$ 500 Hz) acoustic measurements and

the current velocities. This dependence, attributed to flow-noise, is not true, propagating sound and should not be included in ambient noise budgets. Prior research in less energetic environments has identified flow-noise and suggested models for infrasonic flow-noise. These models, however, are not applicable to the higher frequencies due to the scales of turbulence relative to the hydrophones. Chapter 6 uses data sets from the Chacao Channel, Chile and Admiralty Inlet to describe flow-noise characteristics and to develop two flow-noise models that are applicable to a larger range of frequencies than previous models. This work, as it appears (with the exception of formatting changes) has been submitted for publication in the *Journal of the Acoustical Society of America* and is cited as:

> Bassett, C. , J. Thomson, P. Dahl, and B. Polagye, Flow-noise and turbulence in two tidal channels, *J. Acoust. Soc. Am.*, submitted.

Appendix B describes a related study, namely an approach to mitigating flow-noise in measurements of high-energy environments. Given that flow-noise can reduce the quality of acoustic measurements, especially at low frequencies (i.e., < 1 kHz), a mechanical device, referred to as a flow shield, was designed and deployed in Admiralty Inlet. The flow shield works by damping turbulent pressure fluctuations near the hydrophone. The flow shield successfully reduced, but did not entirely eliminate flow-noise. Nonetheless, the device reduces flow-noise measurements to the degree that it would eliminate flow-noise in environments with currents less than 0.5 m/s and may allow other signal processing techniques (e.g., *Chung* [1977]) to be used in concert to eliminate flow-noise in more energetic environments.

Chapters 4 and 5 provide the basic science in support of the applied studies included in Chapters 7 and 8, which cover two subjects: estimates of the range at which different species are expected to be able to detect operating tidal turbines in Admiralty Inlet and estimates of the range at which passive acoustic monitoring techniques will be able to detect killer whale vocalizations at the same location. Without the basic studies presented in this thesis, these studies would be undermined by broad uncertainties. Chapters 7 and 8 are not copied verbatim from submitted manuscripts. Instead, they highlight key results from two manuscripts that have been submitted and are in preparation, respectively. The manuscript on the detection of operating tidal turbines by different marine species, on which Dr. Brian

Polagye is the first author, has been submitted to the *Journal of Oceanic Engineering* and is cited as:

> Polagye, B., C. Bassett, M. Holt, J. Wood, and S. Barr, A framework for detection of tidal turbine sound: A pre-installation case study for Admiralty Inlet, Puget Sound, Washington (USA), *J. Ocean. Eng.*, (in revision).

The second manuscript, which is currently in preparation, is a collaboration between the author of this dissertation, Dr. Brian Polagye, Alexandra Gramling (UW graduate student), and Jason Wood (Sea Mammal Research Unit). In both applications, simple transmission equations are employed, rather than range-dependent numerical modeling techniques Appendix C includes an analysis of the transmission losses calculated using analytical and computational models and comments on the effect analytical models

Chapter 9 concludes with a summary of what has been learned about ambient noise in energetic environments and what research to date suggests that the environmental impact of sound emissions from a demonstration-scale tidal energy project might be. The work covered here not only discusses topics of interest to the acoustics community, but will also inform the design of post-installation monitoring plans at the tidal energy site.

Chapter 2

TIDAL ENERGY AND PROJECT CONSIDERATIONS

2.1 Introduction

The purpose of this chapter is to orient readers unfamiliar with the concepts of tidal hydrokinetic power generation. In addition, this chapter provides additional details about the demonstration-scale project proposed by the Public Utility District No. 1 of Snohomish County and a description of the proposed project site.

2.2 Tidal Energy Background

Tidal energy is a renewable energy resource that relies on the predictable gravitation forcing of the oceans by the moon and sun. There are two approaches to harnessing tidal energy. The first is to extract potential energy from the rise and fall of the tides by utilizing a tidal barrage, which is, in principle, similar to conventional hydropower. The second, which motivates this thesis, is to extract kinetic energy at locations where the tidal exchange is concentrated by narrow or shallow channels. This is analogous to wind energy. Tidal turbines operate by using either hydrodynamic lift or drag to convert the kinetic power in these currents into rotational mechanical power. This is, in turn, is converted to electrical power by a generator. The high density of sea water, approximately 1,024 kg/m^3, results in high energy densities at currents much lower than wind speeds at economically feasible wind power sites. Unlike other renewable energy sources, first order predictions of tidal power production are possible due to the predictability of tides [*Polagye et al.*, 2010; *Polagye and Thomson*, 2013]. Higher order prediction of the available power resource are limited by complex oceanographic interactions that produce highly variable residual currents. Furthermore, predominant bathymetric features at tidal energy sites can result in significant variability in the available resource on small spatial scales (O(200 m)) [*Epler*, 2010; *Palodichuk et al.*, 2013].

The tidal power industry is currently in the early stages of development when compared to the wind power industry. Numerous designs have been developed, although only a relatively small number of devices have been deployed at sea. Most deployments to date operate on hydrodynamic lift and fall into one of two design classes that are distinguished by the orientation of the rotor. Horizontal axis rotors are characterized by a rotational axis that is parallel to the direction of the flow. Cross-flow turbines have rotational axes that are perpendicular to the direction of the flow. Both types of have been successfully deployed in ocean environments, although horizontal axis devices are more common. Figure 2.1 includes images of an OpenHydro horizontal axis turbine and an Ocean Renewable Power Company (ORPC) cross-flow turbine. Rotation rates of these devices have limited the potential for and cavitation at the rotor tip. Cavitation, the growth and subsequent collapse of a vapor bubble due to rapid pressure changes, creates undesirably high loads, reduces hydrodynamic efficiency, and creates sound. In order to suppress cavitation, a rule of thumb is to limit the tip speed of a rotor through the water to approximately 12 m/s [*Fraenkel*, 2007].

Besides the rotor, key components of any tidal energy device design include a mooring or foundation, power train, and an electrical transmission system. There are many possible power train configurations that can be implemented to convert rotational energy from the turbine into electrical energy. Designs may use gearboxes to increase shaft speed to the generator, couple the rotor directly to the generator, or implement a hydraulic connection between the rotor and generator. Designs with gearboxes to increase the generator shaft rotation rate may be an important source of sound from tidal turbine designs given the otherwise low rotation rates of the devices. Cabled moorings or fixed foundations (pile or gravity) can be used to counteract forces generated on the turbine rotor and hold the turbine in place. A more complete summary of device components and existing designs is available in *Polagye et al.* [2011].

For site assessment and potential power extraction, a standard metric is the kinetic power density (P), described by

$$P = \frac{1}{2}\rho\overline{u}^3, \tag{2.1}$$

where ρ is the density of the water and $\overline{u}$ is the mean fluid velocity. Due to the cubic

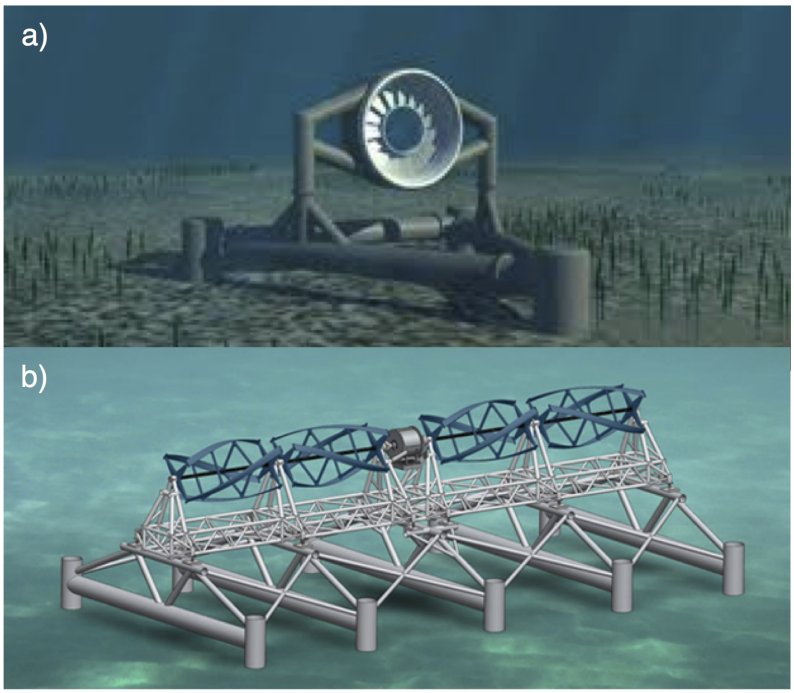

Figure 2.1: a). A rendering of an OpenHydro Open-Centre horizontal-axis turbine (source: www.openhydro.com). b). A rendering on an ORPC TidGen®system (source: www.orpc.co).

dependence of velocity, the kinetic power density increases rapidly with velocity. The power produced by a device is related to the kinetic power density by

$$P = \frac{1}{2}\rho\overline{u}^3 A\eta_e, \tag{2.2}$$

where A is the swept area of the rotor and η_e is the water-to-wire efficiency of the turbine. While other parameters of the flow, such as turbulence intensity and directionality, play an important role in siting devices [*Gooch et al.*, 2009; *Polagye and Thomson*, 2013], the kinetic power density is a commonly used measure of the potential resource.

Economic power generation requires peak currents of 2 m/s in regions with semidiurnal tides and 3 m/s in regions with mixed semidiurnal tides [*Polagye et al.*, 2011]. Mean power densities on the order of 1 kW/m^2 also indicate the potential for economic power extraction. Geographically, such large kinetic power densities are limited to areas with large tidal amplitudes and relatively narrow channels. Economic viability is increased when the need for development of infrastructure for grid connectivity is limited. In order words,

ideal sites include suitable peak kinetic power densities occurring near urban centers. Three regions in the United States best fit these requirements: Puget Sound, the Gulf of Maine, and Cook Inlet, AK.

The natural dissipation of tidal energy is estimated at 3.7 terrawatts (TW) [*Arbic and Garrett*, 2010]. This figure represents only a fraction of global power consumption, but has the potential to be a significant power source on a regional basis [*Polagye et al.*, 2011]. The tidal energy resource available for extraction, considering all possible constraints on power extraction, is the practically recoverable tidal resource. Such constraints include social, environmental, biological, and economic factors. The practically recoverable resource, which represents only a small fraction of the total available resource, is difficult to quantify and is currently an active research area [*National Research Council*, 2011].

2.3 Environmental Impacts: Current Knowledge and Data Gaps

As discussed in Chapter 1, with few projects in operation, quantifying the potential environmental impacts of tidal power extraction is difficult. For the tidal power industry to continue to grow it must be shown that the environmental costs do not exceed the benefits. Consequently, it is preferable to evaluate these aspects of sustainability at the demonstration-scale and to use the results to inform engineering design and project planning to mitigate the potential impacts of commercial-scale projects. In order to identify critical knowledge gaps, researchers, representatives of industry, and regulators participated in the Ecology Effects of Tidal Energy Workshop hosted at the University of Washington in March 2010. During the workshop, participants identified key environmental stressors and receptors, determined the significance of the interaction between the stressors and receptors, and identified the uncertainties [*Polagye et al.*, 2011]. This process was used to determine the key knowledge gaps regarding environmental impacts of both demonstration-scale and commercial-scale projects. The stressors/receptors array for commercial-scale projects from *Polagye et al.* [2011] is included in Figure 2.2. At this scale, moderate to high significance and large uncertainties were identified for a variety of environmental stressors including device presence, acoustic effects, electromagnetic effects, energy removal, and cumulative effects. For acoustic effects, there are large uncertainties related to the potential impacts on invertebrates,

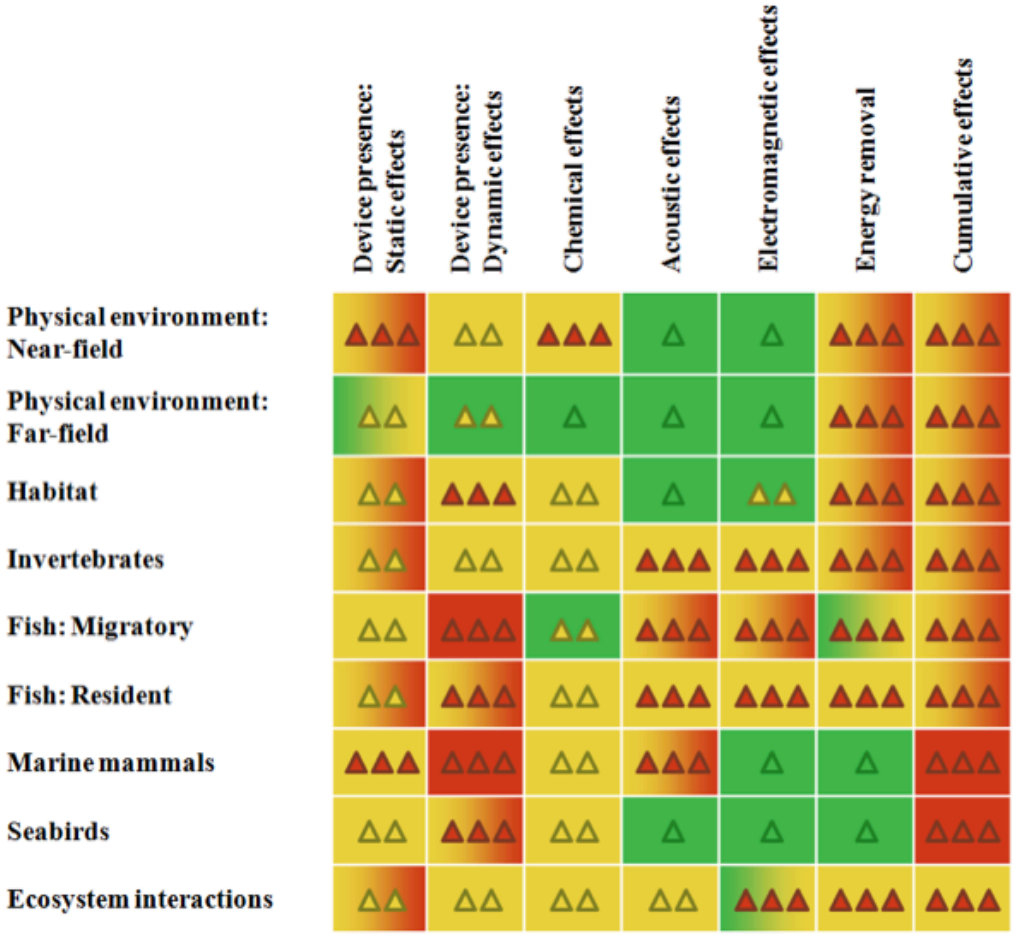

Figure 2.2: A array of knowledge gaps related to the environmental impacts of commercial-scale tidal power projects from *Polagye et al.* [2011]. The columns are the environmental stressors and rows are the receptors. The cell colors highlight the significance of the receptors ranging from low (green) to high (red). The triangles within the cells highlight the uncertainty from low (one triangle) to high (three triangles).

resident and migratory fish, and marine mammals. In particular, sound related to low-frequency tones from rotors and power trains during operation, other broadband increases during operation, and high-pressure transients from emergency breaking of the devices are all identified as important knowledge gaps. To begin to address these knowledge gaps, the document notes that baseline ambient noise measurements are critical to interpreting post-installation measurements.

In an effort to address the the collision risk tidal turbines pose to marine mammals, *Carter* [2007] developed a model taking into consideration marine mammal hearing capabilities, sound propagation, a broad range of ambient noise levels, possible turbine sound ranging from 130 dB to 190 dB re 1μPa at 1 m (broadband), and species response time and swimming capabilities[a]. Not surprisingly, the results suggest that based on variability in source levels and ambient noise conditions a turbine could be audible at very long ranges ($>$ 10 km) or inaudible at short ranges ($<$ 100 m). That conclusion highlights the need to reduce uncertainties in turbine source levels and combine such results with propagation models and information about ambient noise levels to address the acoustic effects of tidal power projects.

2.4 Admiralty Inlet Project

The majority of tidal exchange between the Strait of Juan de Fuca and Puget Sound passes through Admiralty Inlet [*Mofjeld and Larsen*, 1984]. When coupled with the relatively narrow constriction across the sill in northern Admiralty Inlet (≈5 km wide), this tidal exchange results in current velocities that exceed 3 m/s. It is in this environments that the Public Utility District No. 1 of Snohomish County has proposed a demonstration-scale tidal power project. The project will include the deployment of two 6-meter OpenHydro Open-Centre Turbines (Fig. 2.1a) at approximately 48° 09'03.24" N, 122° 41'15.72" W, roughly 1 km west-southwest of Admiralty Head, Whidbey Island[b]. The turbines will be deployed at a depth of between 50–60 meters with a separation distance of approximately 70 meters. The total area that will be occupied by the turbines is less than 0.05% of the cross-sectional area of Admiralty Inlet [*Snohomish PUD*, 2012]. Subsea cables running from the turbines will connect to the grid at a power station and control room on Whidbey Island, approximately 1 km from the site. Figure 2.3 includes a bathymetry map of the proposed

---

[a]The 190 dB re 1μPa at 1 m source levels is highly improbable. A source level of 190 dB re 1μPa at 1 m is comparable to source levels associated with a supertanker vessel traveling at speeds greater than 10 m/s [*McKenna et al.*, 2012].

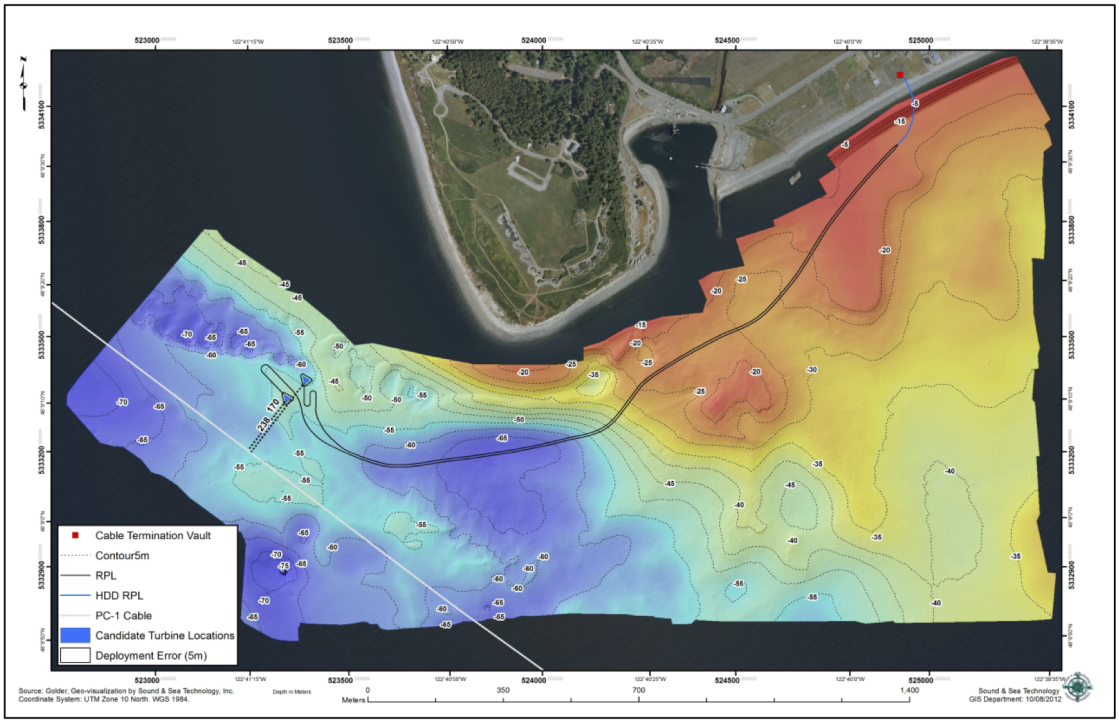

Figure 2.3: A map of the study site including the proposed location of the turbines and subsea cables [*Snohomish PUD*, 2012, Figure 2].

site, the proposed locations of the turbines, and the subsea cabling.

The turbine rotors, which operate at a constant tip-speed ratio, are a high-solidity, horizontal axis design consisting of multiple fixed-pitch blades. A water-lubricated bearing rim bearing provides support for the rotor. Aside from the rotor, the design consists of no moving parts. The major visible structural components form the direct drive permanent magnet generator; the turbine shroud is the stator and the turbine is the rotor. The cut-in speed of the turbines is 0.7 m/s. During peak currents, the predicted power generation of the turbines is 250 kW (125 kW per turbine) and the average power generation will be

[b]With the exception of one chapter, the entirety of this document focuses on the Admiralty Inlet site. The flow-noise chapter, however, includes data from both Admiralty Inlet and a site in the Chacao Channel, Chile. The Chacao Channel is a tidal channel in south-central Chile that is also being considered for tidal power development. A detailed description of the Chacao Channel sites is included in Chapter 6. Any references to the "site" refer to Admiralty Inlet unless otherwise noted.

approximately 15 kW per turbine. Both turbines will be deployed on gravity foundations, will have hub heights of approximately 10 meters above the seabed, and will have no visible surface expression (see Fig. 2.1a).

As discussed in Chapters 4 and 5, there are two important site characteristics that have a significant effect on ambient noise levels: its proximity to vessel traffic lanes and the composition of the seabed. Northern Admiralty Inlet provides shipping access to the ports of Seattle, Everett, and Tacoma, as well as a number of U.S. Navy and Coast Guard facilities (e.g., Puget Sound Naval Shipyard, Bangor Submarine Base). The shipping lanes are located approximately 1.5 km west of the proposed site. Shipping vessels (e.g., bulk carriers and container ships) typically arrive at or depart from the Ports of Seattle, Everett, and Tacoma and transit the area using the shipping lanes. Local commercial traffic such as tugs transit the area frequently transit the area but use the space less predictably than larger, faster moving vessels. Due to the presence of naval bases in the Puget Sound area, military vessel traffic is common. Passenger ferries, serving as a transportation link between coastal communities, and cruise ships also make regular transits in the study area. For example, the passenger ferry route crossing Puget Sound between Coupeville and Port Townsend is located less than 1 km from the site.

The composition of the seabed, which, as shown in Chapter 5 significantly contributes to ambient noise at frequencies greater than 1 kHz, is variable in the vicinity of the proposed site. Quantitative classification of the seabed at the site is difficult due to the water depth (> 50 m), lack of ambient light, and strong currents. Acoustic profiling undertaken in 2009 [*Snohomish PUD*, 2012] indicated a hard substrate, but could not provide a more accurate classification. Transects by a remotely operated vehicle (ROV) [*Greene*, 2011, an appendix to *Snohomish PUD* [2012]], are the most comprehensive data set currently available. Grain size distributions in the ROV survey were determined using ranging lasers separated by 10 cm on the ROV housing. Grain size classification was made based on a modified Wentworth scale where D is the characteristic diameter of the grain [*Wentworth*, 1922]. The reported bottom types included a combination of small boulders (D = 25.6-40.0 cm), cobbles (D = 6.4-25.6 cm), pebbles (D = 3.2-6.4 cm), gravel (D = 0.2-3.2 cm), and coarse sand (D = 0.05-0.2 cm).

Figure 2.4 includes a map of the bed composition from *Greene* [2011]. Notably, there are two dominant substrate types within the immediate vicinity (O(100 m)) of the study site: a soft, unconsolidated bimodal distribution of pebble and gravel likely to be mobilized during strong currents, and a mix of cobble (35-50%), pebbles (<35%), and small boulders. Small boulders and cobbles were typically well rounded and moderately to heavily encrusted with sponges, bryozoans, barnacles, tubeworms, and algae, suggesting these substrates to be stationary [*Greene*, 2011]. Finer-grain constituents have been largely winnowed from the surface pavement. Where pebbles, gravel, and coarse sand were reported, they were unencrusted. Farther from the locations where instrumentation packages were deployed, in areas with weaker currents, pebbles were encrusted. In general, the substrate was unconsolidated and smaller constituents were easily moved by the ROV.

2.5 Noise Studies

Three particular questions must be answered in order to begin to predict and/or identify post-installation changes due to acoustic emissions from tidal turbines:

1. What are the characteristics of ambient noise in the absence of turbine operation?
2. What are the acoustic characteristics (source level intensity and frequency) of the turbines while operating?
3. How would biological receivers be affected when sound produced by the turbines exceeds ambient noise?

The answer to the first question is addressed by Chapters 4 and 5, which discuss the noise from vessels and sediment transport, the two dominant noise sources at the site. Precipitation and biological noise also contribute to the noise budget at the site [*Bassett et al.*, 2010], but subsequent analysis reveals that they are only of secondary importance to overall sound levels.

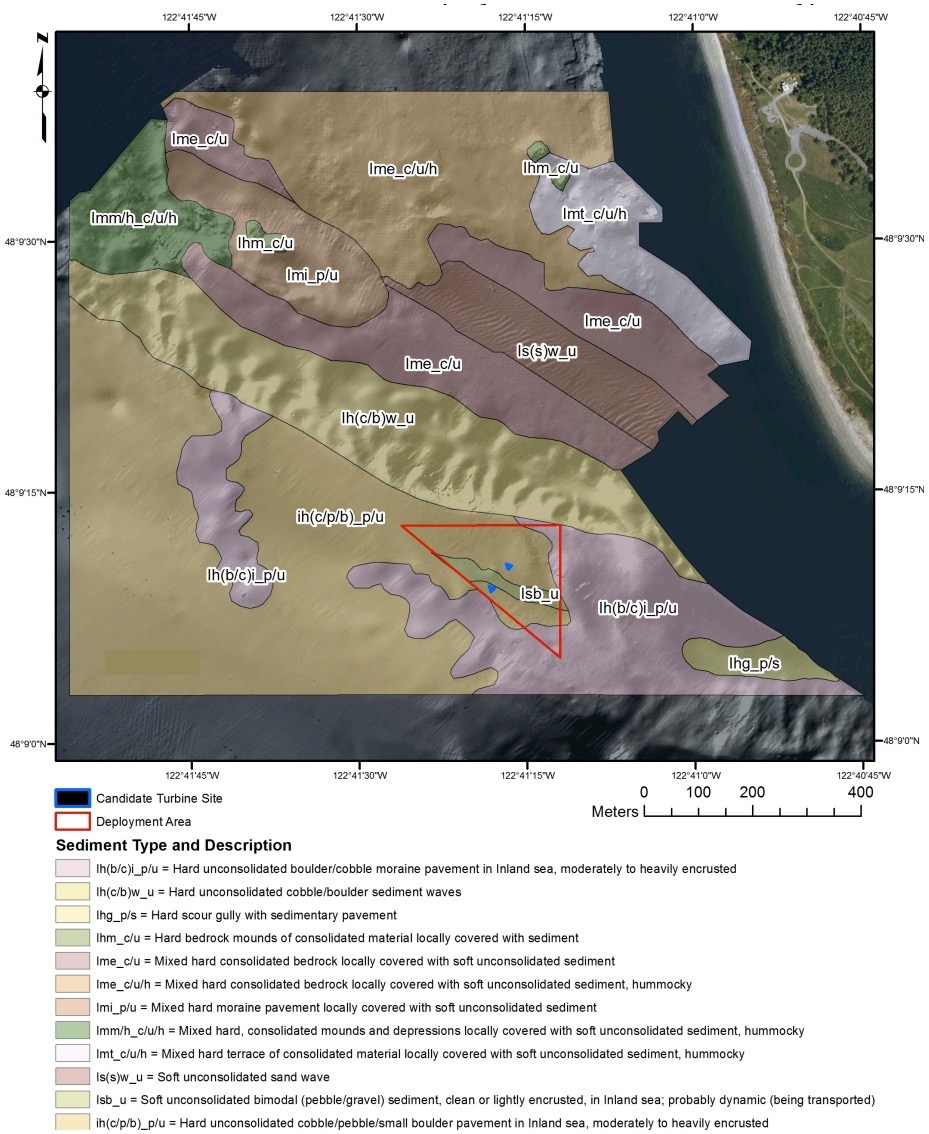

Figure 2.4: Map of seabed composition at the proposed tidal energy site [*Snohomish PUD*, 2012, Appendix].

Chapter 3

BASICS OF UNDERWATER SOUND

3.1 Basics of Sound

Sound is mechanical wave of pressure oscillations that propagate through a compressible medium. From an Eulerian perspective, as the pressure wave passes a point, compression and rarefaction occurs once per wave period. A given sound wave is described, in part, by the frequency (f) and amplitude of the wave. The frequency of the wave determines the perceived pitch; higher frequencies are associated with higher pitches. The amplitude is related to what is perceived as the loudness. The wavelength (λ) is related to the frequency and the speed of sound by $\lambda = c/f$, where c is the speed of sound. The speed of sound in a medium is a basic property that is related to the elastic modulus and density of the medium. The speeds of sound for compressional waves is approximately 340 m/s in air and 1500 m/s in water.

The amplitudes of sound waves in the ocean cover many of orders of magnitude so a logarithmic scale is typically used to describe them. Decibels, the common unit for acoustic measurements, are a logarithmic unit relating the measured quantity to a reference quantity. For acoustic measurements the reference pressure (p_o) accompanies a statement of magnitude. In air the standard reference pressure is 20 μPa, a value associated with the typical human hearing threshold in the range of maximum sensitivity ($\approx$1 kHz) [*Blackstock*, 2000]. A standard reference pressure of 1 μPa is used in water. In contrast, 20 μPa, a value associated with lower limit of human auditory capabilities, is typically used in air. Throughout this document, a reference value of 1 μPa is implied for all measurements.

3.2 Measurements of Underwater Sound

A number of different instruments exist for measuring underwater sounds, including hydrophones and acoustic vector sensors. All measurements of sound in this document were

obtained using hydrophones. A hydrophone is the underwater analog of a microphone and consists of a piezoelectric sensor encased in a filled polymer shell whose material properties are chosen to closely match the acoustic impedance ($Z = \rho c$) of water. Pressure waves in the water are transmitted through the outer shell of the hydrophone and past the piezoelectric material. As the pressure wave passes over the piezoelectric sensor a voltage is induced. Through calibration, that induced voltage can be converted to pressure. In general, hydrophones exhibit some directionality. That is, they have a different sensitivity to pressure waves arriving from different angles. This directionality is frequency dependent. The hydrophones discussed in this document are effectively omni-directional at the frequencies considered in this study.

As the hydrophone responds to the pressure waves, an analog signal taking the form of the arriving pressure waves is produced. To save the data for further use, the analog signal is digitized. The digitization process results in a discrete time series based on the digitization rate of the analog signal. The final digitized time series is a result of the hydrophone's sensitivity to the incoming pressure waves, internal gains in the system, and the frequency response of the data acquisition system. The frequency response of the entire system, along with signal processing techniques discussed in Section 3.5, are used to present recorded data in the different forms presented in this document.

3.3 Terminology

Sound pressure is a measure of pressure deviations from ambient static pressure. The sound pressure level (SPL), is the logarithmic ratio of the root-mean-square (rms) sound pressure to the reference pressure, written as

$$SPL = 10 \log_{10} \left(\frac{p_{rms}^2}{p_o^2} \right) = 20 \log_{10} \left(\frac{p_{rms}}{p_o} \right), \tag{3.1}$$

where p_{rms} is the measured signal and p_o is the reference pressure. The units of the sound pressure level are dB re 1 μPa. The range of frequencies over which a sound pressure level is calculated should accompany the stated SPL. Sound pressure levels are calculated directly from a signal according to Equation 3.1. The SPL may be calculated by integrating the acoustic spectra described in Section 3.5. An acoustic spectrum describes the distribution,

by frequency, of acoustic energy. Sound pressure levels are calculated by integrating spectral levels, or pressure spectral densities, according to

$$SPL = 10\log_{10}\left(\int_{f_1}^{f_2} S_p(f)df\right), \tag{3.2}$$

where f_1 and f_2 frequency limits and S_p is the properly normalized acoustic spectrum in units of dB re $1\mu\text{Pa}^2/\text{Hz}$.

The acoustic intensity (I), or the acoustic energy flux, is related to the sound pressure by

$$I = \frac{p^2}{\rho c}, \tag{3.3}$$

where p is the pressure, ρ is the density of the medium, and c is the sound speed. The denominator of the sound intensity equation is also known as the acoustic impedance. Direct calculation of the intensity by this method assumes a plane wave ($p = vZ$). Generically, the form of the intensity is $I = p\vec{v}$, where $\vec{v}$ is the velocity of a particle displaced by an acoustic wave. The decibel scale acoustic intensity, or the intensity level (IL) is

$$IL = 10\log_{10}\left(\frac{I}{I_o}\right), \tag{3.4}$$

where I_o is the reference intensity, $1\text{pW}/\text{m}^2$. The equation for the SPL may be obtained by substituting Equation 3.3 into Equation 3.4 for both the measured and reference pressures.

3.4 Sound Propagation Basics

3.4.1 Source Levels

When a measured noise level is attributed to a specific source, the proper terminology for the noise produced is the source level (SL). The source level is determined by measuring the acoustic pressure at some distance from the source. All sources would ideally be measured at the same distance. However, because this is not possible or practical in some cases, source levels measurements are made where possible and the recorded levels are used to infer the equivalent source level had the recording been taken at a reference distance of 1 meter. The standard units for a source level underwater is dB re 1μPa at 1 m.

Non-steady pressure fields in a fluid, regardless of the source, result in the generation of sound [*Ross*, 1976]. These non-steady pressure conditions can be caused by a variety

of mechanisms can be related to the expected radiation pattern from the source. Full descriptions of three important types of sound sources; monopoles, dipoles, and quadrupoles; and their radiation patterns are included in *Ross* [1976]. Monopoles are omnidirectional sources (e.g., bubble collapse) whereas dipole sources (e.g., vibrations or two monopoles in close proximity) and quadrupole sources (e.g., turbulence) exhibit radiation patterns.

3.4.2 Transmission Losses

Once sound has been produced by a source it spreads into the surrounding medium. As the sound waves spread the expansion of the wave fronts, interactions with boundaries or changes in the medium, and attenuation of the waves by the medium reduce the amplitude. These combined losses are referred to as transmission losses (TL). Details of transmission losses as a result of boundary interactions and attenuation are discussed in Sections 3.4.3 and 3.4.4.

Geometric spreading is a significant source of transmission losses. Two particular regimes describing the rate of losses due to spreading can be derived intuitively. Those regimes are the spherical and cylindrical spreading regimes. In spherical spreading, a source exists in a lossless, boundless medium with homogenous properties. The source produces a spherical wave that propagates at the same speed in each direction. As the spherical wave expands the total acoustic power must be conserved. Based on the surface area of the spherical wave ($4\pi r^2$, where r is the radius), the intensity of the wave must decrease as a function of r^2. For a wave expanding in a cylindrical environment with rigid boundaries (i.e., no power is transmitted through the boundaries), the power must also be conserved. For the surface area of a cylinder, $2\pi rH$, where r is the radius and H is the depth, the intensity of the wave must decrease as a function of r. These loss terms can be easily converted to a log scale by using the reference distance of 1 meter. Therefore, in these cases the spreading losses become $TL = 20\log_{10}(r)$ for spherical spreading and $TL = 10\log_{10}(r)$ for cylindrical spreading.

The same results can be arrived at by solving the acoustic wave equation,

$$\nabla^2 p - \frac{1}{c^2}\frac{\partial^2 p}{\partial t^2} = 0, \tag{3.5}$$

in the proper coordinate system where the time dependence is neglected for a harmonic source. The wave equation is used in different propagation models to calculated transmission losses. In a coastal environment with complicated bathymetry spherical spreading may exist near the source but sound waves rapidly encounter boundaries. A perfectly cylindrical environment with a rigid, lossless boundary in the marine environment is abstraction. Despite these limitations, by combining range-dependent geometric spreading formulas with attenuation at bottom loss terms, these simple equations can be used in transmission loss estimates (e.g., *Marsh and Schulkin* [1962]).

A number of numerical modeling tools exist to rigorously treat sound propagation in complicated environments. Of these tools, only the range-dependent Parabolic Equation (PE) [*Collins*, 1993, 2000] Fortran codes were used in this thesis. The PE codes allows the user to specify the acoustic frequencies, bathymetry, sound speed profiles, and seabed material properties including complicated seabed with multiple layers. These parameters are used in a finite element approach to determine transmission losses throughout a modeled domain. A further description and comparison of transmission loss models is given in Appendix C.

3.4.3 Reflection and Transmission at Boundaries and Interfaces

In a medium with a constant sound speed the ray paths, which are vectors indicating the direction of propagation of a wavefront, travel in straight lines. When a sound wave traveling through a fluid medium encounters stratification, or an abrupt change in density and sound speed, such as the air-water or water-seabed interface, the energy can be both transmitted through the interface and reflected back into the medium. The energy being transmitted through the interface is also refracted (i.e., the direction of propagation changes).

The following relationships for reflections and transmissions at interfaces are discussed in many texts (e.g., *Urick* [1975] and *Medwin* [2005]). For plane waves at arriving at a interface (Fig. 3.1), two boundary conditions govern the solution for reflection, transmission, and refraction. First, the pressures as a function of time of on both sides of the interface must be equal. Therefore, $p_i + p_r = p_t$, where the subscripts i, r, and t correspond to the incident,

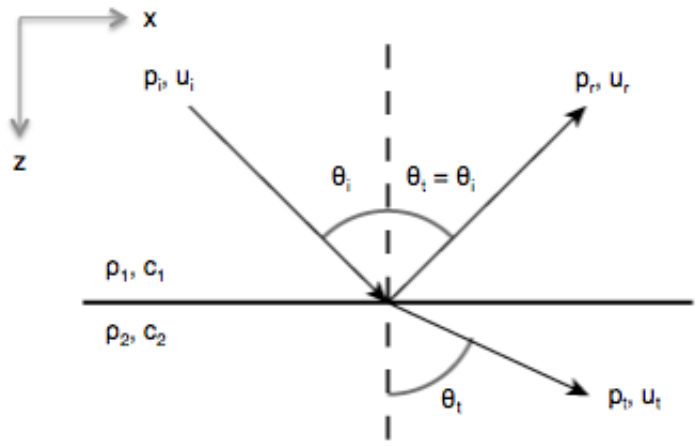

Figure 3.1: Geometry for reflection, transmission, and refraction of plane waves at an interface.

reflected, and transmitted pressures. The second boundary condition is that the components of the velocity normal to the interface, as a function of time, are equal ($u_{yi} + u_{yr} = u_{yt}$). For a harmonic solution, the time dependence does not affect the the solution and can be ignored. By solving for the two boundary conditions, the coefficients for the transmitted (T_{12}) and reflected (R_{12}) waves are described by

$$R_{12} = \frac{\rho_2 c_2 \cos(\theta_i) - \rho_1 c_1 cos(\theta_t)}{\rho_2 c_2 \cos(\theta_i) + \rho_1 c_1 cos(\theta_t)} \quad \text{and} \tag{3.6}$$

$$T_{12} = \frac{2\rho_2 c_2 \cos(\theta_i)}{\rho_2 c_2 cos(\theta_i) + \rho_1 c_1 \cos(\theta_t)}, \tag{3.7}$$

where ρ is the density of c is the sound speed of the mediums described in Figure 3.1. The propagation angle for the transmitted wave is found using Snell's Law according to

$$\theta_t = \sin^{-1}\left(\frac{c_2}{c_1}\sin(\theta_i)\right), \tag{3.8}$$

where θ_i is the incidence angle, θ_t is the refracted angle, c_1 is initial sound speed, and c_2 is the sound speed in the final second medium.

Figure 3.2a includes the reflection coefficients for incidence angles of 0 to 90 degrees for two cases: an air-water interface ($\rho_{air} = 1.25$ kg/m^3, $c_{air} = 343$ m/s) and a sediment-water interface ($\rho_{sed.} = 2{,}000$ kg/m^3, $c_{sed.} = 1800$ m/s). In both cases, the density and sound speed of water are the same ($\rho_{water} = 1{,}024$ kg/m^3, $c_{water} = 1{,}485$ m/s). For the air-water interface, the reflection coefficient is nearly unity for all incidence angles (i.e., nearly all

sound is reflected by the interface). For the sediment-water interface the total amount of reflection is dependent on the incidence angle. At low incidence angles there is significant transmission through the interface. In general, for bottom types with sound speeds and densities much larger than water (e.g., bedrock), more energy is reflected back into the water column.

Above the critical angle ($\theta_c = \sin^{-1}(c_1/c_2)$), although the entire incident wave is reflected, there is partial penetration into the second medium in the form of evanescent waves. To account for this, Snell's law is rewritten to permit imaginary components that later account for the phase shift of the reflected wave. This leads to a formulation of Snell's Law written as

$$\cos(\theta_t) = \left[1 - \left(\frac{c_2}{c_1}\right)^2 \sin^2(\theta_1)\right]^{1/2} = \pm ig, \tag{3.9}$$

where the only meaningful solution is the $-i$ term. A solution for R_{12} with the phase shift is obtained by solving for $cos(\theta t)$ and substituting the value back into Equation 3.7. For cases in which $|R_{12}| = 1$, the equation $R_{12} = exp^{+2i\Phi}$ is used to solve for the phase shift, Φ. The final formulations for the reflection and phase shift become

$$R_{12} = \frac{\rho_2 c_2 \cos(\theta_i) + i\rho_1 c_1 g}{\rho_2 c_2 \cos(\theta_i) - i\rho_1 c_1 g} \quad \text{and} \tag{3.10}$$

$$\Phi = \tan^{-1}\left(\frac{\rho_1 c_1 g}{\rho_2 c_2 \cos(\theta_1)}\right), \tag{3.11}$$

where is R_{12} the expression for reflection allowing phase shift and Φ is the phase shift of the reflected wave. For the sediment-water interface, Figure 3.2 includes phase shifts of reflected waves of difference incidence angles.

The transmission of sound into the seabed can be found by solving $T_{12} = 1 - R_{12}$. This equation is one of the intermediate steps in solving for the reflection coefficient and transmission represents one source of losses that need to be considered in sound propagation. The bottom loss that occurs with each interaction with the bottom is described by $BL = -20\log_{10}(|R_{12}|)$. Therefore, waves arriving at the seabed at angles associated with low reflection coefficients decrease in amplitude rapidly due to interactions with the bottom. In practice, perfect reflection does not occur due to absorption [*Mackenzie*, 1960]. Predicting bottom losses is further complicated by the natural variability of the bottom roughness and

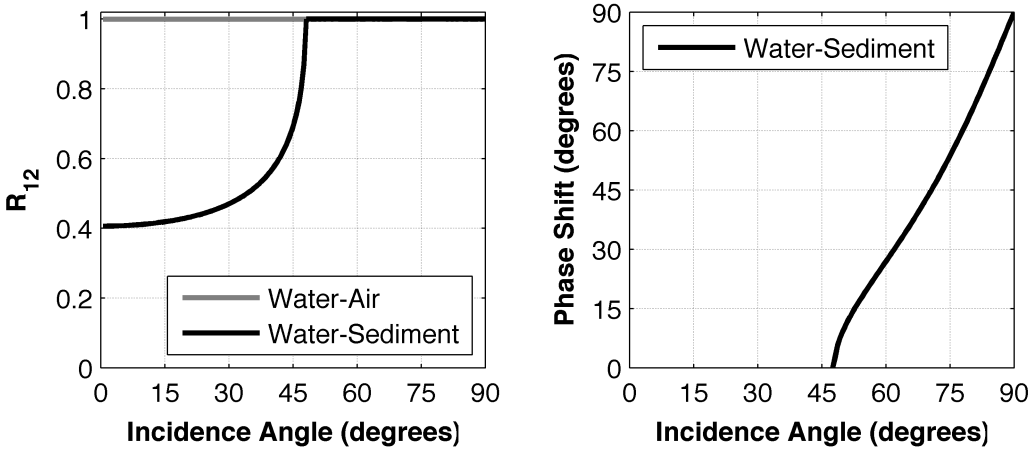

Figure 3.2: Reflection coefficients and phase shifts for an air-water (ρ_{air} = 1.25 kg/m^3, c$_{air}$ = 343 m/s) interface and a sediment-water interface ($\rho_{sed.}$ = 2,000 kg/m^3, c$_{sed.}$ = 1800 m/s). In both cases the properties of the water are ρ_{water} = 1,024 kg/m^3 and c$_{water}$ = 1,485 m/s.

changes in the composition in different layers of the seabed.

Based on conditions, the surface can act as a reflector or as scatterer of underwater sound. The Rayleigh parameter, $\chi = 2kH\sin(\theta_g)$, where H is the rms wave height, k is the acoustic wavenumber, and θ_g is the grazing angle, can be used to determine whether the surface will primarily act as a scatterer ($\chi \gg 1$) or as a reflector ($\chi \ll 1$) [*Urick*, 1975]. For extreme conditions in Puget Sound (H = 1.5 meters) [*Schwendeman et al.*, in revision] and frequencies less than 1 kHz where acoustic spectrum levels are highest in Admiralty Inlet, χ is less than one and should largely result in coherent reflection because the scale of surface roughness is small relative to the acoustic wavelength. These reflections near the air-water interface can interact with incident resulting in an interference pattern. In practice this effect, known as *Lloyd's mirror*, is limited to frequencies below a few kilohertz, ranges under a few hundred meters, calm surface conditions, and shallow sources and receivers [*Urick*, 1975].

3.4.4 Attenuation

Attenuation of sound in seawater is attributed to absorption by molecular and chemical relaxation. Following a pressure perturbation a compressible fluid returns to its former

state. This process is called molecular relaxation and the amount of energy absorbed by this process is related to the viscosity of the fluid. Chemical relaxation is the process of ionic dissociation and subsequent recombination with the passing of, in this case, pressure waves. In the ocean, pure water, boric acid, and magnesium sulfate are responsible for most of the absorption [*Medwin*, 2005]. An empirical equation accounting for the combined attenuation of sound by these three constituents, based on laboratory and field data, was introduced by *Francois and Garrison* [1982a, b]. The attenuation equation, split into terms for each of the three constituents, is

$$\alpha = \frac{A_1 P_1 f_1 f^2}{f^2 + f_1^2} + \frac{A_2 P_2 f_2 f^2}{f^2 + f_2^2} + A_3 P_3 f^2, \tag{3.12}$$

where the first, second, and third terms account for absorption by boric acid, magnesium sulfate, and pure water, respectively. The different A coefficients contain empirical relationships that combine the important variables, which include the salinity, sound speed, depth, temperature, pH of the water, and the relaxation frequencies of the salts. *Ainslie and McColm* [1998] introduced a simpler formulation made by neglecting higher order terms in the coefficients that results in differences of only a few percent. As suggested by the form of Equation 3.12, the attenuation of sound is water is highly dependent on frequency. When the constituents are combined, boric acid is important below 10 kHz, from 10-200 kHz magnesium sulfate dominates, and above 200 kHz pure water is the most significant contributor *Francois and Garrison* [1982a]. Attenuation rates are as little as 10^{-3} dB/km at 100 Hz and exceed 10^2 dB/km at 1 MHz.

Figure 3.3 shows attenuation rates using conditions representative of those typically found in Admiralty Inlet. A pH of 7.8 was used based on a study that included Admiralty Inlet [*Feely et al.*, 2010]. The other input variables are temperature (T = 9°C), salinity (S = 31 psu), and sound speed (c = 1483 m/s). A depth of 30 meters (mid-water column) was arbitrarily used in the calculations. For comparison, the total attenuation curve is split into the different components associated with the contribution of the salts and fresh water.

3.4.5 Sound Speed Profiles

The sound speed and sound speed profiles can affect the propagation of sound, the attenuation rate of sound, and is a necessary term in the acoustic intensity equation. Sound speed profiles are also critical input for numerical models. Multiple times per year University of Washington researchers perform CTD surveys near Admiralty Head as part of the Puget Sound Regional Synthesis Model (PRISM) cruises (www.prism.washington.edu). Using these data, sound speed profiles were calculated from CTD casts using the sound speed equations discussed in *Medwin* [1975]. The sound speed profiles (Fig. 3.4) show that the water column in Admiralty Inlet is generally well-mixed and sound speed typically vary by fewer than 3 m/s in the upper 60 meters of the water column.

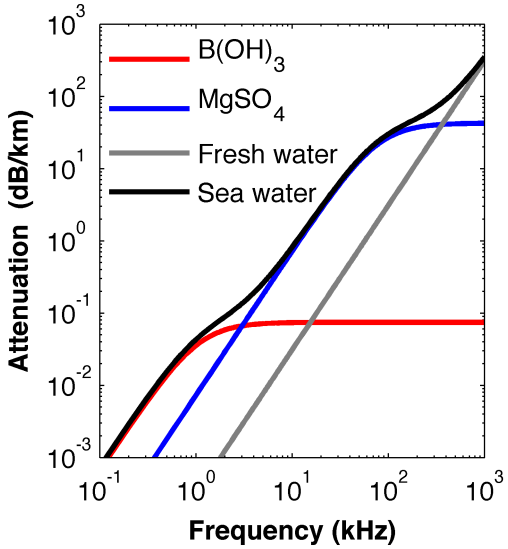

Figure 3.3: Attenuation rates of sound in seawater given typical conditions in Admiralty Inlet ($T = 9°C$, $S = 31$ psu, pH $= 7.8$, and $c =$ 1483 m/s). The attenuation rates attributed to the different components of seawater (salts and fresh water) are included.

3.5 Signal Processing

3.5.1 Discrete Fourier Transforms and Autospectra

A number of digital signal processing techniques exist to determine the frequency content of raw signals and the relationships between sets of signals. Numerous common signal processing techniques rely on the computation of Fourier transforms to convert signals from the time domain to the frequency domain. The most commonly used Fourier Transform algorithm is the Fast Fourier Transform (FFT) [*Cooley and Tukey*, 1965]. An important property of a Fourier transforms is the linear relationship between the time-series and the frequency spectrum (i.e., the total energy in the signal is conserved in the transformation

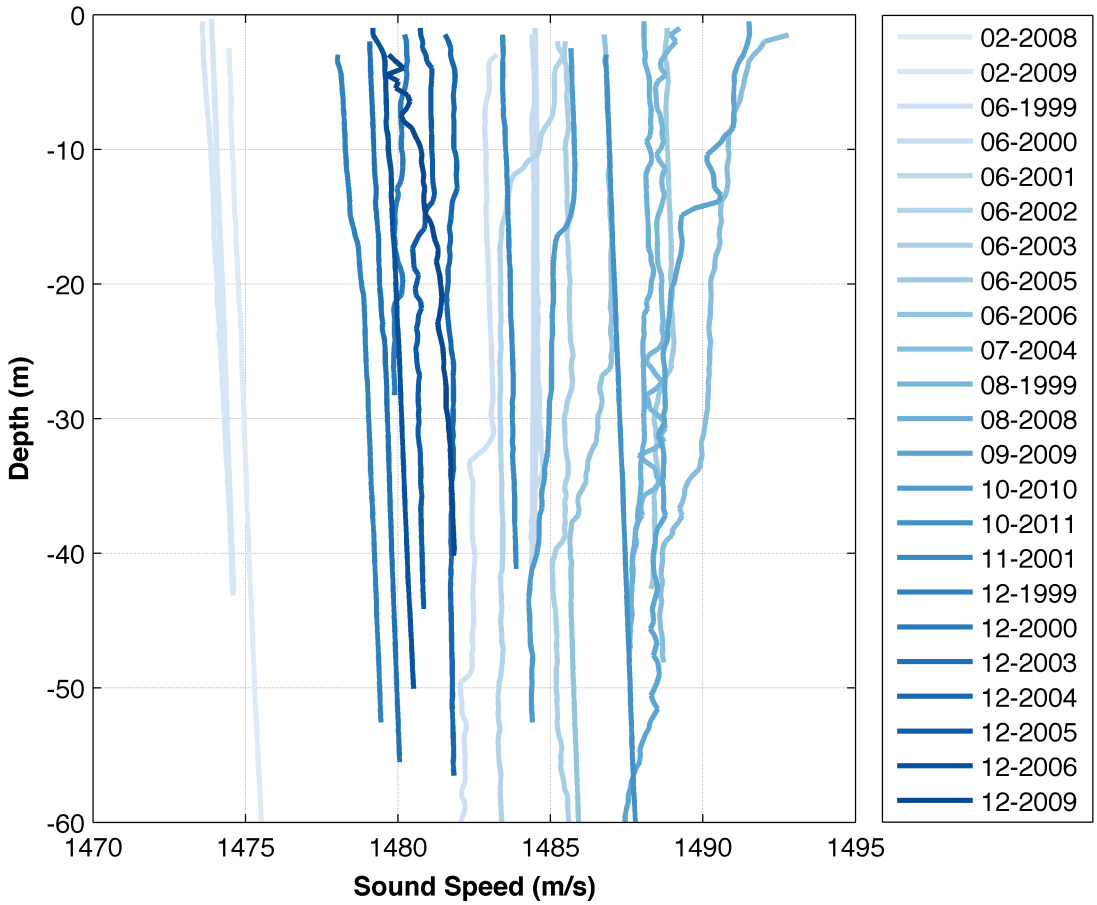

Figure 3.4: Sound speed profiles from PRISM cruise data. The legend highlights the month and year the data were acquired.

from the time domain to frequency domain).

For an infinitely long, continuous, stationary signal, a Fourier transform resolves a continuous spectrum. In practice, limits in sample length, sampling frequency, and data storage result in discrete signals of discrete lengths. Signal processing techniques to limit the effects of FFTs on discrete signals are well studied and covered in texts such as *Priestley* [1981] and *Emery and Thomson* [2004].

The maximum frequency that can be resolved by a FFT, the Nyquist frequency, is one-half of the sampling frequency. Aliasing refers to the distortion of a frequency spectrum that occurs when significant energy in a signal is present at frequencies greater than the Nyquist frequency. If transformed, this energy is folded until the spectrum at a lower frequency that can be resolved by the FFT. To limit the effects of aliasing, a raw signal is ideally filtered

using analog electronics prior to acquisition. In the case that the signal is not pre-filtered, the effects of aliasing are limited if the total energy contained above the Nyquist frequency is insignificant relative to the lower-frequency components of the signal.

Leakage in signal processing refers to the distribution of energy outside of its actual frequency band due to discrete frequency bins, discrete sampling, and the processing of the signal. Leakage can, in practice, limit the identification of unique spectral peaks of comparable magnitude located in adjacent frequency bins or peaks of significantly varying amplitudes in distant frequency bins. Functions that are applied to reduce leakage are referred to as window functions. Applying a window function to a raw signal prior the transformation limits leakage by changing the characteristic amplitude and attenuation of the side-lobes of peaks in the spectrum. In addition, a window that approaches zero at both ends of the signal reduces high-frequency ringing (Gibb's phenomenon) associated with discontinuities in the signal. Common window functions have well understood frequency responses [*Priestley*, 1981; *Emery and Thomson*, 2004].

Proper calculation of the acoustic spectrum, or autospectrum, using a FFT is easily implemented for time-frequency analysis. The spectrum levels (S_p) are calculated by

$$S_p(f) = \frac{2\left|\mathcal{F}\{x\}\right|^2}{N f_s}, \tag{3.13}$$

where $\mathcal{F}\{x\}$ is the FFT of the time series $x(t)$, N is the number of data points in the signal, and f_s is the sampling frequency. The resulting frequency of spectrum contains positive and negative frequencies which are symmetric. The N and f_s terms are included to properly normalize the FFT output. When properly normalized, calculating the spectrum by squaring the absolute values of the FFT of a signal is the mathematical equivalent of the Fourier Transform of the autocorrelation function (discussed below) of a signal. The proper normalization as presented in Equation 3.13 is specific to FFT algorithm used.

Prior to calculation of the FFT, signals are separated into windows. The desired resolution of the frequency spectrum, the length of the signal, and the desired confidence interval determine the number of windows. After transforming each window, an ensemble average determines the resulting spectrum. The underlying statistics of a transformed signal are

described by a χ^2 distribution. The equivalent degrees of freedom resulting from averaging different window functions are found in signal standard processing texts such as *Priestley* [1981] and *Emery and Thomson* [2004]. Band averaging (i.e., merging multiple frequency bands) is another technique of smoothing spectra. The error bars for each spectrum are calculated as

$$\frac{\nu\tilde{S}_p(f)}{\chi^2_{1-\alpha/2,\nu}} < S_p(f) < \frac{\nu\tilde{S}_p(f)}{\chi^2_{\alpha/2,\nu}}, \tag{3.14}$$

where ν is the equivalent degrees of freedom, $\tilde{S}_p(f)$ is the calculated spectrum, α is the confidence interval, and $S_p(f)$ is the actual (unknown) spectrum.

3.5.2 Cross-Spectral Methods

Coherence refers to frequency-space relationship between two independent signals. Commonly presented as the squared-coherence (γ^2_{12}), although often referred to as simply the coherence, it always satisfies the condition $0 \leq \gamma^2_{12} \leq 1$. A coherence of zero indicates uncorrelated signals. The squared-coherence is calculated by

$$\gamma^2_{12} = \frac{|S_{12}(f)|^2}{S_{11}(f)S_{22}(f)} = \frac{[C_{12}(f)]^2 + [Q_{12}(f)]^2}{S_{11}(f)S_{22}(f)}, \tag{3.15}$$

where S_{12} is the one-sided cross-spectrum, S_{11} is the autospectrum of the first signal, and S_{22} is the autocorrelation of the second signal. The coincident spectrum, C_{12}, also called the co-spectrum, consists of the real components of the cross-spectrum and identifies in-phase components of the signals. By contrast the quadrature spectrum, Q_{12}, or quad-spectrum, identifies out-of-phase components of the cross-spectrum. Each component of Equation 3.15 is calculated according to the previously identified signal processing techniques (e.g., windowing) prior to the calculation of the coherence.

Confidence levels for coherence represent the lowest squared-coherence levels that are expected occur randomly. *Thompson* [1979] predicted the significance of squared-coherence values and compared the predictions to Monte Carlo simulations used to identify significant coherence levels. Results from the work demonstrate that the confidence interval is related to the number of degrees of freedom of the squared-coherence by

$$\gamma_{1-\alpha} = 1 - \alpha^{[\frac{2}{\nu-2}]}, \tag{3.16}$$

where $1-\alpha$ confidence level and ν is the number of degrees of freedom is the cross-spectrum calculation.

In addition to the coherence, phase relationships between signals are calculated using cospectra and quadspectra. The phase lag between two signals is calculated by

$$\phi_{12}(f) = \tan^{-1}\left(\frac{-Q_{12}(f)}{C_{12}(f)}\right), \tag{3.17}$$

where ϕ_{12} is the phase lag by frequency, Q_{12} is the quadspectrum, and C_{12} is the cospectrum. Phase lag estimates are suspect, although not necessarily incorrect, when squared-coherence levels do not exceed the chosen confidence level.

3.5.3 Autocorrelation and Crosscorrelation

The autocorrelation is a calculation of a signal's correlation with itself, and is a measure of a how a compares to itself in time. A crosscorrelation, by comparison, measures relationship between signals separated in time. Both the autocorrelation and the crosscorrelation can be used to identify periodic signals and can be applied in spectral analysis methods. The autocorrelation is calculated according to

$$R_{xx}(\tau) = \frac{1}{N}\sum_{\tau=1}^{N}(x_t x_{t+\tau}), \tag{3.18}$$

where R_{xx} is the autocorrelation function as a function of the time lag τ, N is the number of data points in the signal, and x is the value of the signal at each index t. The cross-correlation, R_{xy}, is calculated by replacing the final term in Equation 3.18, $x_{t+\tau}$, with the signal from an independent time series, $y_{t+\tau}$. Zero-crossings and periodicity of autocorrelation functions are associated with decorrelation time scales and harmonic behavior. In cross-correlations functions, significant peaks indicate potentially meaningful time lags between the variables. In this document these functions are only used to identify time lags and decorrelation time scales in Chapter B.

Chapter 4

AMBIENT NOISE: VESSEL NOISE BUDGET

The text of the following chapter was published in the *Journal of the Acoustical Society of America* in December, 2012. With the exception of removing site details and reformatting the text, no changes were made to the content of the original article. The citation for the published document is as follows:

Bassett, C., B. Polagye, M. Holt, and J. Thomson, A vessel noise budget for Admiralty Inlet, Puget Sound, Washington (USA), *J. Acoust. Soc. Am., 132(6)*, 3706-3719, 2012.

4.1 Introduction

The impacts of high energy, impulsive sources of anthropogenic sounds such as sonars and seismic exploration on marine species have been an area of active research [*National Research Council*, 2000, 2003]. Increasingly, concerns have expanded to include continuous, lower energy sources such as shipping traffic. Low-frequency ambient noise levels in the open ocean have long been attributed to maritime traffic [*Wenz*, 1962; *Urick*, 1975; *Ross*, 1976; *Greene and Moore*, 1995; *McDonald et al.*, 2006, 2008; *Hildebrand*, 2009; *Frisk*, 2012]. Low-frequency (<500 Hz), high energy (>180 dB re 1 μPa at 1 m) noise generated by large shipping vessels propagates efficiently across ocean basins, contribut- ing to ambient noise levels over large distances (>100 km). At shorter distances (<10 km), higher frequency noise may also be significant [*National Research Council*, 2003].

The acoustic signature (i.e., spectral characteristics) of a vessel depends on its design characteristics (e.g., gross tonnage, draft), on-board equipment (e.g., generators, engines, active acoustics equipment), and operating conditions (e.g., speed, sea state) [*Ross*, 1976]. The primary sound generation mechanism for commercial vessels is cavitation, which produces broadband noise and tonal components related to the rotation rate of the ship pro-

peller [*Gray and Greeley*, 1980]. Source levels for vessels, referenced to dB re 1 μPa at 1 m, range from 150 dB for small fishing vessels and recreational watercraft to 195 dB for super tankers [*Gray and Greeley*, 1980; *Kipple and Gabriele*, 2003; *Hildebrand*, 2005]. Peaks in spectral levels for shipping traffic occur at frequencies less than 500 Hz with substantial tonal contributions as low as 10 Hz [*Ross*, 1976; *Scrimger and Heitmeyer*, 1991; *Greene and Moore*, 1995]. Small ships are quieter at low frequencies but can approach or exceed noise levels of larger ships at higher frequencies [*Greene and Moore*, 1995; *Kipple and Gabriele*, 2003; *Hildebrand*, 2005]. Radiated noise levels are also directional and vary based on vessel orientation or aspect [*Arveson and Vendittis*, 2000; *Trevorrow et al.*, 2008]. In addition to mechanical noise, active acoustics devices are a significant high-frequency noise source due to the widespread use of fish finding and depth sounding devices [*National Research Council*, 2005]. Source levels for common active acoustics devices are on the order of 150-200 dB at frequencies from 3 to 200 kHz, with the most common commercial devices operating above 50 kHz [*National Research Council*, 2003; *Hildebrand*, 2004]. However, downward directionality and rapid attenuation at high frequencies limit their contribution to broadband noise levels over large spatial scales.

To understand the effects noise may have on marine mammal populations, the frequency content of different noise sources should be evaluated because mammalian hearing is not uniformly sensitive to all frequencies and different species have different hearing ranges. On the basis of available audiograms, *Southall et al.* [2007] proposes a weighting function or "M-weighting" for five groups of marine mammals based on functional hearing ranges to better quantify sound exposure for predicting auditory injury and other exposure effects in these animals. The five functional hearing groups are low-frequency cetaceans (baleen whales), mid-frequency cetaceans (toothed whales and most oceanic dolphins), high-frequency cetaceans (porpoises, river dolphins, and other small cetaceans), pinnipeds (seals, seal lions, and walruses) in water, and pinnipeds in air. Southall *et al.* note that these weighting functions are precautionary and, in some cases, are likely to overestimate the sensitivity of individuals. The four functional hearing groups relevant to this study are low-frequency cetaceans, mid-frequency cetaceans, high-frequency cetaceans, and pinnipeds in water.

Noise budgets quantify the relative contributions of different sources to ambient noise levels. Ambient noise is typically defined as the background noise attributed to natural physical processes and, increasingly, anthropogenic sources [*Dahl et al.*, 2007]. Some definitions exclude identifiable sources such as individual vessels [*National Research Council*, 2003]. Because vessel traffic is ubiquitous in busy coastal areas, the former definition (including individual vessels) is adopted for this study. In the case of shipping traffic, the National Research Council suggests identifying the contributions of unique vessel types over different temporal and spatial scales [*National Research Council*, 2003; *Southall*, 2005]. Such information is needed to assess the impact of vessel noise on marine mammals in coastal waters, which often serve as critical habitat. *Hatch et al.* [2008] undertook a study of vessel noise and estimated a vessel noise budget for the Stellwagen Bank National Marine Sanctuary (SBNMS) to better understand the effect this noise might have on endangered North Atlantic right whales (*Eubalaena glacialis*). A similar methodology is applied to develop a vessel noise budget for Admiralty Inlet, Puget Sound, WA. This study varies from *Hatch et al.* [2008] in that it considers frequencies up to 30 kHz rather than an upper limit of 1 kHz. Furthermore, this study treats anthropogenic noise in a biologically specific manner by comparing M-weighted statistics to unweighted broadband noise statistics.

4.2 Methods

4.2.1 Acoustics Data

Autonomous hydrophones positioned 1 m above the seabed were used to collect acoustic data. The hydrophones were deployed on a fixed tripod at a depth of approximately 60 m. All deployments were within 45 m of the coordinates 48.1530°N, 122.6882°W. The acoustic recording system consisted of a self-contained data acquisition and storage system (Loggerhead Instruments DSG, Sarasota, FL) with a hydrophone (HTI-96-Min) and internal preamplifier. The hydrophone had an effective sensitivity of 166 dB re μPa/V. Digitized 16 bit data were written to a Secure Digital (SD) card. or ambient noise analysis, data were obtained during four deployments of three months duration (May 7, 2010 to May 9, 2011). The sampling frequency was 80 kHz on a 1% duty cycle (7 s continuous recording every

10 min). A shorter deployment (from February 10 to February 21, 2011), sampled at 80 kHz on a 17% duty cycle (10 s at top of each minute), was used to estimate acoustic source levels for different vessel types. Data from all deployments were analyzed from 20 Hz to 30 kHz. Throughout this document, decibels are referenced to 1μPa.

Each recording was post-processed into windows containing 65,536 (2^{16}) data points with a 50% overlap. Windows were detrended, weighted by a Hann function, and a Fast Fourier Transform (FFT) was applied. Resulting spectra were then scaled to preserve total variance. Variable frequency-band merging was applied on a decadal basis to produce smooth, well-resolved spectra with high confidence. The frequencies, number of merged bands, resulting bandwidth, and the equivalent degrees of freedom of the spectra are included in Table 4.1.

Daily, hourly, and monthly statistics for unweighted broadband sound pressure levels (0.02 to 30 kHz) and M-weighted levels were calculated using hydrophone recordings collected between May 7, 2010 and May 1, 2011. For each calculation, recordings were split into subsets representing the statistical value of interest. For example, statistics for the hour of 01:00 to 02:00 were calculated by identifying all recordings taken between these hours over the course of the year. The mean representing the hour from 01:00 to 02:00 was obtained by averaging all recordings included in that subset. For all temporal statistics, M-weighted values for the four marine mammal functional groups (low, mid, and high-frequency cetaceans; pinnipeds in water) were also calculated. Temporal statistics were calculated in local time to account for daily patterns associated with scheduled vessel traffic (e.g., ferries operate on local time).

Cumulative probability distribution functions were calculated by binning unweighted and M-weighted broadband sound pressure levels. The distributions were obtained by defining discrete sound pressure level bins, identifying the number of weighted and unweighted recordings below the defined upper threshold for each bin, and normalizing the results by the total number of recordings in the analysis. The cumulative probability distribution functions highlight the overall temporal distribution of noise level statistics. A modeled cumulative probability distribution of unweighted broadband sound pressure levels was compared with the measured distribution.

Table 4.1: Merged frequency bands.

Freq. (kHz)	0.01-0.1	0.1-1	1-10	10-30
Merged Bands	0	3	19	41
Δf (Hz)	1.2	3.7	23.2	50.0
Degrees of Freedom	10	30	190	410

4.2.2 Current Measurements

Peak tidal currents in northern Admiralty Inlet exceed 3.0 m/s [*Thomson et al.*, 2012]. When strong currents flow over the hydrophone, the turbulent pressure fluctuations are recorded by the hydrophone as additional noise. These pressure fluctuations, often referred to as pseudosound or flow-noise, are non-propagating and are of sufficient intensity to mask propagating noise sources including large ships [*Lee et al.*, 2011]. Because pseudosound is non-propagating, it should not be included in the noise budget. In addition, when depth averaged currents exceed 1 m/s, noise levels increase with current at frequencies greater than 2 kHz. These increases are consistent with the mobilization of gravel, small cobbles, and shell hash [*Thorne et al.*, 1984; *Thorne*, 1990].

Acoustic recordings with depth-averaged currents exceeding 0.4 m/s were excluded from this analysis to prevent biasing the statistics with pseudosound, which also excludes propagating ambient noise from bedload transport. These periods were identified using co-spatial velocity records from an Acoustic Doppler Current Profiler (470 kHz Nortek Continental). Current profiles were calculated in 1-meter bins using 10-minute ensemble averages.

To verify that excluding periods with strong currents from analysis was not likely to bias statistics related to vessel noise, an average vessel presence was calculated in 0.1 m/s velocity bins for all current data. In each bin, a summation of all recorded vessel minutes was normalized by the total number of minutes during which currents in each bin were recorded. The results were compared to justify the assumption that vessel presence was independent of currents.

4.2.3 Automatic Identification System Data

Automatic Identification System (AIS) transponders are used as a real-time collision avoidance tool and are mandated for commercial maritime vessels exceeding 300 gross tons, tugs and tows, and passenger ships [*Federal Register*, 2003]. Although not required, some recreational vessels are also equipped with the AIS transponders. AIS transponders transmit very high frequency radio signals, referred to here as AIS strings, containing dynamic ship information (i.e., position, heading, course over ground, and speed over ground) up to twice per second while a vessel is in transit. Static information, including but not limited to ship name, type, length overall, draft and destination are transmitted every 6 min while in transit. A unique Maritime Mobile Service Identity (MMSI) number is transmitted with both static and dynamic data.

AIS transmissions were logged by a receiver (Comar AIS-2-USB, Comar Systems Ltd., Cowes, UK) on the Admiralty Head Lighthouse at Fort Casey State Park, WA, approximately 1 km from the hydrophone deployment site. The receiver was connected to a data acquisition computer running a PYTHON script to record all incoming AIS strings and append time stamps. In post-processing, a PYTHON package (NOAA data version 0.43) [*Schwehr*, 2010] converted all received AIS transmissions into an array of text data for further manipulation. For each received AIS string with dynamic data, the MMSI number, speed over ground, course over ground, and vessel coordinates were stored. Static information including the vessel length overall, vessel name, and vessel type were recorded in a look-up table containing information about all vessels recorded in the study area.

The vessel coordinates from the processed AIS strings containing dynamic ship information were used to calculate a radial distance between the ship and the hydrophone (given a water depth of approximately 60 m, the radial distance and slant distance were nearly equivalent for most transmissions). Dynamic AIS information for each vessel in the study area at any time was averaged over one-minute periods. Data were filtered to include only those AIS transmissions from vessels underway (speed over ground greater than 0.1 knots) in the contiguous water of Puget Sound within 20 km of the hydrophone deployment. Transmission/receipt of implausible local coordinates (latitude $> 90°$, longitude $> 180°$) occurred

infrequently and has been noted in other studies [e.g., *Harati-Mokhtari et al.*, 2007].

Records of MMSI numbers, ship types, and ship lengths were compared against online public information. Using vessel names, information was found by searching a registered vessel database in the United States or other available online fleet information.[a] To the greatest extent possible, unknown and incorrect ship types were corrected to accurate values, unrealistic speeds over ground removed, incorrect ship lengths updated, and records with invalid MMSI numbers excluded through manual analysis.

The vessels were separated into four broad categories, as defined by their AIS vessel codes: "commercial" (AIS codes 70-89, 30-32, 52), "passenger" (60-69), "other" (90-99), and "various" (all other codes). Within the commercial category, vessels were further separated by AIS vessel code into cargo ships (AIS code 70-79), tankers (80-89), tugs (31,32,52), and fishing vessels (30). The cargo category was subdivided into four different vessel types, using their MMSI numbers, emphasizing differences in vessel design related to the type of transported good. The four cargo types include container vessels, vehicle carriers, general cargo vessels, and bulk carriers. The cargo type for each vessel was determined by cross-checking the vessel name with available fleet information. Throughout the rest of the document, references to cargo vessels include the four types within this category unless otherwise noted.

Within the passenger category, vessels were separated by MMSI into local passenger ferries, cruise ships, and "passenger other" for vessels that do not fit into the first two passenger vessel designations. As for cargo vessels, this categorization was motivated by the presence of vessels with the same AIS vessel code, but different design characteristics. For example, a small whale-watching vessel (length overall < 20 m) and a cruise ship both used AIS code 60 while their expected source levels varied significantly. The category "various"

---

[a]For smaller vessels, including small U.S. flagged cargo vessels, tugs, fishing vessels, and vessels falling into the categories of "other" and "various", registration data (http://www.boatinfoworld.com/) was used. Searches by vessel name result in information that includes vessel type, size, and length, which were cross-checked against AIS data. Similarly, online fleet information was used for many commercial vessels to cross-check registration and AIS data (e.g., http://westerntowboat.com/Tugs/ to confirm registration data for the vessel Western Mariner; http://www.cosco.com/en/fleet/ to confirm COSCO fleet information)

was used to combine uncommon ship types (e.g., underwater operations vessels and anti-pollution equipment) and ship types underrepresented by AIS statistics (e.g., military vessels and pleasure craft). The vessel code "other," an AIS designation, was used by vessels that have no formal designation that fits within another class (e.g., research vessels).

The average and standard deviations of the speed over ground and length overall were determined for each type. These metrics were calculated directly from all one-minute averaged data associated with each type. By this method, slow moving vessels contributed more points to the statistics, potentially biasing the statistics towards the speeds and lengths of the slower vessels. However, the statistics calculated using this method were similar, within 3 knots of speed over ground and 10% of the length overall, to distance-weighted statistics for all vessel types but ferries. For ferries, the statistics were different due to a distribution dominated by a set of small, faster moving ferries and a larger, slower moving ferry.

To visualize vessel traffic, average location data for each one-minute period were gridded into 100-meter bins and the total number of minutes of vessel presence in each bin calculated by vessel type. Opportunistic sightings of vessels not transmitting AIS data (e.g., military vessels) served to inform the interpretation of results but were not included in the analysis.

The AIS data acquisition system was intermittently inactive for approximately 42 days (11% of the year) due to power failures and hardware malfunctions. All statistics and calculations were based on received data and no attempt was made to extrapolate the data to account for receiver outages.

4.2.4 Acoustic and AIS Data Integration

Data from the higher duty cycle deployment (from February 10 to February 21, 2011) were used to estimate the source levels for three vessel types. Acoustic and AIS data were combined and source levels (SL) were backcalculated using the received levels (RL) and the sonar equation. The acoustic source level represents the sound pressure level (SPL) at a nominal distance of 1 m from the source, although for a large, multi-point source such as a cargo vessel, this quantity is an abstraction. Transmission losses account for geometric spreading of an acoustic wave and losses associated with boundaries and attenuation. At

low frequencies (< 1 kHz), where most of the energy from large commercial ship traffic is contained, and at the spatial scales considered in this study, attenuation effects from seawater are negligible [*Ainslie and McColm*, 1998]. Source levels were calculated by

$$SL = RL + N\ \log_{10}(r), \tag{4.1}$$

where N was the transmission loss coefficient and r was the radial distance between vessel and hydrophone in meters, as determined from AIS position data. Source levels for individual ships were calculated from RL data at the closest point of approach (CPA). We used a transmission loss coefficient of 15, a value justified by range dependent parabolic equation (PE) modeling of sound propagation at key frequencies at the site (Appendix 4.6). When no AIS-equipped vessels were within the study area, a received level of 100 dB was assumed, a value consistent with the lowest recorded broadband sound pressure levels (0.02 - 30 kHz) at the site.

For each type of vessel, the total amount of time spent in the survey area (vessel hours) was determined from the AIS data. The energy inputs to the vessel noise budget were calculated for each vessel type on the basis of an assumed source level and time spent within the study area. The assignment of source levels to vessel classes is discussed in Sec. 4.3.3. Source levels, in watts, were converted to power by

$$SL\ [W] = \frac{A\ p^2}{\rho\ c} = 4\pi \frac{\left(10^{-6} * 10^{\frac{SL[dB]}{20}}\right)^2}{\rho\ c}, \tag{4.2}$$

where A was the area of a 1 m sphere surrounding the idealized source, and the source level on the right-hand side was in the units of dB re μPa at 1m. Because of the strong currents over the Admiralty Inlet sill, the water column is generally well-mixed with minimal stratification [*Polagye and Thomson*, 2010] so a constant sound speed (c = 1490 m/s) and density (ρ = 1024 kg/m^3) were appropriate for this location. The energy budget was calculated by combining the source power output and the total amount of time spent by a given vessel type in the study region according to

$$E\ [J] = \sum_{j=1}^{n} SL_j[W] * t_j[s], \tag{4.3}$$

where E was the energy budget in joules, SL was the source level in Watts, t was the time interval, and j was the index for the vessel.

The contribution of vessels to ambient noise was calculated using a first-order reconstruction of received noise levels based solely on information about vessel locations, vessel types, and characteristic source levels. One-minute averaged AIS data and estimates of vessel source levels were used to model the received level at a given time by

$$RL(t)\ [dB] = 10\ \log_{10}\left(\sum_{k=1}^{n}\left(\frac{10^{SL_k\ [dB]}}{r_k^N}\right)^{\frac{1}{10}}\right), \tag{4.4}$$

where $RL(t)$ was the modeled received level during time interval (t), n was the total number of vessels in the area interval during the time interval, SL_k was the source level, r_k was the horizontal distance between the receiver and vessel k (of known class), and N was the single-valued transmission loss coefficient of 15. Regions within 500 m of the local ferry docks on either side of Admiralty Inlet were excluded due to the rapid decrease in source level as the ferry approached the dock. This model presumes that aggregate vessel noise is given by the incoherent addition of multiple vessel sources. The summation was calculated for each one-minute interval to produce a time series of reconstructed received levels attributable to vessels. These were compared to received level statistics derived from hydrophone recordings over the same time period to estimate the contribution of vessel noise to the ambient noise budget.

An energy flux cumulative probability distribution function was constructed by converting the received levels in decibels to acoustic intensities (linear scale), and multiplying the acoustic intensities by the amount of time they are observed. The energy flux distribution was used to compare the contribution of acoustic energy flux from vessels to the total acoustic energy flux measured by the hydrophone.

As discussed in Sec. 4.2.2, periods with strong currents (> 0.4 m/s) were excluded from ambient noise analysis to remove to effects of pseudosound. This is a conservative restriction and only 18.4% of the data (8,856 recordings) satisfied this criterion. Analysis of bin-averaged vessel presence showed that there were, on average, approximately 2.5 vessels in the study area at any given time. Vessel presence was approximately constant during

the lowest 95% of the measured current velocities. During the strongest currents (> 2.3 m/s), overall vessel presence decreased to 1.8 vessels. Given that mean vessel presence across velocity bins was constant, with only modest decreases when currents exceeded the 95^{th} percentile, we concluded statistics were not biased by the exclusion of data due to pseudosound.

4.3 Results

4.3.1 Vessel Traffic

Over the 1-year period (May 1, 2010-May 1, 2011), a total of 1,376 unique vessels were recorded in the study area. Of this total, only 13 were unidentified due to invalid MMSI numbers. Based on overall presence, tugs, passenger ferries, and container ships were the most common vessel types. Other large commercial vessels, including vehicle carriers and bulk carriers, were also common. An AIS-transmitting vessel was found to be present within the study area 90% of the time, and multiple vessels were present 68% of the time. The number of unique vessels and the total number of hours spent in the survey area, by type, are included in Table 4.2. Also included are the average and standard deviations of speed over ground (SOG) and length overall (LOA). Cargo ships, especially vehicle carriers and container ships, transit the study area at higher speeds than the other types of commercial traffic. The fast moving vessels elevate received levels at the hydrophone site for up to 30 min, while slower moving vessels elevate received levels for up to 60 min.

Vessel density maps by type (Fig. 4.1) are used to visualize the temporal and spatial distributions of ships contributing to the noise budget during the study period. Each vessel density plot is presented with a unique color scale to avoid saturation and provide details that would not appear if common colorbar axes were used. Vessel traffic regulations result in limited spatial variability for traffic patterns, with most commercial vessels present in the designated traffic lanes passing through the middle of the inlet. Cargo ships generally arrive from or are bound for the open waters of the Pacific Ocean, while tanker and tug traffic typically transits along the inland Washington coast. Fishing vessels and those classified as "other" or "various" are less likely to utilize the shipping lanes while transiting the study

Table 4.2: Ship traffic summary including the total number of vessels, the total number of vessel-hours spent in the study area, average speed over ground, and average length overall by vessel class and type. SOG and LOA values include the standard deviations.

Vessel Class	Vessel Type	No. Vessels	Vessel-Hours[b]	SOG (kn)	LOA (m)
Commercial	Container	237	2,113	20.1 ± 2.6	264 ± 48
	Vehicle Carrier	123	611	18.8 ± 2.9	212 ± 35
	General Cargo	35	292	12.4 ± 3.1	121 ± 59
	Bulk Carrier	208	755	13.5 ±2.0	206 ± 23
	Tanker	31	240	14.1 ± 2.4	206 ± 49
	Tug	212	8,502	7.7 ± 2.9	29 ± 13
	Fishing	259	1,577	9.3 ± 2.8	46 ± 25
Passenger	Ferry	19	3,868	13.7 ± 7.8	72 ± 21
	Cruise	22	551	16.4 ± 3.7	248 ± 63
	Other	15	75	8.8 ± 5.1	30 ± 14
Other	-	30	330	9.4 ± 4.2	55 ± 52
Various	-	173	1,184	10.8 ± 5.5	63 ± 57
Total		1364	20,100		

[b]AIS system operated for 7,761 hours during the year. Two vessels in the study area during the same time interval count as two vessel-minutes.

area. The passenger vessel map clearly demonstrates that the local ferry route dominates the passenger vessel density map, although ferries en route to Victoria, BC and cruise ships en route to Alaska are also evident.

4.3.2 Ambient Noise

Broadband and one-third octave band sound pressure levels for a 12 h provide important detail on how ambient noise levels vary at the study site (Fig. 4.2). For example, increased noise levels below 50 Hz correspond to pseudosound (velocity $\approx$ 0.5 m/s) at the hydrophone between 0 - 1.5 hours. Unique spectral characteristics associated with individual vessel passages are also present during this 12-hour recording and correspond to AIS ship tracks (Fig. 4.2; Tab. 4.3). The maximum broadband sound pressure level observed during the 12 h period, 140 dB re 1μPa, corresponds to the passage of a container ship in the southbound shipping lane at a range of 2.7 km (CPA 1 in Fig. 4.2; Tab. 4.3). In general, the largest increases in received levels are concentrated at frequencies less than 1 kHz. However, these are broadband events, with acoustic energy increasing in all one-third octave bands (center frequencies up to 25 kHz).

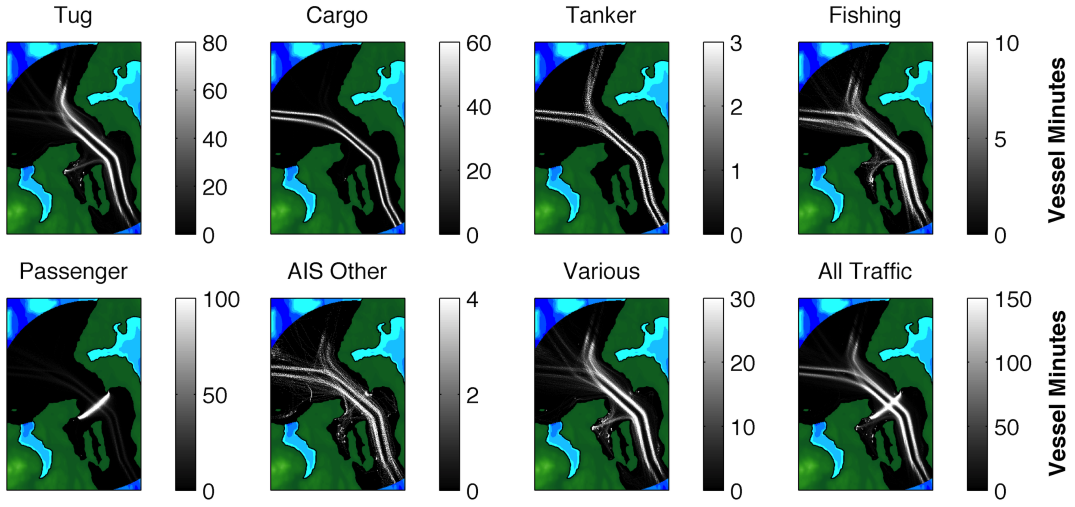

Figure 4.1: Ship traffic density map plotted on a 100 m x 100 m horizontal grid. Each subplot represents an area with the dimensions of 28 km by 40 km. In the passenger vessel density subplot, grid points located under the ferry traffic route are saturated to avoid obscuring the traffic patterns of other passenger vessels such as high-speed ferries.

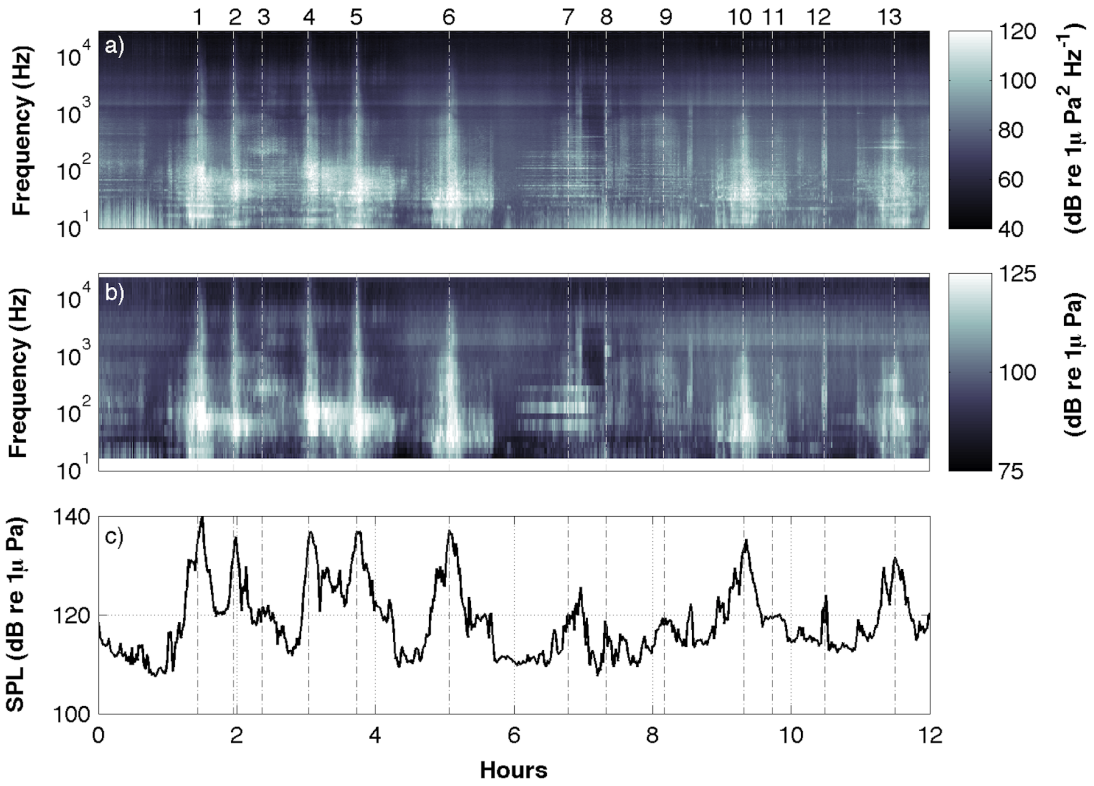

Figure 4.2: Sample acoustic data from February 12, 2011. The time series are constructed from 10 s recordings every minute. a). Spectrogram showing regular increases in energy content over all frequencies due to vessel traffic. b). Time series of one-third octave band SPLs with center frequencies from 16 Hz to 25 kHz. c). Time series of broadband SPLs (0.02 - 30 kHz).

The cumulative probability distribution functions for sound pressure levels are shown in Figure 4.3 on a broadband (unweighted) and M-weighted basis. The mean broadband SPL at the site is 119.2 $\pm$ 0.2 dB (95% confidence interval). Statistics for received M-weighted levels are influenced by the sensitivity of the functional groups to different frequencies. That is, low-frequency cetaceans have the most sensitive hearing at frequencies overlapping peak sources levels from vessel traffic. Therefore, M-weighted levels for low-frequency cetaceans are similar those to the measured distribution. For the other functional groups, M-weighted received levels decrease corresponding to the decreased sensitivity in the range of peak levels from vessel traffic. For high-frequency cetaceans, the functional group least sensitive to low-frequency noise, mean M-weighted sound pressure levels are approximately 5 dB lower than the mean for low-frequency cetaceans.

Table 4.3: Vessel name, type, LOA, SOG, and CPA for events highlighted in Fig. 4.2.

Name	Vessel Type	LOA (m)	SOG (kn)	CPA (km)
1 Manoa	Container	261	23.4	2.7
2 Horizon Kodiak	Container	217	20.5	1.5
3 Norma H	Tug	24	7.2	2.9
4 Hong Yu	Bulk Carrier	226	13.8	1.5
5 Great Land	Vehicle Carrier	243	22.9	1.4
6 Zim Chicago	Container	334	21.1	2.7
7 Chetzemoka	Ferry	83	10.7	2.4
8 Chetzemoka	Ferry	83	9.5	1.2
9 Henry Sause	Tug	33	9.3	3.0
10 Xin Ri Zhao	Container	263	20.9	2.6
11 Ocean Mariner	Tug	29	5.0	2.8
12 Chetzemoka	Ferry	83	12.5	1.3
13 Ever Excel	Container	300	18.5	2.8

Hourly, daily, and monthly mean broadband SPLs and ranges for the percentile statistics are shown in 4.4. Diurnal patterns are primarily attributed to the absence of ferry traffic and periodic lulls in commercial shipping at night. Monthly averages are highest during the summer, in part due to cruise ship traffic. High average noise levels in January, when compared to December and February, are a result of higher levels of commercial ship traffic during the typically less noisy periods in the late evening and early morning. Measured noise levels are comparable to reported values from Haro Strait off of the west coast of San Juan Island, WA (USA) [*Veirs and Veirs*, 2005]. Broadband SPLs (0.1-15 kHz) at that location were 117.5 dB during the summer and 115.6 dB throughout the rest of the year. In Admiralty Inlet, the mean broadband SPL calculated over the same frequency range for the entire year in the current study was 116.2 $\pm$ 0.2 dB (95% confidence interval).

Received level percentile statistics of pressure spectral densities, broadband SPLs, and one-third octave band SPLs were derived from cumulative probability distributions. Figure 4.5 shows the percentile spectra associated with the broadband received levels. One-

third octave band SPLs are nearly constant, around 90 dB from approximately 100 Hz to 20 kHz, during quiet periods. The largest variations in energy content between quiet and loud periods ($f < 1$ kHz) are consistent with commercial ship traffic. A spectral peak at approximately 1.5 kHz was regularly identified in data sets from the site and is approximately 6 dB higher than adjacent frequencies. The peak scales with the energy in the acoustic spectrum (i.e., there is a 6 dB peak at 1.5 kHz relative to both the 5% and 95% spectra). This feature is consistent with constructive interference near the sea bed since the corresponding wavelength of the peak is 1m, the same distance as between the hydrophone and the seabed.

4.3.3 Vessel Source Levels and Energy Budget

A combination of site-specific data and literature values was used to attribute source levels to vessel types. The energy budget and received level model in this study are most sensitive to the source levels of cargo ships, tugs, and ferries due to their relative presence. Less common vessel types in this study show significant variability in length and SOG. Therefore, choosing a characteristic source level for the less common vessel types is difficult. Since the literature is limited the approach used here to assign source levels is, by necessity, ad hoc, with all source level assumptions described in the following section.

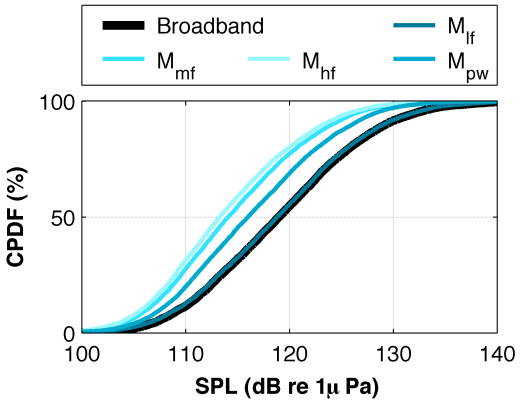

Figure 4.3: Cumulative probability distribution function of unweighted broadband SPLs (0.02 - 30 kHz) and M-Weighted cumulative probability distribution functions for pinnipeds in water (M_{pw}) and low (M_{lf}), mid (M_{mf}), and high-frequency (M_{hf}) cetacean marine mammal functional hearing groups.

The validity of applying a single-valued transmission loss coefficient to estimate source levels based on Eq. 4.1 is contingent on its accuracy at key frequencies of vessel noise. Figure 4.6 includes example spectra for a cargo ship, the local ferry, and a tug at their CPA. In the received spectra from the closest points of approach, peak spectrum levels occur well

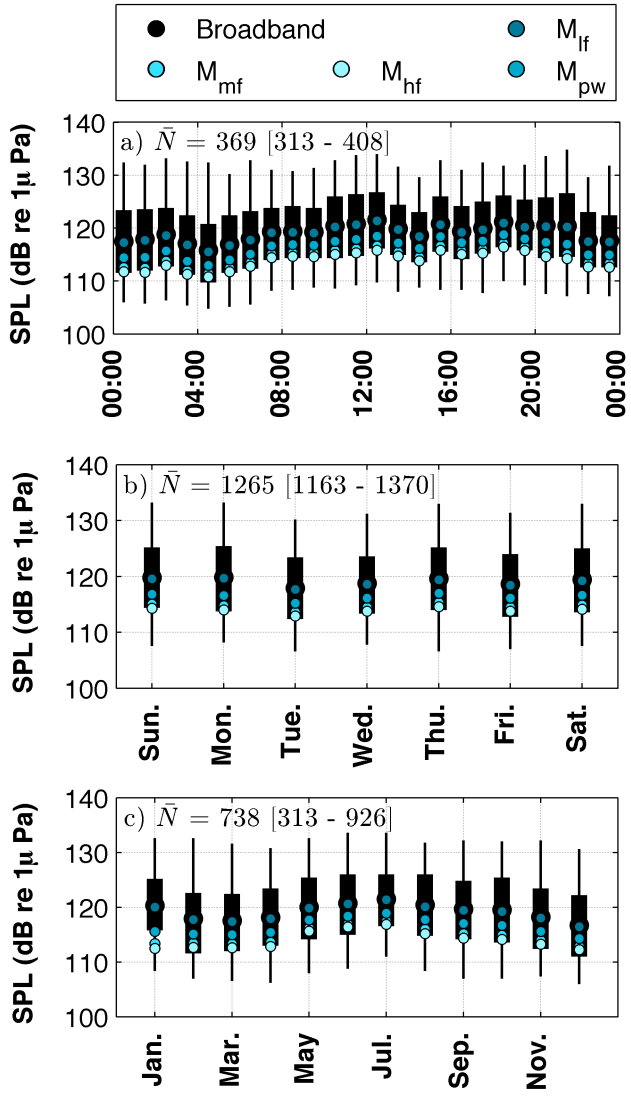

Figure 4.4: Hourly (a), daily (b) and monthly (c) average broadband (0.02 - 30 kHz) and M-weighted sound pressure levels. The box plots show the range for the 25% to 75% thresholds and the whiskers show the range for the 5% to 95% thresholds for broadband SPLs. The mean, minimum and maximum sample sizes ($\bar{N}$) are included for the statistics are included in each subplot. February and August were significantly below the mean due to extended AIS receiver outages and data gaps from bottom-package recovery/redeployment.

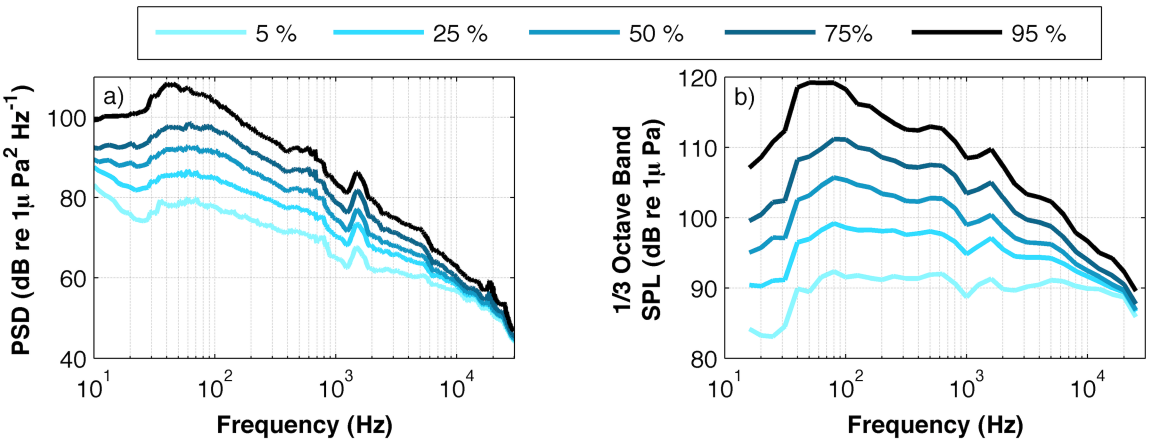

Figure 4.5: a). Percentile calculations of pressure spectral density for unweighted received levels. b). Percentiles for unweighted received levels in one-third octave band SPLs. The received broadband SPLs associated with the percentage thresholds are shown in Fig. 4.2 and are 107.3 dB (5%), 113.4 dB (25%), 119.2 dB (50%), 124.5 dB (75%), and 132.3 dB (95%).

below 1 kHz. Based on these spectra, PE modeling of propagation to justify the use of the single-value transmission loss coefficient was carried out at 50, 100, and 250 Hz (Sec. 4.6).

Source level estimates for different vessel types at the their closest points of approach are shown in Table 4.4. Source levels are only presented for periods when currents are relatively weak (to minimize pseudosound) and when spectra are not contaminated by other ships. Because these are uncommon events at the study site, it is not possible to estimate source levels for all vessel types in Admiralty Inlet.

Given the agreement in average LOA and SOG values, it is unsurprising that sources levels for cargo ships reported in the current study are representative of values reported by others (e.g., *McKenna et al., 2012*). Specifically, the source levels applied in the current study are 186 dB for container ships, 180 dB for vehicle carriers, 180 dB for general cargo ships, 185 dB for bulk carriers, and 181 dB for oil and chemical tankers. The consistency of calculated source levels also supports the use of a single-valued transmission loss coefficient for this study area.

Different source levels are applied to each type of passenger vessel. Although the ferry category includes 19 vessels, the local ferry is temporally dominant. A source level of 173

Table 4.4: Estimated source levels (0.02 - 30 kHz) based on received levels (0.02 - 30 kHz) for selected ships.

Date/Time	Name	Vessel Type	LOA (m)	SOG (kn)	CPA (km)	RL (dB)	SL (dB)
2/15/11 9:20	Victoria Clipper IV	Ferry	36	30.8	1.65	121	170
2/16/11 9:18	Victoria Clipper	Ferry	40	30.5	1.26	121	168
2/13/11 6:51	Eagle	Tug	32	9.6	1.22	127	173
2/16/11 4:41	Valor	Tug	30	8.4	1.46	121	168
2/16/11 12:25	Lela Joy	Tug	24	4.9	1.15	126	172
2/15/11 4:14	Pacific Eagle	Tug	28	8.2	1.36	118	165
2/20/11 18:28	Shannon	Tug	28	9.3	0.58	129	171
2/11/11 23:30	James T Quigg	Tug	30	7.9	1.42	120	167
2/19/11 6:23	Island Scout	Tug	30	5.8	1.47	127	174
2/20/11 12:44	Chief	Tug	34	11.4	1.23	128	174
2/12/11 1:57	Horizon Kodiak	Container	217	20.1	1.53	132	179
2/12/11 3:02	Hong Yu	Bulk Carrier	226	13.6	1.52	135	182
2/12/11 3:44	Great Land	Vehicle Carrier	243	23	1.36	137	184
2/12/11 11:30	Ever Excel	Container	300	18.2	2.78	132	183
2/14/11 7:42	Ever Excel	Container	300	20.8	1.93	136	186
2/12/11 22:24	Hanjin Hamburg	Container	335	23.8	2.82	133	185
2/14/11 2:39	Hanjin Hamburg	Container	335	21.3	1.51	137	185
2/14/11 9:02	CSK Unity	Bulk Carrier	225	13.6	2.07	128	178
2/14/11 19:07	CMA CGM Carmen	Container	334	23.8	1.46	136	183
2/14/11 19:56	MSC Kim	Container	265	22.7	1.35	136	183
2/16/11 9:00	Bremen Bridge	Container	279	21.2	1.02	136	181
2/17/11 7:53	Hyundai Republic	Container	305	24.7	1.49	136	184
2/17/11 22:34	Coastal Sea	General Cargo	55	12.5	1.36	129	176
2/21/11 0:14	Green Point	Vehicle Carrier	180	19.1	1.41	133	180

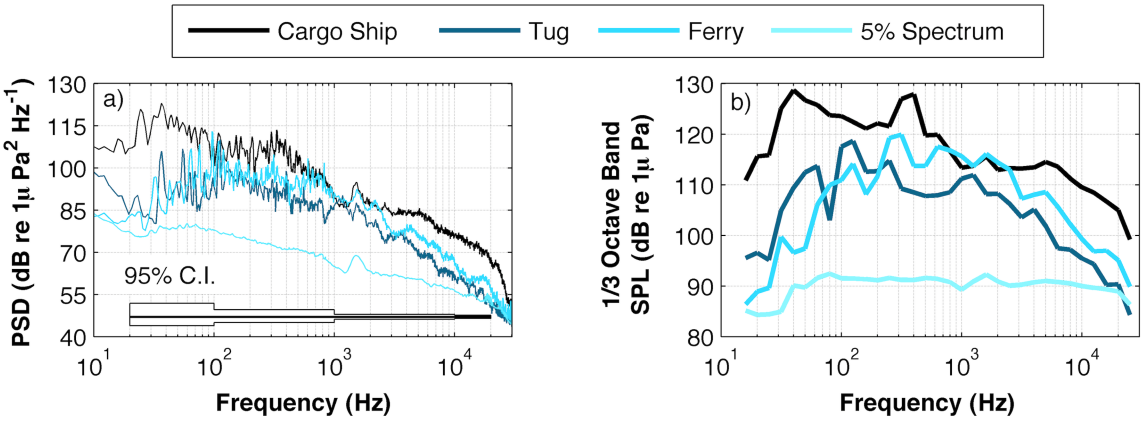

Figure 4.6: a). Acoustic spectra for a cargo ship at 1.5 km, the local ferry at 1.0 km, and a tug at 1.2 km, and the 5th percentile spectrum. b). One-third octave band SPLs for the respective spectra in (a).

dB is used for ferry traffic and is based on recordings of local ferry traffic during the 1 year deployment (Section 4.7). A source level of 180 dB is assigned to cruise ships that depart from Seattle for Alaska during the summer months. This value is consistent with the source level applied by *Hatch et al.* [2008] and measurements made of two large cruise ships at the U.S. Navys Southeast Alaska Acoustic Measurement Facility (SEAFAC) in Ketchikan, AK [*Kipple*, 2004a, b]. The remaining passenger vessels are, on average, smaller than the local ferry and cruise ships and spend less time in the study area. A lower source level of 165 dB is attributed to the remaining passenger vessels. This source level value is between large commercial vessels and small recreational watercraft and is comparable to source levels reported for small commercial vessels and larger recreational vessels [*Greene and Moore*, 1995; *Kipple and Gabriele*, 2003].

Tugs transiting the study site span a broad range of sizes and tow loads. Broadband source levels for tugs reported in literature include 170 dB [*Greene and Moore*, 1995] and 172 dB [*Hatch et al.*, 2008]. A source level of 172 dB for tugs, the average value (in root-mean-square pressure space) for all tugs shown in Table 4.4, is used. Source levels for the remaining ship types are broken into three categories - fishing, other, and various. A source level of 165 dB is used for fishing vessels and is based on one-third octave band spectra of trawlers and small vessels with diesel engines [*Greene and Moore*, 1995]. A source level

of 165 dB is also used to calculate noise budget contributions from the remaining vessel classes (various and other). These categories include a broad range of vessel types and sizes. However, the energy budget is insensitive to errors in source levels for these vessel categories because of their limited presence in the study area.

The total acoustic energy input of vessel traffic equipped with AIS in the study area over the course of the year (Table 4.5) is 438 MJ. Commercial vessel traffic accounts for over 90% of the energy budget with container vessels being the greatest contributor due to high source levels. Despite relatively low source levels, tugs are large contributors to the energy budget due to their relative presence. Passenger ferries and cruise ships represent 9% of the total energy budget. Notably, the energy input from cruise ships is mostly limited to the summer tourist season. When compared to shipping vessels, tugs, and passenger vessels, energy input from all other vessel types is negligible.

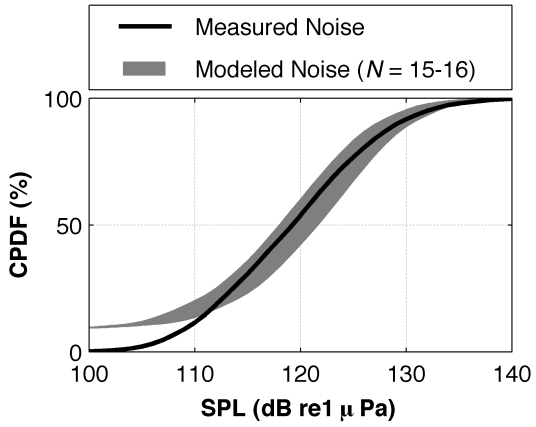

Figure 4.7: Cumulative probability distributions of underwater ambient noise (0.02 - 30 kHz) in study area for measurements (all ambient noise sources) and the model for vessel noise. The gray envelope of modeled noise represents predicted received levels using a transmission loss coefficients from 15 to 16.

The cumulative probability distribution functions for the modeled and observed noise are presented in Figure 4.7. Above the 15$^{\text{th}}$ percentile, the measured noise distribution falls within the model results for the N = 15-16 envelope (Eq. 4.4). The good agreement between measured and modeled results suggests that most of the ambient noise variability at the site can be explained by AIS-equipped vessel traffic. During quieter periods, other noise sources, such as distant shipping, wind, and waves, are likely to dominate. Limited land-based commercial and industrial activity in the immediate vicinity of the study area also suggests that noise from to other anthropogenic sources is limited. Based on temporal variability explained by vessel traffic in Figure 4.7, a cumulative energy flux distribution (not shown) reveals that vessels traffic accounts for 99% of the acoustic energy flux at the measurement location.

Table 4.5: Vessel noise budget calculated by Eq. 4.3.

Vessel Class	Vessel Type	SL (dB)	SL (W)	Time (hr)	Energy (MJ)	% of Budget
Commercial	Container	186	32.8	2,113	249	57
	Vehicle Carrier	180	8.2	611	18	4
	General Cargo	180	8.2	292	9	2
	Bulk Carrier	185	26.0	755	71	16
	Tanker	181	10.4	240	9	2
	Tug	172	1.3	8,502	40	9
	Fishing	165	0.3	1,577	1	<1
Passenger	Ferry	173	1.6	3,868	23	5
	Cruise	180	8.2	551	16	4
	Other	165	0.3	75	< 1	<1
Other	-	165	0.3	330	< 1	<1
Various	-	165	0.3	1,184	1	<1
Total				20,100	438	100

4.4 Discussion

4.4.1 Energy Budget

The sensitivity of the energy budget depends primarily on the source levels assigned to cargo ships, tugs, and passengers vessels due to their temporal dominance. For each 1 dB increase in source levels attributed to tugs and ferries, the total energy added to the budget increases by 10 MJ (2%) and 3 MJ (<1%) respectively. Because these three vessel types spend an order of magnitude more time in the study area than others, the total budget is relatively insensitive to source levels attributed to traffic of other vessel types (with the exception of fishing vessels). Therefore, proper attribution of source levels for less common vessel types, while desirable, is relatively unimportant.

AIS data are a useful tool for quantifying the densities of commercial and passenger vessel traffic. However, small recreational watercraft and fishing vessels, neither of which is required to use AIS, are also common in the area. The vessel noise budget does not include the contribution from vessels without AIS transponders, and this is a notable limitation if relying on AIS as the sole source of vessel traffic data.

In the current study, many fishing vessels are included in the vessel noise budget, but it is unclear what portion of fishing vessels are equipped with AIS. Furthermore, there is a general lack of acoustic measurements of different types and sizes of fishing vessels. Military vessels (the most common vessel type included in the "various" category), do, occasionally, transmit AIS signals but the summary contained in Table 4.2 understates the level of military traffic in the area. Based on opportunistic sightings of naval vessels in the field that are not reflected in AIS data, additional transits are known to occur. It is unclear what portion of the total military traffic is included in the budget and the question is further complicated by variations in vessel design. Given the relatively small number of vessel hours in the study area, a substantially different assumption of source level or presence for vessels classified as various would be required to affect the energy budget. For example, a source level of 176 dB (an 11 dB increase over the current value) or an increase in presence by 1,300% for this vessel category would increase the energy budget by 1% (4.4 MJ). Recreational watercraft and small fishing vessels, although common, have lower

source levels [*Greene and Moore*, 1995; *Erbe*, 2002; *Kipple and Gabriele*, 2003; *Hildebrand*, 2005, 2009] and their exclusion is unlikely to substantially influence the overall vessel noise budget. For example, if a broadband source level of 155 dB is assumed for all recreational watercraft, these vessels would need to spend 47,000 h in the study site per year, more than two times the combined vessel presence of all types in this study, to increase the vessel energy budget by 1%.

An energy budget for vessel noise is useful for identifying the relative contributions of different types of vessels to ambient noise levels, but site-to-site comparisons of the absolute budget are difficult. Comparisons may be possible if the energy budgets are normalized by the study area. The total study area for Admiralty Inlet is 562 km^2 and the resulting vessel noise energy density is 0.78 MJ/km^2-yr. Note again that this figure has not been extrapolated to account for the 11% of the year when no AIS data was obtained due to outages. By contrast, *Hatch et al.* [2008] estimated an annual energy budget of 193 MJ in Stellwagen Bank National Marine Sanctuary. Using the total area of the SBNMS (2,188 km^2), the spatial energy density is 0.09 MJ/km^2-yr, nearly an order of magnitude lower than Admiralty Inlet.

Energy budgets, although effective for measuring the relative contributions of different noise sources, are not static. Such budgets are dependent on overall levels of activity. In the case of Admiralty Inlet, most of the energy budget is related to economic activity in the form of shipping vessels and to ferry traffic. Large changes in shipping traffic at the Ports of Seattle and Tacoma would be reflected in overall energy budget. In addition, after the end of the study period, a second ferry was added to the local ferry route, so an updated energy budget would indicate higher levels of passenger vessel traffic.

4.4.2 Relevance to Marine Species

Behavioral responses of marine mammals to vessel noise depends not only on the RL of noise, but also on other variables, including the individuals hearing sensitivity, current activity state, and previous experience with sounds of similar intensity and frequency [*Southall et al.*, 2007; *Ellison et al.*, 2011]. Most research on vessel noise has focused either on low-frequency,

ocean basin scale contributions from commercial shipping traffic or small watercraft in close proximity to marine mammals [e.g., *Erbe*, 2002; *Clark et al.*, 2009]. Numerous studies of marine mammal reactions to vessels suggest that exposure to elevated vessel noise may alter marine mammal behavior and increase stress hormone levels with potential biological consequences [*Buckstaff*, 2004; *Foote et al.*, 2004; *Holt et al.*, 2009; *Rolland et al.*, 2012].

Broadband SPLs at the study site regularly exceed 120 dB (Fig. 4.2c), the current acoustic criterion for behavioral harassment of marine mammals for continuous sound types (120 dB re 1 μPa) in the United States [*National Marine Fisheries Service*, 2005]. The current acoustic criteria are based on broadband measurements and do not take into account frequency-specific hearing capabilities that differ among marine mammal groups. The weighted cumulative probability distributions of received levels for each marine mammal functional hearing group are shown in Fig. 3 in an effort to address variation in hearing capabilities among groups. Because low-frequency cetaceans and pinnipeds have relatively flat hearing sensitivity over the frequencies associated with commercial shipping, their received levels approach the broadband receiver idealization. However, the M-weighting functions for mid- and high-frequency cetaceans start to roll off at frequencies less than 1 kHz, where the majority of acoustic energy associated with commercial ships is concentrated. Consequently, perceived mean received levels for mid- and high-frequency cetaceans based on these weighting functions are, on average, at least 5 dB lower. As previously mentioned, noise from recreational vessels is unlikely to contribute substantially to the vessel noise budget in the study location. Nonetheless, noise from these smaller vessels may be of concern to mid- and high-frequency cetaceans because their energy is concentrated at higher frequencies than commercial ships [*Erbe*, 2002]. This points to a general need for frameworks that are able to treat anthropogenic noise in a more biologically relevant manner.

At close range (e.g., within 10 km of the source), different types of vessel activity increase noise levels across a broader range of frequencies than is often considered. Below 1 kHz, ship traffic regularly increases noise levels by 25 dB above background levels. At higher frequencies, extending up to 30 kHz, one-third octave band SPLs regularly increase by 1020 dB (Figs. 4.2b and 4.5). These increases in ambient noise from shipping traffic are sufficient to regularly mask communicative sounds used by many marine mammals unless they are

able to compensate vocally [*Holt et al.*, 2009].

Because the Main Basin of Puget Sound is also relatively narrow (approximately 10-20 km wide), large commercial vessels transiting the area are expected to elevate broadband ambient noise levels over the entire width of the channel to levels in excess of 120 dB. The hydrophone deployments in this study are well outside (>1 km) of the shipping lanes and few vessels passed directly over the deployed hydrophones. As a result, moderately higher recorded broadband SPLs would be expected mid-channel, where vessel densities are greater. The proximity to ferry routes, shipping lanes, and populated coastal communities are common throughout Puget Sound. Therefore, the noise levels observed in this study area may be extended, with due caution, to other areas in the region.

4.5 Conclusion

One year of AIS data is paired with hydrophone recordings from a site in northern Admiralty Inlet, Puget Sound, WA to assess ambient noise levels and the contribution of vessel noise to these levels. Admiralty Inlet experiences a high level of vessel traffic due to cargo ships bound for major ports, tugs towing barges, and ferries transporting passengers and vehicles. Results suggest that ambient noise levels between 20 Hz and 30 kHz are largely driven by vessel activity and that the increases associated with vessel traffic are biologically significant.

Throughout the year, at least one AIS-transmitting vessel is within the study area 90% of the time and multiple vessels are present 68% of the time. A vessel noise budget is constructed to assess the relative contributions of different vessel types to underwater noise levels at the site. Results show cargo vessels account for 79% of the acoustic energy in the vessel noise budget. Passenger ferries and tugs have lower source levels but spend substantially more time in the study site and contribute 18% of the energy in the budget. Recreational watercraft contribute to ambient noise levels but are unlikely to contribute substantially to the overall vessel noise budget due to limited presence and lower source levels. All vessels generate acoustic energy at frequencies relevant to all marine mammal functional hearing groups.

A basic model for received levels accounts for vessel types, distance to the hydrophone, and specified characteristic source levels for each vessel type. The model explains 85% of

the temporal variability in observations and demonstrates the predominance of maritime traffic in the overall noise budget at the site.

4.6 Appendix A - Transmission Loss Coefficient

A single-valued transmission loss model (i.e., $15\log(r)$) assumes that the transmission losses are independent of the location of a vessel relative to the hydrophone receiver. Given changing bathymetric profiles between the ship and receiver as a vessel travels in the shipping lanes, the assumption of angular and range independence must be verified. To justify the use of a single-valued transmission loss model, a range dependent parabolic equation code [*Collins*, 2000] is used to calculate transmission losses for site-specific bathymetric profiles at three key frequencies. The modeled frequencies (50 Hz, 100 Hz, 250 Hz) covered the range of frequencies associated with peak spectrum levels of ship traffic at the site (Fig. 4.6).

Important inputs to the model include the geoacoustic parameters, bathymetry, water properties, and the source depth. No detailed information about the geophysical parameters throughout the site is available. However, studies in the immediate vicinity of the hydrophone deployments indicate that the bed is composed of a narrow layer (12 m thick) of gravel pavement above 40 m layer of sand interspersed with larger grains such as gravel [*Landau Associates*, 2011]. For simplicity, the top pavement layer is neglected because it is small relative to the modeled wavelengths and additional deeper layers are neglected. The sediment properties for a coarse, gravely sand used in the model are a sound speed ratio of 1.25, a density ratio of 2.23, and an attenuation rate of 0.7 dB per wavelength [*APL-UW*, 1994]. A constant sound speed of 1490 m/s is used in the water column because it is generally well-mixed [*Polagye and Thomson*, 2010]. Available Puget Sound bathymetry data [*Finlayson*, 2005] are linearly interpolated to obtain the bathymetric profiles for modeled domains. The bathymetric profiles (P1-5, Fig. 4.8a) are typical of southbound traffic in the shipping lanes. Regardless of bearing, for ships traveling in the shipping lanes all bathymetric profiles are characterized by an upslope to shallower water at the hydrophone location near the head- land. A source depth of 10 m was used to approximate the propeller depth of modern cargo vessels. A receiver depth of 57 m is used and is similar to the mean depth

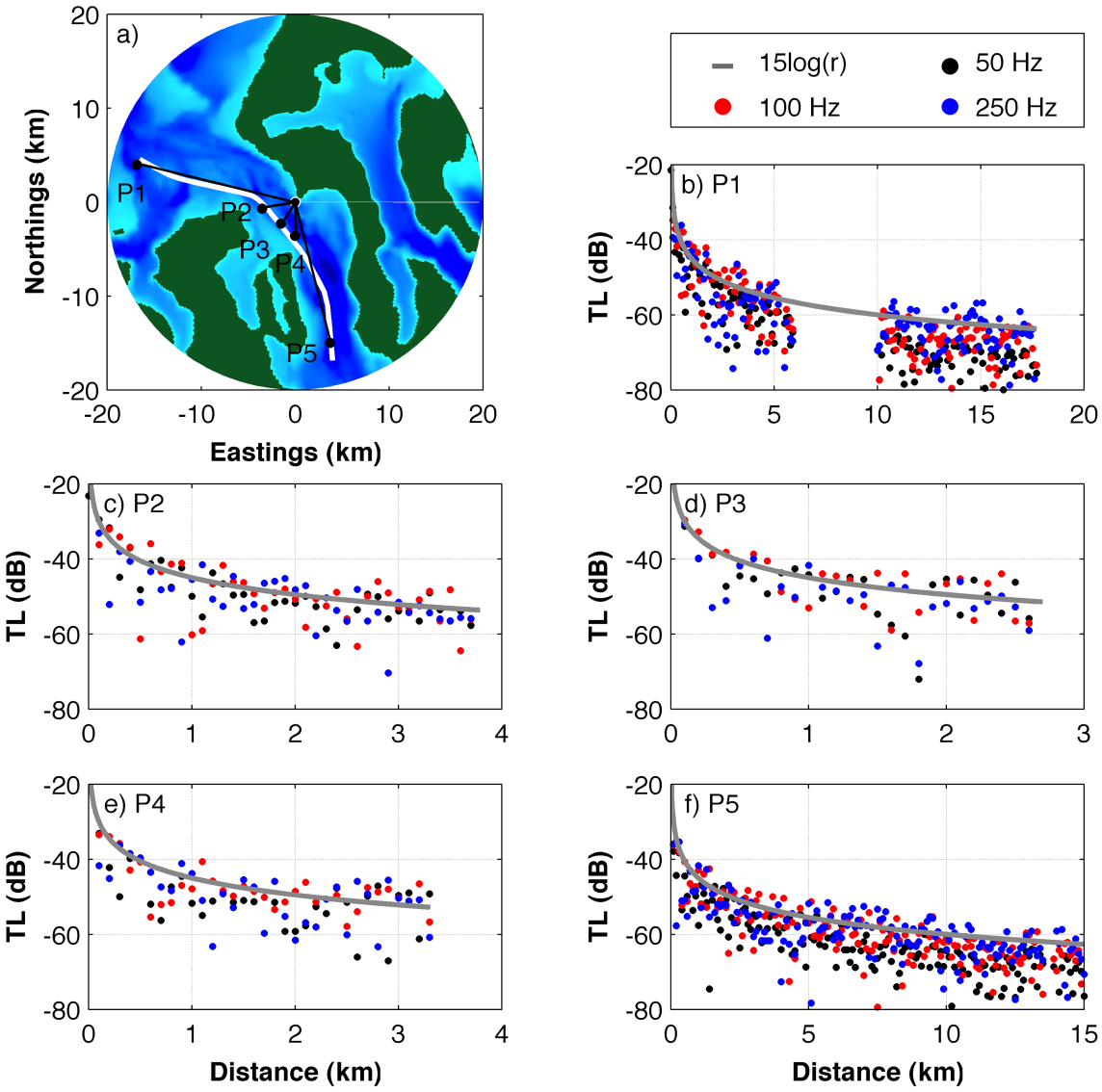

Figure 4.8: a). Site map and profiles locations used for the range dependent PE model. A typical ship track for southbound traffic is included (white line). b-f). Transmission losses modeled at 50, 100, and 250 Hz and a comparison with the simplified model. For P1, the missing points are associated parts of the profile where the receiver depth of 57 meters was below the water-sediment interface. The transmission loss is plotted every 100 meters to reduce the clutter associated with the modal interference patterns. Each transmission loss plot ends at the location of the hydrophone deployment.

at which ambient noise measurements in the study were obtained.

4.7 Appendix B - Ferry Source Level

To estimate the source level of the most commonly present vessel, the local ferry, and empirically estimate the transmission loss coefficient, acoustic data throughout the year were used. Current velocity and AIS data were used to screen for periods in which the currents were weak (< 0.4 m/s) and the local ferry "Chetzemoka" was the only vessel in the study area. Further manual screening was done to remove recordings of the ferry that were not consistent with other ferry measurements and were deemed to be likely contaminated by other noise sources (e.g., a non-AIS equipped vessel). The source level and transmission loss coefficient were calculated by regressing the broadband RL against the log of the distance, in meters, and performing a least squares linear regression analysis. In this instance, estimation of the transmission loss coefficient for the ferry was limited by the Port Townsend ferry terminal at a distance of 7 km. The resulting regression fit yielded a source level of 173 dB re 1 μPa at 1 m (y-intercept) and a transmission loss coefficient of 16 dB (slope). Figure 4.9 shows the results of the regression with the RL plotted against the distance to the ferry on a linear scale.

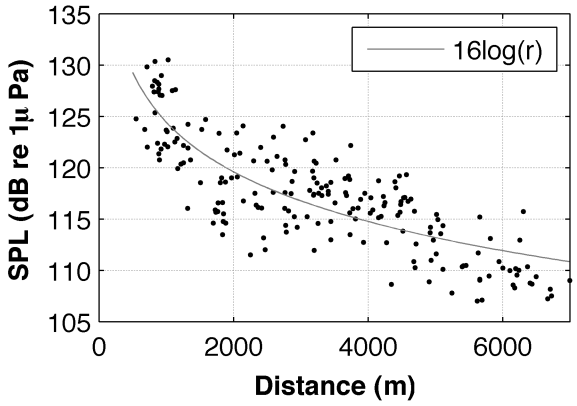

Figure 4.9: Received levels (0.02 - 30 kHz) from local ferry traffic versus the distance between the ferry and the hydrophone.

Chapter 5

AMBIENT NOISE: SEDIMENT-GENERATED NOISE

The text of the following chapter was published in the *Journal of Geophysical Research – Oceans* in March, 2013. With the exception of removing site details and reformatting the text, no changes were made to the content of the original article. The citation for the published document is as follows:

Bassett, C., J. Thomson, and B. Polagye, Sediment-generated noise and bed stress in a tidal channel, *J. Geophys. Res. – Oceans, 118*, 2249–2265, 2013.

5.1 Introduction

Sources of ambient noise in the ocean have been the focus of numerous scientific studies dating back to World War II. Among the most commonly identified sources of ambient noise are shipping traffic [*Wenz*, 1962; *Greene and Moore*, 1995], weather [*Wenz*, 1962; *Nystuen and Selsor*, 1997; *Ma et al.*, 2005], biological sources [*Greene and Moore*, 1995], and molecular agitation [*Mellen*, 1952]. A more limited body of research identifies the motion of different sized sediment grains due to strong currents or surface waves as an ambient noise source [*Voglis and Cook*, 1970; *Harden Jones and Mitson*, 1982; *Thorne*, 1986b; *Thorne et al.*, 1989; *Thorne*, 1990; *Mason et al.*, 2007]. Noise generated by mobilized sediments is referred to as sediment-generated noise. The frequency of sound produced by particle collisions can be related to the size of the mobile particles [*Thorne*, 1986a]. Given that incipient motion of particles is driven by hydrodynamic conditions, for water depths on the order of 100 m noise from coarse-grained sediments is only likely to be produced by high-current environments (e.g., current velocities > 2 m/s), restricting the geographic range in which this sound makes a significant contribution to ambient noise levels. In shallower water (i.e., depths on the order of 10 m or less), noise from the resuspension and transport

of sediments by surface waves and wave-current interactions is also possible and more likely to be observed over a broader geographic range.

A lack of data identifying sediment-generated noise as an important ambient noise source in a range of coastal environments represents a data gap with implications for passive acoustic studies of marine species that inhabit such areas (i.e., SNR for detection, classification, and localization algorithms), and for monitoring anthropogenic noise in these areas. For example, tidal energy projects are in various stages of development in coastal waters of the United States, Canada, the United Kingdom, Ireland, and South Korea. There are significant knowledge gaps with respect to possible environmental impacts of tidal energy projects [*Polagye et al.*, 2011]. Sites suitable for tidal energy experience strong currents (> 2 m/s) that, depending on bottom type, could mobilize sediments. Sediment-generated noise needs to be understood to design effective characterization and monitoring studies of the sound produced by tidal energy projects and its effects on marine mammals.

The conditions under which incipient motion of particles occurs has long been an active research area. *Shields'* [1936] commonly cited work noted that lack of similarity between experiments and a lack of understanding of natural processes affecting motion of the bed were the two most important difficulties faced in developing relationships between hydrodynamic conditions and bedload transport. To address these problems, controlled laboratory experiments were performed on bed types consisting of homogenous grain sizes with different densities. Results were presented in terms of dimensionless parameters to generalize the results. The non-dimensionalized tractive forces, called the Shields parameter (Θ_b), were described as

$$\Theta_b = \frac{\tau_b}{(\rho_s - \rho)gD}, \tag{5.1}$$

where τ_b is the bed stress, ρ_s is the density of the sediment, ρ is the density of the water, g is gravity, and D is the diameter of the sediment grain. Results were presented against the grain Reynolds number (Re_*) using the shear velocity (u_*) as the characteristic velocity scale. For a particular flow regime (i.e., Re_*), once the Shields parameter exceeded a critical value, incipient motion occurred. The empirical relationships identified by Shields have

been revisited numerous times in the literature. For example, *Miller et al.* [1977] and the references therein include relationships for incipient motion of coarse-grained sediments. Miller *et al.* noted that predictions of incipient motion are difficult in complex natural environments due to turbulence, bedforms, and grain size distributions.

Incipient motion of particles is often presented as a function of the mean shear stress or shear velocity. Field data [*Heathershaw and Thorne*, 1985], experimental results [*Diplas et al.*, 2008], and numerical analysis [*Lee and Balachandar*, 2012] have highlighted how drag forces and turbulence can affect critical shear stresses. Unlike *Shields* [1936], these studies suggest that drag forces on individual grains, rather than overall bed stresses, are more appropriate for predicting incipient motion. Instantaneous forces associated with turbulent fluctuations can mobilize grains, even when mean shear stresses are below critical values. Instantaneous near-bed forces are, however, difficult to quantify in high-energy field environments.

Once sediments are mobilized, there are two mechanisms by which sound is generated: bedload and saltation [*Mason et al.*, 2007]. Bedload is the sustained motion of particles as a result of intergranular forcing and saltation is the partial entrainment and resettlement of grains that are too large for sustained motion across the seabed. Regardless of the type of motion, sound is generated as a result of collisions between individual particles.

Laboratory experiments using artificial and real sediments have demonstrated that the spectral structure of sediment-generated noise is related to the material properties and size of the particles by

$$f_r \approx 0.182 \left[\frac{E}{\rho(1-\sigma^2)}\right]^{0.4} \left(\frac{g^{0.1}}{D^{0.9}}\right), \tag{5.2}$$

where f_r is the resonant frequency, E is Young's modulus, σ is Poisson's ratio, ρ is the particle density, g is the gravitational acceleration, and D the particle diameter [*Thorne*, 1985, 1986a]. By applying the material properties, the centroid frequency of sediment-generated noise becomes a function of only the grain diameter. *Thorne* [1986a] related the frequency to the grain diameter according to

$$f_c = \frac{192}{D^{0.9}}, \tag{5.3}$$

which showed good agreement with laboratory measurements. It was also found that the expression for spherical particles could be applied with good agreement to non-spherical particles [*Thorne*, 1986a].

As a result of agreement between radiated noise from non-spherical particles and expected theoretical resonant frequencies of spherical particles, Equation 5.3 can be inverted to solve for the size of arbitrarily shaped agitated sediment grains. *Thorne* [1986a] also applied the inversion of the expected resonant frequency for equivalent particle diameter (Eq. 5.3) to field measurements of sediment-generated noise. The frequencies attributed to noise from moving sediments agreed with video analysis and sediment grabs at the site. Further attempts to apply acoustic data to accurately recreate the particle size distribution of the bed were less successful. They did, however, demonstrate that such estimates can capture the principal components of mobile particles [*Thorne*, 1986a]. Subsequent research applied the results to noise from bedload transport in West Solent, United Kingdom. At this site, a linear relationship between mobilized mass and recorded sound intensity was verified using a hydrophone and video analysis [*Thorne*, 1986b; *Thorne et al.*, 1989; *Williams et al.*, 1989; *Thorne*, 1990]. *Mason et al.* [2007] successfully applied the inversion method to a full-scale shingle transport experiment.

This paper presents data collected from a tidal channel in which peak currents exceed 3 m/s. The results and discussion address three distinct but interrelated topics: the hydrodynamic conditions that give rise to bedload transport, the spectral content of sediment-generated noise, and the relationship of sediment-generated noise given prevailing hydrodynamic conditions. Section 5.2 outlines concepts critical to the interpretation of the results, data acquisition, and processing methods for each area of analysis. In Section 5.3, the results are presented and used to investigate the relationship of sediment-generated noise to near-bed currents. Questions raised by the findings of this study, comparisons to previously published results, and transferability of results to other sites are discussed in Section 5.4.

Table 5.1: Deployments, locations, and instrument packages used in this study.

Deployments	Location	Instruments	Purpose
11-21 Feb. 2011	48 09.120°N	ADV, AWAC	Bed stress, currents
	122 41.152 °W	Hydrophones (x2)	Ambient noise
9 Aug. 2011	48 09.124°N	GoPro Hero (x2)	Video of seabed
	122 41.195°W	Dive lights (x4)	Artificial light
10 Aug. - 14 Nov. 2011	48 9.148°N	AWAC	Current profiles
	122 41.305°W		during drifts
25 Oct. 2011	Drifts	Cabled hydrophones (x2)	Ambient noise
		Pressure logger	Hydrophone depth
12 June - 19 Sept. 2012	48 09.172°N	ADCP	Current profiles
	122 41.171°W	Hydrophone	Ambient noise

5.2 Methods

5.2.1 Data Collection

Oceanographic and acoustics measurements were obtained using a combination of autonomous instrumentation packages built around Sea Spider tripods (Oceanscience, Ltd.) and ship-based cabled instruments. Three primary deployments were used in data analysis and two additional deployments were used to obtain supplementary information. All deployments were in northeastern Admiralty Inlet, near Whidbey Island. A list of the deployments, locations, and instruments used in the analysis are included in Table 5.1. The relationship between noise levels and hydrodynamics are based on the February 2011 deployment (tripod at depth of 55 m). October 2011 (shipboard cabled drifts) data were used to assess the directionality and June-September 2012 data (tripod at depth of 54 m) were used to assess the intermittency and stationarity of sediment-generated noise.

5.2.1.1 Acoustic Wave and Current Profiler

A 1 MHz Nortek Acoustic Wave and Current profiler (AWAC) was used to measure currents from 1.05 to 26.05 meters above the seabed. The AWAC profiled the water column in 0.5-meter bins at a frequency of 1 Hz during the February 2011 deployment. Mean current magnitude and direction were calculated using five-minute ensembles. As shown in *Thomson et al.* [2012], this ensemble period filters out the majority of turbulence. The standard error for a single ping measurement, also referred to as 'Doppler noise', was $\sigma_u = 0.224$ m/s. The uncertainty in each velocity bin as a function of σ_u and the number of raw pings, N, in the ensemble is $\overline{u} \pm \frac{\sigma_u}{\sqrt{N}}$ [*Brumley et al.*, 1991]. For five-minute ensembles, the resulting uncertainty was 0.013 m/s, a value two orders of magnitude smaller than observed maximum non-turbulent currents (i.e., mean currents).

Current profiles obtained using the AWAC during the August-November, 2011 deployment were used to determine current velocities during shipboard drift surveys on October 25, 2011. Each profile was based on 30 second averages obtained every 60 seconds in one-meter spatial bins. The resulting uncertainty in the currents was 0.045 m/s.

5.2.1.2 Acoustic Dopper Current Profiler

A 470 kHz Nortek Continental Acoustic Doppler Current Profiler (ADCP) was used to measure currents from 1.69 to 49.69 meters above the seabed in 1-m bins during the June-September 2012 deployment. Mean current magnitude and direction were calculated using one-minute ensembles. Linear interpolations of the February 2011 data were used to calculate a scalar factor to convert the velocity in the lowest bin of the June-September 2012 data (1.69 m) to the expected near-bed velocity at the same height as the February 2011 data (1.05 m). Current profiles were used only to approximate near-bed currents for the purposes of studying the intermittency and stationarity of sediment-generated noise during strong currents.

5.2.1.3 Acoustic Doppler Velocimeter

Point velocity measurements were acquired by a 6 MHz Nortek Vector Acoustic Doppler Velocimeter (ADV) during the February 2011 deployment. The ADV, deployed 1 m above the seabed, sampled the three components of velocity at 32 Hz for 256 seconds every ten minutes. For each burst sample (8192 points), data were projected on to the principal axis and reviewed for quality. Despiking of the projected velocity components was accomplished using the phase-space method [*Goring and Nikora*, 2002; *Mori et al.*, 2007] and the Matlab (www.mathworks.com) toolbox developed by *Mori et al.* [2007].

5.2.1.4 Hydrophone Data

The standalone acoustic recording system on the tripod consisted of a Loggerhead Instruments DSG data acquisition and storage system with a Hi-Tech hydrophone (HTI-96-MIN) deployed 1 m above the seabed. The hydrophone, when accounting for the internal preamplifier, had an effective sensitivity of -165.9 dB μPa/V. The frequency response of the hydrophone and data acquisition system was approximately flat over the frequency range included in this study (1-30 kHz). Digitized 16-bit data were written to a SD card (32 or 128 GB) contained in the hydrophone pressure case. The data used for relating hydrodynamic and acoustic measurements were obtained from February 11 to February 21, 2011. During this deployment, the hydrophones recorded at 80 kHz for 10 seconds at the top of every minute, a 17% duty-cycle motivated by memory limitations (32 GB SD card).

A Loggerhead Instruments DSG equipped a larger flash memory card (128 GB) was deployed on a tripod from June 12 to September 19, 2012. During this period the hydrophone sampled at 80 kHz for 55 seconds at the top of every minute from 02:00-07:00. These hours were chosen due to relatively low levels of shipping and ferry traffic overnight [*Bassett et al.*, 2012]. The data were saved as 55-second recordings for further processing. These data were used to assess the intermittence and stationarity of sediment-generated noise at the site (Section 5.4.2).

Increased noise levels at frequencies consistent with sediment-generated noise suggested the seabed as the noise source. To further test this hypothesis, measurements of the direc-

tionality were opportunistically carried out on October 25, 2011 during strong spring tidal currents, favorable weather conditions (no precipitation and sea state 0 to 1), and the cancelation of the ferry service that traverses the inlet. A ship-based cabled array consisted of two Cetacean Instruments CR55XS hydrophones with 10x internal preamplifiers separated by 10 cm (one-half of an acoustic wavelength at 7.5 kHz). The hydrophones were connected to an IOtech Personal Daq 3000 (16-bit, 1MHz sampling rate) and to a laptop operating on battery storage to reduce 60 Hz electrical noise. Data were acquired continuously at 400 kHz while drifting through the site (no engines, generators, or active acoustics devices) on the R/V Inferno, a 24' research vessel owned by the Applied Physics Laboratory at the University of Washington. The sampling uncertainty for each channel of the data acquisition system was approximately 1 μs, 130 times shorter than the wave period at 7.5 kHz. After each drift, the vessel was repositioned more than 500 meters upstream of the study area and the drift repeated. Six drifts were carried out from early in the ebb ($\overline{u} < 1$ m/s) to past the peak ($\overline{u} > 3$ m/s). Current velocity was assessed post-hoc using profiles collected by the AWAC deployed on the tripod from August-November 2011. The hydrophones cables were mated to a "hairy rope" fairing to reduce cabled strum. Sash weights attached below the hydrophones were used to limit line angle. To minimize the transmission of boat motion to the hydrophones, the cables were deployed with slack leading to an isolation float tethered to the vessel using a 0.7 m shock cord. A HOBO U20 pressure logger (0.2 Hz sample rate) was deployed 40 cm below the hydrophones to record their depth. The intended deployment depth was approximately 40 m, between 5-15 m above the seabed.

5.2.1.5 Seabed Video

On August 9, 2011 two GoPro Hero high definition video cameras were deployed on a mooring at the site. The cameras were deployed 65 cm above the bed with 55° incidence angles. The cameras were deployed facing opposite directions. The field of view was 170° for each camera. Two dive lights (one Hollis LED5 and one IKELITE PCm) were deployed next to each camera to provide artificial light in the center of the field of view. Due to battery life, the cameras were only able to record video for four hours starting with the

slack tide deployment. Video was obtained continuously throughout the four-hour period at 30 frames per second until the batteries failed, a period during which near-bed currents exceeded than 1 m/s. The video was manually reviewed for mobilization events, including still frame tracking of individual grains.

5.2.2 Hydrodynamics Data Processing

There are three methods commonly used to estimate shear stress at the seabed. Those methods make use of the log layer velocity profile, the inertial dissipation of turbulent kinetic energy, and the turbulent Reynolds stresses. The different methods, each discussed in detail below, can be compared to each other by a drag law according to

$$\tau_b = \rho u_*^2 = C_D \rho \left|\overline{u}\right| \overline{u}, \tag{5.4}$$

where τ_b is the bed stress, u_* is the friction velocity, C_D is the bottom drag coefficient, ρ is the fluid density, and $\overline{u}$ is the mean velocity.

5.2.2.1 Log Layer Velocity Profiles

In a fully developed turbulent flow, the law of the wall provides a self-similar solution relating the mean velocity to the log of the distance from the wall, or in this case, the seabed. In this layer, the vertical gradient of the along-channel velocity (u) is defined by

$$\frac{\partial u}{\partial z} = \frac{u_*}{\kappa z}, \tag{5.5}$$

where u_* is the shear velocity, κ is the von Karmen constant, and z is the distance from the seabed.

Integration of Equation 5.5 yields the logarithmic boundary layer profile

$$u(z) = \frac{u_*}{\kappa}\, ln\left(\frac{z}{z_o}\right), \tag{5.6}$$

where the limits of integration are zero velocity at the roughness height (z_0), and the mean velocity is equal to u at height z. This methodology has been widely used and statistical considerations of the profile accuracy under different hydrodynamic conditions have received

rigorous treatment [*Heathershaw*, 1979; *Gross and Nowell*, 1983; *Grant et al.*, 1984; *Green*, 1992; *Lueck and Lu*, 1997].

The uncertainty of the shear velocity is related to the log layer fit by

$$\Delta u_* = t_{\alpha/2,n-2}\left[\frac{1}{n-2}\left(\frac{1-R^2}{R^2}\right)\right]^{1/2}, \tag{5.7}$$

where $t_{\alpha/2,n-2}$ is the Student's t-statistic for a confidence level α with n degrees of freedom and R^2 is the coefficient of determination [*Gross and Nowell*, 1983]. Since the uncertainty in density is negligible (CTD measurements using a Seabird 16plus recorded density variations of less than 2 kg/m^3, relative to a nominal value of 1024 kg/m^3 during the February deployment), the uncertainty in bed stress from Equation 5.4 is only dependent on the uncertainty in friction velocity. The propagation of uncertainty from friction velocity to the bed stress is calculated according to

$$\Delta_{\tau_b} = 2\tau_b\frac{\Delta u_*}{u_*}, \tag{5.8}$$

where Δu_* is the error calculated using Equation 5.7. Reasonable confidence intervals for shear velocity and bed stress calculations are contingent upon high coefficients of determination for the log layer fits.

In this study, log layer fitting followed the methods discussed in *Lueck and Lu* [1997] and was applied to AWAC data collected during February, 2011. For each profile, a least squares fit to the bottom bins of the profile (1.05 m to 4.05 meters) was first calculated. From the bottom bins, new fits were calculated adding one velocity bin each iteration until the profile extended to 25 meters from the seabed. The log layer depth (z) was defined as the depth at which the highest R^2 value was identified. Only those fits with maximum R^2 exceeding 0.95 were retained. This most often was absent during transitions between flood and ebb tides, so data with near-bed currents below 0.5 m/s were not analyzed.

5.2.2.2 Reynolds Stress

In a turbulent flow, the velocity is described by $(\overline{u_i} + u_i')$, where $\overline{u_i}$ is the mean velocity, u_i' is the velocity fluctuation, and the index (i) denotes the velocity component. The instan-

taneous kinematic stress, based on velocity fluctuations in the vertical and along channel flow, is written as $u'w'$, and is calculated as the covariance of the components. By assuming a constant stress layer, the bed stress is obtained from the Reynolds stress by

$$\tau_b = -\rho\overline{u'w'}, \tag{5.9}$$

where ρ is the fluid density. In general, Reynolds stress calculations are noisy because the variance of each flow component is large relative to the mean [*Gross and Nowell*, 1983]. Rigorous treatment of the Reynolds stress calculations and shear stress estimates is presented in both oceanographic and atmospheric literature [*Tennekes*, 1973; *Heathershaw*, 1979; *Gross and Nowell*, 1983; *Heathershaw and Thorne*, 1985; *Trowbridge et al.*, 1999; *Lu et al.*, 2000].

Turbulent Reynolds stresses were calculated from ADV data for each five-minute interval directly from the covariance of along-channel and vertical velocity components according to Equation 5.9. The correlation coefficient and coefficient of determination for each Reynolds stress calculation were calculated. An autocorrelation of the Reynolds stress was used to identify the decorrelation time scales, which were generally on the order of one second. The number of degrees of freedom was calculated as the full sample length (256 seconds) divided by the event duration (twice the decorrelation time) [*Gross and Nowell*, 1983]. The degrees of freedom, t-statistic, and R^2 value were used in Equation 5.7 to calculate the uncertainty in the shear velocity which is propagated to the bed stress. To remove spurious data, when the relative Reynolds stress uncertainties exceeded 100% (data with low velocities when the variance of the velocities fluctuations was large relative to the mean velocity), the data were excluded from analysis. As for the log layer method, the excluded data were associated with the transition flows.

5.2.2.3 Inertial Dissipation

Kolmogorov hypothesized large, turbulent eddies transfer energy to increasingly smaller eddies until viscous dissipation takes place at scales on the order of the Kolmogorov length. Although the largest scales of turbulence may not be isotropic, Kolmogorov noted that the

energy cascade through the inertial subrange from the large, energy containing eddies to dissipation scales consists of isotropic turbulent eddies. For an isotropic turbulent energy cascade, the frequency spectrum of turbulent kinetic energy is described by

$$S(f) = \alpha \epsilon^{2/3} f^{-5/3} \left(\frac{\overline{u}}{2\pi} \right)^{2/3}, \tag{5.10}$$

where α is a constant taken to be 0.69 when using the vertical velocity spectrum, ϵ is the dissipation rate, f is the frequency, and $\overline{u}$ is the mean along-channel velocity at a given depth. Dissipation can be calculated by fitting a line to the portion of the turbulence spectrum with the $f^{-5/3}$ slope.

For a fully developed, unstratified flow with negligible advection, the turbulent kinetic energy budget reduces to a balance between the production and dissipation of turbulence. This balance is described by

$$\epsilon = -\overline{u'w'} \frac{\partial u}{\partial z}, \tag{5.11}$$

where ϵ is the dissipation rate and $\overline{u'w'}$ is the kinematic stress. By assuming a constant stress layer and substituting the friction velocity for the kinematic stress ($u_*^2 = -\overline{u'w'}$), the bed stress can be found by

$$\tau_b = \rho \left(\epsilon \kappa z \right)^{2/3}, \tag{5.12}$$

where κ is the von Karmen constant.

The dissipation of turbulent kinetic energy was calculated using the turbulent velocity spectrum for each ADV burst. Each 256 second record was broken up into individual windows with 1,024 data points and an overlap of 50%. After removing the mean, windows were multiplied by a Hann function and rescaled to preserve variance. An ensemble average of all windows in each burst produced the final spectrum. The first window was removed because the overlapping process resulted in zero padding of the first window. The resulting spectra have 40 degrees of freedom [*Priestley*, 1981]. The 95% confidence interval, obtained from a chi-squared distribution, is $0.61\ S(f) < S(f) < 1.48\ S(f)$ where $S(f)$ is the turbulence spectrum.

The vertical velocity spectrum was used to estimate the dissipation rate of turbulent kinetic energy because the ADV beam geometry resulted in less noise in the vertical direction. The vertical velocity spectrum was multiplied by $f^{5/3}$ to obtain a flat spectrum in the inertial subrange. The slope of the spectrum was calculated over a series of frequency ranges: 0.25 - 1 Hz, 0.5-2 Hz, 1-6 Hz, 4-8 Hz, 8-12 Hz, and 12-16 Hz. The fits for the frequency ranges contained either 25, 65, or 81 points. The frequency range with the minimum slope was defined as the inertial subrange. The dissipation was calculated by setting the mean value over this range equal to $\alpha\epsilon^{2/3}\left(\frac{\overline{u}}{2\pi}\right)^{2/3}$ and solving for ϵ. Uncertainties were calculated by finding the standard deviation and 95% confidence intervals for the spectrum values in the frequency range of the fit. The relative uncertainty bounds for the bed stress, obtained by propagating the uncertainty in the dissipation rate through Equations 5.10 and 5.12, are

$$\Delta\tau_b = \sqrt{\frac{4\rho^2\kappa^2 z^2}{9\left(\kappa\epsilon z\right)^{2/3}}\left(\Delta\epsilon\right)^2}, \tag{5.13}$$

where the uncertainties of all of the variables, with the exception of the dissipation rate, are negligible.

On the tripod, the ADV was deployed immediately adjacent to a second hydrophone shrouded in a shield intended to reduce measurements of flow-noise (10 cm diameter, 43.2 cm height). The sampling volume was approximately 15 cm from the flow shield. A projection of the wake in the direction of the flow revealed that when ebb velocities exceeded 0.5 m/s, the ADV sampling volume was immediately downstream of the flow shield. As a result, the measurements from the ADV during ebb tides may have been compromised by the wake and are not presented.

5.2.2.4 Drag Coefficients

The drag coefficients for flood and ebb tides and their respective uncertainties were calculated by regressing the shear velocity versus the mean current squared. The regressions were performed in both log space and linear space. In linear scale calculations large shear velocities are emphasized whereas log scale calculations emphasize small shear velocities [*Lueck and Lu*, 1997]. For comparison, the drag coefficients were calculated for Reynolds

stress and inertial dissipation techniques. For both techniques, Equation 5.4 governs the relationship between the calculated bed stresses, shear velocities, and drag coefficients.

5.2.3 Acoustic Data Processing

Acoustics data were processed using standard signal processing techniques. For the primary data set of February 2011, the digitized signals were converted to voltage and split into windows containing 2^{16} data points with a 50% overlap. For each window the mean voltage was removed, a Hann function applied, and the signal scaled to preserve variance before applying a Fast Fourier Transform (FFT). Calibration curves were applied to convert voltage spectra to pressure spectra. Ensemble averages of the windowed pressure spectra were calculated to improve the underlying statistics in each 10-second recording (ensemble size of 23, bandwidth of 1.2 Hz). The one-third octave band sound pressure levels (TOLs) [1-25 kHz center frequencies] were calculated by integrating under the spectra.

The June-September 2012 data were processed in two ways to support the analysis of stationarity and intermittency. First, to produce spectrograms with high temporal resolution ($\Delta t \approx 0.025$ seconds), data were processed using 2^{12} data points (bandwidth of 19.5 Hz). Spectra and broadband sound pressure levels (2-20 kHz) were also calculated in 1-second windows (ensemble size of 38). These data were used to highlight mobilization events in the direct vicinity of the hydrophones. Stationarity was investigated by subsampling each 55-second recording to obtain five total signals (4 subsamples and the original). The subsampled signals were the first 1, 5, 10, and 30 seconds of each recording. These four signals and the entire 55-second recording were used to calculate the TOLs (ensemble sizes: 40, 196, 391, 1172, 2344). The resulting TOLs were used to compare the results of different duty cycles by subtracting the TOLs of the 55-second recordings from those calculated using the 1, 5, 10, and 30 second subsamples. A distribution of the results, using 0.5 decibel bins, was calculated for three different frequencies (4, 8, and 16 kHz) during all periods when sediment-generated noise occurs and in one velocity bin (ebb currents between 1.15-1.35 m/s).

5.2.3.1 Frequency Dependence of Sediment-Generated Noise

The equivalent grain diameter for the particles in this study were calculated using the theoretical expression in the form of Equation 5.3, based on a fit to Equation 5.2, for site specific material properties. Available information about the composition of the seabed note a mix of plutonic and metamorphic rocks [*Greene*, 2011]. Using the material properties of basalt ($\rho = 2500$ kg/m^3, $E = 60$ GPa, and $\sigma = 0.15$) the theoretical centroid frequencies for equivalent grain sizes were related by

$$f_c = \frac{206}{D^{0.9}}. \tag{5.14}$$

The resonant frequencies for equivalent grain sizes present at the site did not vary significantly from the results obtained for basalt if other possible material types were assumed. Specifically, the material properties of granite, rhyolite, quartize, gneiss, and slate all resulted in equivalent grain diameters within 15% of those obtained under an assumption of basalt for a given frequency. This difference was relatively small when compared to the distributions of grain sizes which spans nearly two orders of magnitude from coarse sand to cobbles.

5.2.3.2 Directionality

The directionality of sound can be determined using cross-spectral methods. In an array, the phase (ϕ_{12}) relationship between two independent signals can be calculated when coherence (γ_{12}) values are statistically significant. The squared coherence is calculated by

$$\gamma_{12}^2 = \frac{|S_{12}(f)|^2}{S_{11}(f)S_{22}(f)}, \tag{5.15}$$

where S_{12} is the cross-spectrum, S_{11} is the autospectrum of the first signal, and S_{22} is the autospectrum of the second signal [*Priestley*, 1981]. Each component of Equation 5.15, as well as the coincident and quadrature spectra, is calculated from the October 2011 drift study according to the previously identified signal processing techniques (i.e., windowing and averaging) prior to the calculation of the coherence. Data windows contained 2^{15} points with a 50% overlap, resulting in spectra with a bandwidth of 39.1 Hz. Processed data were used

to calculate the phase lags between the two hydrophones at frequencies of interest during strong currents to indicate whether the noise was generated above or below the hydrophones (Section 5.2.3.2). Mean squared coherence was calculated for 10-second sequences (ensemble size 180). Phase lags were calculated with respect to the deeper hydrophone such that a negative phase lag indicates noise generated below the array. The maximum uncertainty of the phase attributable to the DAQ, based on the sampling uncertainty, was less than 3° at the frequencies of interest.

Confidence levels for coherence represent the lowest mean-squared coherence that is expected to occur randomly. *Thompson* [1979] calculated the significance of squared-coherence values and compared the results to Monte Carlo simulations. The work demonstrated that the confidence interval is related to the number of degrees of freedom in the calculations for the mean-squared coherence by

$$\gamma^2_{1-\alpha} = 1 - \alpha^{\left[\frac{2}{\nu-2}\right]}, \tag{5.16}$$

where $1-\alpha$ is the confidence level and ν is the equivalent number of degrees of freedom for the cross-spectrum [*Priestley*, 1981, Tab. 6.2].

The phase relationships between signals are calculated using coincident and quadrature spectra. The phase lag, as a function of frequency, between signal one and signal two is calculated by

$$\phi_{12}(f) = \tan^{-1}\left(\frac{-Q_{12}(f)}{C_{12}(f)}\right), \tag{5.17}$$

where ϕ_{12} is the phase lag, Q_{12} is the quadspectrum, and C_{12} is the cospectrum [*Priestley*, 1981]. Phase lag estimates are suspect, although not necessarily incorrect, when squared-coherence does not exceed the desired confidence level.

For sediment-generated noise and a vertical line array of two hydrophones measuring collisions directly in-line with the array (i.e., collisions directly below the hydrophones for a vertical array), the estimated phase lag between two measurements is related to the acoustic frequency (f), speed of sound (c), and the separation distance between the hydrophones (L). As frequency increases, the phase lag of the signal is expected to increase linearly for a

localized source directly below the array. Under ideal conditions, the phase lag relationship, in degrees, for the vertical line array is described by

$$\tilde{\phi}_{12}(f) = 360\left(\frac{f\ L}{c}\right), \tag{5.18}$$

where $\tilde{\phi}$ denotes the idealized phase lag for a source directly below a vertical array. In practice, the incidence angle (the location of the source relative to the line array) and the orientation angle for a line array (i.e., angle from vertical) are important. In both cases, deviations from the ideal case reduce the measured phase lag relative to the idealized value.

5.2.3.3 Noise Level Regressions

To asses the relationship between between near-bed current velocities and sediment-generated noise, regressions were performed using terms developed from the one-third octave band sound pressure levels and the near-bed velocity cubed. The velocity-cubed metric was used because it provides a logical balance between the units of sound and velocity. Using the plane wave assumption, the TOLs can be easily be converted to an acoustic intensity (i.e., power per unit area). Likewise, the velocity-cubed metric, normalized by an area of 1 m^2, can be readily interpreted as a rate of energy input (i.e., power) per unit area. Thus, the regression coefficients may be thought of as representing the efficiency with which hydrodynamic power is converted to acoustic power through the mobilization of sediment. The final equations and units for the terms used in the regression are described by

$$P_{a,m} = 10\ \log\left(10^{\frac{TOL_m}{10}}\frac{p_o^2}{\rho c}\right) \qquad [\text{dB re 1 W/m}^2], \tag{5.19}$$

$$P_h = \frac{\frac{1}{2}\rho U^3}{A} \qquad [\text{W/m}^2], \tag{5.20}$$

where $P_{a,m}$ is the acoustic power in the m^{th} TOL, P_h is the near-bed hydrodynamic power, p_o is the underwater reference pressure (1μPa), ρ is the density (1024 kg/m^3), c is the sound speed (1490 m/s^1), U is the along-channel, near-bed, mean velocity, and A is the area (1 m^2). The regression, described by

$$P_{a,m} = a_m + b_m P_h, \tag{5.21}$$

provides the coefficients a_m and b_m which may be conceptually thought of as the background noise intensity (y-intercept, dB re 1W/m^2) and the efficiency with which the power input to the seabed by currents is converted to sound (slope, dB re 1W/m^2 per unit increase in near-bed hydrodynamic power). We note that this should be considered only a conceptual framework to give physical context to the regression coefficients since, for example, the power input to the seabed is likely related to U^3. One could construct a similar conceptual framework around a U^2 dependence on the basis of drag forces acting on the seabed. In practice, we found that the use of a U^3 versus U^2 has little effect on the statistical power of the derived regression coefficients.

Prior to estimating the regression coefficients, Automatic Identification System data (Sec. 5.2.4.1) were used to remove measurements with co-temporal vessel traffic within 10 km of the site. For the remaining data, mean measured TOLs were calculated in 0.1 m/s velocity bins. Only periods when TOLs exceed the quiescent mean ($\overline{TOL}$ for $|U| < 0.3$ m/s) by 3 dB or more were used in the regression. A separate regression was performed for each one-third octave band. The lowest velocity bin in which the 3 dB increase was noted for each TOL was considered the critical velocity. This critical velocity was used to estimate the critical shear stress for mobilization of the equivalent grain sizes according to the inversion of the spectrum. It should be noted that defining the critical shear stress as the point at which TOLs have increased by 3 dB is inherently conservative. *Miller et al.* [1977] notes that the threshold should be defined as the conditions (bed stress) just lower than that which results in incipient motion. By relying on increases in sound intensity above ambient noise levels (which are attributed to other sources) to identify critical bed stresses, the thresholds reported here differ from established definitions. However, no other method to identify incipient motion is suitable for these indirect observations.

The access the regression quality, the R^2 values are calculated fits to velocity bin-averaged TOLs according to Equations 5.19, 5.20, and 5.21. Similarly, near-bed currents were used to create a reconstruction predicted TOLs using the regression results according

to Equation 5.22. The R^2 values were then calculated using observed TOLs and the TOLs predicted from the regression coefficients. These R^2 values represent the degree to which mean noise levels in a one-third octave band were dependent on the the near-bed currents. To qualitatively demonstrate this dependence, the regression coefficients were used to construct a 24-hour spectrogram of noise levels from 1-25 kHz. Using the regression, the output was converted to TOLs according to

$$TOL_m(t) = 10\log_{10}\left(\frac{\rho c}{p_o^2}10^{\frac{a_m}{10}}\right) + \frac{1}{2}b_m\rho U^3 \qquad \text{[dB re } 1\mu\text{Pa]}, \tag{5.22}$$

with terms as defined in Equations 5.19, 5.20, and 5.21. The regression coefficients were only applied to conditions when mean currents exceeded the critical values. When near-bed velocities were below the critical value, the TOL values were taken to be only the first term of Equation 5.22 (i.e., mean ambient noise during weak currents).

5.2.4 Exclusion of Other Noise Sources

5.2.4.1 Vessel Noise

While noise from vessel traffic is often considered at frequencies lower than those of interest for this study (i.e., $<$ 1 kHz), *Bassett et al.* [2012] identifies vessel traffic noise as an important contributor to ambient noise at the frequencies considered in this study. Consequently, a field assessment of sediment-generated noise from a location with high vessel traffic density needs to exclude periods when vessel traffic might substantially contribute to ambient noise. An Automatic Identification System (AIS) was deployed at the Admiralty Head Lighthouse in Fort Casey State Park, less than 1 km from the site, to log real-time vessel traffic data. An AIS receiver (Comar AIS-2-USB) and data acquisition computer recorded incoming AIS strings and appended them with a timestamp using a Python script written to record and archive the data. Data were post-processed using a Python package (NOAA data version 0.43) [*Schwehr*, 2010]. This process converted raw AIS transmissions into ASCII format text.

Vessel coordinates and speed over ground were extracted from each AIS string. The coordinates were used to calculate the radial distance from the vessel to the hydrophone.

To prevent vessel noise from biasing analysis of sediment-generated noise, all recordings of ambient noise with an AIS transmitting vessel in transit (vessel speed > 0.05 m/s) within 10 km of the site were excluded. In addition, acoustic data were reviewed manually and recordings with signals consistent with vessel traffic were also removed. This can occur when vessels that do not consistently transmit AIS information, such as military vessels, transit the site. Due low signal-to-noise ratios relative to flow-induced pseudosound, such events were difficult to identify during periods of strong currents and were not removed from the data set [*Bassett*, 2010]. As demonstrated in Section 5.3.2, this should not have an impact on the results because peak levels from vessel noise are exceeded by sediment-generated noise at the frequencies under consideration during strong currents.

5.2.4.2 Pseudosound

Hydrodynamic flow-noise, or pseudosound, is a result of turbulent pressure fluctuations measured by hydrophones. This non-propagating noise is a low-frequency phenomenon and should not be included in a discussion of ambient noise. Studies have reported flow-noise from oceanic turbulence at frequencies as high as 110 Hz [*Gobat and Grosenbaugh*, 1997]. In a series of papers on hydrodynamic flow-noise and wind screen noise, Strasberg noted that the frequency of noise generated by turbulent pressure fluctuations is related to the wavelengths of the spatial velocity fluctuations and the mean velocity [*Strasberg*, 1979, 1985, 1988]. The upper frequency limit for flow-noise is described by $f = |U|\,\eta_o^{-1}$, where U is the mean current and η_o is the Kolmorgorov microscale, the smallest scale that can occur before viscosity damps out the turbulent fluctuations. The microscales are related to the dissipation rate by $\eta_o = (\nu^3/\epsilon)^{0.25}$ where ν is the kinematic viscosity and ϵ is the dissipation rate. For an extreme example, a peak dissipation rate of 0.002 m^2/s^3, consistent with previous findings at the site in this study [*Thomson et al.*, 2012] is used. This dissipation rate implies bed stresses on the order of 10 Pa and suggests a microscale of 0.2 mm. With near-bed currents on the order of 2 m/s, the peak at the site, the maximum theoretical frequency at which flow-noise is expected is approximately 10 kHz. However, when the size of the hydrophone element is larger than the turbulent microscales, as is

the case in this extreme example where the hydrophone diameter (0.019 m) is nearly two orders of magnitude larger the Komolgorov microscale, the signal of pseudosound at these frequencies will be attenuated. This attenuation is a result of phase changes across the hydrophone that cause the pressure differences to partially cancel [*Strasberg*, 1979, 1985], such that the measurable limit of flow-noise is lower than the theoretical maximum. For peak conditions, the scales of turbulence of the same size as the hydrophone would result in noise up to 100 Hz.

The basic characteristics of the acoustic spectra during periods with strong currents suggest that flow-noise is not the source of the increases above 1 kHz. Figure 5.1 includes an example spectrum from a period with a near-bed velocity of 1.6 m/s. Between 1-2 kHz noise levels in this example, and in general for periods with strong currents, are within the range of observed noise levels during slack tide conditions (Sec. 5.3.2). Furthermore, above 1 kHz the observed spectra diverge from the observed, and expected, "red" spectrum associated flow-noise. Given that the analysis in this study focuses on frequencies greater than 1 kHz, we conclude that pseudosound is not of primary importance in this study and is "masked" by propagating ambient noise in the frequency range of interest.

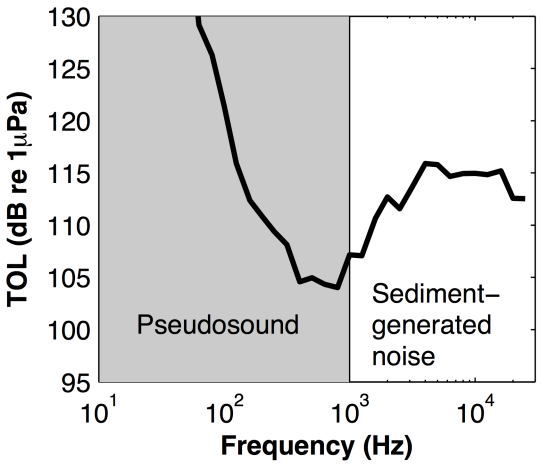

Figure 5.1: An example spectrum typical of acoustic measurements during strong currents. In this example with currents of 1.6 m/s, at frequencies below 1 kHz the spectrum is "red" is as expected for measurements of flow-noise. Above 1 kHz the patterns are not consistent with flow-noise measurements, but rather with sediment-generated noise.

5.3 Results

There is a strong dependence of observed noise levels on near-bed currents (Figure 5.2). The combination of acoustic and hydrodynamics measurements are used further to analyze the relationships between sediment-generated noise levels and the near-bed currents. As for the methods, hydrodynamic results precede acoustics results. Following the hydrodynamics results, sections discussing the directionality, intermittency, and stationarity of observed noise are presented along with a comparison of the observed noise measurements during comparable conditions during the three deployments. These relationships are summarized using a frequency dependent regression.

5.3.1 Hydrodynamics

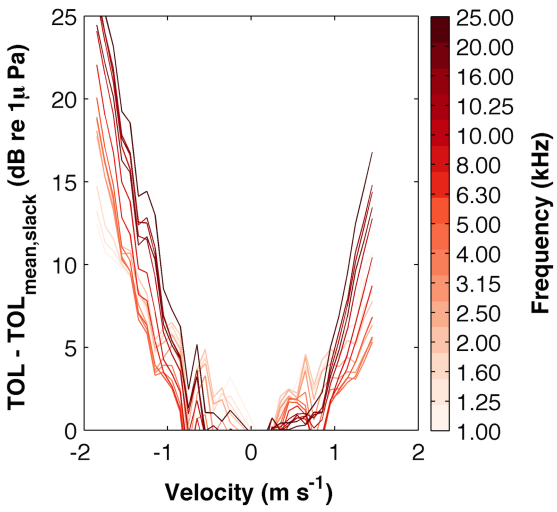

Figure 5.2: TOLs with the mean quiescent noise levels ($|U| < 0.3$ m/s) subtracted versus near-bed current from 1-25 kHz.

Bed stresses obtained via the log layer, Reynolds stress, and inertial dissipation techniques are plotted against the mean current for the bottom velocity bin (1.05 m) in Figure 5.3. Each measurement has unique errors bars obtained according to the methodology discussed in Section 5.2.2. For clarity, a single relative uncertainty representative of each method is included.

A total of 75% of log layer fits meet the $R^2 > 0.95$ criterion. Periods when R^2 values are lower than 0.95 are typically associated with slack currents. When currents exceed 1 m/s, 99% of log layer fits have an R^2 value exceeding 0.95. No fits with R^2 values greater than 0.95 have fewer than 10 degrees of freedom (i.e., the log layer height is always at least ten bins high). The propagation of the uncertainty to the shear stress calculation results in a maximum uncertainty of ±36%, although for currents greater than 1 m/s the maximum uncertainty in shear stress is typically less than ±10%.

Representative uncertainties for the Reynolds stress method are evaluated using the cumulative probability density of uncertainties (not shown). Fifty percent of uncertainties for this method are ±15% or less. A more conservative representative uncertainty for bed stresses of ±35%, the 95% value from the distribution, is chosen. For the inertial dissipation method, the representative uncertainty is chosen as the 95% value from a cumulative probability density function of relative uncertainties of the bed stress. The representative uncertainty is ±27%.

Mean bed stresses, roughness length calculated by the log layer fits, and drag coefficients obtained using the Reynolds stress and inertial dissipation techniques are included for 0.25m/s velocity bins in Table 5.2. The methods show good agreement and are in closest agreement when currents exceed 1m/s. As discussed in Section 5.3.2, these are the same periods in which significant increases of ambient noise are observed. Figure 5.3 also includes plots of the bed stresses estimated by the Reynolds stress method versus the inertial dissipation and log layer methods. During flood tides there is good agreement between the results for all three methods. During ebb tides the log layer and Reynolds stress methods agree well. As mentioned in Section 5.2.2, the dissipation rate of turbulent kinetic energy during ebb currents are not included in Table 5.2 and Figure 5.3 because the measurements may have been compromised by the wake of another instrument. Bed stresses calculated by all methods are found to exceed 1 Pa at the site for currents greater than 0.5 m/s. Above 1m/s mean bed stresses are approximately 5 Pa, and peak bed stresses exceed 20 Pa.

The drag coefficient is calculated on both linear and log scales for comparison. Drag coefficients calculated using Reynolds stresses for the log and linear fits are indistinguishable with values of 0.0039 and 0.0045 for ebb and flood tides. The drag coefficients calculated using the Reynolds stress and inertial dissipation techniques during flood tides are comparable to values obtained at other sites with coarse-grained beds [*Williams et al.*, 1989; *Thorne et al.*, 1989; *Lueck and Lu*, 1997]. Based on the good agreement between the flood tide drag coefficients and measured data, the drag coefficient ($C_D = 0.0044$, linear scale) is applied later to calculate critical shear stresses.

Table 5.2: Mean bed stresses in 0.25 m/s velocity bins for Reynolds stress, inertial dissipation, and log layer fit techniques, roughness length calculated by log layer fits, and drag coefficients.

τ_b (Pa)	Velocity Bin (m/s)	0-0.25	0.25-0.5	0.5-0.75	0.75-1.0	1.0-1.25	1.25-1.5	1.5-1.75	> 1.75
Flood	Reynolds Stress	0.2	0.8	2.0	3.6	6.4	8.6	14.3	15.7
	Inertial Dissipation	0.1	0.5	1.8	3.2	6.4	10.8	14.3	13.5
	Log Layer	-	-	3.2	4.7	7.2	10.6	14.1	15.8
Ebb	Reynolds Stress	0.2	0.7	1.7	3.2	5.8	8.1	16.7	27.1
	Inertial Dissipation	-	-	-	-	-	-	-	-
	Log Layer	-	-	3.2	5.0	8.7	12.4	17.3	19.8

z_0 (m)	Velocity Bin (m/s)	0-0.25	0.25-0.5	0.5-0.75	0.75-1.0	1.0-1.25	1.25-1.5	1.5-1.75	> 1.75
Flood	Log Layer	-	-	0.018	0.008	0.007	0.007	0.005	0.005
Ebb	Log Layer	-	-	0.025	0.015	0.012	0.011	0.012	0.008

C_D	Linear		Log	
	Ebb	Flood	Ebb	Flood
Reynolds Stress	0.0039 ± 0.0011	0.0044 ± 0.0002	0.0039 ± 0.0010	0.0045 ± 0.0001
Inertial Dissipation	-	0.0033 ± 0.0001	-	0.0042 ± 0.0001

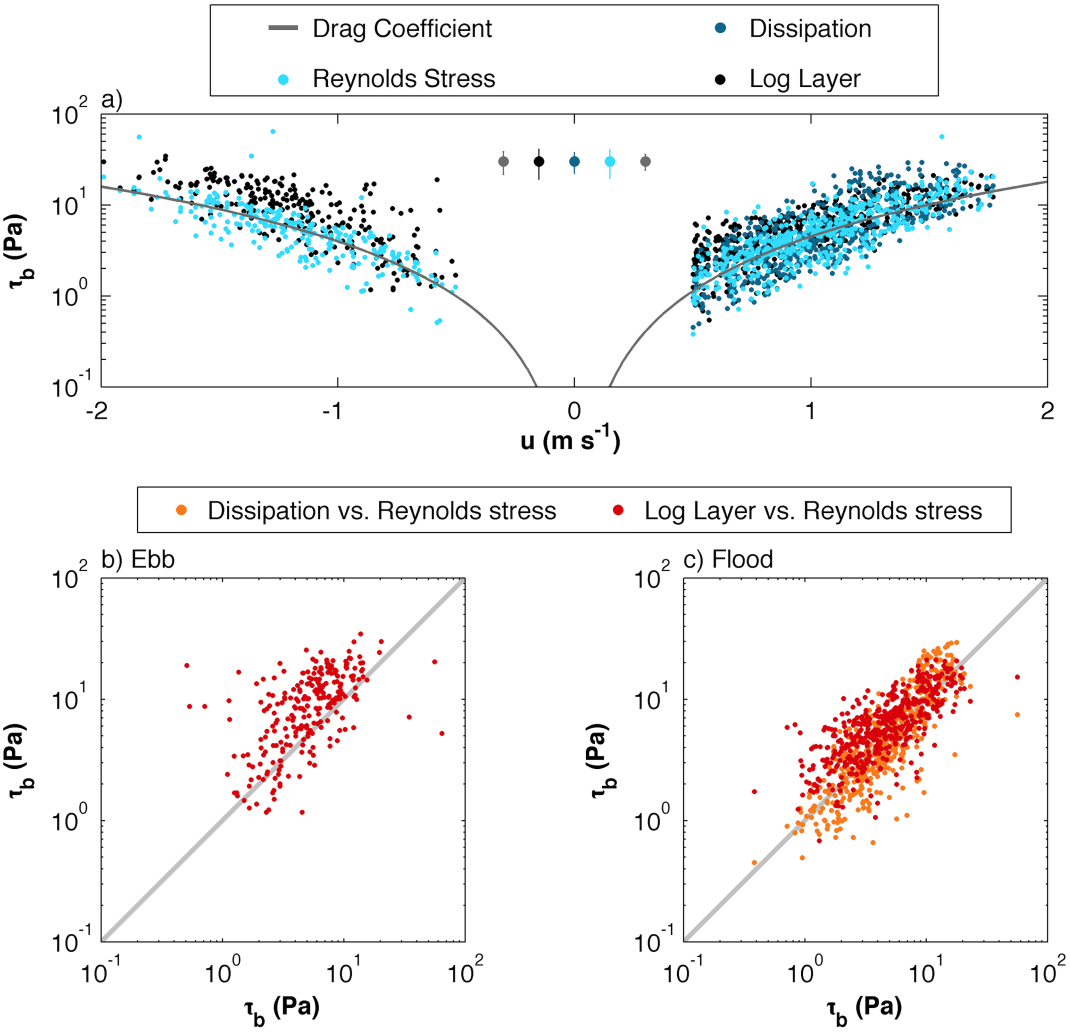

Figure 5.3: a). Measured bed stresses versus mean velocity using inertial dissipation, Reynolds stress, log layer fits, and a drag coefficient (calculated from Reynolds stress estimate). Error bars highlight the representative 95% uncertainty values for each method. The drag coefficients and their uncertainties are calculated using a linear fit to Reynolds stress data (0.0039 for ebb tides and 0.0044 for flood tides, Table 5.2). b). A comparison of bed stresses calculated by two methods for ebb tides. c). A comparison of bed stresses calculated by three methods for flood tides.

5.3.2 Acoustics

5.3.2.1 Frequency Dependence of Sediment-Generated Noise

When noise levels are considered across all stages of the tide, there are significant increases in noise levels relative to near-quiescent conditions above 1 kHz that are correlated with

strong currents, as shown in Figure 5.4 for mean noise spectra in one-third octave bands in 0.2 m/s near-bed velocity bins. Previous analysis of data from the same site provide context for the increases in ambient noise attributed to the mobilization of the bed. *Bassett et al.* [2012] presents ambient noise levels, primarily associated with vessel traffic, for periods when near-bed currents (referenced to the bottom bin of current profiler) were less than 0.4 m/s. At the site, vessel presence is uncorrelated with the tide [*Bassett et al.*, 2012]. The shaded portions of Figure 5.4 highlight the 5% to 95% percentile spectra for periods with currents less than 0.4 m/s as presented in *Bassett et al.* [2012]. During the strongest currents, ambient noise levels above 1 kHz exceed the 95^{th} percentile for quiescent conditions.

These noise level increases are consistent with the production of sound by increasingly large sediment grains with stronger near-bed velocities. An estimate of the grain sizes that would contribute to noise level increases at a specific frequency is obtained by inverting Equation 5.14. Each inversion is carried out on the lowest frequency that includes significant

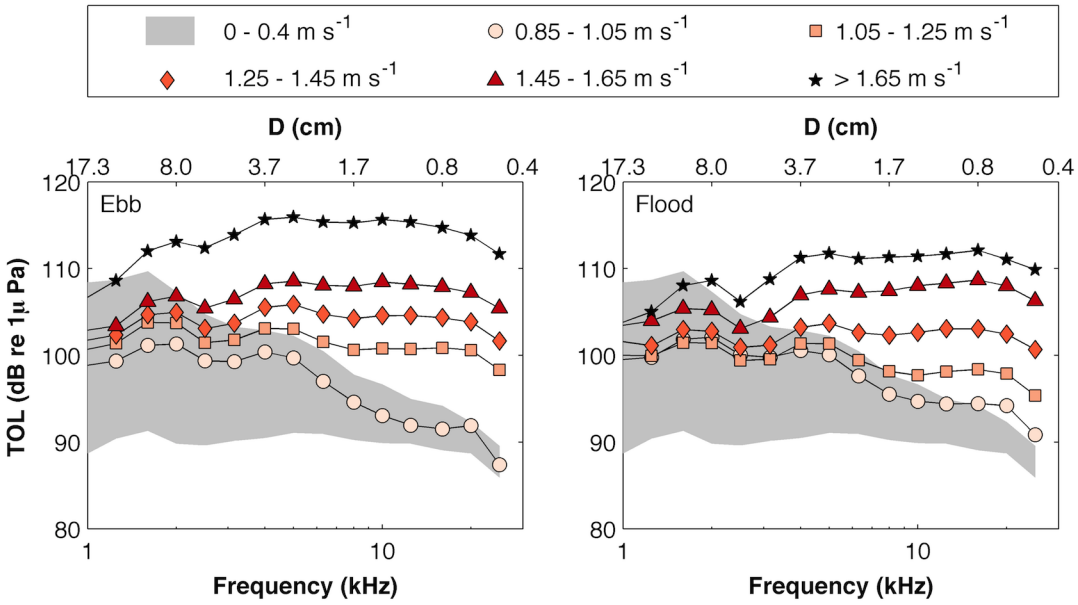

Figure 5.4: One-third octave band sound pressure levels versus frequency. The solid gray area highlights the 5% to 95% ambient noise statistics for currents less than 0.4 m/s [*Bassett et al.*, 2012]. Spectra are not shown for period with currents less than 0.85 m/s because SGN during these periods has no significant impact on noise levels. a). Ensemble averaged acoustic spectra by velocity bin during flood tides. b) Ensemble averaged acoustic spectra by velocity bin during ebb tides.

noise increases (+3 dB from quiescent conditions) for a given velocity. The equivalent grain sizes for the frequencies in the spectra (Fig. 5.4), calculated using Equation 5.14, are included on the secondary x-axis. Based on the inversion, the first increases in noise levels (i.e., at $f > 25$ kHz) are associated with grain sizes smaller than 1 cm and ebb currents of 0.65 m/s. As the currents and shear stresses increase, higher noise levels are attributed to grains as large as 17 cm (cobble). The greatest increases in noise intensity are associated with frequencies that, when inverted, would be categorized by the ROV survey as gravel. More modest increases also occur at frequencies that are associated with pebbles. As previously noted, a survey indicates that small cobbles, pebbles, and gravel are the primary grain sizes present on the seabed in the immediate vicinity of the site. Given the noted linear relationship between mobilized mass and sound intensity [*Thorne*, 1986b; *Thorne et al.*, 1989; *Williams et al.*, 1989; *Thorne*, 1990], the spectra suggest that mobile gravel is the most significant contributor to increased noise levels. As previously discussed, ROV survey notes indicate that larger sediments (boulder, cobble) are generally heavily encrusted while smaller sediments (gravel, pebble, and coarse sand) are not. This suggests that the modest increases in sound levels below 4 kHz are more likely caused by smaller, mobile grains impacting the larger, but immobile grains (e.g., cobbles).

This hypothesis is supported by video data. In one particular sequence, a piece of mobilized gravel strikes a large pebble causing it to shift and strike an even larger pebble. In total, three pebbles shift as a result of the impact. Upon shifting, each pebble exposes a number of smaller gravel grains, comparable in size to the grain involved in the initial collision, which are rapidly entrained by the currents. A video of the described mobilization event, annotated snapshots from the video, and a spectrogram of the audio are provided as supplemental material (online).

As discussed in the methodology, the data used to identify the characteristics of sediment-generated noise were obtained during three deployments over a period of more than 18 months. The February 2011 and June-September 2012 sets both included fixed measurements 1 m above the seabed and the October 2011 drift measurements were taken at a depth of approximately 40 m (10-15 m above the seabed). Using velocity data from the Doppler profilers a period of strong, near-bed, ebb currents of approximately 1.65 m/s is identified

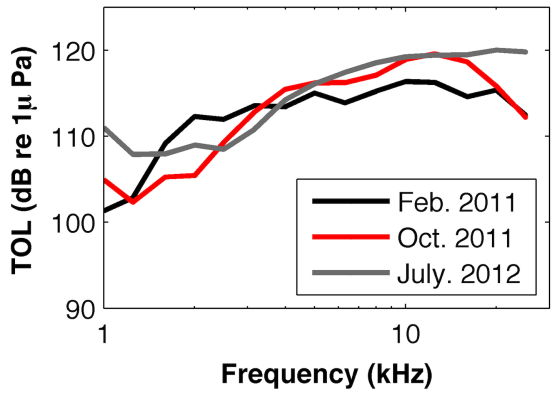

Figure 5.5: Observed one-third octave band sound pressure levels obtained during three deployments. The Feb. 2011 and July 2012 recordings were obtained 1 m above the seabed and the Oct. 2011 measurements were obtained 10-15 m above the bed while drifting.

in each of the data sets. Example acoustic spectra from these periods are included in Figure 5.5. The frequency content and amplitude of the observed noise in all three data sets are comparable under similar hydrodynamic conditions. When compared to other spectra in Figure 5.4, it is clear that the TOLs are typical of those that are only found during periods with strong near-bed currents. The similarities between the spectra suggest no significant changes in the composition of mobile particles at the site.

5.3.2.2 Directionality of Sediment-Generated Noise

Vertical array results provide additional evidence that elevated noise levels are associated with sediment movement. Figure 5.6 includes plots of coherence and phase lag obtained using the cabled hydrophone array. At the time the data in Figure 5.6 were recorded near-bed currents were 1.65 m/s (ebb tide). These currents would be expected to result in significant sediment-generated noise above 3 kHz (Fig. 5.4). The depth of the hydrophones at the time of the recordings was 41.2 m (between 10 and 15 m above the seabed).

For the entire frequency range in Figure 5.6 (0.02-10 kHz), mean square coherence levels exceed the 99% confidence levels. The increasing negative phase lag with frequency suggests that the seabed is the noise source for frequencies from 2 kHz to 10 kHz. Below 2 kHz, the dominant sound sources would likely be more distant sources (e.g., vessels) for which arrival angles are expected to be nearly horizontal (i.e., phase lag approaching 0°). The slope of the line above 2 kHz also indicates a mean phase lag associated with near vertical arrival angles. A similar pattern of phase lags with the expected phase wrapping occurs at higher frequencies, but above 10 kHz the coherence levels do not exceed the 99% confidence

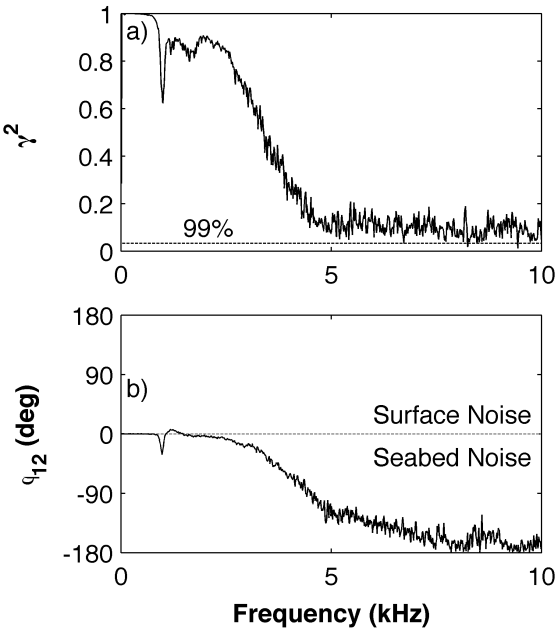

Figure 5.6: a). Mean-squared coherence versus frequency. Coherence values exceed the 99% confidence level below 10 kHz. b) Phase lag versus frequency calculations. The dotted gray line separates the domains for surface and seabed generated noise. The spike at 1 kHz is associated with an peak the the ambient noise spectra from an unidentified source.

level. Decreases in the coherence above 2 kHz may be attributable to the nonstationarity of the signal due to the intermittent nature of the sediment-generated noise, changing vessel position, or the diffuse nature of mobilization events on the seabed due to turbulence (as indicated by video observations). Although the precise location of the source of the noise cannot be determined by the array, the negative phase lag is not only consistent with a sound source originating from below the array, but the increasingly negative phase lag with frequency is also consistent with near-vertical arrival angles. Differences between the idealized phase lag for a source directly below the array and observed phase lag ($\tilde{\phi}$ and ϕ) may be attributed to a number of factors including the location of the noise sources on the seabed and off-vertical hydrophone orientation. Although there was no significant wire angle observed during the deployment, it is possible that vertical shear lower in the water column may have resulted in a horizontal displacement between the upper and lower hydrophones changing the vertical separation distance and the orientation angle of the line array resulting in a decreased phase lag.

5.3.2.3 Intermittency and Stationarity

The sound produced by sediment grains shifting on the seabed is not continuous. That is, bed load transport is not sustained at a given location throughout the tidal cycle. The mean spectra are representative of characteristic noise levels integrated over an area of the seabed under different hydrodynamic conditions, but do not provide details about transient events. For example, a series of one-second average spectra, a spectrogram with the 55-second mean spectrum subtracted, and a time-series of broadband (2 kHz - 20 kHz) sound pressure levels, presented in Figure 5.7, show the dominant signal associated with a single local mobilization event. The peak intensities suggest that the both pebbles and gravel were mobilized. Manual review of the recorded audio reveals elevated noise levels attributable to sediment motion although the identification of individual events is generally not possible (i.e., the spectra in Figure 5.7 are representative of a minority of recordings when sediment generated noise is present). However, when localized events occur near the hydrophone, the identification of sound from individual events is possible. During these instances, the sound is similar to what one hears when gravel is poured over a pile of gravel. During these events, broadband sound pressure levels increase by up to 15 dB with energy contained in frequency bands between 1 and 30 kHz.

As demonstrated in Figure 5.7, intermittent signals associated with highly localized mobilization events have the potential to impact sediment-generated noise statistics based on the averaging period or the duty cycle of the recording instrument. Figure 5.8 includes the probability distribution functions of the difference between TOLs calculated using 55-second averages and those calculated using 1, 5, 10, and 30-second averages for three frequencies (4, 8, and 16 kHz). For each frequency, the mean TOL is the approximately the same (< 1 dB difference) regardless of the length of the recording. However, as is expected for a weakly stationary signal, in each case the distribution is narrower for longer averaging periods.

5.3.3 Noise Level Regressions

Regression statistics for the sound intensity versus near-bed hydrodynamic power per unit area are included in Table 5.3 for the velocity bin averaged acoustic data and for the time

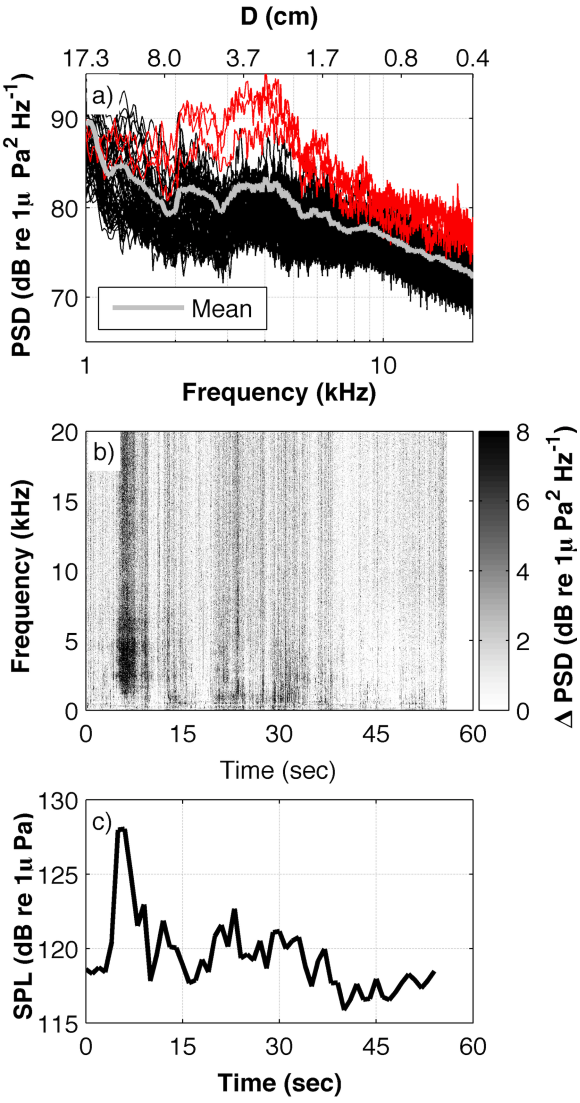

Figure 5.7: Example of intermittent acoustic data for a 55-second recording with mean currents of 1.15 m/s (ebb) recorded on July 27, 2012. a). One-second average acoustic spectra (black), the spectra associated with the local mobilization event beginning at five seconds in the recording (red), and the 55-second average spectrum (gray). b). Spectrogram with one-minute mean spectrum subtracted. c). Time series of broadband SPLs (2-20 kHz).

seres data using the regression coefficients obtained from the bin averaged data (note again that the bin averaged data are required to identify critical near-bed velocities). The regression coefficients suggest that, in the absence of sediment-generated noise, these frequency bands would be relatively quiet and that the conversion of hydrodynamic to acoustic power is inefficient. These are both physically realistic relations and consistent with the prior discussion. For bin-averaged data, the R^2 values for both flood and ebb currents exceed 0.9 for all frequency bands.

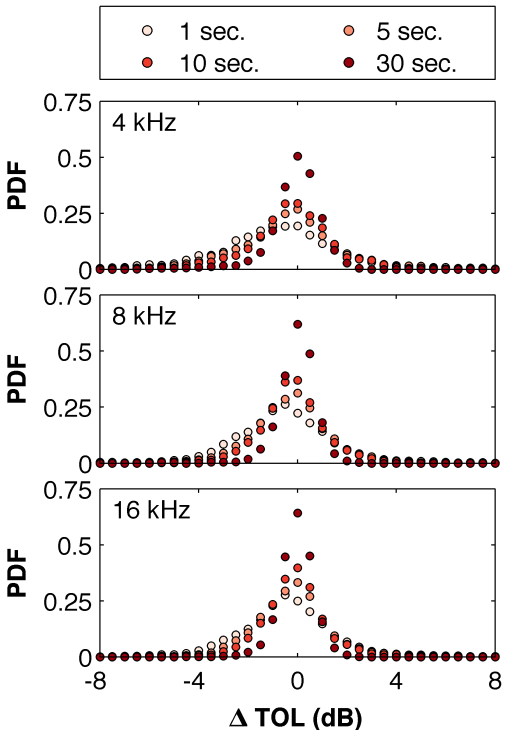

Figure 5.8: Probability distribution functions of the difference between 55-second TOLs and 1, 5, 10, and 30-second TOLs for ebb currents between 1.15 and 1.35 m/s. Other velocity bins and frequencies bins are not shown but have similar distributions.

The R^2 values for the unbinned time series data are lowest at the low frequencies, but still highly significant given the total number of data points included in the regressions. The source of the lower R^2 values, specifically at lower frequencies, can be explained by the low signal-to-noise ratio of sediment-generated noise to other ambient noise sources and the section on intermittency and stationarity (Sec. 5.3.2.3). Especially below 4 kHz, noise levels during periods of strong currents fall within the range associated with quiescent conditions. As such, scatter in the data at these frequencies may be in part attributed to other noise sources. In all frequency bands, there is also more scatter in the acoustic data during low currents.

Based on the method, the onset of noise level increases is correlated with bed stresses on the order of 3 Pa. In general, the regression slope coefficient increases with frequency, suggesting that hydrodynamic power is more efficiently converted to acoustic power for small grain sizes. Just as mean shear stresses in a velocity bin vary between flood and ebb

currents, noise levels and the efficiencies also vary between flood and ebb tides. The ebb efficiencies, converted to an approximate noise level increase in 0.1m/s bins, range from approximately 0.9 (1 kHz) to 3 dB (25 kHz) per 0.1 m/s increase in the near-bed velocity. During flood tides, the comparable coefficients are 1.5 (1 kHz) to 3.6 (25 kHz) dB per 0.1m/s increase in the near-bed velocity.

To provide a qualitative example of the predictive value of the regression coefficients, a time series of TOLs and currents is included in Figure 5.9 for a 24-hour period. Both regression coefficients are only applied to TOLs when the mean currents exceeds the critical velocity (Table 5.3). Vessel traffic, which is not represented using the regressions, regularly increases TOLs in all measured frequency bands (as previously discussed, the regression values are derived from observations without vessel traffic). During strong currents there is good agreement in received levels across all frequency bands included in the regressions. This agreement demonstrates that sediment-generated noise levels at the sites are highly predictable from the near-bed velocity, once site-specific regression coefficients have been obtained. At this site, strong spatial gradients result in significant reductions in currents at scales on the order of 100's of meters [*Palodichuk et al.*, 2013]. As a result, sediment-generated noise levels are expected to change at comparable length scales.

5.4 Discussion

The results presented here demonstrate a rich relationship between hydrodynamics, the physics of incipient motion and mobilization of heterogeneous, coarse-grained beds, and ambient noise in high-energy environments. As demonstrated in Figure 5.4, sediment-generated noise is a significant source of ambient noise at this location. The intensity and regularity of sediment-generated noise is dependent on hydrodynamic conditions and seabed composition. If conditions regularly mobilize the bed, sediment-generated noise can contribute significantly to ambient noise over a broad frequency range related to the local composition of the seabed.

Table 5.3: Results and statistics for the noise versus velocity-cubed regressions. Coefficients a_m (ambient noise) and b_m (efficiency) correspond respectively to the y-intercept and slope of the acoustic intensity versus hydrodynamic power for one-third octave bands. R^2 values are calculated for the time series data with no vessels present using the coefficients from the velocity bin averaged regressions. The total number of points used to calculate raw R^2 values is n. The threshold for significant noise increases, +3 dB from mean slack tide conditions is $\overline{u}_{cr}$(m/s).

	Ebb						Flood					
f_c (kHz)	a_m	b_m	$\overline{u}_{cr}$ (m/s)	R^2 Time Series	n	R^2 Bin Ave.	a_m	b_m	$\overline{u}_{cr}$ (m/s)	R^2 Time Series	n	R^2 Bin Ave.
1	-85.4	0.0024	1.25	0.15	463	0.97	-87.6	0.0042	1.25	0.23	438	0.93
1.25	-85.1	0.0031	1.25	0.25	463	0.99	-88.4	0.0048	1.25	0.32	438	0.94
1.6	-83.5	0.0042	1.25	0.39	463	0.99	-87.7	0.0055	1.25	0.38	438	0.95
2	-83.6	0.0046	1.25	0.44	463	0.98	-87.9	0.0056	1.25	0.42	438	0.94
2.5	-86.1	0.0052	1.25	0.54	463	0.99	-89.3	0.0054	1.25	0.45	438	0.92
3.15	-86.1	0.0058	1.25	0.62	463	0.99	-89.9	0.0064	1.25	0.46	438	0.93
4	-84.5	0.0060	1.25	0.62	463	0.99	-88.0	0.0068	1.25	0.42	438	0.91
5	-84.9	0.0064	1.15	0.60	564	0.99	-86.6	0.0065	1.15	0.47	645	0.93
6.3	-86.6	0.0069	1.05	0.65	700	0.99	-88.9	0.0074	0.95	0.59	1049	0.96
8	-87.7	0.0075	0.95	0.67	782	0.98	-90.4	0.0082	0.85	0.70	1256	0.98
10	-88.2	0.0078	0.85	0.68	837	0.98	-91.1	0.0089	0.85	0.73	1256	0.98
12.5	-88.1	0.0076	0.85	0.62	837	0.98	-91.0	0.0091	0.85	0.70	1256	0.98
16	-88.1	0.0075	0.85	0.55	837	0.97	-90.8	0.0090	0.85	0.67	1256	0.98
20	-87.8	0.0069	0.85	0.52	837	0.97	-91.0	0.0088	0.85	0.67	1256	0.98
25	-91.6	0.0078	0.65	0.59	949	0.96	-95.2	0.0102	0.85	0.72	1256	0.97

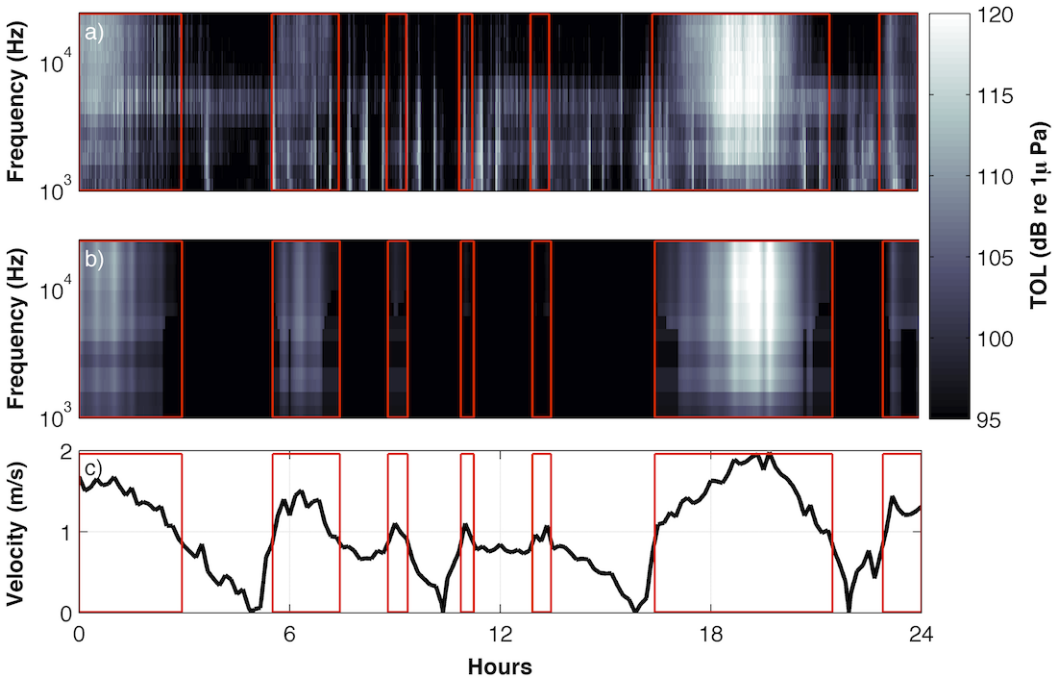

Figure 5.9: Comparison of observed noise levels and a time series constructed from the regressions coefficients for February 17, 2011. Periods with currents exceeding 1 m/s are highlighted. a.) Measured spectrogram. The regular increases in broadband noise levels during weak currents are a result of vessel traffic. b). Spectrogram reconstructed using regression coefficients. c). Near-bed currents.

5.4.1 Bed Stress and Sediment Mobilization

The shear stresses at which increases in ambient noise are attributed to sediment-generated noise are lower than previous estimates discussed in Section 5.1. Again, we note that the thresholds defined in this study are based on increases in TOLs, which require regular mobilizations or collisions between grains. In this study, noise levels for equivalent grains sizes up to 6 cm ($f > 2.5$ kHz) increase with shear stresses greater than 7 Pa. By contrast, comparable values were noted by *Thorne et al.* [1989] for sand and gravel in a tidal channel and by *Miller et al.* [1977] for 1 cm equivalent grain sizes in experimental work. A comparison between critical shear velocities (u_{*c}) calculated for site specific data, the Shield's parameter (assuming $\Theta_c = 0.06$), and *Hammond et al.* [1984] are included in Figure 5.10. The site specific critical shear stresses were calculated assuming a drag coefficient of 0.0044 (Section 5.3.1) and the critical velocity thresholds included in Table 5.3. The critical shear

stresses for all calculated grain sizes are lower than the critical values using the Shields parameter and *Hammond et al.* [1984].

The referenced thresholds for sediment movement, described in *Miller et al.* [1977], which covers literature dating back to *Shields* [1936], are derived from simplified experimental studies intended to reduce scatter in the data sets. Amongst the common design parameters are unidirectional flows, flumes with parallel sidewalls, and beds consisting of rounded, uniformly sized grains. Lower observed thresholds for larger grains in natural environments can be related, in part, to differences in hydrodynamics conditions (e.g. turbulence), bed roughness, grain size distribution, grain spacing, and grain protrusion into the flow. In a heterogeneous bed, larger grain sizes carry a disproportionately large fraction of bed stress which, in turn, leads to mobilization at lower bed stresses than those that would be expected for a uniform bed consisting of smaller grains [*Hammond et al.*, 1984]. Turbulent bursts, particularly events with positive along-channel velocity fluctuations, have been found to be related to the most significant transport events [*Heathershaw and Thorne*, 1985; *Thorne et al.*, 1989]. Lower turbulence in controlled laboratory experiments may also contribute to differences between mean thresholds in the laboratory and the marine environment.

5.4.2 Intermittency and Stationarity

During an observation period, sediment-generated noise levels are not constant. When turbulent bursts cause the motion of larger grains, more grains are exposed to entrainment. This process can result in sudden transport of many smaller, less exposed particles [*Hammond et al.*, 1984; *Heathershaw and Thorne*, 1985]. Transport events have also been attributed to significant intermittent increases in bed stresses above the mean that are associated with turbulence. Mean recorded sound intensities are a result of the summation of received levels from individual events in surrounding areas of the seabed. This summation represents the average conditions at the site. When a mobilization event occurs in the immediate vicinity the hydrophone, integrated received levels from the seabed are dominated by the mobilization event closest to the hydrophone. While unpredictable, these intermittent events do not have a significant impact on the overall predictability of noise levels from

sediment transport, as shown in Section 5.3.3. This result is attributed to the cumulative nature of noise measurements near the seabed. That is, although transport events are intermittent for these coarse grains, mobilization events distributed over the seabed result in predictable noise levels. Based on the relationship of TOLs to near-bed currents, duty cycling and averaging periods can be increased to reduce scatter but should not exceed the time scales over which tidal currents can be considered stationary (approximately 5 minutes at this site).

5.4.3 Masking of Other Noise Sources

Sediment-generated noise at the study site in Admiralty Inlet is the most significant contributor to ambient noise above 2 kHz during periods of strong currents. From 2 to 30 kHz sediment-generated noise is sufficiently loud to regularly mask all other common noise sources, including rain, breaking waves, and vessel traffic in the same frequency range. The masking potential of sediment-generated noise at the site is particularly striking above 4 kHz. These noise levels exceed the 95% noise levels during quiescent conditions, which are attributed primarily to vessel traffic, by up to 20 dB.

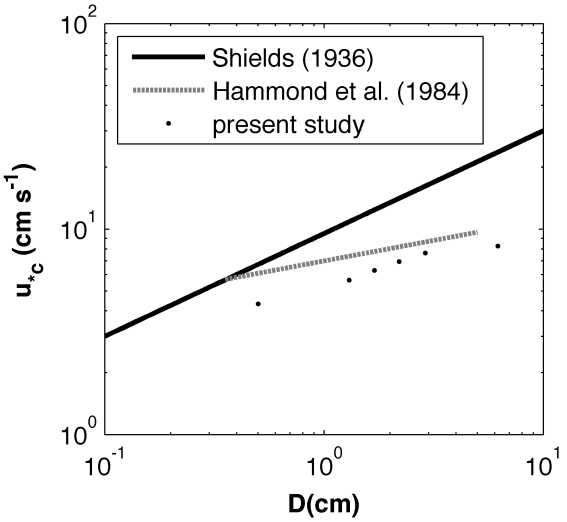

Figure 5.10: Critical shear velocities versus equivalent grain diameter.

From a practical standpoint, the limitations placed on passive acoustic studies due to sediment-generated noise are mostly limited to frequencies greater than 2 kHz. In highly energetic coastal environments this noise source could reduce the effective range of passive acoustic monitoring techniques. For example, sediment-generated noise overlaps with higher frequency components of vessel traffic noise that are often neglected in anthropogenic noise studies. In coastal environments, these contributions to anthropogenic noise can be

significant [*Bassett et al.*, 2012].

There is growing interest in developing tidal energy projects in energetic coastal environments. In these environments, sediment-generated noise may be common, emphasizing the need to better understand sediment-generated noise and its relevance to monitoring anthropogenic and biological noise sources. As a practical example, echolocation clicks of mid- and high-frequency cetaceans overlap with the frequencies of sediment-generated noise from coarse and fined grained sediments (1 kHz $< f <$ 200 kHz). Sediment-generated noise at these frequencies can be recorded by echolocation click detectors tuned to these frequencies (e.g., Chelonia C-POD) complicating biological assessments using these instruments.

5.4.4 Applicability to Other Sites

Highly energetic sites such as the one discussed here represent a very small subset of coastal environments. Although research in such environments has resulted in a limited body of literature on the subject, we expect that high levels of ambient noise due to bedload transport are common in comparable areas. Sediment-generated noise from the resuspension and transport of sediments by surface waves in shallow waters may also be common over a wider geographic range.

Sediment-generated noise is highly dependent on hydrodynamic conditions and seabed composition, limiting the direct application of results presented here to other sites. Nonetheless, a series of basic conclusions can be drawn with respect to sediment-generated noise. In general, sites with bed stresses that are sufficiently large to mobilize coarse grained sediments are unlikely to have significant amounts of exposed fine grain sediments (i.e., sand and clay) due to winnowing of these constituents. As a result, at sites with comparable hydrodynamic conditions, sediment-generated noise is unlikely to be significant at high frequencies ($f >$ 50 kHz, $D \approx 0.1$ cm, the upper limit for coarse sand) except in the cases of energetic estuaries with large suspended sediment loads from local inflows. More energetic sites are likely to produce noise at lower frequencies, unless scoured to bedrock, because larger shear stresses can support the motion of larger grain sizes.

5.5 Conclusion

Analysis of hydrodynamic and acoustic measurements from a site in Admiralty Inlet, Puget Sound, WA (USA) suggest sediment-generated noise is the dominant noise source between 1 kHz and 30 kHz during periods of strong currents. Peak sediment-generated noise levels from 4 kHz to 20 kHz are associated with mobile gravel and pebbles. Sediment-generated noise levels in one-third octave bands exceed noise levels attributed to vessel noise by up to 20 dB. Equivalent grain sizes, estimated by inverting the acoustic spectra associated with sediment-generated noise, are in agreement with the known distribution of grain sizes present at the site. Three methods of calculating the bed stress show good agreement for periods of strong currents. Using increases in noise levels at different frequencies, critical shear stresses for different grain sizes are estimated and found to be lower than laboratory studies despite the use of a more conservative definition of critical shear stress. Regressions of the sound intensity versus the near-bed hydrodynamic power per unit area show that noise levels are predictable and that the largest increases in noise levels are associated with smaller grains (higher frequencies). Localized, intermittent events can increase recorded noise levels by more than 10 dB over a periods of seconds. Due to such events, the distribution of TOLs recorded in a velocity bin is narrower for longer recording periods, as long as near-bed velocities can still be considered stationary.

Chapter 6

FLOW-NOISE

The text of the following chapter was submitted for publication in the *Journal of the Acoustical Society of America* in August, 2013. With the exception of reformatting the text, no changes were made to the content of the article. The citation for the article, pending publication, is as follows:

Bassett, C. , J. Thomson, P. Dahl, and B. Polagye, Flow-noise and turbulence in two tidal channels, *J. Acoust. Soc. Am.*, submitted.

6.1 Introduction

Pressure fluctuations occur when fluid moves relative to an immersed body at high Reynolds numbers. If sufficiently large in magnitude, these fluctuations can be measured by a pressure sensitive transducer. This phenomenon, called *flow-noise* or *pseudosound*, is a result of both advected ambient turbulence and interactions with the transducer in the flow. Unlike other ambient noise sources, flow-noise does not propagate and should not be included in ambient noise statistics. In some cases, the magnitude of these pressure fluctuations is much greater than those associated with ambient noise. Although flow-noise is fundamentally a low frequency phenomenon, the range of frequencies over which flow-noise can interfere with ambient noise measurements is dependent on the intensity of turbulence and the transducer geometry.

Flow-noise in the ocean has been identified in a number of applications utilizing stationary measurement platforms. In Narragansett Bay, Rhode Island measurements in the octave band centered at 25 Hz [*Willis and Dietz*, 1965] and frequency bands from 40 to 100 Hz [*Dietz et al.*, 1960] were found to be strongly correlated with tidal cycles. *Webb* [1988] identifies infrasonic flow-noise in the bottom boundary layer. Flow-noise induced by

wave orbital motion has been reported up to 500 Hz [*Gobat and Grosenbaugh*, 1997], and flow-noise on moored instruments in shallow water has been reported at frequencies below 50 Hz [*Deane*, 2000].

While flow-noise often appears in measurements, predicting its acoustic spectrum is a more difficult task. *Webb* [1988] and *Strasberg* [1979, 1985] identify and suggest models for infrasonic flow-noise based largely on scaling arguments related to the mean flow velocity. Beyond the infrasonic range ($f < 20$ Hz), there are no generalized models for flow-noise. For advected turbulence with a length scale that is small in comparison to the characteristic size of the hydrophone, phase variations across the surface of the hydrophone cause pressure fluctuations to partially cancel and increase the spectral slope of flow-noise relative to turbulence [*Strasberg*, 1979]. This study focuses on flow-noise associated with turbulent scales that are similar to and smaller than the size of the hydrophone.

There are few published ambient noise studies in highly energetic environments, defined here as locations where turbulent kinetic energy (TKE) exceeds 0.0025 m^2/s^2 and mean currents in exceed of 0.5 m/s. In recent years, an interest exploiting strong currents for tidal power generation has led to ambient noise studies in such locations to understand the potential environmental impacts of power production (e.g., *Polagye et al.* [in revision]). One of the primary environmental concerns associated with commercial-scale tidal power extraction is the acoustic emissions from tidal turbines because of their potential to affect marine mammal behavior [*Polagye et al.*, 2011]. At tidal energy sites, flow-noise presents a significant challenge to quantifying ambient noise, especially at low frequencies.

Drifting platforms are one approach to characterizing sound in high-flow environments since the relative velocity between drifters and the mean flow is small. This limits both the advection of turbulence across the transducer and turbulence shed by the transducer. However, drifter studies are labor intensive, convolve space and time, and cannot cost-effectively quantify temporal variations in sound over long time scales (e.g., hours to months). Therefore, a robust assessment of ambient noise conditions or turbine noise requires that instrumentation packages must be deployed over time periods longer than permitted by drifting studies, and thus must be exposed to strong currents.

6.1.1 Turbulent Velocity Fluctuations

Currents in tidal channels have velocity components related to deterministic tides, meteorological currents (e.g., storm surges and wave-induced currents), and turbulence [*Polagye and Thomson*, 2013]. If meteorological currents are negligible, the current velocity can be represented as $u = \overline{u} + u'$, where $\overline{u}$ is the mean, deterministic velocity which is nearly constant over short (e.g., 5-10 minute) sample periods and u' are the turbulent velocity fluctuations. In general, u is a vector with along-channel, cross-channel, and vertical components when projected along the principal axis. Hereafter, all velocity references refer to the component projected along the principal axis of the flow.

Identification of the range of temporal and spatial scales of turbulence is critical to the interpretation of fluctuations sensed by a pressure sensitive transducer. Previous work in high-current environments identifies two important turbulent domains: the large-scale, horizontal eddies containing most of the turbulent kinetic energy, and the small-scale isotropic eddies of the inertial subrange [*Thomson et al.*, 2012]. Turbulent kinetic energy is dissipated at smaller length scales (dissipation range). *Kolmogorov* [1941] provides the theoretical basis for the assumption of isotropic turbulence and an analysis of measurable spatial patterns in isotropic turbulence. The theoretical wavenumber spectrum in the inertial subrange is written as

$$S_u(k) \;=\; a\epsilon^{2/3}k^{-5/3}, \tag{6.1}$$

where $S_u(k)$ is the turbulent spectrum, ϵ is the dissipation rate of turbulent kinetic energy, a is a constant, and k is the spatial wavenumber of the turbulence scales. Invoking Taylor's frozen turbulence hypothesis [*Taylor*, 1938] and substituting the frequency for the wavenumber, the turbulence spectrum in the inertial subrange is described by

$$S_u(f) \;=\; a\epsilon^{2/3}f^{-5/3}\left(\frac{\overline{u}}{2\pi}\right)^{2/3}, \tag{6.2}$$

where a f is the frequency and $\overline{u}$ is the mean advected velocity.

The turbulent energy of large-scale, typically anisotropic, eddies is transferred to smaller scales, a process that continues until viscous forces damp out the fluctuations. Basic scaling

arguments are used to identify the spatial and temporal scales at which turbulent fluctuations occur. The smallest turbulent scales found in the inertial subrange, the Kolmorogov microscales, are related to the viscosity and the dissipation rate of turbulent kinetic energy. The Kolmorogov length scale (η_o) is defined as

$$\eta_o = \left(\frac{\nu^3}{\epsilon}\right)^{1/4}, \tag{6.3}$$

where ν is the kinematic viscosity. At frequencies greater than those associated with the Kolmorogov mircoscales the spectral slope is steeper than in the inertial subrange due to preferential damping by viscosity.

6.1.2 Turbulent Pressure Fluctuations

Turbulence in the ocean can generate noise through multiple mechanisms: sound radiated by turbulence and noise resulting from the presence of a pressure sensitive transducer in the flow. *Proudman* [1952] and *Lighthill* [1952, 1954] provide a theoretical basis for the radiation of sound by turbulence. The relationships developed in these papers highlight that the sound radiation efficiency has a strong dependence on the Mach number (M^5), defined as $\overline{u}/c$, where $\overline{u}$ is the advected velocity and c is the celerity. Given the celerity of seawater ($\approx$ 1500 m/s), the Mach number is small and sound generated by turbulence underwater is radiated inefficiently. Noise levels attributed to this radiated sound are well below typical ambient noise levels in the ocean [*Wenz*, 1962; *Ross*, 1976].

The second mechanism, pressure fluctuations associated with turbulence, cannot be measured remotely because they do not produce propagating sound waves. The non-propagating pressure fluctuations that can be locally measured are advected turbulent pressure fluctuations and fluctuations resulting from the interaction between the sensor and the turbulent flow [*Strasberg*, 1979, 1985; *Webb*, 1988]. In their analyses, *Strasberg* [1979, 1985] and *Webb* [1988] identify spectra associated with flow-noise at low frequencies ($<$ 20 Hz) in relatively low-velocity conditions ($\overline{u} < 0.5$ m/s) without co-temporal turbulence data. These studies serve as the starting point for this analysis. In the absence of interactions between pressure fluctuations and the sensor, the wide-band pressure fluctuations are related to the velocity

fluctuations according to

$$\overline{p^2} = \rho^2 \left(\overline{u'^2}\right)^2, \tag{6.4}$$

where $\overline{p^2}$ is the mean-square pressure fluctuation, ρ is the ambient density, and $\overline{u'^2}$ is the mean-square along-channel velocity fluctuation [*Kraichnan*, 1956]. *Strasberg* [1979] hypothesized a relationship between velocity and pressure spectra,

$$S_p(f) = \rho^2 \overline{u'^2} S_u(f), \tag{6.5}$$

where $S_p(f)$ is the pressure variance spectrum and $S_u(f)$ is the velocity variance spectrum. While Eq. 4 can be obtained by integrating over all frequencies in Eq. 5, as *Strasberg* [1979] notes, there is no theoretical basis for this relationship.

Strasberg [1979, 1985] related frequency-dependent pressure fluctuations to velocity fluctuations according to

$$S_p(f) = \rho^2 \overline{u}^2 S_u(f), \tag{6.6}$$

where the turbulent velocity term in Eq. 6.5 is replaced with the mean velocity. When velocity fluctuations are advected across the sensor, the observed frequency is related to mean velocity and wavelength of the velocity fluctuation (λ) according to $f = \overline{u}/\lambda$. It is expected that a sensor in the flow will be most sensitive to turbulent scales that exceed the largest dimension (d) of the sensor such that $fd/\overline{u} \ll 1$ is satisfied (i.e., the turbulent "gust" engulfs the entire sensor). In this regime, the observed trend (e.g., slope) of the turbulent velocity spectrum is expected to be equivalent to that in the pressure spectrum. In this study, the frequencies under consideration exceed 20 Hz and it will be shown that the associated spatial scales do not satisfy $fd/\overline{u} \ll 1$. Therefore, attenuation of the pressure signal due to partial cancelation of the pressure fluctuations is expected, which increases the slope of the spectrum in this regime. Analysis of flush-mounted hydrophones suggests the attenuation scales with the dimensionless frequency according to $(fd/\overline{u})^n$ and n is related to the hydrophone geometry [*Urick*, 1975].

This paper presents velocity and noise data obtained in two energetic tidal channels: the Chacao Channel, Chile and northern Admiralty Inlet, Puget Sound, Washington. At both sites, peak tidal currents exceed 3 m/s, and these strong currents produce significant flow-noise for moored transducers. Co-temporal turbulence and noise measurements from the Chacao Channel are used to develop models for flow-noise and extend previous analyses of flow-noise to higher frequencies. These models are then compared to observations from Admiralty Inlet. The following sections discuss the theoretical principles and results of the flow-noise models. Sec. 6.2 includes a description of the measurement sites, moorings, data acquisition systems, and signal processing methods. Sec. 6.3 presents the data from both sites and Sec. 6.4 interprets the results and discusses the implications for studies in high velocity environments.

6.2 Methods

6.2.1 Sites

Co-temporal hydrodynamic and acoustic measurements were obtained from two locations in this study: the Chacao Channel near Carelmapu, Chile and Admiralty Inlet near Port Townsend, Washington, USA. Because of large dynamic range of velocities at both sites, there are no periods with true "slack" currents throughout the water column. Here "slack" refers to periods when $\overline{u} < 0.3$ m/s at the depth of the sensor platforms.

In Chacao Channel, Chile a mooring, referred to as the Tidal Turbulence and Acoustics Mooring (TTAM), was deployed to obtain hydrodynamic and acoustic measurements at S 41° 45.75', W 73° 40.95' from February 11, 2013 to February 14, 2013 (Fig. 6.1a-b). The mooring was deployed at a depth of approximately 38 m from the R/V Dr. Jurgen Winter, a research vessel operated by the Universidad Austral de Chile.

By using a mooring instead of a rigid platform deployed on the seabed, measurements were taken outside of the region in which boundary layer effects are most significant without utilizing a prohibitively large and expensive platform. The TTAM, further described in *Thomson et al.* [2013], consisted of three major components: a heavy anchor ($\approx$ 1050 kg in water) to hold the mooring in place, a vane on which the instruments were mounted, and a

94 cm float (≈ 317 kg of buoyancy) to hold the mooring line in tension.

The vane for mounting the instrumentation was deployed in-line between the anchor and the float 9 m above the seabed at slack water. Swivels mounted to both ends of the vane provided a passive yawing mechanism to keep the instruments aligned into the principal axis of the flow and minimized the risk of mooring components interfering with the sensors. Two acoustic Doppler velocimeters (ADVs) and two autonomous hydrophone packages were deployed on the vane. The dual-package approach provided redundancy and maintained symmetry across the vane.

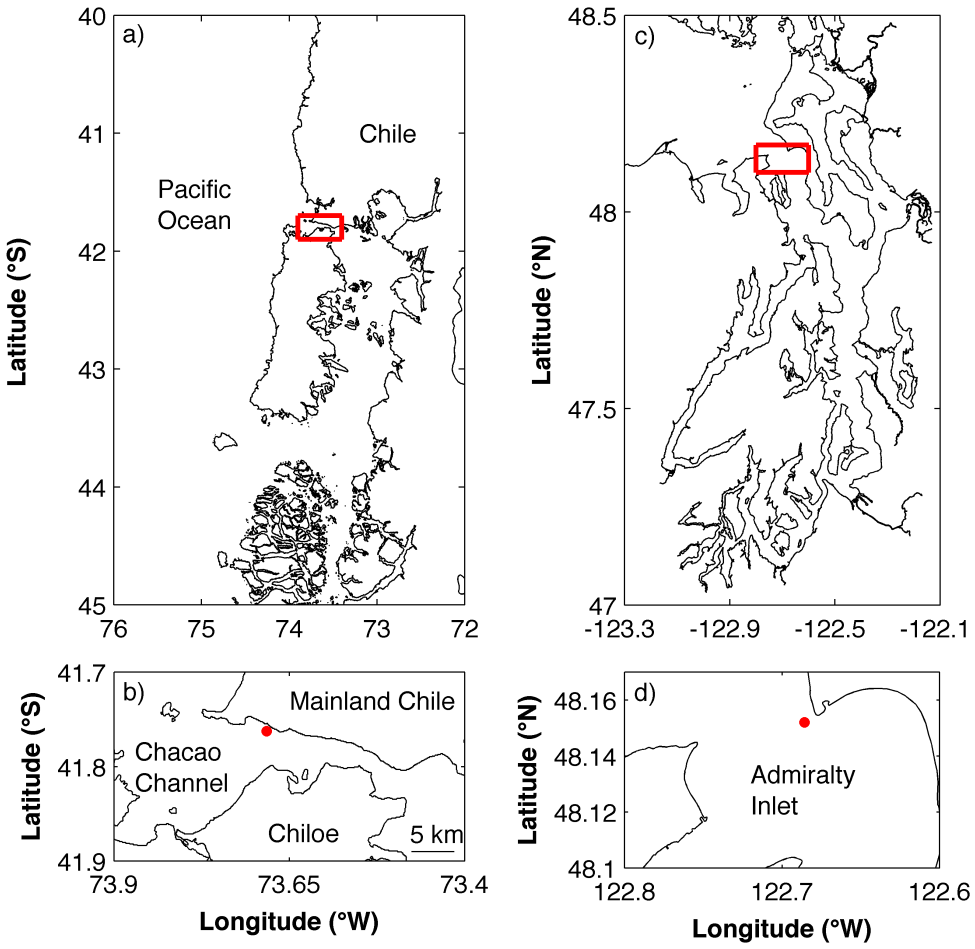

Figure 6.1: a-b). South-central Chile, the study area (red rectangle), and the deployment site (red circle). c-d). Puget Sound, the study area (red rectangle), and the deployment site (red circle).

The Chacao Channel, in comparison with many coastal environments in the United States, has relatively small amounts of commercial shipping traffic. Shipping vessels and cruise ships bound for Puerto Montt occasionally transited the site and three large vessels were noted during daytime hours throughout the deployment period. While large shipping traffic may operate without considering the local currents, local fishing patterns are determined by them. Local fishers leave the village prior to slack tide to dive for 40 minutes near the deployment site before retuning. The local fishing vessels were, in general, less than 10 m long and have operating air compressors for surface-supplied diving. With the exception of overnight slack tides, the acoustic signals of small vessels appeared in nearly all of the slack tide recordings.

During slack water, the spectrum levels increase to approximately 80 dB re $1\mu\text{Pa}^2/\text{Hz}$ at 5 kHz, which is consistent with noise from snapping shrimp [*Everest et al.*, 1948; *Readhead*, 1997]. Above 1 kHz, there are also increases in noise levels that diverge from the expected flow-noise spectrum. Energetic sites like these with beds composed of grains smaller than 10 cm can produce significant amounts of sediment-generated noise [*Bassett et al.*, 2013]. The data to confirm this noise source are not available; however, the observed increases at frequencies greater than 1 kHz during non-slack conditions are consistent with the noise that would be produced by a mobilized bed composed of pebbles and gravel [*Thorne*, 1985, 1986a].

In Admiralty Inlet, USA, co-temporal velocity and noise measurements were obtained using autonomous instrumentation packages on a tripod deployed from the R/V Jack Robertson at 48° 09.120' N, 122° 41.152' W (depth 55 m) from February 11-21, 2011 (Fig. 6.1c-d). In this area, Admiralty Inlet is about 5 km wide and shipping lanes and local ferry traffic result in high densities of vessel traffic [*Bassett et al.*, 2012]. This site has been the subject of acoustic studies including vessel noise [*Bassett et al.*, 2012] and sediment-generated noise [*Bassett et al.*, 2013] in addition to turbulence studies (Thomson et al., 2012; Thomson et al., 2013).

An Oceanscience (www.oceanscience.com) Sea Spider tripod with additional lead ballast was modified to allow for the deployment of a variety of instrumentation packages and recovery floats. The instruments relevant to this study, an ADV and two hydrophones,

were mounted vertically on one side of the tripod. The sampling volume of the ADV and the hydrophones were vertically aligned such that they each recorded 1.05 m from the seabed. There was a horizontal separation distance of approximately 30 cm between the hydrophones. The ADV was deployed such that the sampling volume was located at the midpoint between the hydrophones.

6.2.2 Turbulence and Mean Velocity Measurements

The ADVs used to measure mean current velocities and turbulence at both sites were 6 MHz Nortek Vectors. In the Chacao Channel, the ADVs sampled at 16 Hz for 300 sec every 10 min. Velocity spectra were calculated for 128 sec time windows with 50% overlap. In Admiralty Inlet the sampling frequency was 32 Hz for 256 sec every 10 min and spectra were calculated using 32 sec time windows with 50% overlap. In the case of the Chacao Channel, an x-IMU (inertial motion unit) was mounted within the ADV pressure housing. IMU data was used to remove mooring motion contamination from the velocity spectra [*Thomson et al.*, 2013]. For both data sets, each sample period were projected on to the principal axis, reviewed for quality, and despiked using the phase-space method [*Goring and Nikora*, 2002; *Mori et al.*, 2007]. ADV data were used to calculate turbulence spectra, mean velocities, and the dissipation rate. Mean current velocities were linearly interpolated to form a times series with 1-min resolution.

6.2.3 Acoustic Measurements

In both the Chacao Channel and Admiralty Inlet, the autonomous hydrophones were Loggerhead Instruments DSG data acquisition systems equipped with Hi-Tech (HTI-96-MIN) hydrophones approximately 1.9 cm in diameter and 5 cm long. In the Chacao Channel, the hydrophones were deployed on the mooring vane at a -20° angle relative to the horizontal such that the change of angle due to drag on the mooring resulted in the hydrophones being oriented roughly lengthwise into the along-channel flow. Throughout the deployment, the systems recorded ambient noise continuously with a sampling frequency of 80 kHz. Spectra were calculated using windows with 65 636 data points ($\approx$ 0.8 sec) and a 50% overlap. Each

window was tapered using a Hann window. The resulting spectra had a frequency resolution of $\Delta f = 1.22$ Hz and were truncated to only include frequencies between 0.020-25 kHz (low frequency linear limit to the hydrophone through maximum frequencies of interest). Given that each recording was 62.5 sec long, timestamps were rounded down to the nearest minute for comparison to ADV data.

The motion and vibrations of the mooring caused by strong currents and turbulence contributed to self-noise. Using a combination of manual review of the audio and visual inspection of spectrograms, the signatures of two types of self-noise produced by the mooring were identified. The first type, clanging and creaking sounds associated with floats, shackles, and mooring vane, occurred occasionally. The most easily identifiable peaks attributed to this self-noise occurred around 700 Hz although energy was present between 300-1000 Hz (Fig. 6.2). Even during noisy periods, these sounds were identifiable.

The second type mooring noise, attributed to mooring vibrations, appeared in spectrograms as continuous noise when current velocities exceeded 0.9 m/s. In individual recordings, these peaks appeared as a constant, lower intensity noise. Examples of these peaks are visible in Fig. 6.6. In the spectrum associated with current velocities from 0.9-1.2 m/s there was a notable peak around 90 Hz that shifts to higher frequencies with increases in current velocity. These peaks in the spectra were relatively narrow and adjacent frequency bands are consistent with the characteristics of flow-noise.

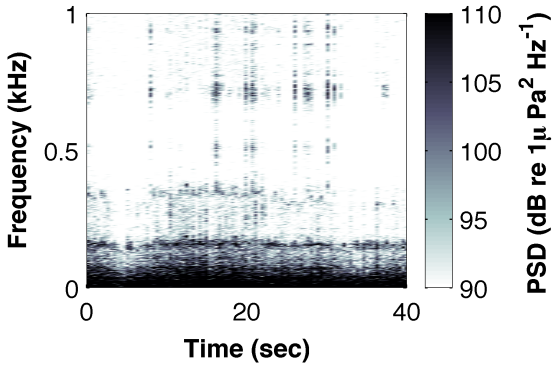

Figure 6.2: A 40-second spectrogram from the Chacao Channel showing the transient signals associated with clanging and creaking noise centered around 700 Hz.

These noises were not removed from the recordings; instead, further analysis focuses on the characteristics of the spectra outside of these frequency bands. More specifically, the analysis of flow-noise was limited to frequencies below 500 Hz and those that didn't have peaks that regularly diverged from the expected spectrum of flow-noise. It should

also be noted that these increases were not consistent with vortex shedding from the hydrophone. For example, the Strouhal number for associated with a cylinder in such flows is approximately 0.2 [*Schewe*, 1983], which implies a shedding frequency of 12 Hz during peak currents, was too low to explain the 90 Hz noise.

Signals from vessel traffic in the Chacao Channel was, at times, easily identifiable, particularly during slack currents. The sound produced by local fishing vessels, cruise ships, and shipping vessels resulted in increased noise levels across a broad range of frequencies. To remove these points from the data set, all data were manually reviewed for signals consistent with vessel noise. Such signal characteristics included a series of tones below 500 Hz and broadband increases up to 20 kHz that evolved on time scales consistent with the passage of a vessel – up to 30 minutes depending on the vessel type [*Greene and Moore*, 1995; *McKenna et al.*, 2012; *Bassett et al.*, 2012]. These recordings were flagged and not included in the analysis of flow-noise. A total of 466 recordings out of a total 2,959 were removed due to obvious vessel traffic. Although some of the retained recordings likely include some degree of vessel traffic, this was limited to signals with relatively low pressure spectral densities.

The same hydrophones and processing techniques were used in Admiralty Inlet with two exceptions: the hydrophones recorded 10 sec at the top of every minute and they were deployed such that the hydrophones elements were oriented vertically in the water column. Admiralty Inlet has been previously identified as a noisy environment in which vessel traffic is a significant contributor to ambient noise levels [*Bassett et al.*, 2012]. To identify vessel traffic, an Automatic Identification System (AIS) receiver located near the site was used to record real-time vessel traffic. In post-processing, times when an AIS transmitting vessel was within 10 km were identified and removed from the data set. The exclusion of all instances when an AIS transmitting vessel was present within the detection range of the AIS system ($\approx$20 km) would have resulted in few data points to analyze. In addition, many small vessels do not transmit AIS data. Unlike the Chacao Channel data, manual review of the data was not used to remove vessel traffic not identified by the AIS system due to the challenges of identifying these signals in a noisy environment.

6.2.4 Flow-Noise Models

Two models relating the flow-noise pressure spectra to current velocity and turbulence are developed using observations at the Chacao Channel site, which has more favorable measurement conditions (i.e., less vessel traffic). The two models are based on the frequency-dependent relationship between velocity and pressure (Eq. 6.6) as given by *Strasberg* [1979, 1985]. The first model estimates flow-noise from measured mean velocity and turbulence, while the second model estimates flow-noise on the basis of mean velocity alone.

Eq. 6.5 also provides a basis for the development of a model; the only difference between Eqs. 6.5 and 6.6 is that the first contains the mean-square velocity fluctuation term while the second contains a mean-velocity squared term. This results in a difference of approximately 3 orders of magnitude between the two models. Given the agreement between observed data and models based on Eq. 6.6, the models based on Eq. 6.5 are not of primary importance. The development of these models in the following sections refer forward, by necessity, to some of the results formally presented in Sec. 6.3.

6.2.4.1 Flow-Noise Model 1: Pressure Spectra Derived from Turbulence Measurements

The first model, referred to as the "turbulence model", relates the pressure spectra to the mean velocity and turbulence spectra. A semi-empirical approach is applied to scales where the assumption that the $fd/\overline{u} \ll 1$, where d is the size of the transducer, is violated. This approach requires the quantification two terms empirically: the slope of the observed pressure spectra due to partial cancelation of pressure fluctuations over the surface of the hydrophone (m) and the frequencies at which the change in slope due to decreased sensitivity occurs. The frequency at which the transition occurs is referred to as the shoulder frequency (f_{sh}). Through the substitution of the turbulence spectrum (Eq. 6.2) into the relationship for the pressure and velocity spectra (Eq. 6.6), the velocity spectrum is converted to a pressure spectrum based on the scales of the turbulence according to

$$\tilde{S}_p(f) = \begin{cases} a\rho^2\overline{u}^2\epsilon^{2/3}f^{-5/3}\left(\dfrac{\overline{u}}{2\pi}\right)^{2/3}, & \text{if } f < f_{sh} \quad (6.7) \\ a\rho^2\overline{u}^2\epsilon^{2/3}f^{-m}\left(\dfrac{\overline{u}}{2\pi}\right)^{2/3}, & \text{if } f > f_{sh} \quad (6.8) \end{cases}$$

where the tilde denotes the model.

To determine the empirical constants (f_{sh} and m) the slopes of the observed pressure spectra are calculated from 30-70 Hz. These frequencies are chosen because below 30 Hz, the frequency response of the recording system begins to roll-off and above 70 Hz mooring self-noise and lower signal-to-noise ratios (flow-noise being the signal) reduce the method accuracy. These fits are further discussed in Sec. 6.3.2, but for the purpose of model development we note that the observed slope follows $f^{-3.2}$, thus $m = -3.2$. This slope is applied to Eq. 6.8 and the shoulder frequency is identified by iteratively adjusting this term to maximize agreement with the observed pressure spectra. The best relationship between the modeled and observed spectra occurs when

$$f_{sh} = 0.1 \left(\frac{\overline{u}}{d} \right). \tag{6.9}$$

In other words, the sensitivity to turbulent scales decreases due to partial cancellation if these scales not at least 10 times larger than the characteristic size of the hydrophone. In this formulation, the size of the hydrophone that is applied in both models is length of the hydrophone in the direction of the along-channel flow (i.e., 5 cm in Chacao Channel and 1.9 cm in Admiralty Inlet). The shoulder frequency is always less than the frequencies included in this study (< 20 Hz). Therefore, further development of the flow-noise model is limited to Eq. 6.8.

Modeled spectrum levels (in dB re $1\mu\text{Pa}^2/\text{Hz}$) are given by

$$\tilde{S}_p(f) = 10 \log_{10} \left(\frac{a\rho^2 \overline{u}^2 \epsilon^{2/3} f_{sh}^{-5/3} \left(\frac{\overline{u}}{2\pi} \right)^{2/3} \left(\frac{f}{f_{sh}} \right)^{-3.2}}{10^{-12}} \right), \qquad \text{if } f > f_{sh} \tag{6.10}$$

and the modeled pressure spectra are obtained by applying the dissipation rate, mean velocity, and water density (1024 kg/m^3). The modeled spectra are calculated for the same frequencies as the measured acoustic spectra.

6.2.4.2 Flow-Noise Model 2: Pressure Spectra Derived from Mean-Flow

One major limitation in the development of the turbulence model is that it requires an estimate for the dissipation rate, which is more difficult to obtain in high flow environments than the mean velocity. As an alternative, turbulence scaling arguments are used to develop a flow-noise model, referred to as the "mean-flow model," based on the mean advected velocity and the slope of the pressure spectra. The first scaling argument relates the dissipation rate to the largest scales of turbulence in a flow. An estimate of the rate of transfer of energy to turbulence yields $\epsilon \propto u_{rms}^3/l$, where u_{rms} is the root-mean-square of the velocity and l is the scale of the energy containing scales [*Lumley and Terray*, 1983; *Thorpe*, 2007]. The velocity is decomposed as $u = \overline{u} + u'$ and the turbulence intensity is defined as

$$I = \sigma_{u'}/\overline{u}, \tag{6.11}$$

where $\sigma_{u'}$ is the standard deviation. If $I^2 \ll 1$, then by the mathematical definition root-mean-square velocity, $u_{rms} \approx \overline{u}$ and

$$\epsilon \propto \frac{\overline{u}^3}{l}. \tag{6.12}$$

Thomson et al. [2012] showed that the dominant scales of the TKE in two well-mixed, energetic tidal channels to be well represented by three times the water depth, assuming the tidal elevation is small compared to the depth. Therefore, the eddy scale l in the Chacao Channel is assumed to be constant so that $\epsilon \propto \overline{u}^3$. As shown in Sec. 6.3.1, the observed dissipation rates are consistent with this scaling at the Chacao Channel site.

Assuming that the hydrophone-specific attenuation factor $(fd/\overline{u})^n$, combined with Eq. 6.6, is able to describe the flow-noise, it follows that the observed velocity and frequencies dependencies should be satisfied. Therefore, the pressure spectrum scales as

$$\tilde{S}_p(f) = \rho^2 \overline{u}^2 S_u(f) \left(\frac{fd}{\overline{u}}\right)^n. \tag{6.13}$$

By combining Eqs. 6.2 and 6.6 and substituting $\overline{u}^3$ for ϵ, the pressure spectrum becomes

$$\tilde{S}_p(f) = a\rho^2 \overline{u}^{14/3} f^{-5/3} \left(\frac{fd}{\overline{u}}\right)^n, \tag{6.14}$$

where the water depth (l) is rolled into the constant a. This is an underdetermined system in which both the $\overline{u}$ and f dependencies must be satisfied by n. A slope of $f^{-3.2}$ is identified, resulting in $n \approx -1.5$, a value that agrees well with the observed velocity dependence in the Chacao Channel. The final formulation (in $\mathrm{Pa}^2/\mathrm{Hz}$) based on this semi-empirical approach is

$$\tilde{S}_p(f) = c\rho^2 \overline{u}^{6.1} f^{-3.2}, \tag{6.15}$$

where c is a constant which now represents a combination of the constant from the power fit scaling between the dissipation rate and $\overline{u}$ (including the length scale l), the prior constant (a), and the slope transition associated with the sensitivity to turbulence of different scales. Notably, the magnitude of this scalar offset is dependent, in part, on the mechanisms responsible for the production and dissipation of turbulence, which vary significantly in natural environments. Because of this, the model's framework may be applicable to other sites where $\epsilon \propto \overline{u}^3$, but the magnitude is expected to vary. To simplify the analysis and demonstrate the effectiveness of this method, the results from Eq. 6.15 are regressed against the observed noise levels to identify this constant. The final, spectral form (in dB re $1\mu\mathrm{Pa}^2/\mathrm{Hz}$) is

$$\tilde{S}_p(f) = b + 10\log_{10}\left(\frac{\rho^2 \overline{u}^{6.1} f^{-3.2}}{10^{-12}}\right), \tag{6.16}$$

where b is a constant.

6.3 Results

6.3.1 Turbulence results

The measurements of turbulence and mean currents made during five-minute periods are affected by two types of mooring motion. The first, a change in the angle of the mooring line due to drag forces on the float, is related to the mean currents. During peak currents, 40° angles relative to the vertical are observed, resulting in a measurement position approximately 6 m above the bed in comparison to 9 m above the bed during slack currents [*Thomson et al.*, 2013]. However, the change occurs over time scales longer than 5 minutes

and along-channel currents may be obtained by correcting for orientation from the internal ADV sensor. The second type of mooring motion is caused by turbulence, and can contaminate the velocity measurements. *Thomson et al.* [2013] includes analysis of the same velocity data set and demonstrates that data can be post-processed to obtain accurate turbulence spectra, as shown on a mean-velocity bin-averaged basis in Fig. 6.3. The inertial subrange for isotropic turbulence, which has a $f^{-5/3}$ dependence and is used to determine the dissipation rate of TKE, is evident in all of the bin-averaged spectra. The $f^{-5/3}$ slope continues until viscous dissipation damps out the turbulent fluctuations and the flattening of the spectra at high frequencies in Fig. 6.3 is caused by the lower limit of the instrument's sensitivity. The peaks in the TKE spectra during low current periods are caused by low-frequency mooring oscillations. When currents exceed 0.6 m/s the amplitude of the peaks in the spectra decreases due to increased tension in the mooring line.

Consistent with scaling arguments, the dissipation rate of turbulent kinetic energy increases with the mean current velocity. Fig. 6.4 includes time series data for the mean current velocity and the dissipation rate. The observed current velocities range from 0 to 3 m/s on both flood and ebb tides. The dissipation rates, which are shown to scale with $\overline{u}^3$ (Fig. 6.5a), range from less than 10^{-5} m^2/s^3 around slack water to greater than 10^{-3} m^2/s^3 during peak currents. While the dissipation rate scales with $\overline{u}^3$ at this site, it should be noted that the scaling of turbulence is largely dependent on local features of the flow (e.g., bathymetry) so this result cannot be assumed to apply in other tidal channels [*Thomson et al.*, 2013]. A time series of the theoretical maximum frequency of turbulent pressure fluctuations in the inertial subrange (Eq. 6.3), also included in Fig. 6.4c, shows microscale

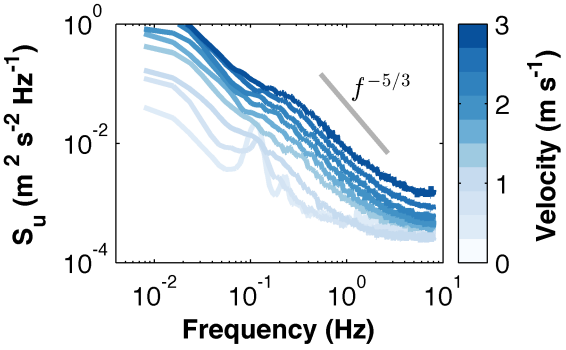

Figure 6.3: Velocity-bin averaged (0.3 m/s bins) TKE spectra from the Chacao Channel show the expected $f^{-5/3}$ slope associated with isotropic turbulence. During periods with weak currents ($\overline{u} < 0.3$ m/s), there is significant mooring motion contamination. However, during these periods flow-noise has little impact on observed ambient noise levels.

frequencies ranging from 100 Hz during slack currents to greater than 10 kHz during peak currents.

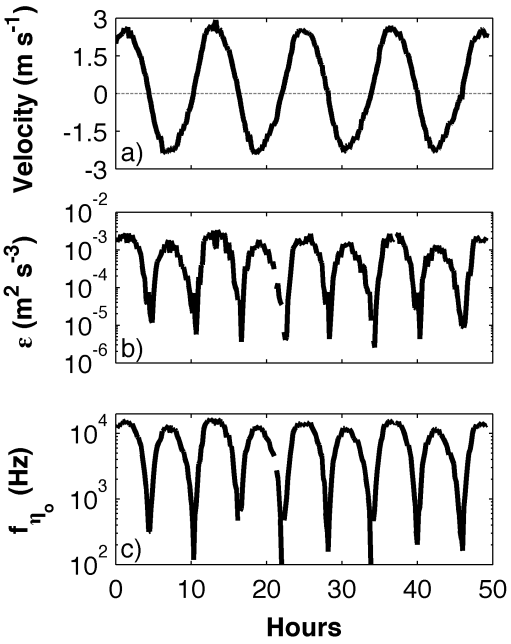

Figure 6.4: Hydrodynamics data from the Channel Channel. a). Time series of the mean current velocity. b). Time series of the dissipation rate of turbulent kinetic energy. c). Time series of the microscale frequency.

The mean current velocity and turbulence measurements in Admiralty Inlet, just as in the Chacao Channel, reveal a highly energetic environment with peak observed near-bed current velocities of approximately 2 m/s. Unlike the measurements in the Chacao Channel, the measurements in Admiralty Inlet are within the bottom boundary layer where a large velocity gradient is observed [*Bassett et al.*, 2013] and the dissipation rates do not scale with $\overline{u}^3$ over the entire range of $\overline{u}$ (Fig. 6.5b).

6.3.2 Acoustic Results

In the Chacao Channel, slack current noise levels are relatively flat below 500 Hz with spectrum levels between 60-70 dB re 1 μPa^2/Hz. These low current conditions provide the baseline for analyzing increases due to flow-noise. Fig. 6.6 includes average spectra in 0.3 m/s velocity bins. Once current velocities reach approximately 0.3 m/s an acoustic signature consistent with flow-noise begins to dominate low-frequency measurements. At 20 Hz the difference between slack current noise levels and those produced by flow-noise are 10 dB, and increases are observed up to 100 Hz. As currents increase, the noise levels at the lowest frequencies do so as well, reaching levels up to 70 dB above those during slack currents. At the same time, flow-noise is observed over a wider range of frequencies. A simple analysis based on when observed noise levels diverge from the expected "red" spectrum of flow-noise suggests that it is likely to mask other sound sources at frequencies up to 800 Hz during the strongest currents. Both the velocity-bin averaged spectra and individual spectra show that

the spectral slope of the flow-noise follows a $f^{-3.2}$ dependence. As previously mentioned, the theoretical maximum frequency at which flow-noise could be measured, given these dissipation rates, exceeds 10 kHz at the site during peak currents. Although flow-noise is not observed at frequencies greater than 1 kHz at this site, it is reasonable to speculate that at a site with less other noise above 1 kHz – for example, a site without sediments (i.e., scoured bedrock) and no snapping shrimp – flow-noise could be observed at higher frequencies.

The flow-noise observed in Admiralty Inlet is comparable to that observed in the Chacao Channel. Fig. 6.8a includes bin-averaged noise spectra up to 200 Hz in Admiralty Inlet. During slack tide periods, observed spectrum levels are approximately 80 dB re $1\mu\text{Pa}^2/\text{Hz}$. Flow-noise is measured at frequencies less than 30 Hz once currents exceed 0.3 m/s and at frequencies greater than 200 Hz during peak currents. Peak flow-noise levels exceed slack tide conditions by up to 50 dB at 20 Hz. The observed slopes of the pressure spectra in Admiralty Inlet are in agreement with those the Chacao Channel.

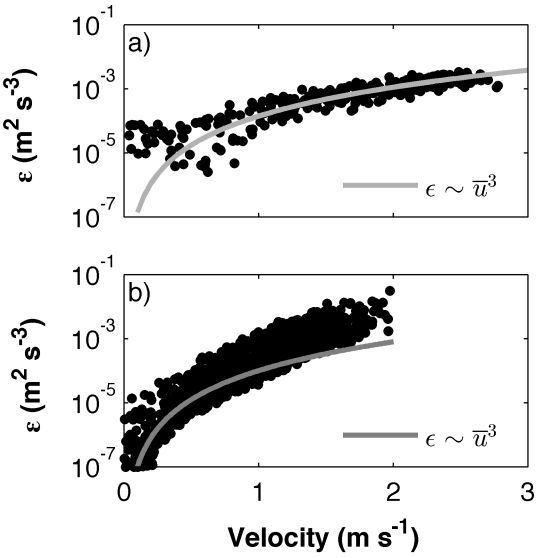

Figure 6.5: Scatter plots of the dissipation rate of turbulent kinetic energy versus current velocity in the Chacao Channel (a) and Admiralty Inlet (b). In Admiralty Inlet, the scaling used in the formulation of the mean-flow model ($\epsilon \sim \overline{u}^3$) is not valid.

6.3.2.1 Model-Data Comparisons

In the Chacao Channel, the magnitude of the constant (b) used in the mean-flow model (Eq. 6.16) is 48 dB re $1\mu\text{Pa}^2/\text{Hz}$. Physically, this constant combines both the scalar constant from the dissipation scaling and the shoulder frequency (f_{sh}). The contribution of the scalar constant for the dissipation scaling, calculated as $20\log_{10}\left(1.4\ 10^{-4}/10^{-6}\right)$, yields an offset of 43 dB. Using a typical f_{sh} of 3 Hz, a value associated with current velocities of 1.5 m/s, the spectrum shift is calculated as $10\log_{10}(20/3)$, or 8 dB. This term can be thought of as a shift necessary to account for neglecting the consideration of the hydrophone's sensitivity to different turbulent scales in the initial model. Combining these terms leads to an offset of 51 dB, a value close to the 48 dB offset shown in Fig. 6.7.

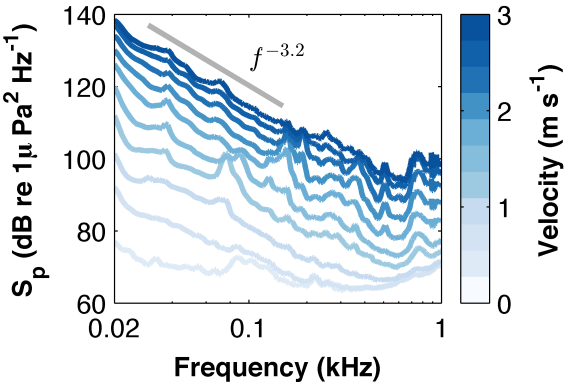

Figure 6.6: Velocity bin-averaged (0.3 m/s bins) pressure spectra from the Chacao Channel. The observed flow-noise has a $f^{-3.2}$ dependence.

A comparison of nine representative, observed pressure spectra at current velocities covering the entire dynamic range in the Chacao Channel versus modeled pressure spectra using both models are included in Fig. 6.7, which demonstrates that both models agree well with observed spectra over most current velocities at the site (i.e., the spectra cover current velocities from 0.3-2.7 m/s). With the exception of the 0.3 and 0.6 m/s spectra, which diverge from the expected behavior of flow noise above 100 and 200 Hz, respectively, the models show good agreement up to 500 Hz. With the exception of frequencies at which self-noise from the mooring is identified, the model typically agrees with observations to within a few decibels.

Also included in Fig. 6.7 are scatter plots of observed pressure spectral densities in the Chacao Channel versus modeled pressure spectral densities at five frequencies between 30 and 480 Hz. Again, generally good agreement is found between the models and the observations. In the case of the higher frequencies (240 and 480 Hz) measurements associated

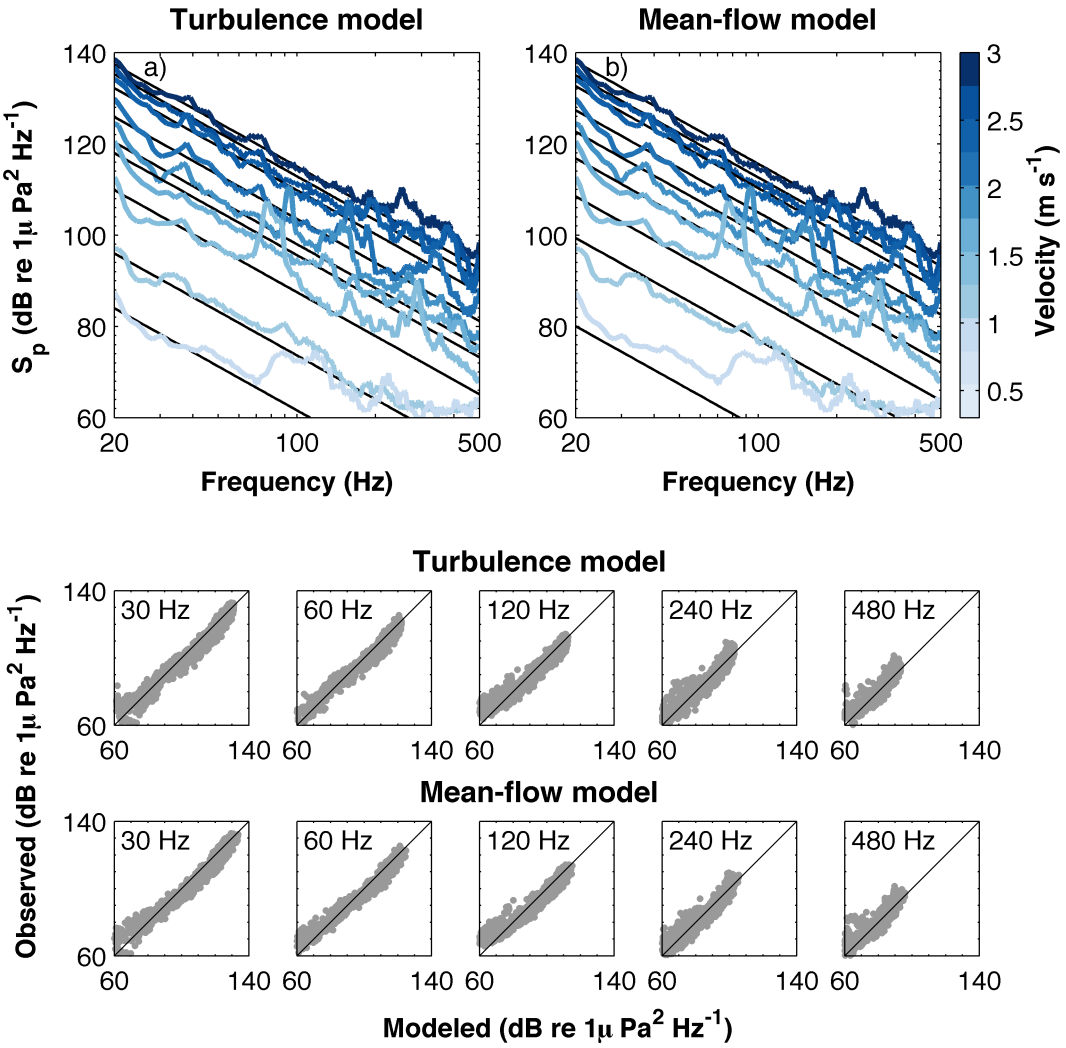

Figure 6.7: A comparison of observed and modeled flow-noise levels using the turbulence and mean-flow models in the Chacao Channel. a,b). Modeled and observed pressure spectra for both models. The black lines are the modeled spectra using the hydrodynamic measurements at the time of the hydrophone recordings. The range of current velocities is 0.3-2.7 m/s in 0.3 m/s increments. The ten small insets includes comparison of observed and modeled pressure spectral densities at five frequencies for the turbulence and mean-flow models. The black lines are the show the 1-1 relationship.

Table 6.1: R^2 values for both flow-noise models and the observed spectrum levels in the Chacao Channel at selected frequencies.

	Frequency (Hz)				
	30	60	120	240	480
Turbulence Model R^2	0.95	0.89	0.83	0.77	0.65
Mean-Flow Model R^2	0.95	0.87	0.83	0.80	0.68

with the weakest currents are cut-off by the y-axis. In this regime there is poor agreement between the observations and models because flow-noise does not have a significant impact at these frequencies during low current periods. At these same frequencies, there is also less agreement during peak currents (highest pressure spectral densities), with observations always exceeding the models. These differences, which can also be seen in Figs. 6.7a and 6.7b, are also attributed to mooring noise. To quantify the performance of both models, R^2 values for the modeled versus observed spectra level for the five frequencies in Fig. 6.7 are determined and included in Table 6.1. The R^2 values for both models range from 0.95 for both models at 30 Hz to less than 0.7 at 480 Hz. The decreased R^2 values at higher frequencies are attributed to lower signal-to-noise ratios at higher frequencies.

Fig. 6.8b includes a comparison between observed and modeled flow-noise levels in Admiralty Inlet using the turbulence model at three frequencies: 30 Hz, 60 Hz, and 120 Hz. There is good agreement between the model and observations at these frequencies but there is more scatter than the results for the Chacao Channel. The additional scatter is attributed, in part, to the shorter length of the recordings in Admiralty Inlet, which results in pressure spectra with larger uncertainties. Additionally, the acoustic recordings are much shorter than the averaging periods for the turbulence spectra and are not sufficiently long to record throughout the entire period of the largest turbulent scales at the site. In comparison to the Chacao Channel data, there is also significantly more scatter in the estimated dissipation rates at a given velocity in Admiralty Inlet (Fig. 6.5). Disagreement at the lowest noise levels occurs during periods of low current when flow-noise levels are below ambient levels. Other significant outliers are attributed to other sources such as vessels without AIS

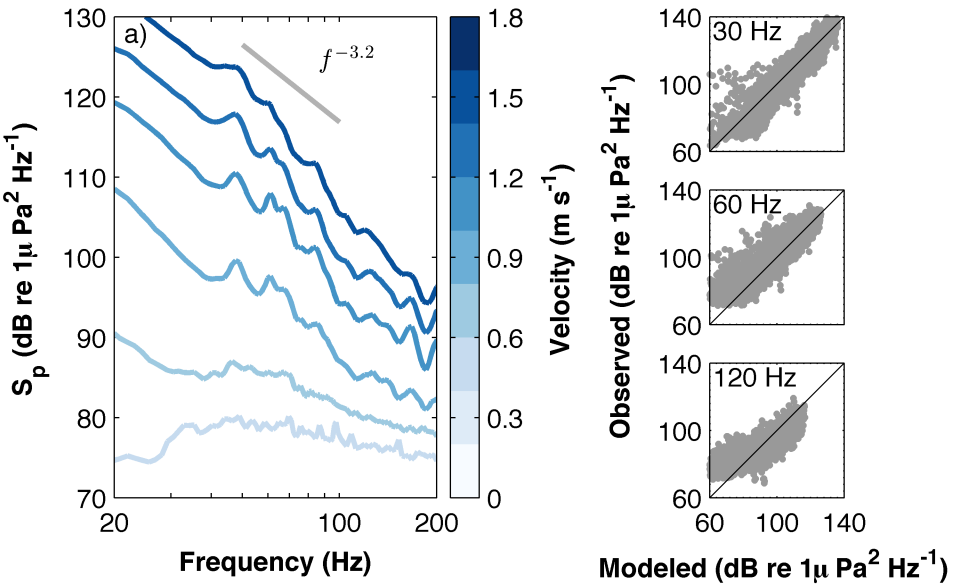

Figure 6.8: a). Velocity-bin averaged spectra (0.3 m/s velocity bins) in Admiralty Inlet for periods with no AIS transmitting vessels with 10 km of the hydrophone. The small insets include a comparison between the modeled and observed pressure spectra in Admiralty Inlet for the turbulence model at three frequencies. The mean-flow model is not shown because ϵ does not scale with $\overline{u}^3$.

transponders (such as military traffic).

The mean-flow model is not a good predictor of flow-noise in Admiralty Inlet. A comparison of the observations and the mean-flow model is not included due to the poor agreement. Specifically, the observed flow-noise increases at a more rapid rate than predicted by the model. This is not surprising given the dissipation rate increases more rapidly than $\overline{u}^3$ as shown in Fig. 6.5b. Therefore, a critical assumption in the mean-flow model is not valid at the site.

6.4 Discussion

As shown in Sec. 6.3.2, it is necessary to consider flow-noise when quantifying low-frequency ambient noise levels in areas characterized by high turbulence and currents. While the geographic distribution of such environments is quite limited, ongoing development in these areas, as well as their importance as biological choke points, will likely lead to more acoustics

studies prone to high levels of flow-noise. For example, flow-noise will exceed received levels for close-range vessel traffic [*Bassett et al.*, 2012] by 30 dB or more at frequencies less than 100 Hz.

To properly quantify propagating low-frequency noise in these environments using stationary, autonomous platforms, the development of flow-noise mitigation techniques would be beneficial. While signal processing using multiple transducers can be used to reduce or eliminate flow-noise using cross-correlation techniques [*Chung*, 1977; *Buck and Greene*, 1980], these methods are of little practical value when flow-noise exceeds ambient noise levels by more than 50 dB (i.e., signal-to-noise ratios are too low for signal processing to be effective). Flow-noise can also be partially mitigated through the use of larger transducers, which will cause pressure fluctuations to cancel more rapidly over the surface [*Urick*, 1975; *Strasberg*, 1979]. However, due to the large range of length scales of turbulence in energetic tidal channels, this may also be of limited utility. Ultimately, this work demonstrates a need to develop devices that are compact (to reduce drag) and shield transducers from the flow.

The models presented here, based on the basic formulations by *Strasberg* [1979, 1985], show good agreement with the observed data. This data set spans a wider range of current velocities than has been previously described in the literature, with peak currents nearly one order of magnitude greater than those discussed in *Strasberg* [1979, 1985] and *Webb* [1988]. In addition, the frequencies studied here extend the regime of modeled flow-noise to well beyond the infrasonic range. It is expected that different hydrophone aperture geometries would have unique values for empirical constants (e.g., m, f_{sh}), although the same scaling relations would apply. To facilitate the application of higher frequency flow-noise models, further research regarding the response of hydrophones to small-scale pressure fluctuations is needed.

Both the turbulence and mean-flow models for flow-noise pressure spectra face certain limitations in application to other sites. For example, the turbulence model requires estimates of the dissipation rate or turbulence spectra in the inertial subrange. Ideally, turbulent kinetic energy spectra would be measured in the frequency range overlapping with hydrophone measurements to allow a direct evaluation of Eq. 6.6. However, the low-frequency response of the hydrophones employed in this study did not overlap with the

velocity measurements. As such, extrapolation based on theoretical turbulence scaling was necessary. Nonetheless, the turbulence model is shown to perform well in two energetic tidal channels. The mean-flow model, by contrast, does not require turbulence measurements but relies on scaling arguments that are not universally valid. In addition, the scalar constant for the mean-flow model is expected to be site-specific. However, when these assumptions are valid, the scaling arguments can lead to accurate predictions of flow-noise levels.

The turbulence model relates mean-velocity and dissipation rate measurements to observed flow-noise levels. The good agreement between the model and measurements suggest that flow-noise spectra could be used to estimate the dissipation rate given measurements of the mean velocity when the response of the hydrophone (f_{sh} and m) is known.

Finally, the measurements presented here suffer from self-noise contamination attributed to mooring noise. This is not surprising given the engineering challenges associated with the development of a mooring to be deployed in such a dynamic environment. Isolating connection points between different mooring components using noise dampening material is one method of reducing the self-noise, which represents only one of many engineering challenges associated with the acquisition of quality ambient noise measurements in such environments.

6.5 Conclusions

Measurements of ambient noise in the Chacao Channel, Chile, and Admiralty Inlet, Puget Sound, Washington, two sites where peak currents exceed 3 m/s, reveal pressure spectral densities attributed to flow-noise that exceed 135 dB re μPa^2/Hz at 20 Hz. These peak levels can exceed ambient noise by more than 50 dB. Flow-noise is observed to frequencies greater than 500 Hz. It is found that the slope of pressure spectra attributed to flow-noise is $f^{-3.2}$, a value that is expected to depend on the geometry of the hydrophone.

Two semi-empirical models are presented for flow-noise that extend the frequency range of prior models for infrasonic flow-noise. The first model utilizes direct measurements of turbulence and mean current velocities while the second uses scaling arguments to model flow-noise only on the basis of mean currents. Unlike other flow-noise studies, the frequency ranges considered here are associated with scales of turbulence that are similar to and

smaller than the hydrophone. Both models are shown to agree well with flow-noise observations over the range of current velocities observed in the Chacao Channel measurements. In the Admiralty Inlet measurements, the turbulence model also agrees well with observations. However, the dissipation rate scales differently with velocity and the mean-flow model performs poorly. The agreement between the turbulence model and two observations in these dynamic channels extends the dynamic range of flow-noise models by nearly an order of magnitude.

Chapter 7

APPLICATION: ACOUSTIC DETECTION OF OPERATING TIDAL TURBINES BY MARINE ANIMALS

7.1 Introduction

The acoustic impacts are one of the environmental concerns relating to tidal energy projects. Specifically, the concern is that sound produced by operating tidal turbines could lead to behavioral changes in marine species. Currently, there are significant knowledge gaps related to both sound emissions from tidal turbines and the auditory capabilities of species. Despite these uncertainties, available data can be applied to bound the areas over which environmental impacts could occur. By applying the available information to a case study of a proposed demonstration-scale tidal energy project in northern Admiralty Inlet, Puget Sound (WA), *Polagye et al.* [in revision] develops a framework for performing such environmental impacts analyses. This chapter provides a summary of the results from this case study.

The basis for determining whether acoustic effects may be observed is related to the probability of detecting sound from operating turbines given ambient noise conditions, which is related to the signal excess. The signal excess, or the signal-to-noise ratio of the received level to ambient noise, is described by

$$SE = RL - NL, \tag{7.1}$$

where SE is the signal excess, RL is the received level, and NL is the ambient noise level. In this context, the received level refers to received sound from operating tidal turbines and the noise level refers to ambient noise in the absence of operating turbines. This formulation results in a detection when the signal excess is positive. The received level term in the signal excess is described by

$$RL = SL - TL + AG, \tag{7.2}$$

where SL is the source level of the sound (referenced to 1 meter), TL is the transmission loss, and AG is the auditory gain associated with the signal processing capabilities of the receiver. Therefore, the application of this formulation to the detection of tidal turbine noise requires information about the auditory capabilities of the receiver, the sound produced by tidal turbines, and the ambient noise. Section 7.2 provides the background information and methods used to estimate the detection range of operating turbines, including summarizing the previous results from this thesis for application to Equation 7.2. Section 7.3 presents the results of the case study and Section 7.4 discusses the implications of the results.

7.2 Background and Methodology

The energy associated with sound is frequency-dependent and can be interpreted using a number of different measures. One-third octave band sound pressure levels are commonly used in bioacoustic studies. Here, sound pressure levels are calculated over the entire frequency range of interest (25 Hz - 25 kHz). Within each decade, adding or subtracting a power of ten accordingly, one-third octave band sound pressure levels are calculated at 100, 125, 160, 200, 250, 315, 400, 500, 630, and 800 Hz. The following sections detail the methodology used to obtain model inputs in these frequency bands.

7.2.1 Turbine Operation and Sound Production [a]

Once deployed, the power output by the 6-m OpenHydro Open Centre turbines can be modeled to vary with time according to

$$P(t) = \begin{cases} 0, & \text{if} \quad \overline{u}(t) < \overline{u}_{cut-in} \\ \frac{1}{2}\rho\overline{u}(t)^3 A\eta, & \text{if} \quad \overline{u}_{cut-in} < \overline{u}(t) \leq \overline{u}_{rated} \\ \frac{1}{2}\rho\overline{u}_{rated}^3 A\eta, & \text{if} \quad \overline{u}(t) > \overline{u}_{rated} \end{cases} \tag{7.3}$$

where ρ is the density (1025 kg/m^3), A is the swept area, η is the water-to-wire efficiency (which is assumed to be constant), $\overline{u}(t)$ is the inflow velocity in time, $\overline{u}_{cut-in}$ is the cut-in speed of the turbine, and $\overline{u}_{rated}$ is the rated speed of the turbine. The three regimes are:

[a]The analysis of sound production from tidal turbines, which is summarized here, was performed by Dr. Brian Polagye.

- below the cut-in velocity no power is produced;
- between the cut-in and rated velocities the power production is related to the mean velocity cubed, the water-to-wire efficiency, and the swept area;
- and above the rated velocity the power production is constant (the rated power).

In Admiralty Inlet, the values used for turbine cut-in speed is 0.7 m/s and the rated speed is 3.2 m/s, though these are preliminary values that may change during final design.

Currently, comprehensive measurements of sound from tidal turbines that include operational data are not available at more than one operating condition. This lack of data is, in part, attributed to the challenges associated with obtaining quality acoustic measurements in highly energetic environments [*Bassett et al.*, 2010]. To provide source level inputs for the case study, acoustic measurements of an operating OpenHydro turbine, originally described in *Barr* [2010], were reanalyzed. The data were obtained at the at the European Marine Energy Centre on August 23, 2010 using a drifting data collection package referred to as the "drifting ears." The package consisted of a hydrophone suspended 5 meters below a surface drogue. A GPS logged the position of the package during the drift. The hydrophone, a Cetacean Research CR55XS with an effective sensitivity of -160 dB V/1μPa, sampled continuously at 96 kHz. Due to high levels of anthropogenic noise in the area, the analysis of turbine noise was limited to one drift with no major changes in the operational state of the turbine. During the drift the distance to the turbine was 190-260 meters and the water depth was 15 meters. A 64-second recording of the turbine was divided into 8-second intervals. The acoustic spectra for each interval were calculated using 2^{16} data points, a 50% window overlap, and a Hamming window resulting in a frequency resolution of 1.5 Hz. The spectra were integrated in one-third octave bands. The final spectrum was calculated as the mean of the spectra from the 8 intervals.

Background noise without the turbine operating are not available so peaks in the acoustic spectra are attributed to turbine operation. Therefore, from 7-11 kHz the acoustic spectra were linearly interpolated to remove the peak. In general, the turbine spectrum was "red," decreasing a rate of 13 dB per decade. Tonal clusters were identified around 12.5, 16, 40, 160, 500, and 1600 Hz and may be associated with the operating turbine. The increased spectrum levels between 10-30 kHz may be attributable to rain but are included here as

sound from the turbine.

The source level was calculated using the SONAR equation [*Urick*, 1975],

$$SL = RL + TL, \tag{7.4}$$

where SL is the one-third octave band source level (dB re 1 μPa at 1m), RL is the received level, and TL is the transmission loss, which contains terms accounting for the spreading and absorption of the sound waves. The spreading losses were calculated using spherical spreading to 8 m (the hub height) and cylindrical spreading thereafter. This formulation assumed that the turbine was an omni-directional source and that there was no azimuthal variability in transmission losses. The SONAR equation, when including attenuation terms from *Ainslie and McColm* [1998], is described by

$$SL(f) = RL(f) + 10\log_{10}(D_s D) + \alpha(f)D, \tag{7.5}$$

where D is the distance between the source and the receiver, D_s is the range for spherical spreading (8 meters), and α is the absorption coefficient.

Using the previously identified methods, the source levels in one-third octave bands were determined at one operating condition. However, as demonstrated by Equation 7.3, the tidal turbine in Admiralty Inlet will produce power over a range of inflow conditions. Given that no measurements of tidal turbines under different operational states are available, *Polagye et al.* [in revision] used wind power and underwater sound analogues to scale the source levels with the inflow conditions. This scaling relied on three assumptions:

- the frequency content of the sound from the turbines does not vary with inflow velocity;
- turbines are omni-directional sound sources;
- and the broadband sound pressure level produced by an operating turbine scales linearly with their power output.

Therefore, the source level is described as a function of frequency and power output according to

$$SL(f, P_o) = 20\log_{10}\left(\frac{p_0}{p_{ref}}\right) \quad \text{[dB re 1}\mu\text{Pa 1 m]}, \tag{7.6}$$

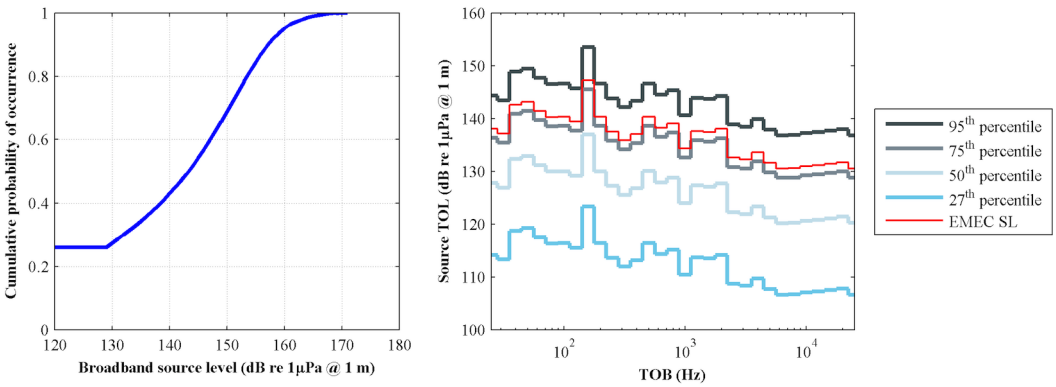

Figure 7.1: Scaled broadband and one-third octave band source levels for an operating turbine.

where P_0 refers to reference power generation state, p_0 is the measured rms pressure at the reference power generation state, and p_{ref} refers to the reference pressure (1 μPa). Based on the assumption that the sound production scales with the power output, Equation 7.6 can be rewritten for all power generation states as

$$SL(f,P) = SL(f,P_0) + 10\log_{10}\left(\frac{P^2}{P_0^2}\right), \tag{7.7}$$

where P is the power as a function of the inflow velocity. By substituting Equation 7.3 into Equation 7.7, the final form for the source level becomes

$$SL(f,P) = SL(f,P_0) + 10\log_{10}\left(\frac{\overline{u}^6}{\overline{u}_0^6}\right), \tag{7.8}$$

where $\overline{u}_0$ is the inflow velocity for the reference measurements. Equation 7.8 suggests that the source levels should depend strongly on the inflow velocity. The distribution of current velocities at the site of the case study in Admiralty Inlet is applied to Equation 7.8 to obtain the source level input models for the case study. Figure 7.1 includes broadband and one-third octave band source levels for selected source level percentiles.

7.2.2 Ambient Noise in Admiralty Inlet [b]

The ambient noise inputs are discussed in detail in Chapters 4 and 5. For the purposes of this study, the results from these chapters are broken into two regimes: a low-frequency

[b]The ambient noise analysis is drawn from the dissertation author's body of research.

regime (25-1,000 Hz) and a high-frequency regime (1,000-25,000 Hz). At low frequencies, vessel traffic is the dominant noise source during all stages of the tide. At high frequencies, sediment-generated noise dominates ambient noise levels when current velocities exceed the turbine cut-in speed. In the low-frequency regime, a probabilistic approach for the sound levels is taken given that vessel traffic densities are uncorrelated with the current velocity [*Bassett et al.*, 2012]. In the high-frequency regime, a probabilistic approach is also applied noting that the distribution of noise levels is dependence on near-bed current velocity [*Bassett et al.*, 2013].

7.2.3 Detection of Turbine Sound [c]

The signal excess, as defined in Section 7.1, is not sufficient for detection in this context. In order for a detection (biological or other computation) to occur, the signal excess must also exceed the hearing threshold of the receiver in that frequency band. Assuming that the auditory gain is 0 dB, the signal excess is redefined as

$$SE = \begin{cases} 0, & \text{if} \quad RL < HT \\ max(RL, 0), & \text{if} \quad RL \geq HT \end{cases} \tag{7.9}$$

where HT is the hearing threshold. By this definition, the signal excess is always non-negative.

Four species are chosen as biological receivers in this study. These species are representative species for four classes of marine species that are known to regularly occur in Puget Sound: fish, mid-frequency cetaceans, high-frequency cetaceans, and pinnipeds. For fish, cod is used because of the availability of audiograms. The marine mammal species chosen are killer whales (mid-frequency cetacean), harbor porpoise (high-frequency cetacean), and harbor seals (pinniped). These species were chosen due to their relative abundance and availability of audiograms (harbor porpoise and harbor seals) or their conservation status (killer whales). The hearing thresholds for these species at the six frequencies modeled in this study are included in Table 7.1.

---

[c]The analysis of detection of turbine sound was carried out primarily by Drs. Jason Wood and Marla Holt.

Table 7.1: Hearing thresholds in dB re 1 μPa for the representative species (− denotes no auditory responsiveness in the one-third octave band).

Species	$\frac{1}{3}$-octave band center frequency (kHz)					
	0.05	0.16	0.5	2	8	25
Atlantic cod (*Gadus morhua*)[a]	83	75	110[e]	–	–	–
Killer whale (*Orcinus orca*)[b]	–	120[f]	98	63[g]	57[g]	40[f]
Harbor porpoise (*Phocoena phocoena*)[c]	–	–	92	72	59	39[f]
Harbor seal (*Phoca vitulina*)[d]	–	74[f]	63	57	60	58

With the hearing sensitivities determined, the received levels are modeled with two turbines operating at the site. First, the received level equation is rewritten to integrate the source level dependence on turbine power output such that

$$RL(x,y,z,f,P) = \begin{cases} SL(f,P) - 20\log_{10}(D) - \alpha(f)D, & \text{if} \quad D \leq D_s \\ SL(f,P) - 10\log_{10}(DD_s) - \alpha(f)D, & \text{if} \quad D > D_s \end{cases} \tag{7.10}$$

where D_s is the transition between spherical and cylindrical spreading. With the exception of the absorption and spreading terms, no additional losses (e.g., those due to interactions at boundaries) are included. Therefore, the received levels determined by this formulation understate transmission losses (as shown in Appendix C). In the case of Admiralty Inlet, D_s is assumed to be 30 m for a turbine hub height of 10 meters in 55 meters of water. While this

[a] *Chapman and Hawkins* [1985]

[b] *Szymanski et al.* [1999] and *Johnson* [1967]

[c] *Kastelein et al.* [2002]

[d] *Kastelein et al.* [2009]

[e] Based on threshold at 470 Hz.

[f] Interpolated from behavioral audiogram.

[g] No behavioral thresholds available at this frequency. Value in table is 9 dB below the reported physiological threshold since ABR thresholds are reported in $\text{dB}_{peak\ to\ peak}$ and not dB_{rms}.

[h] As measured, from behavioral audiogram.

approach neglects some losses and cannot account for modal interference patterns resulting from sound propagation, a more complicated propagation model is unnecessary given the uncertainties that exist in other parts of the analysis.

To calculate the received levels, the source levels for both turbines are assumed to be equal. Received levels from the pair of turbines are calculated throughout a three-dimensional grid, to a range of 5 km, with a horizontal grid spacing of 10 meters. The turbines, separated by 70 meters, are placed 35 meters on each side of the grid center at a depth of 45 meters. The received sound pressure levels at all points in the grid are calculated as an incoherent sum of the sound from the turbines as

$$RL(x, y, z, f, P) = 10 \log_{10} \left(10^{RL_1/10} + 10^{RL_2/10} \right), \tag{7.11}$$

where the subscripts 1 and 2 refer to the individual turbines at their respective deployment locations.

7.2.3.1 Application: Studies to Characterize Turbine Sound

Following the installation of the tidal turbines at the site, studies will characterize sound produced by the operating turbines. The effectiveness of this characterization study is determined by considering the number of one-third octave bands likely to be identified above ambient noise at different ranges and operating states. Here, a likely identification is defined as an instance in which the received levels from the turbines exceed the 75^{th} percentile of ambient noise in the same frequency band by 5 dB or more. Therefore, the identification ($\tilde{I}_f$) in a particular frequency band is defined as a binary function,

$$\tilde{I}_f(x, y, z, f, \overline{u}) = \begin{cases} 1, & \text{if} \quad RL(x, y, z, f, \overline{u}) - NL_{75\%} \geq 5dB \\ 0, & \text{if} \quad RL(x, y, z, f, \overline{u}) - NL_{75\%} < 5dB \end{cases} \tag{7.12}$$

where 1 indicates identification and 0 indicates no identification. A summation of $\tilde{I}_f$ across all frequency bands yields $\tilde{I}$, the total number of one-third octave bands in which the identification occurs. $\tilde{I}$ is determined for four current velocities: 1.0, 1.5, 2.0 and 2.5 m/s.

7.2.3.2 Application: Marine Animal Detection of Turbine Noise

Post-installation monitoring studies at the site will study the behavioral responses of marine mammals, should they occur, to the sound produced by operating turbines. For marine species, the auditory gain is assumed to be zero. Therefore, the signal excess is only a function of the received level, ambient noise levels, and the hearing threshold. For each of the representative species, the probability of detection is determined in six frequency bands throughout the domain: 60 Hz, 160 Hz, 500 Hz, 2 kHz, 8 kHz, and 25 kHz. The lowest four frequency bins, for which noise levels are not correlated with current velocity, correspond to the peaks in the one-third octave band source levels attributed to the turbine. The 8 kHz and 25 kHz one-third octave bands correspond to frequencies in which ambient noise is correlated with current velocity at the site. Given that received levels and ambient noise levels vary in time, probabilities are used to analyze the potential for detection of operating turbines by marine animals. The probability of detection is defined as

$$p(d_{x,y,z,f}) = \sum_i \left(\sum_j \ d(NL_j, RL_i, HT) p(NL_j | RL_i) \right) p(RL_i), \tag{7.13}$$

where p is the probability and d is the detection of turbine sound given a location and one-third octave band. The indices i and j correspond to the frequency bands and discretization of noise levels, respectively. The $d(NL_j, RL_i, HT)$ term corresponds to a detection given noise levels, received levels, and hearing thresholds. The second term, $p(NL_j|RL_i)$, represents the probability of an ambient noise level given a received level. The product of these two terms is summed over all ambient noise levels, giving the probability of detecting turbine sound given a received level. The summation of the product of this summation and the final term over all received levels is the probability of detecting turbine sound. Received and ambient noise levels are discretized to 1 dB and 4 dB resolution, respectively. All received levels are calculated at a depth of 30 m. This approach simply provides an upper bound on the range of detection of turbine noise, which is not sufficient to determine the likelihood of response to turbine noise.

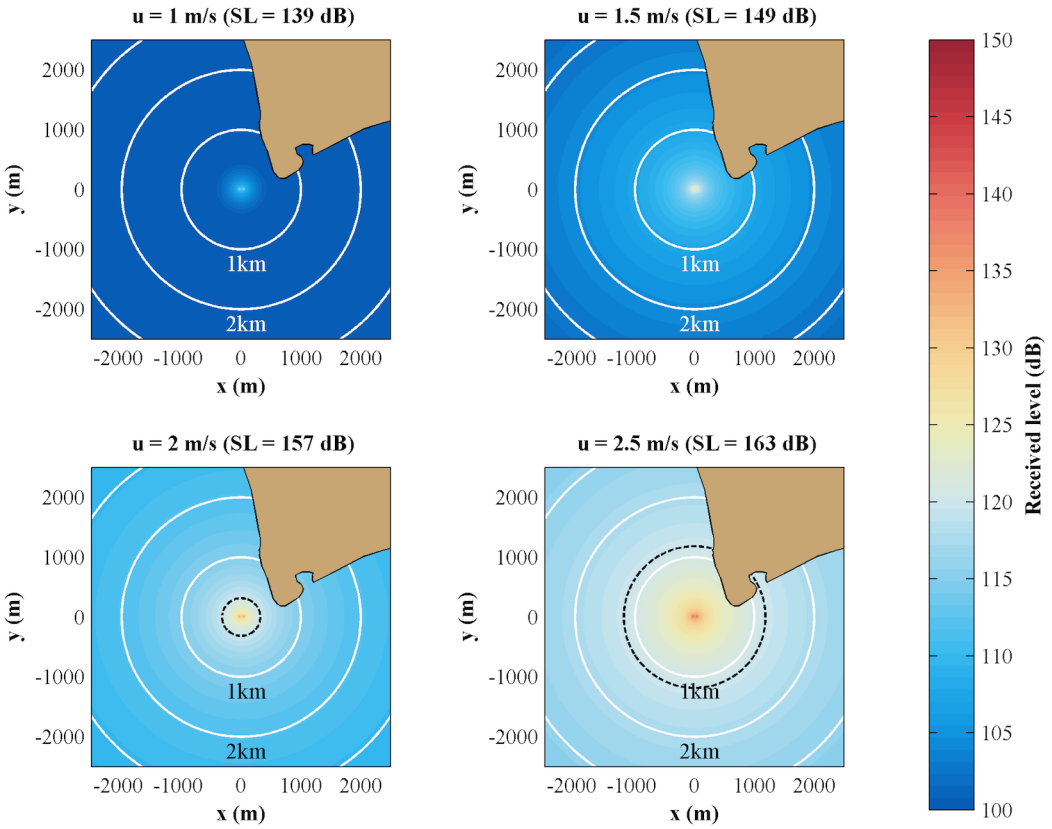

Figure 7.2: Modeled broadband received levels during four turbine operating states. Black dotted lines in the figure highlight the 120 dB re 1μPa isobel.

7.3 Results

Figure 7.2 shows the broadband received levels (0.025-25 kHz) expected given with two turbines at the four operation states. The 120 dB isobels, which are included in the figure, are important for two reasons: they corresponds to closely with the mean ambient noise levels at the site [*Bassett et al.*, 2012] and continuous noise at this level meets the acoustic criterion for harassment of marine mammals in the United States [*National Marine Fisheries Service*, 2005]. Only when current velocities exceed 2 m/s do the 120 dB isobels extend beyond a range of a couple hundred meters. When current velocities reach 2.5 m/s, this radius is approximately 1 km, roughly 20% of the width of Admiralty Inlet.

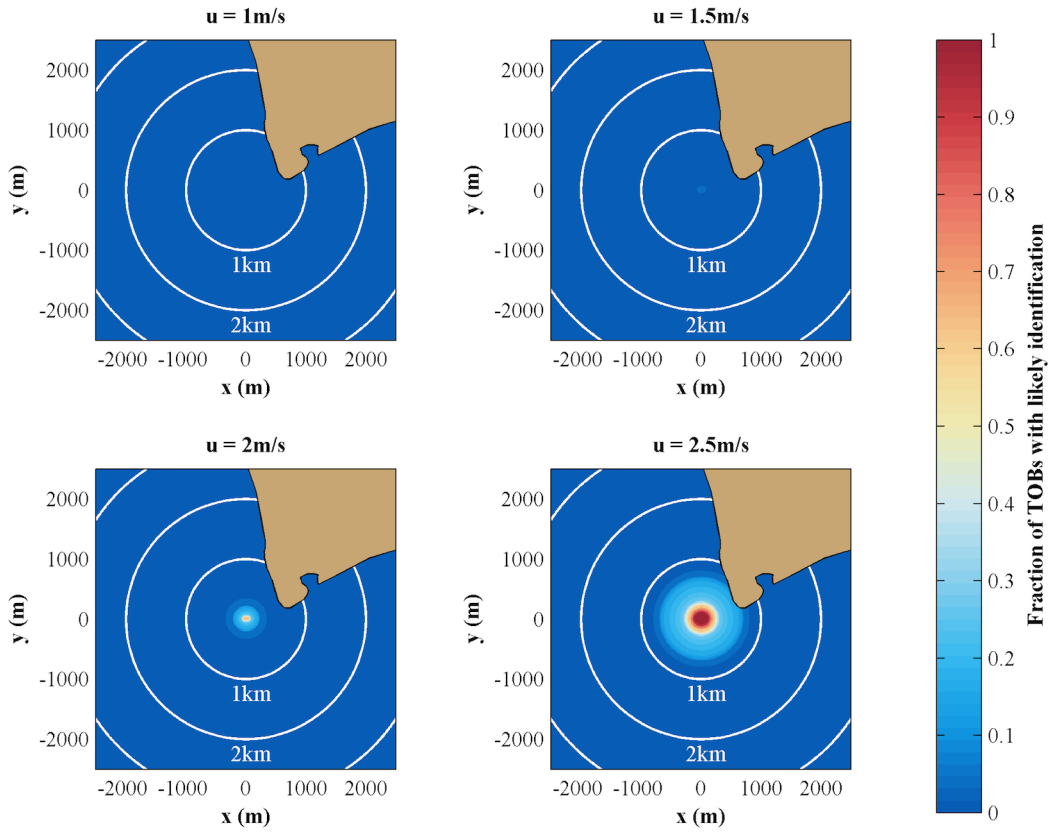

Figure 7.3: Fraction of one-third octave bands detected by a hydrophone receiver at a depth of 5 meters.

7.3.1 Studies to Characterize Turbine Noise

Figure 7.3 shows the fraction of one-third octave bands in which turbine characterization studies have at least a 75% probability of detecting turbine noise over ambient noise conditions at four current velocities. For currents less than 1.5 m/s, the fraction of one-third octave bands detected is, for practical purposes, zero at all ranges. With current velocities of 2 m/s, a fraction of the bands are detectable at ranges up to a few hundred meters. Once current velocities exceed 2.5 m/s, turbine sound from all one-third octave bands are detectable near the turbines ($<$ 200 meters) with roughly one-third of the bands detectable up to ranges of approximately 700 meters.

7.3.2 Detection of Turbine Sound by Marine Animals

Figures 7.4-7.5 show the results for two groups: mid-frequency cetaceans and pinnipeds. Given the assumption that turbines will be undetectable while not operating, the probability of has an upper bound of 73%, the percentage of the time that turbines will be operational. Despite the uncertainties associated with audiograms and turbine noise spectra, the detection probabilities at various ranges provide results that will inform post-installation monitoring plans. For both mid- and high-frequency cetaceans the probability of detection is less than 25% at ranges beyond a few hundred meters. Pinnipeds on the other hand have similar detection probabilities to a range of approximately 1 km. This difference is attributed to the hearing sensitivities of the species in the range of peak turbine source levels.

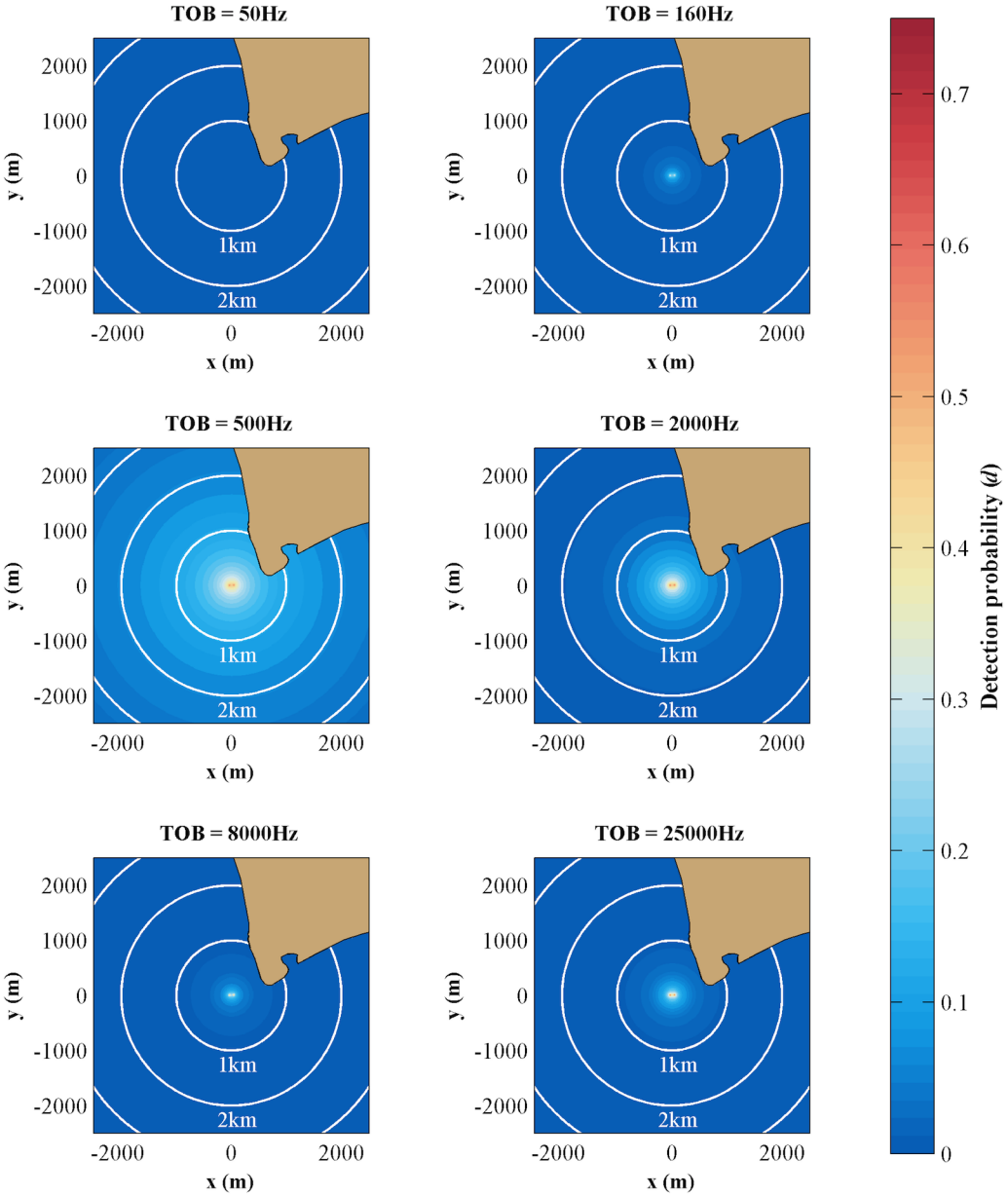

Figure 7.4: Probability of detecting operating turbines for killer whales (mid-frequency cetaceans).

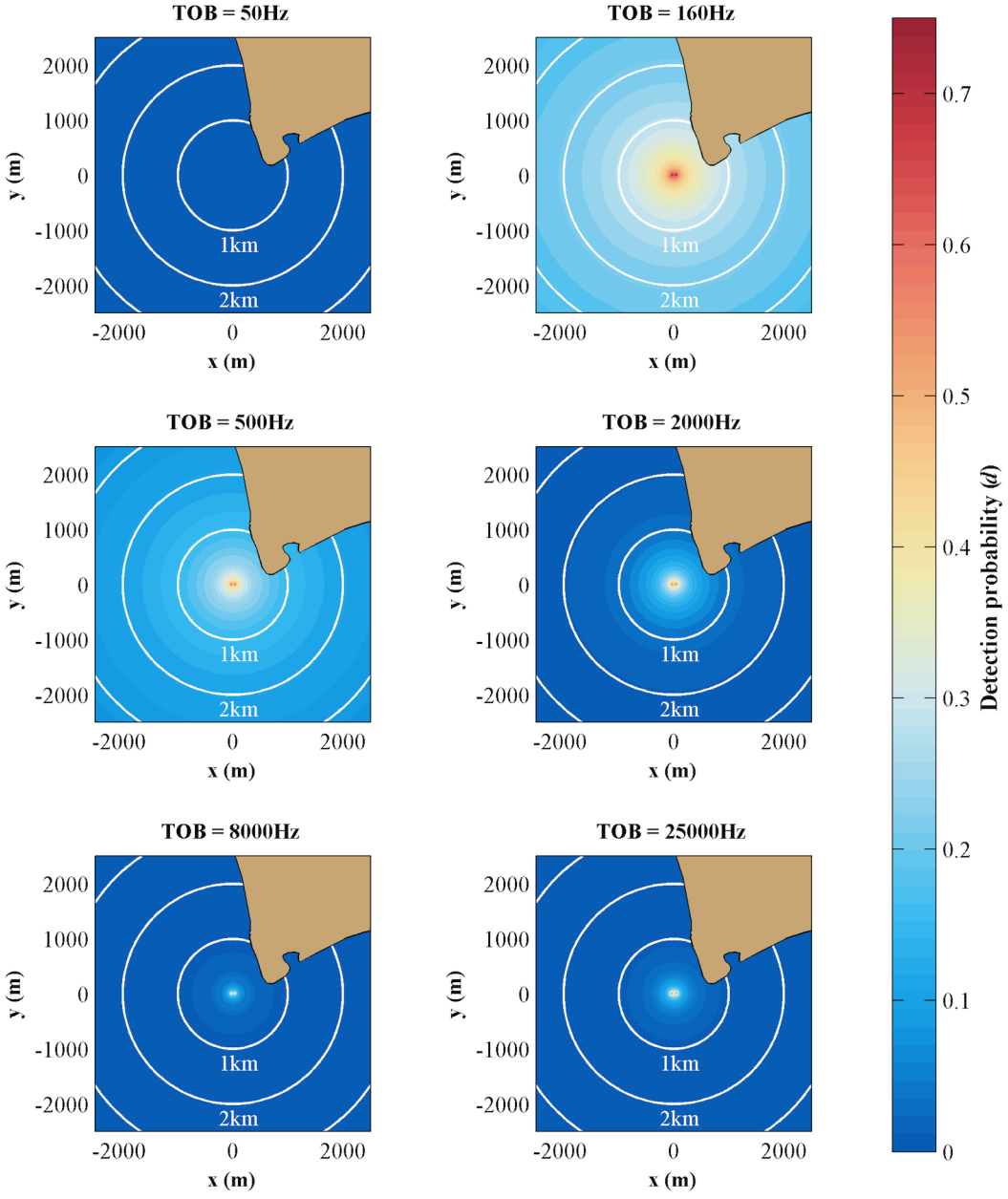

Figure 7.5: Probability of detecting operating turbines for harbor seals (pinnipeds).

7.4 Discussion

The models for the detection of operating tidal turbines by both hydrophones and biological receivers suggest post-installation studies should focus on areas within 1 km of the site. Beyond this range, detections will be limited to periods when peak currents overlap with otherwise low levels of anthropogenic noise. Critically, the detection of turbine sound by a marine animal does not imply a behavioral response. As a result of these estimated detection ranges post-installation monitoring plans will focus on both characterizing turbine noise and studying potential behavioral changes in the presence of operating turbines at ranges less than 1 km. Figure 7.6 includes a satellite image of northern Admiralty Inlet with overlays of the turbine site and the recommended post-installation monitoring area. In addition, the figure includes an outline of the post-installation plans prior to this study. Notably, the post-installation study area has decreased by more than 90%, which will allow time and energy to be focused specifically in the areas where sound from turbines may be detectable. The post-installation monitoring at this site will be begin to address some of the critical knowledge gaps that were sources of uncertainty in this study. Future tidal energy projects will benefit from these studies and the framework for considering the acoustic impacts of tidal power projects.

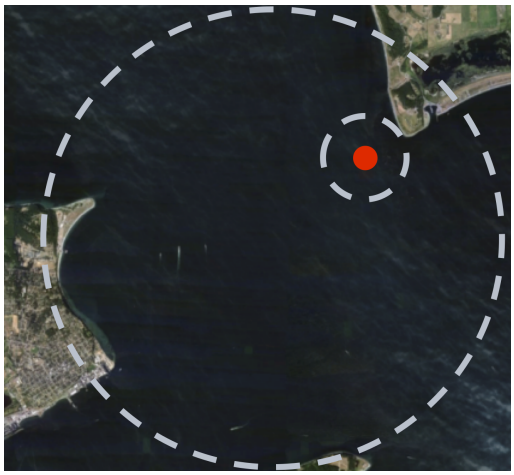

Figure 7.6: Study range for post-installation monitoring. The red dot is the turbine deployment site and the small gray circle is the are for post-installation studies. The large gray circle was the study area prior to these results.

Chapter 8

APPLICATION: ACOUSTIC DETECTION OF KILLER WHALE VOCALIZATIONS DURING TURBINE OPERATION

8.1 Introduction

Studying marine species is, in general, difficult due to the limitations of optical methods in the marine environment. Therefore, both passive and active acoustics technologies are often employed. The ability to use sound to study marine life is contingent upon the signal-to-noise ratio of the desired signal over background noise levels. Vessel noise, for example, is commonly cited as an important stressor that can also be a limiting factor in communication between conspecifics or in passive acoustic studies [*Morton and Symonds*, 2002; *Buckstaff*, 2004; *Foote et al.*, 2004; *Hatch et al.*, 2008; *Holt et al.*, 2009; *Rolland et al.*, 2012]. In some environments, natural sources (e.g., breaking waves, rain, and sediment transport) can be the limiting noise source. Noise resulting from the impacts of mobilized sediment grains can be an important ambient noise source over a range of frequencies from 1-300 kHz [*Voglis and Cook*, 1970; *Harden Jones and Mitson*, 1982; *Thorne*, 1986a; *Bassett et al.*, 2013]. Although not commonly referenced as an important ambient noise source, in environments suitable for hydrokinetic power generation, signals consistent with sediment-generated noise have been reported and may be widespread [*Bassett et al.*, 2013].

In environments suitable for tidal hydrokinetic power generation, noise from sediment transport can result in high levels of ambient noise at frequencies that overlap with the vocalizations and echolocation clicks of mid- and high-frequency cetaceans [*Bassett et al.*, 2013]. This study focuses on the use passive acoustic monitoring (PAM) techniques to identifying vocalizations of a mid-frequency cetacean, the Southern Resident killer whale (*Orcinus orca*), at a site with sediment-generated noise. The study site, as discussed in other chapters, is the proposed site of a demonstration-scale tidal hydrokinetic power project in Admiralty Inlet, Puget Sound. This area is located within a designated critical habitat area

for the endangered Southern Resident killer whale (SRKW) population [*National Marine Fisheries Service*, 2006].

A variety of sounds are produced by SRKWs under different circumstances. Echolocation clicks are used while foraging. Whistles and pulsed calls are commonly used during social interaction. Echolocation clicks typically have center frequencies between 40-85 kHz with bandwidths of up to 50 kHz [*Au et al.*, 2004]. The three martrilines, referred to as pods (J, K, and L), each have a set of stereotyped calls specific to the pod. Common calls for each pod have been characterized alphanumerically according to the frequency content [*Ford*, 1987]. Despite differences, the vocalizations are similar in that they have strong tonal characteristics with most energy between 1-6 kHz, although some calls contain energy at frequencies up to 30 kHz [*Ford*, 1987]. SRKWs also produce whistles during social communication. The whistles typically include single narrowband tones that are sometimes frequency modulated. In general, whistles are less predictable and have lower source levels than stereotypes calls [*Miller*, 2006].

Numerous methods for automated detection of marine mammal vocalizations including spectrogram correlations [*Mellinger and Clark*, 2000; *Mellinger*, 2004], neural networks [*Mellinger and Clark*, 2000; *Mellinger*, 2004], likelihood ratio tests [*Urazghildiiev*, 2006; *Urazghildiiev and Clark*, 2007], and information entropy [*Erbe and King*, 2008]. In important applications, humans with practice identifying vocalizations specific to the target species review autodetections. Regardless of the detection method, a higher signal-to-noise ratio increases the likelihood of a positive detection while high thresholds for detection limit the likelihood of false-positives. Therefore, a balance must be struck between the ability to identify vocalizations and the acceptable number of false-positives.

This study quantifies the estimated range of detection of SRKW vocalizations under different ambient noise conditions in Admiralty Inlet, Puget Sound. At the site, sediment-generated noise is the limiting factor at the critical frequencies during strong currents. Given the dependence of sediment-generated noise levels on currents, the likely range of detection is estimated for different turbine operating conditions at the site. As discussed in Chapter 7, power output by tidal turbines and the likely detection range of turbines by marine species are dependent on the current velocity. This analysis provides a basic methodology for

considering the use of passive acoustic techniques in post-installation monitoring. Section 8.2 describes the site, instrumentation, ambient noise levels, currents, transmission losses, vocalization characteristics, and the detection criteria. This information is combined into an algorithm for determining the estimated range of detection for SRKW vocalizations. Sections 8.3 and 8.4 include the results and a discussion.

8.2 Methods

8.2.1 Ambient Noise

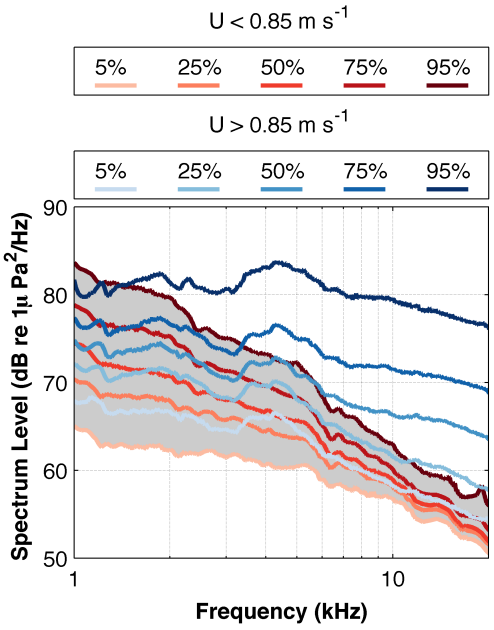

Figure 8.1: Ambient noise spectra (5^{th}, 25^{th}, 50^{th}, 75^{th}, and 95^{th} percentiles) for near-bed currents less than 0.85 m/s (reds) and greater than 0.85 m/s (blues). Noise level variability in the two current regimes are driven by vessel traffic and sediment-generated noise.

The ambient noise statistics used in this analysis were derived from the analyses in Chapters 4 and 5, which include information about the deployments, processing, and interpretation of the data. *Bassett et al.* [2012, 2013] identify the range of spectrum levels associated with the two most significant ambient noise sources at the site: vessel traffic and sediment-generated noise. Vessel traffic densities near the site are high due to the presence of shipping lanes, passenger vessel routes, and military installations in Puget Sound. Sediment-generated noise occurs when bed stresses mobilize the seabed and sediment grains collide, creating sound.

For the purpose of this study, the ambient noise spectra from *Bassett et al.* [2012, 2013] are the ambient noise inputs to the detection model. Percentile statistics of ambient noise spectra for the 5, 25, 50, 75, and 95% thresholds are spectra used to determine the decreases in detection area due to sediment-generated noise. These

percentile statistics, derived from low current periods [*Bassett et al.*, 2012], are suitable for conditions when currents are below 0.85 m/s [*Bassett et al.*, 2013], the threshold for sediment-generated noise. When currents exceed 0.85 m/s, percentile statistics corresponding to the 5, 25, 50, 75, and 95% thresholds from sediment-generated noise are used. The sediment-generated noise spectra are calculated at times when no vessels are in the study area as in *Bassett et al.* [2013]. The input spectra for the detection model are included in Figure 8.1.

8.2.2 Currents

Velocity profiles at the site are obtained using a 470 kHz Nortek Continental Acoustic Doppler Current Profiler (ADCP) and a 1 MHz Nortek Acoustic Wave and Current Profiler (AWAC). Results from the current profiles are used to determine probability density functions of the currents. Velocity profiles are determined using one-minute ensemble averages. As discussed in Section 8.2.1, noise levels during periods of strong currents at the frequencies of interest in this study are driven sediment-generated noise and therefore hydrodynamic conditions. Current velocities are an important model input because ambient noise measurements are predictable based on near-bed currents at the site [*Bassett et al.*, 2013]. Results presented for the current velocity distribution and noise levels are covered in more detail by *Polagye and Thomson* [2013] and *Bassett et al.* [2013], respectively. For the purpose of this study, a cumulative probability distribution function of near-bed current velocity is used to relate detection algorithms results to the temporal current velocity distribution.

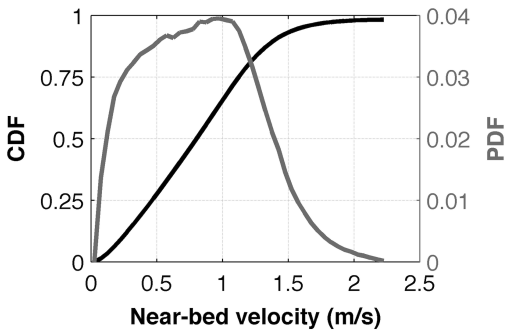

Figure 8.2: Cumulative probability density and probability density functions for near-bed currents at the site. The critical threshold for sediment-generated noise (0.85 m/s) corresponds to the 55^{th} percentile of near-bed currents.

8.2.3 Vocalization Source Levels

Based on the vocabulary and frequency of use of specific vocalizations within the SRKW vocal repertoire, three unique vocalizations were chosen to as input to the detection range algorithm. The S1, S16, and S19 calls correspond to the J Pod, K Pod, and L Pod, and are the most common stereotyped calls of the three SRKW Pods [*Foote et al.*, 2008]. The calls used in the analysis are the same vocalizations included in *Holt et al.* [2011, Figure 1]. The data were obtained by Holt et al. using a Reson TC-4033 hydrophone with a sensitivity of -203 dB re 1V/μPa and a Reson VP1000 preamplifier with a high pass filter (1 kHz). A spectrum representing each vocalization was created using a subset of the data in each

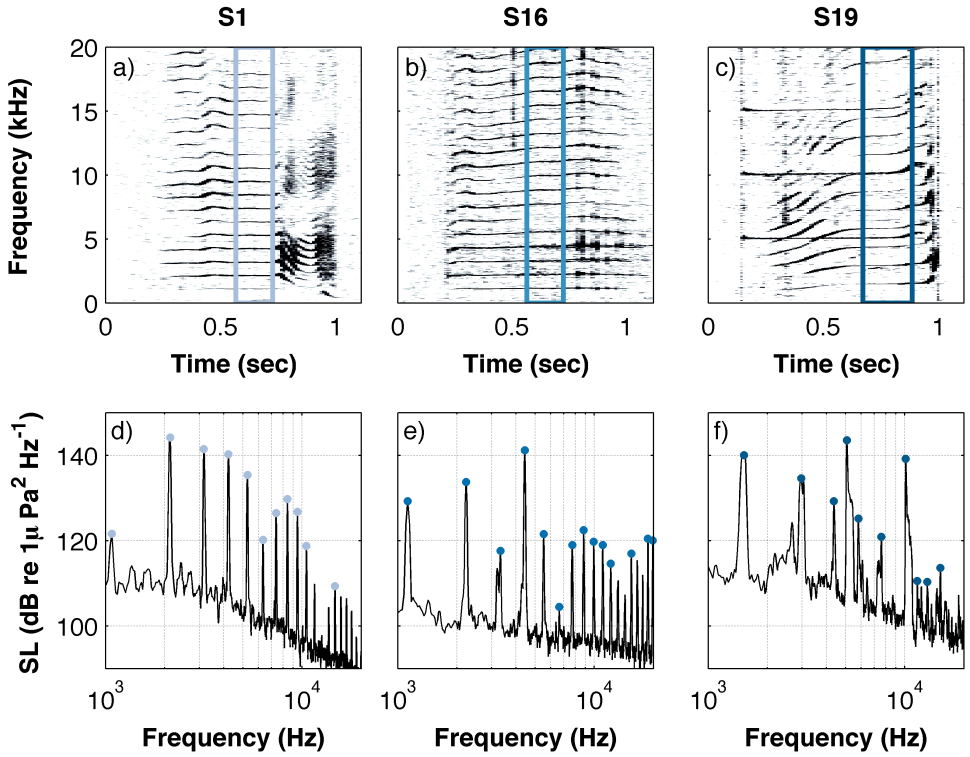

Figure 8.3: a-c) Spectrograms of the S1, S16, and S19 vocalizations highlighted in *Holt et al.* [2011]. Boxed portions of the spectrograms highlight the averaging periods used to produce the scaled source levels estimates. d-f) Scaled source spectra for the four modeled vocalization components. The source levels in are 164, 159, and 166 dB re 1μPa at 1 m, the 95$^{\text{th}}$ percentile source levels for each vocalization [*Holt et al.*, 2011]. The points in each source spectrum highlight the peaks used in detection model.

spectrogram. The spectrograms and the averaging period used for the source spectra are highlighted in Figure 8.3. The spectra were calculated directly from signal processing of the wav files (2^{12} data points, 75% overlap, Hann window) without conversion into pressure space. Power spectra were converted to source levels by integrating under the spectra and scaling the results to the chosen source levels. To provide consistent input to the model, each vocalization was scaled to the 95^{th} percentile source level associated with the call according to *Holt et al.* [2011]: 164 dB re 1μPa for the S1, 159 dB re 1μPa for the S16, and 166 dB re 1μPa for the S19. These source levels near the upper limits reported in other studies (e.g., *Erbe* [2002] if the adjusted for the transmissions losses, *Miller* [2006]). After being scaled to the appropriate broadband source level, inputs to the detection model are the source levels and frequencies associated with the notable peaks in the spectra (Fig. 8.3d-f).

The vocalizations are modeled as omnidirectional. Directionality is noted to be important for only specific components of some calls containing separately modulated harmonics [*Miller*, 2002; *Holt et al.*, 2011]. In the case of this study, only the S19 vocalization contains these directional components. The 5 kHz tone and its higher harmonics are the directional components with higher source levels in the S19 call. Given the added complexity of assuming an orientation distribution during the vocalization, these components are also modeled as omnidirectional.

8.2.4 Transmission Losses

The sound field resulting from a source in a shallow water environment is complex and can be estimated using a number approaches. Of greatest concern to this study are characteristic transmission losses (TL) between the source and receiver that take into consideration important terms including the spreading of sound waves from the source, interactions with the surface and seabed, and attenuation. The model described in *Marsh and Schulkin* [1962] is used to estimate transmission losses. This simplified model considers transmission losses terms, noting that with a water depth of more than 4 times the acoustic wavelength, as is the case in this study, there is no dependence on the depths of the source and receiver [*Marsh and Schulkin*, 1962].

A set of three equations govern the transmission losses in this model. The skip distance (H), or the range between successive interactions with the surface, is defined as $H = \left[\frac{1}{8}(D+L)^{\frac{1}{2}}\right]$, where D is the water depth and L is the depth of the thermocline. In the case of Admiralty Inlet, the water column is generally well mixed [*Polagye and Thomson*, 2010], so the thermal structure is expected to have little impact on sound propagation. The transmission loss domains, based on the skip distance are defined as

$$TL = \begin{cases} 20\log_{10}(R) + \alpha R + 60 - k_L, & \text{if} \quad R < H \\ 15\log_{10}(R) + \alpha R + 60 + a_T(R/H - 1) & \\ \qquad + 5\log_{10}(H) + 60 - k_L, & \text{if} \quad H \leq R \leq 8H \\ 10\log_{10}(R) + \alpha R + a_T(R/H - 1) & \\ \qquad + 10\log_{10}(H) + 64.5 - k_L, & \text{if} \quad R > 8H \end{cases} \tag{8.1}$$

where R is the distance from the source, k_L is the near field anomaly, α is the frequency dependent attenuation, and a_T is the loss coefficient for each interaction with the bed. The near field anomaly and loss coefficients are available as tables in *Marsh and Schulkin* [1962]. The bottom type is assumed to be sand, representing a simplification of the variability in the local substrate. Attenuation is calculated according to *Francois and Garrison* [1982a, b]. For frequencies greater than 10 kHz, the near-field anomaly and loss coefficients are extrapolated using the log of the frequency. When the sea surface is rough, additional losses occur with each surface interaction. In this study, all transmission losses are calculated assuming sea state 1. In the Strait of Juan de Fuca, sea state 2 or less is observed in 68% measurements [*Graber et al.*, 2011].

The depth is also an important input to the transmission loss equations because a shallower depth results in more bottom and surface interactions. The bathymetry is complex with depths between 0-200 meters near the study area. The transmission loss at each grid point is calculated based only the depth at the point being modeled using the best available bathymetric data set [*Finlayson*, 2005]. With the exception of points along the shore, most of the modeled domain is deeper than the receiver. Therefore, this approach underestimates accumulated losses through boundary interactions.

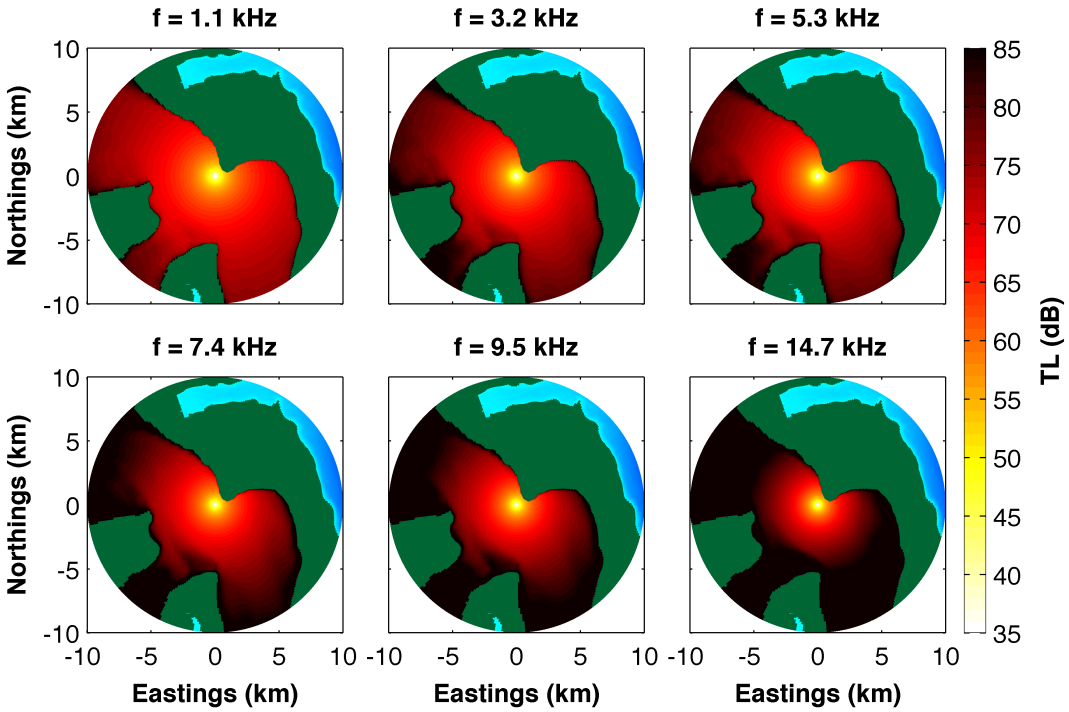

Figure 8.4: Example transmission losses (*Marsh and Schulkin* [1962] model) for selected S1 vocalization components.

The frequencies identified for the peaks in the vocalization spectra (Sec. 8.2.3) provide the inputs for the transmission loss terms, which are mapped throughout the modeled domain. Figure 8.4 includes an example transmission loss map of some of the peaks in the S1 vocalization spectrum. Throughout the entire domain transmission losses are less than 85 dB for 1.1 kHz peak but transmission losses exceed 85 dB throughout much of the domain for 14.7 kHz. The differences in transmission losses with at frequencies are not only attributed to more rapid attenuation but also greater losses with each bottom interaction. For example, *Marsh and Schulkin* [1962] notes a difference in bottom losses of 1.9 dB/bounce at 1 kHz versus 4.5 dB/bounce at 10 kHz for a sandy bottom with a sea state of 1.

8.2.5 Signal-to-Noise Ratios for Autodetection

Whether a human- or computer-based, detection methods that are used to identify vocalizations all require that the vocalization have a minimum signal-to-noise ratio (SNR) above

ambient conditions. For autodetection methods, a balance must be struck between the required SNR and the likelihood of false-detections. In general, a higher SNR threshold will result in fewer detections, but also fewer false positives. Therefore, the choice of a SNR is driven by the intended application. For example, if the sole purpose of identifying to vocalizations is the monitor the presence and absence of killer whales a higher false-positive rate may be acceptable, which permits the use of a lower SNR. However, if the purpose were to identify the presence of killer whales to initiate an intensive monitoring program or adjust turbine operation, a higher level of confidence and lower false-positive rate would be desired and a higher signal-to-noise ratio would be chosen. An analysis of the appropriate signal-to-noise ratios under different scenarios is beyond the scope of this work.

Rather than identify a single detection method and SNR to model, this study considers three SNRs to demonstrate the how the detection range changes. Signal-to-noise ratios can be calculated in different ways: in this study, the SNR refers to the difference between signals at a given frequency. The modeled SNRs are 0 dB, 5 dB, and 10 dB. The first case represents idealized conditions under which any received vocalization above ambient noise can be detected. This case also represents the maximum range at which the calls can be detected (though, as noted in *Miller* [2006], biological detection of conspecifics may be possible for SNR $<$ 0 dB). The second case, a SNR of 5 dB, represents a system in which some level of false detections are acceptable. The final case uses a 10 dB SNR. For SRKW vocalizations, signals with a 10 dB SNR should be detectable with relatively low false-positive rates using open source software such as PAMGUARD [*Gillespie et al.*, 2008, www.pamguard.org] (personal communication with Jason Wood, Sea Mammal Research Unit).

8.2.6 Detection Distance

For each peak in the vocalization spectra, the transmission losses and ambient noise levels are determined. The inequality describing the detection criteria is

$$NL(f) < SL(f) - TL(f) - SNR, \tag{8.2}$$

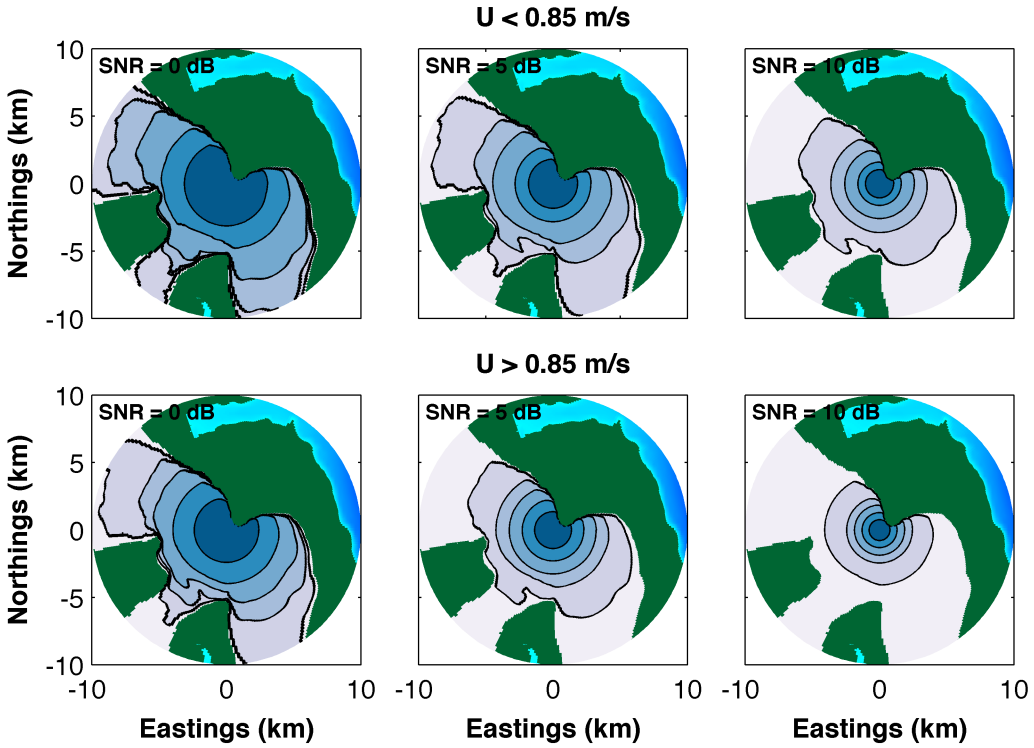

Figure 8.5: S1 call detection maps (SL: 164 dB re μPa at 1 m) for three SNRs and 10 ambient noise conditions. The black contours correspond to the 5, 25, 50, 75, and 95^{th} percentile noise conditions for the respective current regimes.

where NL is the ambient noise level, SL is the vocalization source level, TL is the transmission loss, and SNR is the signal-to-noise ratio for detection. An algorithm loops through Equation 8.2 for each component of the vocalization highlighted in Section 8.2.3. If any peak in the vocalization spectrum is detected, the signal is classified as detected. The results of the detection algorithm are stored for each spatial bin in the study domain and used to map and integrate the total detection area.

8.3 Results

Given the vocalization sources levels, calm conditions (sea state 1), and a detection SNR, the calculated detection ranges for the vocalizations, based on ambient noise statistics for the periods with and without sediment-generated noise, are included in Figures 8.5-8.7. These figures include the S1, S16, and S19 vocalizations with the three signal-to-noise ratios.

The maximum detection range associated with an S1 vocalization (SL = 164 dB re 1μPa) for a 0 dB signal-to-noise ratio extends beyond the modeled domain for the 5^{th} percentile noise levels. The S19 detection area also extends past the domain during the quietest periods at the site. However, the S16 does not due to a lower source level. As ambient noise levels increase, the area over which the vocalizations are detectable decreases. During the noisiest periods, those resulting from peak sediment-generated noise levels during strong currents, the detection range is only a fraction of the detection range during periods associated with peak slack current noise levels attributed to anthropogenic noise. The differences in the reduction in range are associated with frequency content of the vocalizations and the frequency distribution of sediment-generated noise with near-bed velocity. For example, the S1 detection area contracts less than the other vocalizations because the peak spectrum levels are at lower frequencies where the increases in sediment-generated noise are smallest.

Detection areas for each vocalization under the 10 ambient noise conditions modeled in the study are included in Table 8.1. During the noisiest periods, the detection areas are less than 10% of the detection are during the quietest periods. The detection area only includes the entire width of the inlet (approximately 5 km) during the least noisy periods under the assumption of a high source level (166 dB re 1μPa). In general, the detection areas at the threshold for sediment-generated noise (5^{th} percentile) are similar to those under mean slack current ambient noise conditions. During peak noise levels, the estimated ranges for detection, even using an unrealistically low signal-to-noise ratio of 0 dB, are 2.2 km for the S1 vocalization, 1.4 km for the S19, and 1 km for the S16. With SNRs of 10 dB, these ranges reduces to less than 800 meters for the S1 call and less than 500 meters for the S16 and S19 calls.

8.4 Discussion

Sediment-generated noise occurs in the same frequency ranges that can be used in passive acoustic monitoring of killer whales. As a result, the effective range for traditional passive acoustic monitoring techniques decreases as the near-bed velocity increases. With the exception of peak near-bed currents (i.e., 2 m/s), the expected detection range for the three vocalizations with a 10 dB SNR exceeds 1 km. As Chapter 7 shows, killer whales are un-

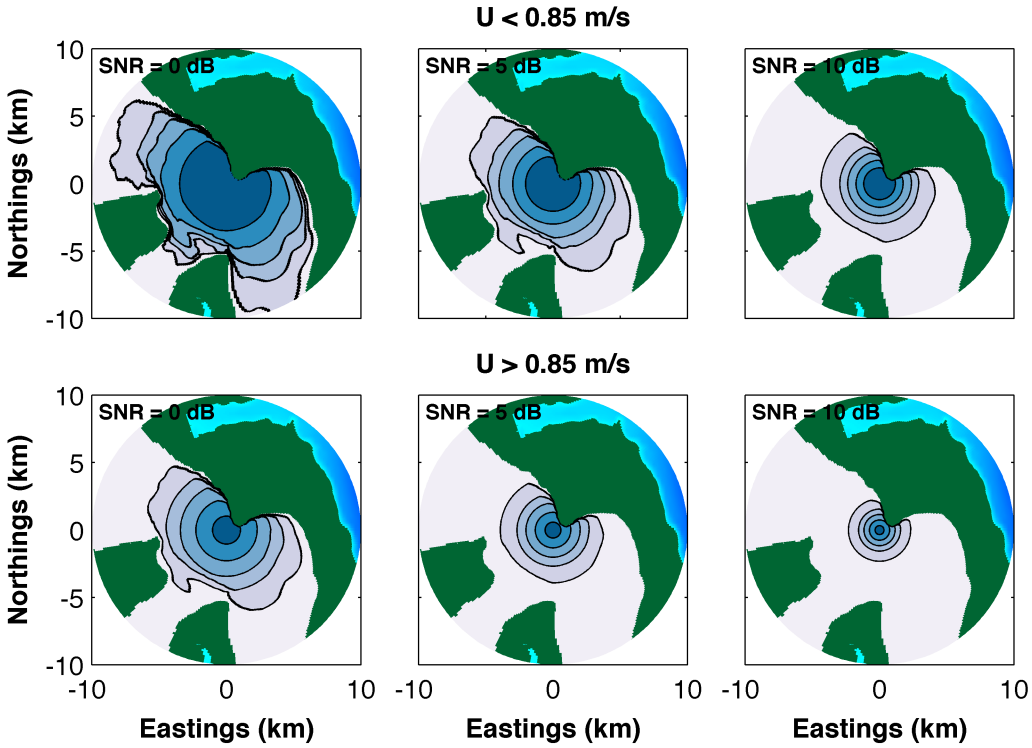

Figure 8.6: S16 call detection maps (SL: 159 dB re μPa at 1 m) for three SNRs and 10 ambient noise conditions. The black contours correspond to the 5, 25, 50, 75, and 95^{th} percentile noise conditions for the respective current regimes.

likely to detect turbine noise at a range greater than 1 km. Therefore, despite a decrease in detection range, passive acoustic techniques are likely to detect killer whale vocalizations at a greater range than that at which the whales will detect the sound from the turbine, allowing passive acoustics to be used to evaluate behavioral changes both inside and outside the zone of detection. Nonetheless, there are a number of uncertainties included in this analysis that affect the results. The following sections detail these uncertainties and discuss their relative impacts on the results.

8.4.1 Sensitivity to Detection Criteria

Vocalization Considerations: In the case of the S19 vocalizations of the L-pod, the loudest tone is a directional, high-frequency component. The second most common call used by the L Pod also contains similar energetic high-frequency components. These components of

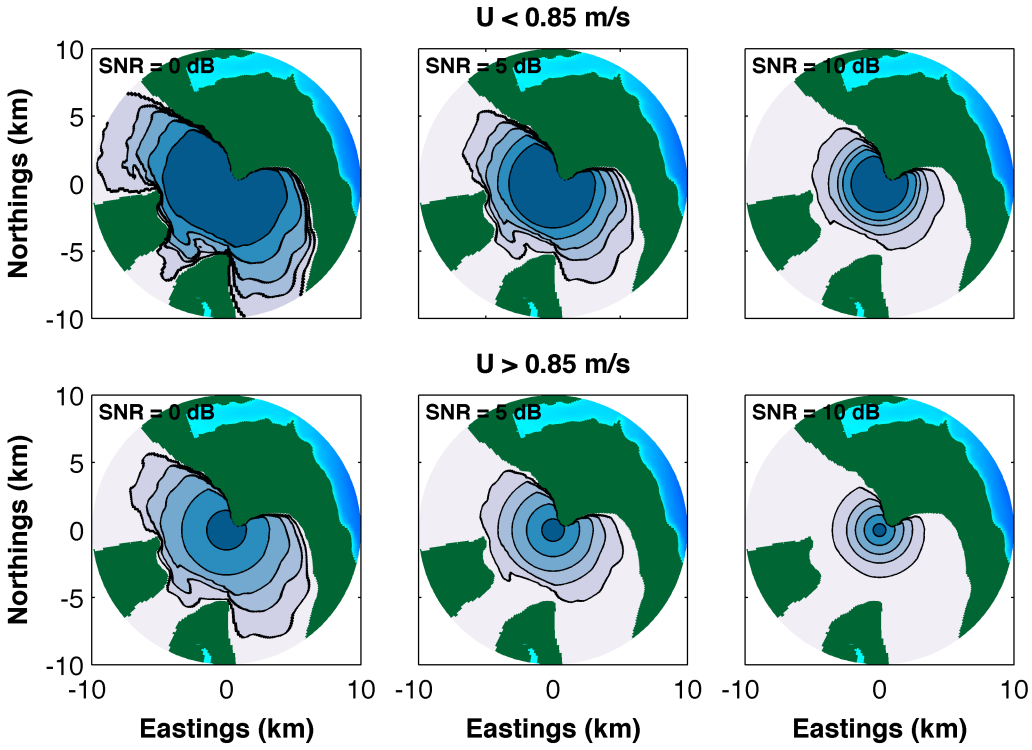

Figure 8.7: S19 call detection maps (SL: 166 dB re μPa at 1 m) for three SNRs and 10 ambient noise conditions. The black contours correspond to the 5, 25, 50, 75, and 95^{th} percentile noise conditions for the respective current regimes.

the vocalization were assumed to be omnidirectional in the detection model. The assumption of omnidirectional high-frequency components does result in an optimistic detection range for these particular tones. At large ranges, the frequency component that is most likely to be detected is the lowest harmonic (1.5 kHz) due to lower frequency dependent losses and smaller increases in ambient noise levels with current. Therefore, the effects of the assumption of omnidirectional high-frequency components on the results are likely to be limited.

Source Levels: In this analysis, the 95^{th} percentile source levels for the three vocalizations were used. This choice of source level was used to simplify the analysis and because *Holt et al.* [2009, 2011] note the Lombard effect; an increase vocalization source levels to compensate for increases in background noise. For the three vocalizations, the differences

Table 8.1: The estimated area over which the S1, S16, and S19 vocalizations are detected given different signal-to-noise ratios.

		Detection Area (km^2)								
		S1			S16			S19		
SNR		0 dB	5 dB	10 dB	0 dB	5 dB	10 dB	0 dB	5 dB	10 dB
Ambient Noise Percentile		Currents < 0.85 m/s								
	5 %	150.4	130.6	77.7	122.2	79.9	42.7	138.2	93.1	54.5
	25 %	127.4	74.4	32.6	90.4	51.5	22.3	107.7	68.0	34.2
	50 %	93.7	46.6	17.5	73.7	37.5	14.8	91.7	54.1	24.5
	75 %	53.2	20.6	7.1	52.4	22.8	8.3	71.3	38.8	19.2
	95 %	24.9	9.0	3.2	29.9	11.2	4.0	49.7	26.8	11.9
		Currents > 0.85 m/s								
	5 %	135.8	85.1	39.8	71.9	71.9	14.1	101.9	62.4	30.2
	25 %	88.7	42.6	15.8	45.1	45.1	6.7	73.7	38.6	15.7
	50 %	65.0	27.0	9.4	29.1	29.1	3.9	52.6	23.6	8.7
	75 %	38.3	13.9	4.8	13.7	13.7	1.8	27.6	10.4	3.8
	95 %	15.2	5.3	1.9	3.2	3.2	0.4	6.1	2.2	0.7

between the 25^{th} and 95^{th} percentiles are roughly 15 dB, or 5 dB more than the range of SNRs considered. Figures 8.5-8.7 show that the true variation in source level could significantly reduce the detection range. These source levels (159-166 dB re 1μPa at 1 m) are also typical of the range for the other vocalizations highlighted in *Holt et al.* [2011]. The use of source levels 10 dB lower than those applied here combined with SNRs of 5 dB would result in detection ranges smaller than the 1 km range currently planned current post-installation monitoring during peak currents.

Transmission Losses: An increased sea state reduces the range over which detection is possible. The decrease in range is a result of larger losses due to the scattering by surface when the surface is rough. In general, the decreases in detection area between sea state 1 and

sea state 3 are dependent on the frequency content of the vocalization; a vocalization with higher frequency components will experience additional losses due to higher sea states. For models with sea state 3 (not shown), the decreases in detection ranges were approximately 10-20%. Sea states greater than 3 are uncommon in Admiralty Inlet because the fetch is limited in many directions. However, at a site with larger variability in sea state, decreases in detection ranges would be more significant.

The bathymetry, seabed properties, and water properties (i.e., sound speed profile) also affect the propagation of sound. In order to integrate more detailed bathymetry into this study, range-dependent numerical models would have to be utilized. The sound speed profiles can affect transmission losses and propagation by refracting the waves. Section 3.4.5 includes sound speed profiles from Admiralty Inlet. Throughout the year, the sound speed profiles range from slightly downward refracting to slightly upward refracting; however, the sound speed gradients are small and typically vary by no more than 3 m/s in the upper 60 meters of the water column. As such, the impact of the sound speed profiles on propagation and transmission loss is limited.

The seabed properties also contribute to transmission losses when propagating waves interact with the seabed. In this study, the seabed was assumed to be sand to permit the use of the *Marsh and Schulkin* [1962] model. However, the composition of the seabed throughout the domain is unknown. The available data suggest that in the immediate vicinity of the site the bed is composed of a thin layer (< 2 m) of cobbles, pebbles, and gravel due to the winnowing of fine-grained sediments by tidal currents. Beneath the upper layer is a larger layer of fine-grained sediments [*Landau Associates*, 2011]. Further from the site there are various bed types including, but not limited to, coarse grained sediments of different sizes and sand waves [*Greene*, 2011]. Due to a paucity of data regarding the composition of the seabed throughout the modeled domain, any conclusions regarding the effects of this assumption would be speculative.

Signal-to-Noise Ratios:

The analysis has not addressed one of the primary goals of post-installation passive acoustic monitoring: to utilize passive acoustic array to localize biological source near the

project site. Although analyzing the impact of signal-to-noise ratios on a localizing array is beyond the scope of this study, some conclusions can be drawn about noise source localization. In order to localize a source in space, a time-of-arrival difference (TOAD) approach, which utilizes the differences in the arrival time of signals at known transducer locations to constrain the location of the source [*Wahlberg et al.*, 2001], will be used. Uncertainty in the receiver positions, sampling rates, and ambient noise can result in localization errors, the third of which will be the focus of future work. During periods with strong currents and low signal-to-noise ratios, processing must identify the arrival of the vocalizations above ambient noise. With low signal-to-noise ratios, uncertainty in the time of arrival may be a major source of uncertainty in the localization algorithms.

8.4.2 Implications for Monitoring Plans

It is clear that sediment-generated noise has the potential to reduce the effective range of passive acoustic monitoring techniques at frequencies relevant to particular marine mammal functional groups. In particular, this work suggests the importance of sediment-generated noise for monitoring for mid-frequency cetaceans; however, unpublished measurements at the site reveal sediment-generated noise also complicates monitoring for high-frequency cetaceans. For example, click detectors (e.g., Chelonia C-PODs) are unable to distinguish between cetacean clicks and collisions between sediment grains, leading to high rates of false click detection during high current periods. Furthermore, unpublished results from the drifting work highlighted in *Bassett et al.* [2013] indicate that ambient noise increases due to sediment motion occurs up to frequencies of 100 kHz or more.

If increasing the effective range of passive acoustic monitoring techniques is desired the only option is to move the receiver away from the noise source. In other words, hydrophones would need to be deployed outside of the areas with the strongest currents and bed stresses. Studies of currents in Admiralty Inlet indicate large variability in measured currents over relatively small spatial scales [*Palodichuk et al.*, 2013; *Polagye and Thomson*, 2013] that, in the absence of better options, could be used to reduce impact of sediment-generated noise by moving the hydrophones away from the areas where the highest levels of bed mobilization

are expected. Additionally, hydrophones should be deployed away from surf zone where mobilized sediments could also produce sound that interferes with passive acoustic measurements [*Mason et al.*, 2007]. However, this would complicate the logistics of collecting passive acoustic information relative to an arrangement in which hydrophones are placed on or near the turbines due to the need to run additional cabling for real-time monitoring.

Post-installation monitoring plans at the site include planned and rapid response marine mammal observations in order to study potential behavioral changes attributable to operating tidal turbines. To support these observations, a localization array consisting of four hydrophones will be deployed on each turbine and the intersection of the over-determined bearings used to localize the vocalizations. Assuming that turbine noise does not interfere with noise measurements at these same frequencies, these results indicate that, under most conditions, the passive acoustic array will be able to detect killer whales vocalizations throughout the planned post-installation monitoring area. Future work should focus on developing models to quantify the uncertainty that will be associated with localization given the noisy conditions at the site.

8.5 Conclusion

Sediment-generated noise overlaps with sounds produced by killer whales. Increases in noise due to sediment transport begin at roughly the cut-in speed of the turbine. Therefore, ambient noise levels at the frequencies necessary to identify killer whale vocalizations during turbine operation are dependent on current velocity. Although sediment-generated noise significantly reduces the range over which passive acoustic measurements are likely to be able to record vocalizations, even during strong currents the range is comparable in scale to the planned post-installation monitoring area. The impact of these higher noise levels on localization errors has not yet been determined, but should be the focus of future work.

Chapter 9

CONCLUSIONS

This dissertation presents a detailed analysis of the most important ambient noise sources at the location of a proposed tidal power project Admiralty Inlet, Puget Sound, Washington. Although other common sources such as precipitation, biology, and breaking waves do contribute to ambient noise levels at this location, measurements taken over a four-year period show vessel traffic and sediment-generated noise dominate the observed variability. Figure 9.1 shows the range of noise levels and frequencies over which these two propagating noise sources, as well as non-propagating flow-noise, are commonly measured in Admiralty Inlet.

Based on one-year of Automatic Identification System data paired with hydrophone recordings, vessel traffic is identified as the most important source of ambient noise at frequencies below 1 kHz. Above 1 kHz, signals associated with vessel traffic are also important, but only during periods with near-bed currents less than 0.85 m/s. The noisy conditions attributed to vessel traffic at the site are a result of high densities of ferries and commercial shipping traffic (i.e., shipping vessels and tugs/barges). Notably, a model combining a simply transmission loss term, incoherent addition of vessel noise sources, and source level attribution based on vessel type agrees with the measured noise level distribution for the upper 85% of the noise level distribution.

Given the multiple ports, naval facilities, ferry routes, and the prevalence of fishing vessels and recreational traffic within a relatively narrow waterway, it is not surprising that noise measurements are indicative of a highly urbanized environment. The predictive power of even simple models for vessel noise suggests that such an approach could be used to both project future changes in the soundscape based on changes in vessel traffic patterns (e.g., new ferry routes or increases in vessel traffic) or due to the adoption of vessel quieting technologies.

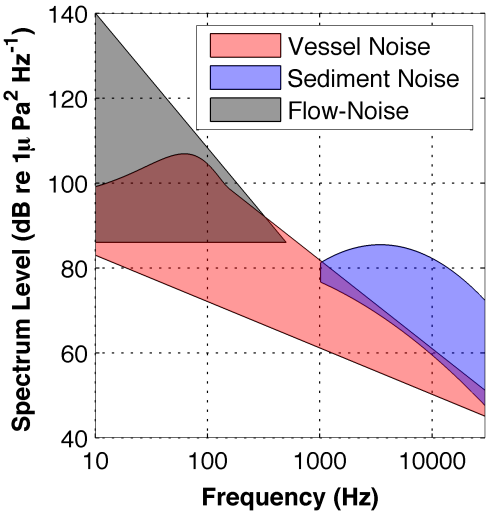

Figure 9.1: Vessel noise, sediment-generated noise, and flow-noise dominate the variability in ambient noise measurements in Admiralty Inlet. Here, the envelopes show the range of noise levels and frequencies at which these source are regularly observed at the site.

When near-bed current velocities exceed 0.85 m/s, shear stresses begin to mobilize sediment at the Admiralty Inlet site. When a mobilized sediment grain collides with another sediment grain, sound is created at frequencies related to the grain sizes. The frequency of the increases in sound levels recorded during periods with strong currents is consistent with the known composition of the seabed and that the shear stresses at which the coarse-grained sediments are mobilized is lower than the thresholds identified in previous studies. Most importantly, noise levels at frequencies from 1-30 kHz are highly predictable given the near-bed currents.

Noise levels are attributed to mobilized sediments at the site and qualitative conclusions are drawn regarding the intermittency and stationarity of this noise. However, these conclusions are based solely on acoustic observations. This line of research, which is likely to increase in importance as more measurements are taken in highly energetic environments, could be further developed in a number of ways. First, an array of bottom mounted hydrophones could be used to address variability on spatial scales from less than 20 m to determine the distribution of mobilization events, to greater than 100 m where variability can be attributed to large-scale differences in the magnitude of the current velocities. To aid in these measurements, instruments capable measuring current velocities and turbulence with high temporal resolution (e.g., ADVs) should be deployed. Finally, camera systems could be used to both quantify the degree of mobilization and the size of the grains involved with mobilization events.

Pressure fluctuations associated with turbulent velocity fluctuations can result in flow-noise, which poses a significant challenge to obtaining quality low-frequency acoustic mea-

surements in highly turbulent environments. In both Admiralty Inlet and the Chacao Channel, Chile, flow-noise is shown to result in spectrum levels exceeding 140 dB re 1μPa/Hz. The noise increases associated with these pressure fluctuations can exceed slack current ambient noise levels by more than 50 dB and are observed at frequencies greater than 500 Hz. Here, previously published models for flow-noise are extended to a higher range of frequencies by directly applying measurements of mean-currents and turbulence. When directly applying both of these hydrodynamic terms, the model was shown to agree with flow-noise observations at both sites. A second model, which relies on scaling arguments to remove the turbulent velocity fluctuations, is shown to perform well in the Chacao Channel but performs poorly in Admiralty Inlet, a difference attributed to the large-scale generation of turbulence.

Based on the understanding of flow-noise demonstrated both in this document and in previous research, there are two important lines of research that would benefit future acoustic measurements in highly turbulent environments. First, the response of hydrophones to turbulence at scales comparable to and smaller than the transducer size is dependent on the transducer geometry. Therefore, future studies regarding how different hydrophone geometries respond to turbulence would facilitate the development of a general model for flow-noise. Second, given that the mechanisms that result in flow-noise are understood, steps should be taken to develop tools to mitigate flow-noise. Currently, such techniques include using signal processing to identify coherent ambient noise signals. However, these techniques are not sufficient when flow-noise levels exceed ambient noise levels by many orders of magnitude, as is the case in highly turbulent environments. The development of techniques to mitigate flow-noise without attenuating ambient noise signals (e.g., flow shields or domes) would allow signal processing techniques to identify meaningful correlations associated with ambient noise to reduce the effects of flow-noise. Furthermore, the development of mechanical techniques that entirely mitigate flow-noise at the hydrophone would permit the use of single hydrophones rather than arrays to quantify ambient noise levels, even in highly turbulent environments.

By applying the results of the ambient noise studies highlighted in this document, specifically the vessel noise and sediment-generated noise studies, with the estimated source spec-

tra of operating turbines and marine animal hearing sensitivities, the range at which species will be able to detect operating turbines is estimated. The results of this study indicate that the detection ranges are typically limited to less than 1 km. Given that a detection is not indicative of a behavioral change and that this 1 km range is only a fraction of Admiralty Inlet's width, these results suggest that the acoustic impacts of the demonstration-scale project are likely to be small and difficult to detect.

In addition to estimating the detection ranges, the study provides a framework that can be used to estimate potential environmental impacts of future tidal power projects. In order to improve such models, future work must identify and reduce the uncertainties in the model. Currently, the most significant unknowns relate to the hearing sensitivities and behavioral responses of marine animals and the source levels of operating turbines. Similarly, the source levels of operating tidal turbines are hypothesized to depend on their operational state and future work should focus on both identifying the sound generation mechanisms and how this sound scales with current velocity or turbine power. Post-installation monitoring plans in Admiralty Inlet will focus on answering these questions, but such analyses should also be performed on other devices. These studies should be performed on a range of devices used standardized techniques.

The energetic conditions that make sites suitable for tidal power projects can also lead to sediment-generated noise, unless the seabed is scoured bedrock. One consequence of these increased noise levels is a reduction in the range at which vocalizations and echolocation clicks from mid- and high-frequency cetaceans can be detected. This reduction is a result of an overlap in the frequencies at which collisions between sediment grains produce sound and the frequencies at which these animals produce sound. It is shown that sediment-generated noise levels can reduce the estimated detection area of killer whale vocalizations by 90% or more when compared to the least noisy conditions in Admiralty Inlet. The frequencies at which sediment-generated noise is produced is dependent on the composition of the seabed. In future applications that utilize passive acoustic techniques to study marine animals, both the potential reduction in detection range and the interference of sediment-generated noise with click detectors (e.g., Chelonia C-PODs) should be addressed.

The geographic distribution of highly energetic sites suitable for tidal power extraction

is quite limited. In addition, the strong currents pose significant engineering challenges to working in these environments. As a result, relatively few measurements from such sites have been published. As development of tidal power projects in these energetic environments continues, passive acoustics will be an important tool to study both the sound produced by tidal turbines and marine mammal behavioral responses to their presence. The research presented in this dissertation highlights the characteristics of ambient noise levels that may be observed at other potential tidal power sites. Obtaining quality measurements of ambient noise and characterizing construction and operational noise from tidal power projects will be critical to addressing the environmental impacts of tidal power generation. To facilitate the development of the tidal power industry, addressing these issues at the demonstration-scale is imperative.

BIBLIOGRAPHY

Ainslie, M., and J. McColm, A simplified formula for viscous and chemical absorption in sea water, *J. Acoust. Soc. Am.*, *103*(3), 1671–1672, 1998.

APL-UW, High-frequency ocean environmental acoustic models handbook, *Tech. rep.*, Applied Physics Laboratory at the University of Washington TR 9407, 1994.

Arbic, B. K., and C. Garrett, A coupled oscillator model of shelf and ocean tides, *Cont. Shelf Res.*, *30*(6), 564 – 574, doi:10.1016/j.csr.2009.07.008, 2010.

Arveson, P., and D. Vendittis, Radiated noise characteristics of a modern cargo ship, *J. Acoust. Soc. Am.*, *107*(1), 118–129, 2000.

Au, W. W., J. K. Ford, J. K. Horne, and K. A. Newan Allman, Echolocation signals of free-ranging killer whales (*Orcinus orca*) and modeling of foraging for chinook salmon (*Oncorhynchus tshawytscha*), *J. Acoust. Soc. Am.*, *115*(2), 901–909, 2004.

Barr, S., Acoustic characterization of the open-centre turbine, *Tech. rep.*, OpenHydro, Ltd., 2010.

Bassett, C., Underwater ambient noise at a proposed tidal energy site in Puget Sound, Master's thesis, University of Washington, 2010.

Bassett, C., J. Thomson, and B. Polagye, Characteristics of underwater ambient noise at a proposed tidal energy site in Puget Sound, in *Oceans 2010*, doi: 10.1109/OCEANS.2010.5664380, 2010.

Bassett, C., B. Polagye, M. Holt, and J. Thomson, A vessel noise budget for Admiralty Inlet, Puget Sound, Washington (USA), *J. Acoust. Soc. Am.*, *132*(6), 3706–3719, doi: 10.1121/1.4763548, 2012.

Bassett, C., J. Thomson, and B. Polagye, Sediment generated noise and bed stress in a tidal channel, *J. Geophys. Res.: Oceans*, *118*, 2249–2265, doi:10.1002/jgrc.20169, 2013.

Blackstock, D. T., *Fundamentals of Physical Acoustics*, John Wiley & Sons, Inc., 2000.

Brumley, B., R. Cabrera, K. Deines, and E. Terray, Performance of a broad-band Acoustic Doppler Current Profiler, *J. Ocean. Eng.*, *16*(4), 402–407, doi:10.1109/48.90905, 1991.

Buck, B., and C. Greene, A two-hydrophone method of eliminating the effects of nonacoustic noise interference in measurements of infrasonic ambient noise levels, *J. Acoust. Soc. Am.*, *68*(5), 1306–1308, 1980.

Buckstaff, K., Effects of watercraft noise on the acoustic behavior of bottlenoise dolphins, *Tursiops truncatus*, in Sarasota, Florida, *Mar. Mam. Sci.*, *20*(4), 709–725, 2004.

Carter, C., Marine renewable energy devices: A collision risk for marine mammals?, Master's thesis, University of Aberdeen, 2007.

Chapman, C., and A. Hawkins, A field study of hearing in the cod, *Gadus morhua l.*, *J. Comp. Physiol. A Neuroethol. Sens. Neural. Behav. Physiol.*, *85*(2), 147–167, 1985.

Chung, J., Rejection of flow noise using a coherence function method, *J. Acoust. Soc. Am.*, *62*(2), 388–395, 1977.

Clark, C., W. Ellison, B. Southall, L. Hatch, S. V. Parijs, A. Frankel, and D. Ponirakis, Acoustic masking in marine ecosystems: intuitions, analysis, and implications, *Mar. Ecol. Prog. Ser.*, *395*, 201–222, 2009.

Collins, M., A split-step Pade solution for the parabolic equation method, *J. Acoust. Soc. Am.*, *93*(4), 1736–1742, 1993.

Collins, M., *User's Guide for RAM Versions 1.0 and 1.0p*, Naval Research Laboratory, Washington, DC, 2000.

Cooley, J., and J. Tukey, An algorithm for the machine calculation of complex fourier series, *Math. Comput.*, *19*(90), 297–301, 1965.

Dahl, P., J. Miller, D. Cato, and R. Andrew, Underwater ambient noise, *Acoust. Today*, *3*(1), 23–33, 2007.

Deane, G., Long time-base observations of surf noise, *J. Acoust. Soc. Am.*, *107*(2), 758–770, 2000.

Deecke, V., J. Ford, and P. Slater, The vocal behaviour of mammal-eating killer whales: communicating with costly calls, *Anim. Behav.*, *69*(2), 395–405, 2005.

Dietz, F., J. S. Hahn, and W. Birch, Nonrandom associations between shallow water ambient noise and tidal phase nonrandom associations between shallow water ambient noise and tidal phase, *J. Acoust. Soc. Am.*, *32*(7), 915 (A), doi:10.1121/1.1936433, 1960.

Diplas, P., C. Dancey, A. Celik, M. Valyrakis, K. Greer, and T. Akar, The role of impulse on the initiation of particle movement under turbulent flow conditions, *Science*, *322*(5902), 717–720, doi:10.1126/science.1158954, 2008.

Ellison, W., B. Southall, C. Clark, and A. Frankel, A new context-based approach to assessing mammal behavioral responses to anthropogenic sounds, *Conserv. Biol.*, *26*(1), 1–8, 2011.

Emery, W. J., and R. E. Thomson, *Data Analysis Methods in Physical Oceanography*, 2 ed., Amsterdam: Elsevier, 2004.

Epler, J., Tidal resource characterization from acoustic doppler current profilers, Master's thesis, University of Washington, 2010.

Erbe, C., Underwater noise of whale-watching boats and potential effects on killer whales (*Orcinus orca*), based on acoustic impact model., *Mar. Mam. Sci.*, *18*, 394–418, 2002.

Erbe, C., and A. King, Automatic detection of marine mammals using information entropy, *J. Acoust. Soc. Am.*, *124*(5), 2833–2840, doi:10.1121/1.2982368, 2008.

Everest, F., R. Young, and M. Johnson, Acoustics characteristics of noise produced by snapping shrimp, *J. Acoust. Soc. Am.*, *20*(2), 137–142, 1948.

Federal Register, *Automatic Identification System; vessel carriage requirements*, Coast Guard, U.S. Department of Homeland Security, 60559-60570, 2003.

Feely, R., S. Alin, J. Newton, C. Sabine, M. Warner, A. Devol, C. Krembs, and C. Malor, The combined effects of ocean acidification, mixing, and respiration on pH and carbonate saturation in an urbanized estuary, *Estuar. Coast. Mar. Sci.*, *88*(4), 442–449, doi:doi:10.1016/j.ecss.2010.05.004, 2010.

Finlayson, D., Combined bathymetry and topography of the Puget Lowland, Washington State, 2005.

Foote, A., R. Osborne, and A. Hoelzel, Whale-call response to masking boat noise, *Nature*, *428*, 910, 2004.

Foote, A., R. Osborne, and A. Hoelzel, Temporal and contextual patterns of killer whale (*Orcinus orca*) call type production, *Eythology*, *114*(6), 599–606, doi:10.1111/j.1439-0310.2008.01496.x, 2008.

Ford, J. K., A catalogue of underwater calls produced by killer whales (*Orcinus orca*) in British Columbia, *Can. Data Rep. Fish. Aquat. Sci.*, *633*, 1–165, 1987.

Ford, J. K., Vocal traditions among resident killer whales (*Orcinus Orca*) in coastal waters of British Columbia, *Can. J. Zool.*, *69*, 1454–1483, 1991.

Fraenkel, P., Marine current turbines: Pioneering the development of marine kinetic energy converters, *J. Power Energy*, *221*, 159–169, doi:10.1243/09576509JPE307, 2007.

Francois, R., and G. Garrison, Sound absorption based on ocean measurements: Part I: Pure water and magnesium sulfate contributions, *J. Acoust. Soc. Am.*, *72*(3), 896–907, 1982a.

Francois, R., and G. Garrison, Sound absorption based on ocean measurements. part II: Boric acid contribution and equation for total absorption, *J. Acoust. Soc. Am.*, *72*(6), 1879–1890, 1982b.

Frisk, G., Noiseonomics: The relationship between ambient noise levels in the sea and global economic trends, *Scientific Reports*, *2*(437), 1–4, 2012.

Gauss, R., J. Fialkowski, R. Menis, E. Kunz, C. Sellers, and J. Jech, Measurements and modeling of midfrequency clutter from fish aggregations over georges bank in the gulf of maine, *J. Acoust. Soc. Am.*, *125*(4), 2642, 2009.

Gillespie, D., J. Gordon, R. Mchugh, D. McLaren, D. Mellinger, P. Redmond, and A. Thode, PAMGUARD: Semiautomated, open source software for real-time acoustic detection and localisation of cetaceans, *Proc. Inst. Acoust.*, *30*(67-75), 2008.

Gobat, J., and M. Grosenbaugh, Modeling the mechanical and flow-induced noise on the Surface Suspended Acoustic Receiver, in *OCEANS '97. MTS/IEEE Conference Proceedings*, vol. 2, pp. 748–754, doi:10.1109/OCEANS.1997.624086, 1997.

Gooch, S., J. Thomson, B. Polagye, and D. Meggitt, Site characterization for tidal power, in *MTS/IEEE Oceans 2009, Biloxi, MI*, 2009.

Goring, D., and V. Nikora, Despiking acoustic Doppler velocimeter data, *J. Hydraul. Eng.*, *128*(1), 117–126, doi:10.1061/(ASCE)0733-9429(2002)128:1(117), 2002.

Graber, J., J. Thomson, B. Polagye, and A. Jessup, Land-based infrared imagery for marine mammal detection, in *SPIE Photonics + Optics*, San Diego, CA August 20-25, 2011.

Grant, W., A. Williams III, and S. Glenn, Bottom stress estimates and their prediction on the Northern California continental shelf during CODE-1: The importance of wave-current interaction, *J. Phys. Oceanogr.*, *14*(3), 506–526, doi:10.1175/1520-0485(1984)014¡0506:BSEATP¿2.0.CO;2, 1984.

Gray, L., and D. Greeley, Source level model for propeller blade rate radiation for the world's merchant fleet, *J. Acoust. Soc. Am.*, *67*(2), 516–522, 1980.

Green, M., Spectral estimates of bed shear stress at subcritical reynolds numbers in a tidal boundary layer, *Journal of Physical Oceanography*, *22*(8), 903–917, doi:10.1175/1520-0485(1992)022¡0903:SEOBSS¿2.0.CO;2, 1992.

Greene, C. R., Jr., and S. Moore, Man-made noise, in *Marine Mammals and Noise*, pp. 101–158, Academic Press, 1995.

Greene, H., Habitat characterization of the SnoPUD turbine site - Admiralty Head, Washington State, *Tech. rep.*, Sound and Sea Technology, 2011.

Greenlaw, C., Acoustical estimation of zooplankton populations, *Limnol. Oceanogr.*, *24*(2), 226–242, 1979.

Gross, T., and A. Nowell, Mean flow and turbulence scaling in a tidal boundary layer, *Cont. Shelf Res.*, *2*(2-3), 109–126, doi:10.1016/0278-4343(83)90011-0, 1983.

Hammond, F., A. Heathershaw, and D. Langhorne, A comparison between Shields' threshold criterion and the movement of loosely packed gravel in a tidal channel, *Sedimentology*, *31*, 51–62, doi:10.1111/j.1365-3091.1984.tb00722.x, 1984.

Harati-Mokhtari, A., A. Wall, P. Brooks, and J. Wang, Automatic identification system (AIS): Data reliability and human error implications, *J. Navig.*, *60*, 373–389, 2007.

Harden Jones, F., and R. Mitson, The movement of noisy sandwaves in the Strait of Dover, *ICES J. Mar. Sci.*, *40*(1), 53–61, doi:10.1093/icesjms/40.1.53, 1982.

Hatch, L., C. Clark, R. Merrick, S. Van Parijs, D. Ponirakis, K. Schwehr, M. Thompson, and D. Wiley, Characterizing the relative contributions of large vessels to total ocean noise fields: A case study using the Gerry E. Studds Stellwagen Bank National Marine Sanctuary, *Environ. Manage.*, *42*, 735–752, 2008.

Heathershaw, A., The turbulent structure of the bottom boundary layer in a tidal channel, *Geophys. J. Roy. Astron. Soc.*, *58*, 395–430, doi:10.1111/j.1365-246X.1979.tb01032.x, 1979.

Heathershaw, A. D., and P. D. Thorne, Sea-bed noises reveal role of turbulent bursting phenomenon in sediment transport by tidal currents, *Nature*, *316*(6026), 339–342, doi:10.1038/316339a0, 1985.

Hildebrand, J., Sources of anthropogenic sound in the marine environment, *Tech. rep.*, Report to the Policy on Sound and Marine Mammals: An International Workshop. U.S. Marine Mammals Commission and Joint Conservation Committee U.K. London, England. http://www.mmc.gov/sound/internationalwrkshp/pdf/hildebrand.pdf, 2004.

Hildebrand, J., *Impacts of Anthropogenic Sound*, The Johns Hopkins University Press, Baltimore, Maryland, 2005.

Hildebrand, J., Anthropogenic and natural sources of ambient noise in the ocean, *Mar. Ecol. Prog. Ser.*, *395*, 5–20, 2009.

Holt, M., D. Noren, V. Veirs, C. Emmons, and S. Veirs, Speaking up: Killer whales (*Orcinus orca*) increase their call amplitude in response to vessel noise, *J. Acoust. Soc. Am.*, *125*(1), EL27–EL32, 2009.

Holt, M., D. Noren, and C. Emmons, Effects of noise levels and call types on the source levels of killer whale calls, *J. Acoust. Soc. Am.*, *130*(5), 3100–3106, doi:10.1121/1.3641446, 2011.

Johnson, C., Sound detectiomn thresholds in marine mammals, in *Proceedings Marine Bioacoustics, Volume 2, p. 247*, 1967.

Kastelein, R., P. Bunskoek, M. Hagedoorn, W. Au, and D. de Haan, Audiogram of a harbor porpoise (*Phocoena phocoena*) measured with narrow-band frequency-modulated signals, *J. Acoust. Soc. Am.*, *112*(1), 334–344, 2002.

Kastelein, R., P. Wensveen, L. Hoek, W. Verboom, and J. Terhun, Underwater detection of tonal signals between 0.125 and 100 khz by harbor seals (*Phoca vitulina*), *J. Acoust. Soc. Am.*, *125*(2), 1222–1229, doi:10.1121/1.3050283, 2009.

Kipple, B., Coral princess underwater acoustic levels, *Technical report*, Naval Surface Warfare Center, Bremerton Detachment, 2004a.

Kipple, B., Volendam underwater acoustic levels, *Technical report*, Naval Surface Warfare Center, Bremerton Detachment, 2004b.

Kipple, B., and C. Gabriele, Glacier Bay watercraft noise: report to Glacier Bay National Park by the Naval Surface Warfare Cent-Detachment Bremerton, *Technical report nswccd-71-tr-2003/522*, 2003.

Knight, A., Flow noise calculations for extended hydrophones in fluid- and solid-filled towed arrays, *J. Acoust. Soc. Am.*, *100*(1), 245–251, 1996.

Kolmogorov, A., Dissipation of energy in the locally isotropic turbulence, *Dokl. Akad. Nauk. SSSR*, *30*(1), 301–305, 1941.

Kraichnan, R., Pressure field within homogenous anisotropic turbulence, *J. Acoust. Soc. Am.*, *28*(1), 64–72, 1956.

Landau Associates, Preliminary geologic characterization: proposed tidal turbine site Island County, Washington, *Tech. rep.*, Landau Associates, 2011.

Lee, H., and S. Balachandar, Critical shear stress for incipient motion of a particle on a rough bed, *J. Geophys. Res.*, *117*(F01026), 1–19, doi:10.1029/2011JF002208, 2012.

Lee, S., S. Kim, Y. Lee, J. Yoon, and P. Lee, Experiment on effect of screening hydrophone for reduction of flow-induced ambient noise in ocean, *Jpn. J. Appl. Phys.*, *50*(07HG02), 1–2, doi:10.1029/2011JF002208, 2011.

Lighthill, M., On sound generated aerodynamically. I. General theory, *Proc. R. Soc. Lond.*, *211*(1107), 564–587, 1952.

Lighthill, M., On sound generated aerodynamically. II. Turbulence as a source of sound, *Proc. R. Soc. Lond.*, *222*(1148), 1–32, 1954.

Lu, Y., R. Lueck, and D. Huang, Turbulence characteristics in a tidal channel, *J. Phys. Oceanogr.*, *30*, 855–867, doi:10.1175/1520-0485(2000)030¡0855:TCIATC¿2.0.CO;2, 2000.

Lueck, R., and Y. Lu, The logarithmic layer in a tidal channel, *Cont. Shelf Res.*, *17*(14), 1785–1801, doi:10.1016/S0278-4343(97)00049-6, 1997.

Lumley, J. L., and E. A. Terray, Kinematics of turbulence convected by a random wave field, *J. Phys. Oceanogr.*, *13*, 2000–2007, 1983.

Ma, B., J. Nystuen, and R.-C. Lien, Prediction of underwater sound levels from rain and wind, *J. Acoust. Soc. Am.*, *117*(6), 3555–3565, doi:10.1121/1.1910283, 2005.

Mackenzie, K., Reflection of sound from coastal bottoms, *J. Acoust. Soc. Am.*, *32*(2), 221–231, 1960.

Marsh, H., and M. Schulkin, Shallow-water transmission, *J. Acoust. Soc. Am.*, *34*(6), 863–864, 1962.

Mason, T., D. Priestley, and D. Reeve, Monitoring near-shore shingle transport under waves using a passive acoustic technique, *J. Acoust. Soc. Am.*, *122*(2), 737–746, doi: 10.1121/1.2747196, 2007.

McDonald, M. A., J. A. Hildebrand, and S. M. Wiggins, Increases in deep ocean ambient noise in the Northeast Pacific west of San Nicolas Island, California, *J. Acoust. Soc. Am.*, *120*(2), 711–718, 2006.

McDonald, M. A., J. A. Hildebrand, S. M. Wiggins, and D. Ross, A 50 Year comparison of ambient ocean noise near San Clemente Island: A bathymetrically complex coastal region off Southern California, *J. Acoust. Soc. Am.*, *124*(4), 1985–1992, 2008.

McKenna, M., D. Ross, S. Wiggins, and J. Hildebrand, Underwater radiated noise from modern commercial ships, *J. Acoust. Soc. Am.*, *131*(1), 92–103, 2012.

Medwin, H., Speed of sound in water: A simple equation for realistic parameters, *Journal of the Acoustical Society of America*, *58*(6), 1318–1319, 1975.

Medwin, H., *Sounds in the Sea: From Ocean Acoustics to Acoustical Oceanography*, Cambridge University Press, 2005.

Mellen, R., The thermal-noise limit in the detection of underwater acoustic signals, *J. Acoust. Soc. Am.*, *24*(5), 478–480, doi:10.1121/1.1906924, 1952.

Mellinger, D., A comparison of methods for detecting right whale calls, *Can. J. Acoust.*, *32*(2), 55–65, 2004.

Mellinger, D., and C. Clark, Recognizing transient low-frequency whale sounds by spectrogram correlation, *J. Acoust. Soc. Am.*, *107*(6), 3518–3529, 2000.

Miller, M., I. McCave, and P. Komar, Threshold of sediment motion under unidirectional currents, *Sedimentology*, *24*(4), 507–527, doi:10.1111/j.1365-3091.1977.tb00136.x, 1977.

Miller, P., Mixed-directionality of killer whale stereotyped calls: A direction of movement cue?, *Behav. Ecol. Sociobiol.*, *52*(3), 262–270, doi:10.1007/s00265-002-0508-9, 2002.

Miller, P., Diversity of sound pressure levels and estimated active space of resident killer whale vocalizations, *J. Comp. Physio. A*, *192*(5), 449–459, 2006.

Mofjeld, H., and L. Larsen, Tides and tidal currents in the island waters of Western Washington, *Tech. rep.*, NOAA Tech. Memo. ERL PMEL-56 (PB84-237379), Seattle, 52 pp., 1984.

Mori, N., T. Suzuki, and S. Kakuno, Noise of acoustic Doppler velocimeter data in bubbly flows, *J. Eng. Mech.*, *133*(1), 122–125, doi:10.1061/(ASCE)0733-9399(2007)133:1(122), 2007.

Morton, A., and H. Symonds, Displacement of *Orcinus orca* (L.) by high amplitude sound in British Columbia, Canada, *ICES J. Mar. Sci.*, *59*, 71–80, 2002.

National Marine Fisheries Service, Endangered fish and wildlife; notice of intent to prepare an environmental impact statement, Federal Register [Docket No. 05-525, 11 January 2005] 70(7):1871-1875., 2005.

National Marine Fisheries Service, Endangered and threatened species; designation of critical habitat for southern resident killer whales., Federal Register [Docket No. 060228057-6283-02, 29 November 2006] 71(229):69054-69070., 2006.

National Research Council, *Marine Mammals and Low-Frequency Sound.*, National Academy Press, Washington, DC, 2000.

National Research Council, *Ocean Noise and Marine Mammals*, National Academy Press, Washington, DC, 2003.

National Research Council, *Marine Mammal Populations and Ocean Noise: Determining When Ocean Noise Causes Biologically Significant Effects*, National Academy Press, Washington, DC, 2005.

National Research Council, *Assessment of Marine and Hydrokinetic Energy Technology:Interim Letter Report*, The National Academies Press, Washington DC, 2011.

Normandeau Associates, Inc., Effects of noise on fish, fisheries, and invertebrates in the u.s. atlantic and arctic from energy industry sound-generating activities. a literature synthesis for the u.s. dept. of the interior, bureau of ocean energy management. contract no. m11pc00031. 153 pp., *Tech. rep.*, 2012.

Nystuen, J., and H. Selsor, Weather classification using passive acoustic drifters, *J. Atmos. Ocean. Tech.*, *14*, 656–666, doi:10.1175/1520-0426(1997)014¡0656:WCUPAD¿2.0.CO;2, 1997.

Palodichuk, M., M., B. Polagye, and J. Thomson, Resource mapping at tidal energy sites, *J. Ocean. Eng*, *PP*(99), 1, doi:10.1109/JOE.2012.2227578, 2013.

Panton, R., and J. Miller, Resonant frequencies of cylindrical Helmholtz resonators, *J. Acoust. Soc. Am.*, *56*(6, Part II), 1533–1535, 1975.

Polagye, B., and J. Thomson, Admiralty Inlet water quality survey report: April 2009 - February 2010., *Technical report*, Northwest National Marine Renewable Energy Center, University of Washington, Seattle, WA., 2010.

Polagye, B., and J. Thomson, Tidal energy resource characterization: methodology and field study in Admiralty Inlet, Puget Sound, US, *IMechE, Part A: J. Power and Energy*, *227*(3), 352–367, doi:10.1177/0957650912470081, 2013.

Polagye, B., J. Epler, and J. Thomson, Limits to the predictability of tidal current energy, in *MTS/IEEE Oceans 2010, Seattle, WA*, 2010.

Polagye, B., B. Van Cleve, A. Copping, and K. Kirkendall, Environmental effects of tidal en-

ergy development, *Tech. rep.*, U.S. Dept. Commerce, NOAA Tech. Memo. NMFS F/SPO-116, 186 p., 2011.

Polagye, B., C. Bassett, M. Holt, J. Wood, and S. Barr, A framework for detection of tidal turbine sound: A pre-installation case study for Admiralty Inlet, Puget Sound, Washington (USA), *J. Ocean. Eng.*, in revision.

Priestley, M., *Spectral Analysis and Time Series*, 467, 660-661 pp., London: Academic Press, 1981.

Proudman, I., The generation of noise by isotropic turbulence, *Proc. R. Soc. Lond.*, *214*(1), 119–132, 1952.

Readhead, M., Snapping shrimp noise near Gladstone, Queensland, *J. Acoust. Soc. Am.*, *101*(3), 1718–1722, 1997.

Richardson, W. J., C. R. Greene, C. I. Malme, and D. H. Thomson, *Marine Mammals and Noise*, Academic Press, 1995.

Rolland, R., S. Parks, K. Hunt, M. Castellote, P. Corkeron, D. Nowacek, S. Wasser, and S. Kraus, Evidence that ship noise increases stress in right whales, *Proc. R. Soc. B*, *279*(1737), 2363–2368, 2012.

Ross, D., *Mechanics of Underwater Noise*, 47-54 pp., Permagon Press, 1976.

Schewe, G., On the force fluctuations acting on a circular cylinder in crossflow from subcritical up to transcritical Reynolds numbers, *J. Fluid Mech.*, *133*, 265–285 doi:10.1017/S0022112083001,913, 1983.

Schwehr, K., Python software for processing ais data. v0.43., 2010.

Schwendeman, M., J. Thomson, and J. Gemmrich, Observtions of wave breaking in a fetch-limited sea, *J. Phys. Oceanogr.*, in revision.

Scrimger, P., and R. Heitmeyer, Acoustic source-level measurements for a variety of merchant ships, *J. Acoust. Soc. Am.*, *89*(2), 691–699, 1991.

Shields, A., Application of similarity principles and turbulence research to bedload movement, *Translated from Anwendung der Achnichkeits Geschiebebewegung, in: Mitt. Preuss. VersAnst. Wasserb. Schiftb. by W.D. Ott and J.C. von Vcheten. Publ. Calif. Inst. Technol. Hydrodyn. Lab.*, *167*, 36, 1936.

Snohomish PUD, Admiralty Inlet Pilot Tidal Project, FERC project no. 12690, *Tech. rep.*, Public Utility District No. 1 of Snohomish County, 2012.

Southall, B., Shipping noise and marine mammals: a forum for science, management, and technology., *Tech. rep.*, Final Report of the National Oceanic and Atmospheric Administration (NOAA) International Symposium. U.S. NOAA Fisheries, Arlington, Virginia, May 18-19, 2004., 2005.

Southall, B., R. Shusterman, and D. Kastak, Acoustic communication ranges for northern elephant seals (*Mirounga angustirostris*), *Aquatic Mammals*, *29*(2), 202–213, 2003.

Southall, B., et al., Marine mammal noise exposure criteria: Initial scientific recommendations, *Aquatic Mammals*, *33*, 411–521, 2007.

Strasberg, M., Nonacoustic noise interference in measurements of infrasonic ambient noise, *J. Acoust. Soc. Am.*, *66*(5), 1487–1493, doi:10.1121/1.383543, 1979.

Strasberg, M., Hydrodynamic flow noise in hydrophones, in *Adaptive Methods in Underwater Acoustics*, edited by H. G. Urban, NATO ASI Series, pp. 125–143, Springer Netherlands, 1985.

Strasberg, M., Dimensional analysis of windscreen noise, *J. Acoust. Soc. Am.*, *83*(2), 544–548, doi:10.1121/1.396148, 1988.

Szymanski, M., D. Bain, K. Kiehl, S. Pennington, S. Wong, and K. Henry, Killer whale (*Orcinus orca*) hearing: Auditory brainstem response and behavioral audiograms, *J. Acoust. Soc. Am.*, *106*(2), 1134–1141, doi:10.1121/1.427121, 1999.

Taylor, G., The spectrum of turbulence, *Proc. R. Soc. Lond.*, *164*, 476–490, doi:10.1098/rspa.1938.0032, 1938.

Tennekes, H., The logarithmic wind profile, *J. Atmos. Sci.*, *30*, 234–238, doi:10.1175/1520-0469(1973)030¡0234:TLWP¿2.0.CO;2, 1973.

Thompson, R. O., Coherence significance levels, *J. Atmos. Sci.*, *36*, 2020–2021, doi:10.1175/1520-0469(1979)036¡2020:CSL¿2.0.CO;2, 1979.

Thomson, J., B. Polagye, V. Durgesh, and M. Richmond, Measurements of turbulence at two tidal energy sites in Puget Sound, WA (USA), *J. Ocean. Eng.*, *37*(3), 363–374, doi:10.1109/JOE.2012.2191656, 2012.

Thomson, J., L. Kilcher, M. Richmond, J. Talbert, A. deKlerk, B. Polagye, M. Paris, and R. Cienfuegos, Tidal turbulence spectra from a compliant mooring., in *Proceedings of the 1st Marine Energy Technology Symposium, Washington, D.C.*, 2013.

Thorne, P., The measurement of acoustic noise generated by moving artificial sediments, *J. Acoust. Soc. Am.*, *78*(3), 1013–1023, doi:10.1121/1.393018, 1985.

Thorne, P., Laboratory and marine measurements on the acoustic detection of sediment transport, *J. Acoust. Soc. Am.*, *80*(3), 899–910, doi:10.1121/1.393913, 1986a.

Thorne, P., An intercomparison between visual and acoustic detection of seabed gravel movement, *Mar. Geol.*, *72*, 11–31, doi:10.1016/0025-3227(86)90096-4, 1986b.

Thorne, P., Seabed generation of ambient noise, *J. Acoust. Soc. Am.*, *87*(1), 149–153, doi:10.1121/1.399307, 1990.

Thorne, P. D., A. D. Heathershaw, and L. Troiano, Acoustic detection of seabed gravel movement in turbulent tidal currents, *Mar. Geol.*, *54*, M43–M48, 1984.

Thorne, P. D., J. J. Williams, and A. D. Heathershaw, In situ acoustic measurements of marine gravel threshold and transport, *Sedimentology*, *36*, 61–74, doi:10.1111/j.1365-3091.1989.tb00820.x, 1989.

Thorpe, S., *An Introduction to Ocean Turbulence*, Cambridge Univ. Press, 2007.

Trevorrow, M., B. Vasiliev, and S. Vagle, Directionality and maneuvering effects on a surface ship underwater acoustic signature, *J. Acoust. Soc. Am.*, *124*(2), 767–778, 2008.

Trowbridge, J., W. Geyer, M. Bowen, and A. Williams III, Near-bottom turbulence measurements in a partially mixed estuary: Turbulent energy balance, velocity structure, and along-channel momentum balance, *J. Phys. Oceanogr.*, *29*(2), 3056–3072, doi: 10.1175/1520-0485(1999)029¡3056:NBTMIA¿2.0.CO;2, 1999.

Urazghildiiev, I., Acoustic detection of North Atlantic right whale contact calls using the generalized likelihood ratio test, *J. Acoust. Soc. Am.*, *120*(4), 1956–1963, doi: 10.1121/1.2257385, 2006.

Urazghildiiev, I., and C. Clark, Detection performances of experienced human operators compared to a likelihood ratio based detector, *J. Acoust. Soc. Am.*, *122*(1), 200–204, doi:10.1121/1.2735114, 2007.

Urick, R., *Principles of Underwater Sound for Engineers*, 332-334 pp., McGraw-Hill, Inc., 1975.

Veirs, S., and V. Veirs, Average levels and power spectra of ambient sound in the habitat of southern resident orcas, unpublished report to NOAA/NMFS/NWFSC, 2005.

Voglis, G., and J. Cook, A new source of acoustic noise observed in the North Sea, *Ultrasonics*, *8*, 100–101, doi:10.1016/0041-624X(70)90049-1, 1970.

Wahlberg, M., B. Møhl, and P. Telberg Madsen, Estimating source position accuracy of a large-aperture hydrophone array for bioacoustics, *J. Acoust. Soc. Am.*, *109*(1), 397–406, doi:10.1121/1.1329619, 2001.

Webb, S. C., Long-period acoustics and seismic measurements and ocean floor currents, *J. Ocean. Eng.*, *13*(4), 263–270, 1988.

Wentworth, C. K., A scale of grade and class terms for clastic sediments, *J. Geol.*, *30*(5), 377–392, 1922.

Wenz, G., Acoustic ambient noise in the ocean: Spectra and sources, *J. Acoust. Soc. Am.*, *34*(12), 1936–1956, doi:10.1121/1.1909155, 1962.

Whale Museum, Review of historical information and site-specific synthesis, *The Whale Museum, SMRU Ltd., Orca Network*, 2009.

Williams, J., P. Thorne, and A. Heathershaw, Measurements of turbulence in the benthic boundary layer over a gravel bed, *Sedimentology*, *36*, 959–971, doi:10.1111/j.1365-3091.1989.tb01533.x, 1989.

Willis, J., and F. Dietz, Some characteristics of 25-cps shallow-water ambient noise, *J. Acoust. Soc. Am.*, *37*(1), 125–130, doi:10.1121/1.1909289, 1965.

Appendix A

MARINE MAMMAL HEARING

A.1 Species of Concern

Without biological receivers, a study of potential noise impacts from tidal energy development would be unnecessary. The four groups of biological receptors that could potentially be affected by tidal turbine noise in Admiralty Inlet are marine mammals, fish, invertebrates, and diving seabirds. Environmental protections are greatest for the species that are federally listed as threatened or endangered. The following section provides a listing of the marine mammal species that have been reported in the area and what is known about their auditory capabilities. Although there is some concern about the effect of noise on fish, invertebrate and diving seabird species, little is known about their auditory capabilities and their responses to sub-lethal sound [*Normandeau Associates, Inc.*, 2012]. All details regarding the species of concern are drawn from the Federal Energy Regulatory Commission (FERC) final license application for the Admiralty Inlet pilot tidal power project [*Snohomish PUD*, 2012]. These lists, the level of concern about the species, the relative abundance of a species in the study area, and the available audiograms were used to identify the species used in the pre-installation acoustic detection study discussed in Chapter 7 and *Polagye et al.* [in revision].

Marine mammal species use sound for a variety of reasons ranging from maintaining social cohesion to foraging for food. Unique species and suborders use different frequencies to communicate. Pinnipeds (e.g. seals, sea lions), odontocetes (e.g. porpoise, killer whales, dolphins), and mysticetes (e.g. minke, humpback, and gray whales) are all known to occur in the area of the project. Although general patterns exist in each suborder, different species within each suborder communicate at different frequencies. The marine mammals known to occur in the project area, their conservation status if endangered, and the frequency range of their sounds are included in Table A.1. These species cover four marine mammal

Table A.1: Marine mammal species occurring in the project area, conservation status [*Snohomish PUD*, 2012], and the frequencies over which they communicate. All information is referenced from *Richardson et al.* [1995] unless otherwise noted.

Species	Federal Status	Freq. Range (kHz)
Harbor porpoise (*Phocoena phocoena*)[a]	-	0.04 - 12; 110 - 150
Dall's porpoise (*Phocoenoides dalli*) [a]	-	2; 135 - 149
Southern Resident killer whale (*Orcinus orca*) [a,e]	Endangered	0.5 - 25; 30 - 80 [b]
Minke whale (*Balaenoptera acutorostrata*)	-	0.060 - 20
Gray whale (*Eschrichtius robustus*)	-	0.020 - 20
Humpback whale (*Megaptera novaeangliae*)	Endangered	0.025 - 8
California sea lion (*Zalophus californianus*)[c]	-	1 - 8
Harbor seal (*Phoca vitulina*)[c]	-	0.1 - 150
Northern elephant seal (*Mirounga angustirostris*)[c]	-	0.02 - 20 [d]
Steller sea lion (*Eumetopias jubatus*)[c]	-	-

functional groups: low, mid, and high-frequency cetaceans and pinnipeds (in water). The following paragraphs highlight what is known about the hearing and relative presence of these species.

Both harbor porpoise and Dall's porpoise are high-frequency cetaceans that are known to occupy the project area. Of the two species, harbor porpoise are much more abundant

[a]The lowest frequency ranges refer to sounds that are not associated with echolocation. The higher frequency ranges refer to echolocation clicks.

[b]*Au et al.* [2004] describes the echolocation clicks of foraging killer whales.

[c]Pinnipeds have unique thresholds for hearing in air and in water. These frequency ranges refer to the underwater hearing for the species.

[d]*Southall et al.* [2003] suggests these limits as the upper and lower limits of the species auditory filters.

[e]Transient killer whales also transit the site but do not permanently inhabit the area. The table refers to the the conversation status and vocalization characteristics of SRKWs which vocalize more than their transient counterparts.

in the inland waters of the Salish Sea. Studies of echolocation clicks at the proposed tidal energy site report porpoise encounters, a measure of the number of confirmed recorded echolocation clicks in a small spatial area, ranging from 30 to 48 per day from October, 2009 to April, 2010. Land based studies over the same period recorded harbor porpoise at the site 63% of the days and 56% of monitored hours [*Snohomish PUD*, 2012].

Southern Resident killer whales (SRKW) are mid-frequency cetaceans known to occupy the inland waters of the Salish Sea. Of the species in Table A.1, only the SRKW has critical habitat designated in Washington. This designated critical habitat includes the study area [*National Marine Fisheries Service*, 2006]. The resident killer whale populations, unlike their transient counterparts, feed primarily on fish. Given their status as an endangered species and as an iconic species of Pacific Northwest, they are one of the primary species of concern. Their vocal repertoire consists of whistles, stereotyped calls, and echolocation clicks. Whistles and stereotyped calls for social communciation span the frequency range from 1 - 20 kHz [*Ford*, 1991; *Miller*, 2006] where as echolocation clicks used for foraging have a bandwidths that exceed 35 kHz and center frequencies greater than 45 kHz [*Au et al.*, 2004]. The Lombard effect, a vocal compensation involving increases in source levels when vocalizing in noisy environments, has been reported for SRKWs [*Holt et al.*, 2009, 2011]. In another study, sound from acoustic harassment devices at 10 kHz, intended to deter harbor porpoise from salmon farms, resulted in the displacement of a killer whale population until the devices were removed, at which point presence returned to baseline levels [*Morton and Symonds*, 2002]. Transient killer whales also occur in Puget Sound but are typically less vocal than their resident counterparts [*Deecke et al.*, 2005]. Analysis from 2001-2008 estimate that 1,442 individual SRKW animal transits occur annually in Admiralty Inlet [*Whale Museum*, 2009; *Snohomish PUD*, 2012].

Three mysticete species are occasionally reported in Puget Sound although none have an established population. The species are the Minke whale, the gray whale, and the humpback whale, which are all categorized as low-frequency cetaceans. The upper and lower frequencies of associated with mysticete whales span the range from infrasound to 20 kHz. However, the dominant frequencies of the mysticete species occurring in Puget Sound are below a few kilohertz [*Richardson et al.*, 1995]. Despite their rare transits into Puget

Sound, the frequency overlap between mysticete hearing sensitivity and peak spectrum levels expected from tidal turbine noise suggests a higher likelihood of detection than other species if present during turbine operation.

Pinnipeds have an auditory system that allows them to hear in both air and water. With no significant air-side noise expected from tidal turbines, only underwater hearing is important in this context. Air-side vocalizations are common amongst all of the pinniped species occurring in the project area, but relatively little is known about their use of sound underwater [*Richardson et al.*, 1995]. Of the four species occuring in the area, only the Steller sea lion is endangered. There are no dedicated critical habitat areas for pinnipeds in Washington. Steller sea lions are, however, regularly sighted in and around the project area [*Snohomish PUD*, 2012]. Underwater audiograms of harbor seals do show auditory capabilities at the frequencies of tidal turbine sound [*Richardson et al.*, 1995].

The frequency range values presented in Table A.1 highlight the range over which the species are known to communicate. These ranges may not be representative of their true hearing capabilities. Furthermore, mammalian hearing is not uniformly sensitive across the entire audible range for a species. Based on available audiograms *Southall et al.* [2007] proposes a series weighting functions for hearing sensitivity of the different marine mammal function groups. The "M-weighting" functions provide a method for describing the frequency dependence of noise in a manner that is more relevant to the species under consideration and is analogous to a bandpass filter. The frequency dependence of the M-weighting functions for each functional group are described by

$$R(f) = \frac{(f^2 f_h^2)}{(f^2 + f_h^2)(f^2 + f_l^2)}, \tag{A.1}$$

where f is the frequency, f_h is the upper frequency limit for the functional group, and f_l is the lower frequency limit for the functional group. The values from Equation A.1 are converted to the functional group's M-weighting by

$$M(f) = 20 \log 10 \left(\frac{R(f)}{max(R(f))} \right). \tag{A.2}$$

Based on Equations A.1 and A.2 the M-weighting functions for the four functional groups relevant to the project are presented in Figure A.1. The intention of the M-weightings is

to provide a more biologically meaningful measure of sound perceived by mammals as it relates to the potential for injury. Nevertheless, the M-weighting approach has been used in discussions of general ambient noise. *Southall et al.* [2007] also note that the weighting functions are precautionary and, if anything, overestimate that sensitivity of individual animals.

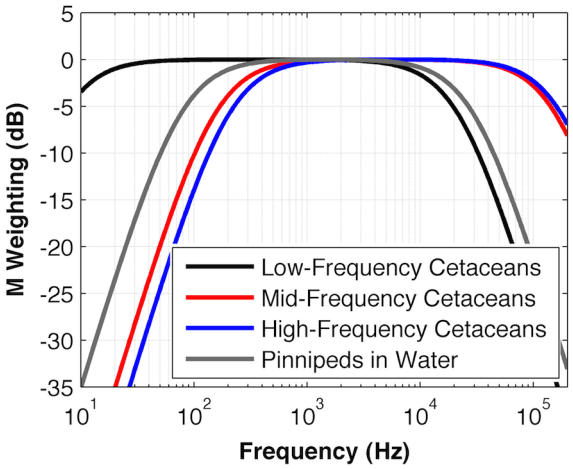

Figure A.1: M-weighting functions for the four marine mammal functional groups occurring in the project area.

The Marine Mammal Protection Act defines two levels of harassment: Levels A and B. Level A harassment constitutes an action that could could or harm an individual or population of marine mammals. Level B harassment includes actions which could disturb a marine mammals and temporary changes in behavior patterns. Under current guidelines, 180 dB re 1μPa is considered Level A harassment. Type B harassment is defined as 160 dB re 1μPa for pulsed sources and 120 dB re 1μPa continuous sources [*National Marine Fisheries Service*, 2005]. Such exposure guidelines do not take into account that that behavioral response to sound is also dependent on variables such as the previous experiences with a similar sound source, individual hearing sensitivity, and activity states [*Southall et al.*, 2007; *Ellison et al.*, 2011].

Appendix B

FLOW SHIELD

B.1 Introduction

Flow-noise, or pseudosound, is not a true ambient noise signal and should not be included in ambient noise statistics. Chapter 6 demonstrates that in energetic environments flow-noise can exceed ambient noise levels by up to 50 dB at low frequencies making ambient noise measurements difficult. To properly quantify ambient noise during periods of strong currents three sets of techniques can be applied. These methods includes the use of signal processing techniques, the application of mechanical devices to damp out turbulent pressure fluctuations sensed by transducers, and drifting recordings, which reduce flow-noise by moving with the mean current.

By applying cross-spectral methods, the magnitude of the non-random noise, indicative of propagating noise rather than flow-noise, can be identified and used to remove contamination by flow-noise. *Buck and Greene* [1980] and *Chung* [1977] discuss the application of such techniques for systems containing two and three transducers respectively. *Chung* [1977] notes that the application of cross-spectral methods for reducing flow-noise requires that flow-noise at the transducers must be statistically independent. The three-transducer method makes use of coherence functions for the combinations of hydrophones to identify correlations between propagating sound waves. In theory, this method can completely remove Gaussian noise, but in practice *Chung* [1977] reported limits in the reduction of flow-noise of between 10-15 dB due to the experimental apparatus and numerical errors. The two-hydrophone method discussed by *Buck and Greene* [1980] used the power spectra for the two transducers and the cross-correlation between the receiver signals to calculate the intensity of ambient noise signals. Although such techniques have been studied for removing flow-noise, the fact that pseudosound may exceed ambient noise levels by more than 30 dB with coherence well below significant levels, may limit the applicability of these

methods to remove flow-noise on their own.

Flow shields, analogous to wind screens used on microphones, are a mechanical means of reducing turbulent pressure fluctuations. In the seismic surveying industry, navies, and increasingly biological applications, towed arrays of hydrophones within elastic, fluid-filled are used to reduce the effects of flow-noise [*Knight*, 1996; *Gauss et al.*, 2009]. These filled elastomeric tubes result in pressure fluctuations from the boundary layer turbulence on the outer surface rather than the transducers, effectively reducing the flow-noise. Similar devices can be created for different transducer and transducer array geometries but were not considered in this study and it is unclear how effective the application of similar tubes would be in smaller single hydrophone applications in highly turbulent environments. It should be noted that any attempt to reduce turbulent pressure fluctuations that results in correlated flow-noise signals would reduce the effectiveness of digital signal processing techniques to reduce flow-noise measurements.

In order to study the feasibility of designing mechanical devices to reduce flow-noise in highly energetic environments, a compact flow shield, analogous to a windscreen for microphones, was designed for the hydrophone. The flow shield was similar to the device used in *Lee et al.* [2011] but the results are reported over a larger range of frequencies and currently velocities. The flow shield was deployed on a tripod in Admiralty Inlet, Puget Sound. As the following sections demonstrate, the flow shield reduced flow-noise by up to 30 dB during peak currents and did not result in any attenuation of ambient noise signals at any frequencies below 30 kHz. In addition to highlighting the results of the flow shield, this section also addresses methods of identifying flow-noise.

B.2 Methods

B.2.1 Hydrophone Data

The August 18 to November 8, 2010 experiment was carried to both analyze ambient noise and to investigate the coherence ($f < 1$ kHz) to identify the frequencies at which flow-noise masks propagating ambient noise. Two Loggerhead Instruments systems were deployed 6 inches apart and 1 meter above the seabed with the duty cycling described in Chapter 4.

Due to the interest in using the data to analyze coherence, the instruments needed to be synchronized in a way that could account for potential clock drift and time lags between the acquisition of the near-synchronous recordings. While synchronous recording would be preferred, the Loggerhead systems can not be deployed in this manner. To synchronize the time series, the raw time series data was digitally high pass filtered with a cut-off frequency 1 kHz to remove the portion of the frequency affected by flow-noise (which should be uncorrelated). A cross-correlation was carried out on the filtered signals from co-temporal measurements. The maximum value of the cross-correlation was found and used to identify the time lag between the recordings. Throughout the deployment, the time lag between the two signals remained constant suggesting the preprocessing algorithm properly identified the time lag. Once the recordings were synchronized the acoustics data were processed using standard signal processing techniques highlighted in Chapter 6. Based on the processing techniques used there were 45 degrees of freedom. The 95% confidence level was 0.07. Two Loggerhead DSG systems were also deployed from February 11-21, 2011. The sampling and processing for these data are described in Chapters 4 and 5.

B.2.2 Hydrophone Shield

The flow shield, analogous to wind screens used on microphones, was intended to operate by damping out turbulent pressure fluctuations. An ideal flow shield for underwater applications is one that effectively damps out turbulent pressure fluctuations while not attenuating propagating noise at any frequencies measured by the hydrophone contained within the flow shield. The flow shield (Fig. B.1) constructed for field deployments consisted of three primary features: two washer-shaped end caps (1.25 cm and 3.75 cm thick) cut from sheets of Delrin®, a rigid case of made from a Polypropylene mesh, and low density, 10 pore-per-inch foam. The thick end cap forms the open end of the shield while the thinner end cap was attached to the end of the shield aligned with the hydrophone pressure case. The mesh, bent around the end caps, formed the inner and outer walls of the annulus. The gap between the inner and outer mesh was filled with the foam. The outer wall extended 25 cm beyond one end of the annulus such that the flow shield could be attached to the

pressure case containing the data acquisition system and batteries. To prevent failure associated with corrosion of metallic hardware, the final construction was held together using Delrin®hardware mounted through the end caps.

B.2.3 Current Measurements

Figure B.1: A hydrophone with a flow shield prepared for deployment.

Velocity measurements were obtained in order to aid in the interpretation of acoustic data. The measurements of near-bed currents during the August to November, 2010 and February, 2011 deployments are described in Chapter 4.

B.3 Results

The results obtained from the study of flow-noise and flow shield are presented in the following sections. First, current velocity and acoustic measurements from an unshielded hydrophone are used to demonstrate the intensity of recorded flow-noise levels and their dependence on current. Chapter 6 includes a discussion of flow-noise noise developed and applied in both Admiralty Inlet and the Chacao Channel, Chile

Notably, peak currents and turbulent kinetic energy dissipation at the Chilean site exceed those in Admiralty Inlet [*Thomson et al.*, 2012; *Thomson et al.*, 2013]. Based on signal processing techniques, the range of frequencies over which flow-noise is an important noise source are identified. The decreases in flow-noise by the flow shield are determined using the co-temporal shielded and unshielded hydrophone recordings.

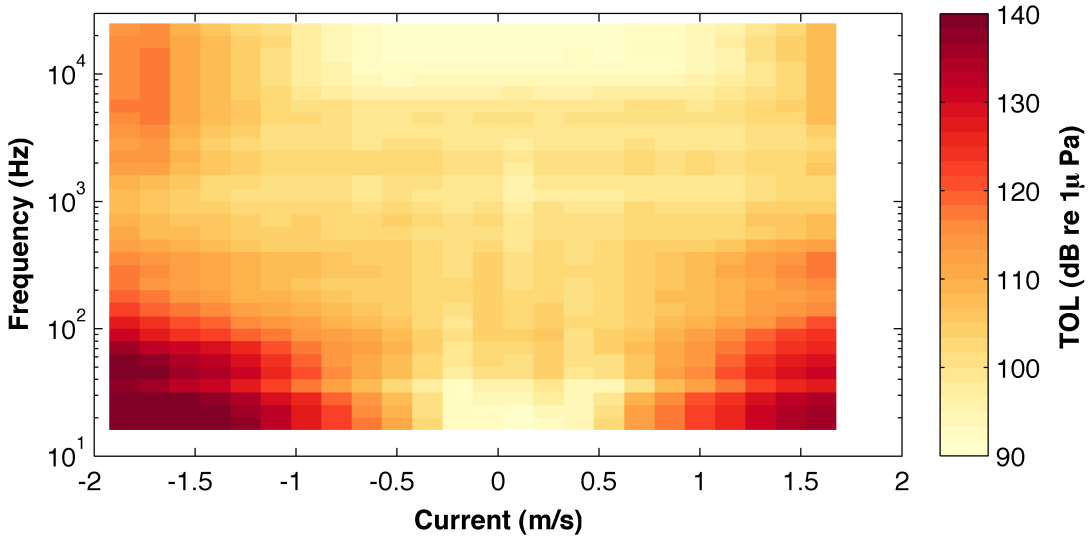

Figure B.2: One third-octave band SPLs versus velocity where the color presents the mean TOL for each current bin (0.15 m/s). Increases in currents result in increased mean ambient noise levels in one-third octave bands. Increases at frequencies greater than 1 kHz are a result of noise from sediment transport.

B.3.1 Measurements of Flow-Noise

Under slack tide conditions variability in ambient noise levels at the site is dominated by vessel noise (Chapter 4). As current velocity increases the lowest levels of ambient noise associated with periods of no vessel traffic are no longer recorded. This pattern of increasing noise levels begins at the lowest recorded frequencies and affects higher frequencies with stronger currents. Accompanying the upward shift in frequencies at which flow-noise is important are increased noise levels. The pattern of increasing noise levels and frequencies over which they occur is included in Figure B.2. Results are presented based on velocity bin averages (0.15 m/s bins) of currents measured 1.05 meters from the seabed. Noise levels are calculated in one-third octave bands with center frequencies from 16 Hz to 25 kHz.

Figure B.2 shows that the mean ambient noise conditions at the site are lowest during slack tides, especially at low frequencies. When currents exceed approximately 0.4 m/s, moderate increases in TOLs begin at 16 Hz. At peak currents, increases in TOLs are noted across all frequencies bands. Notably, from 1 to 2 kHz increases in noise levels are the

lowest. These frequencies fall in the range in which flow-noise and sediment-generated noise do not significantly affect noise levels. Above 1 kHz, increased noise levels are attributed to noise from sediment transport (Ch. 5). Below 1 kHz these increases are related to the measurement of turbulent pressure fluctuations as described in detail in Chapter 6.

The dependence of noise levels on current is not by itself indicative of masking by flow-noise (e.g., in theory, there could be a low-frequency process that produces propagating sound). Unlike other propagating noise source, turbulence is stochastic and non-radiated pressure fluctuations are not correlated at small scales. Therefore data analysis techniques can be used to verify the flow-noise hypothesis. For two hydrophones placed near each other, mean-squared coherence should approach unity for propagating noise and decrease to zero as the correlating propagating noise is masked by flow-noise. Two spectrograms of co-temporal measurements made by two hydrophones and a time series of the near-bed currents are included in Figure B.3. As the results demonstrate, the acoustic spectra are in agreement regardless of the current.

Figure B.4 includes the time series from first inset in Figure B.3 and a time series of the mean-squared coherence for the same period. Under low current conditions the coherence of the signals approaches unity across all frequencies included in the figure. However, just as sound levels increase with stronger currents, the coherence levels rapidly decrease to zero. These decreases begin at low frequencies and shift to higher frequencies until coherence levels are insignificant at frequencies that exceed a few hundred Hertz. Such significant decreases in correlation over distances that are much smaller one acoustic wavelength are representative of random processes and suggest flow-noise to be the source of the noise increases.

As shown in Figure B.4, during slack tides γ^2 is nearly unity at low frequencies. To better quantify the upper limit of frequencies at which masking by flow-noise occurs additional processing of the coherence spectra was performed. An arbitrary γ^2 value of 0.95, a value well above the 95% significance level, was chosen as representative of conditions at which flow-noise was no longer masking ambient noise. The lowest frequency at which this mean-squared coherence are recorded and a time series of currents for August 22, 2010 are included in Figure B.5. Figure B.4 also shows that below a critical threshold γ^2 values rapidly

decrease to zero. As a result, the high coherence threshold of 0.95 has relatively little impact on these results. This analysis suggests that flow-noise at the site can mask ambient noise well above 100 Hz, although the effect is most significant below 100 Hz.

B.3.2 Shielded Hydrophone

The effectiveness of the flow-shield is determined by comparing shielded and unshielded hydrophone data from the February 2011 deployment. Figure B.6a includes two spectra

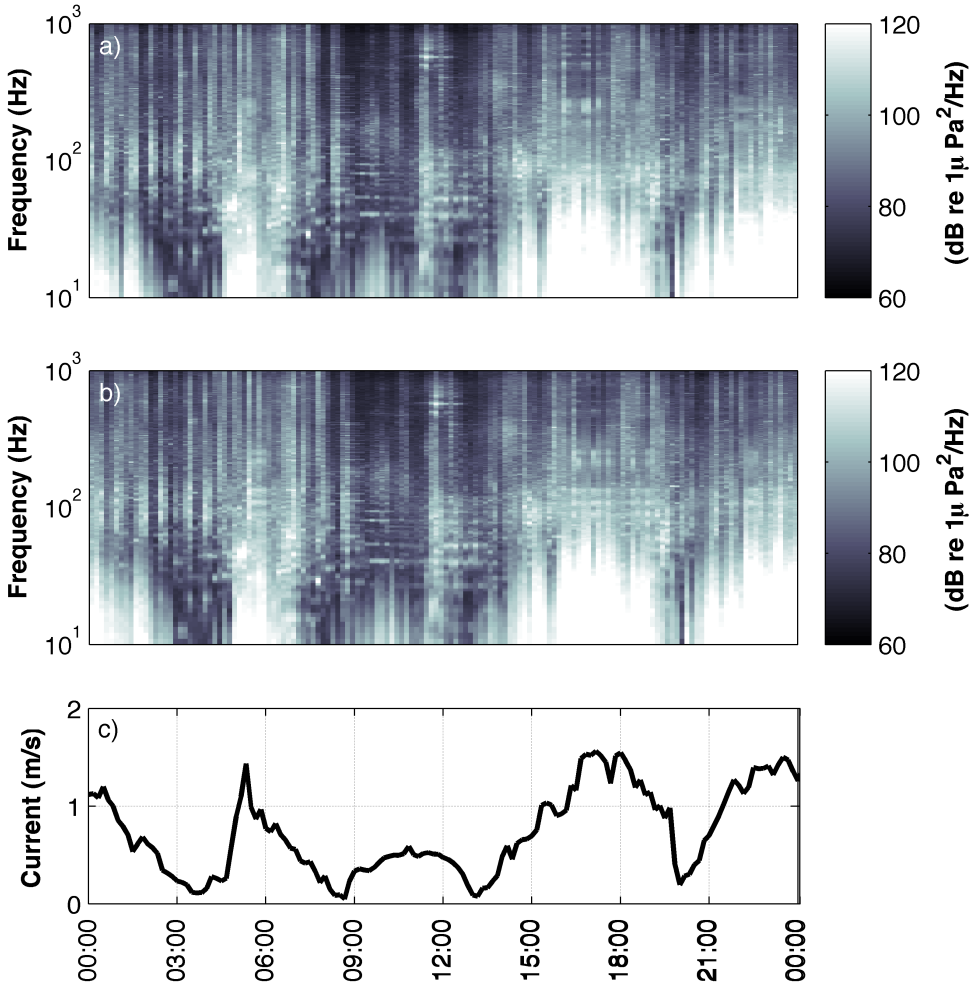

Figure B.3: Spectrograms and near-bed current velocity for August 22, 2010. Insets (a) and (b) show co-temporal measurements from the two co-deployed hydrophones. c). Time series of near-bed current velocity.

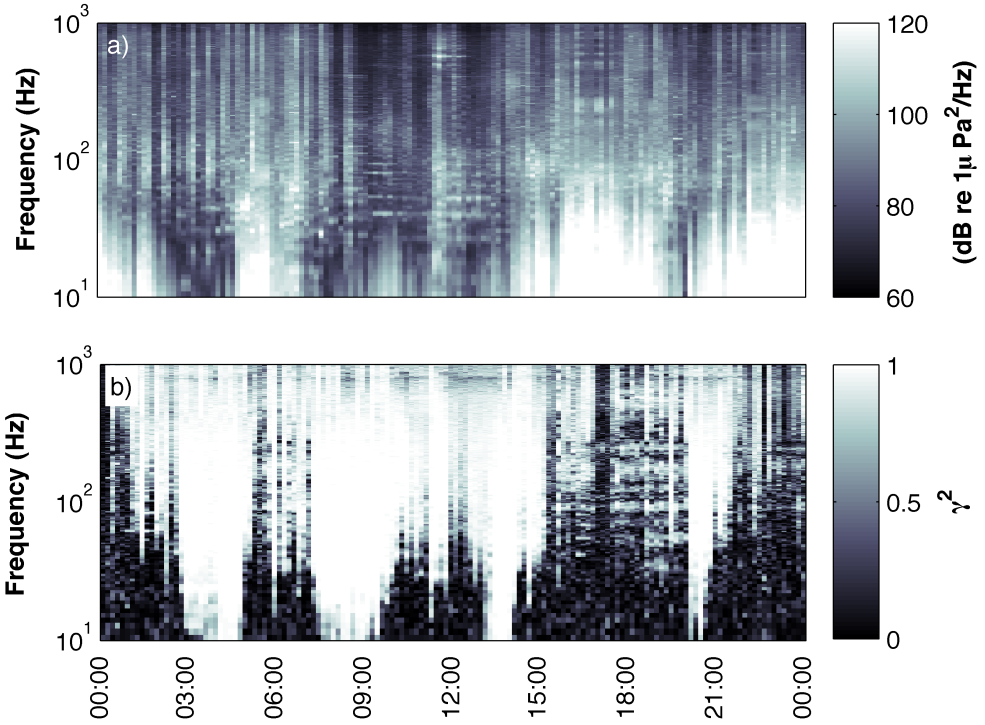

Figure B.4: Spectrogram and coherence time series for August 22, 2010. a) Spectrogram for one hydrophone (top inset Fig. B.3). b). Mean-square coherence time series for the same period.

obtained during slack tide conditions. Below 1 kHz the resulting acoustic spectra are well within the 95% confidence intervals associated with the processing techniques. Above 1 kHz agreement is generally good between the spectra. The small differences may also be attributed, in part, to misalignments ($<$ 3 seconds or 30% of the recording length) in timestamps between the recordings.

The low current results demonstrate that during under weak currents the shielded and unshielded hydrophones produce similar acoustic spectra. Therefore, during periods of strong currents, any differences between acoustic spectra should be attributed to reductions in flow-noise by the shield. Figures B.6b and B.6c include spectra from both hydrophones recorded during a moderate current (0.5 m/s) and a strong current (1.2 m/s). During the moderate current, the acoustic spectra agree above 40 Hz. Below 40 Hz the spectrum from

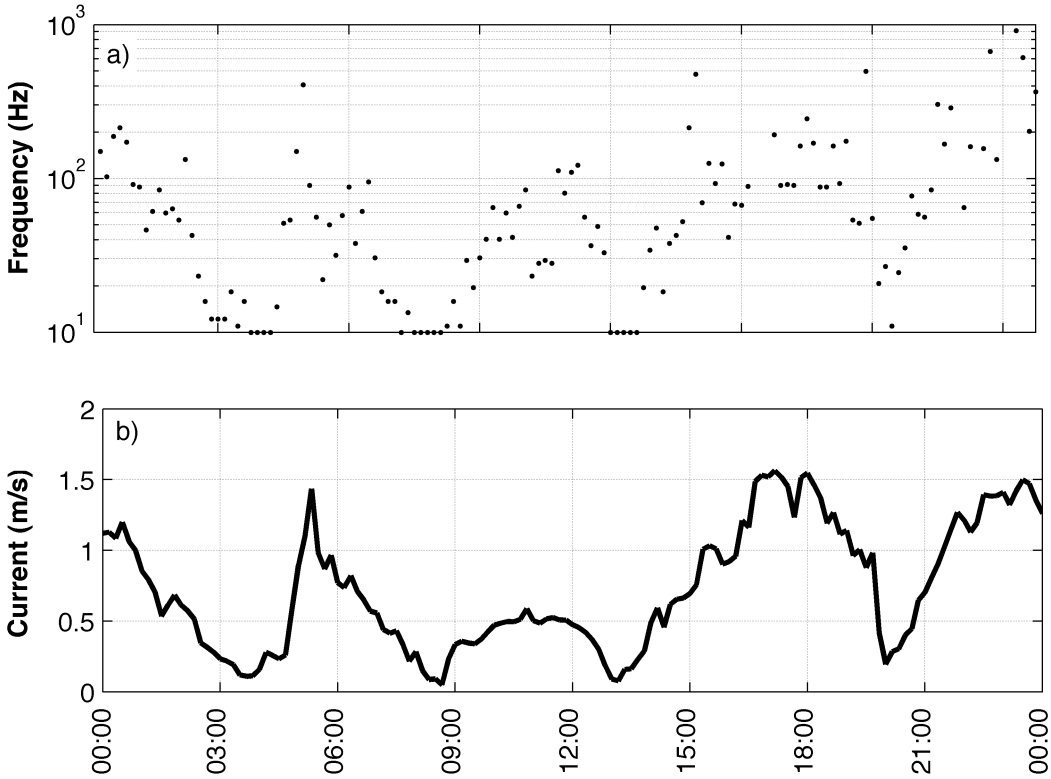

Figure B.5: a) August 22, 2010 time series of lowest frequencies at which γ^2 exceeds 0.95. b). Time series of near bed currents for the same period. Although currents are not particularly strong, flow-noise can mask ambient noise at frequencies well above 100 Hz despite high ambient noise levels at the site.

unshielded hydrophone is typical of flow-noise. By contrast, the shielded hydrophone shows slight decreases in noise with decreasing frequency suggesting that the flow-noise at these currents is mostly damped by the flow shield.

In the case of the strong currents, both spectra show the spectral characteristics consistent with flow-noise; however, the unshielded hydrophone results in much higher spectrum levels than the shielded hydrophone below 300 Hz. At 20 Hz, the difference below the two hydrophones is over 30 dB when unshielded spectrum levels exceeding 130 dB. These results suggest that flow shield functions as an attenuator of turbulent pressure fluctuations. The broadband sound pressure level (20 Hz - 30 kHz) is indicative of the extent to which the flow attenuates flow-noise. Figure B.7 includes a time series of the broadband sound pressure

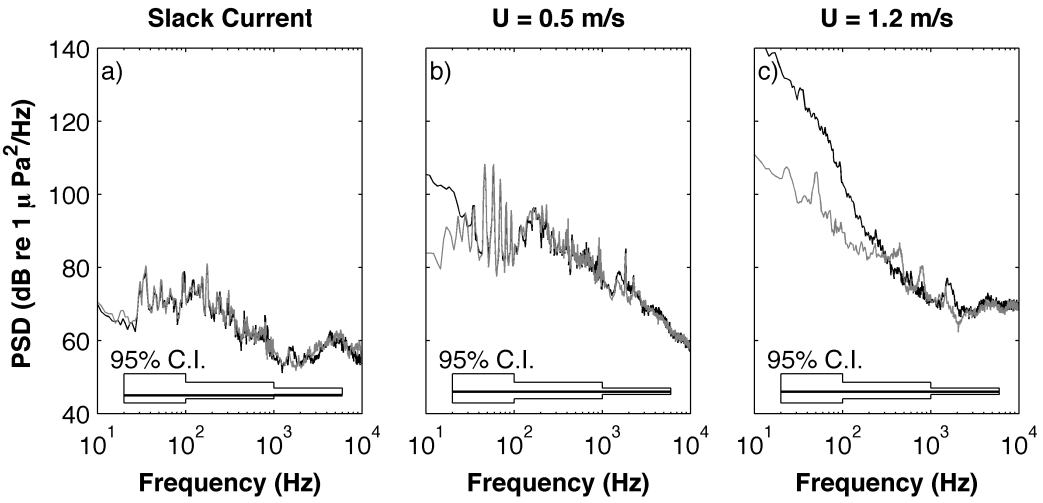

Figure B.6: A comparison of shielded and unshielded hydrophone data for different near-bed current velocities. a) Slack current. b) 0.5 m/s. c) 1.2 m/s. In (b) and (c) the lower spectrum levels at low frequency show that the flow shield attenuates flow-noise.

levels from both hydrophones and the near-bed currents. During the low current periods, the shielded and unshielded hydrophones are indistinguishable regardless of ambient noise conditions. Similarly, during moderate to strong currents the hydrophones show agreement when very noisy signals ($>$ 135 dB re 1μPa associated with vessel traffic are present; peaks near 20:00 and 23:00). The overall difference between the two hydrophones increases with current velocity unless vessel noise is significant. The differences in broadband SPLs exceed 20 dB during peak currents.

A spectrogram of the unshielded and shielded hydrophones, a time series of the differences between the spectra, and the currents for the same data included in the plot of the broadband data (Fig. B.7) is included in Figure B.8. During weak currents, differences between the spectra are not statistically significant in most measurements. During strong currents the difference between the spectra is indicative of the effectiveness of the flow shield. Although flow-noise is not entirely mitigated by the flow shield, it is reduced flow-noise by up to 30 dB. Furthermore, by damping out flow-noise at currents in excess of 0.5 m/s the flow shield would be effectively remove flow-noise in most ocean environments.

While low frequency noise from flow-noise is damped out below about 0.5 m/s, above

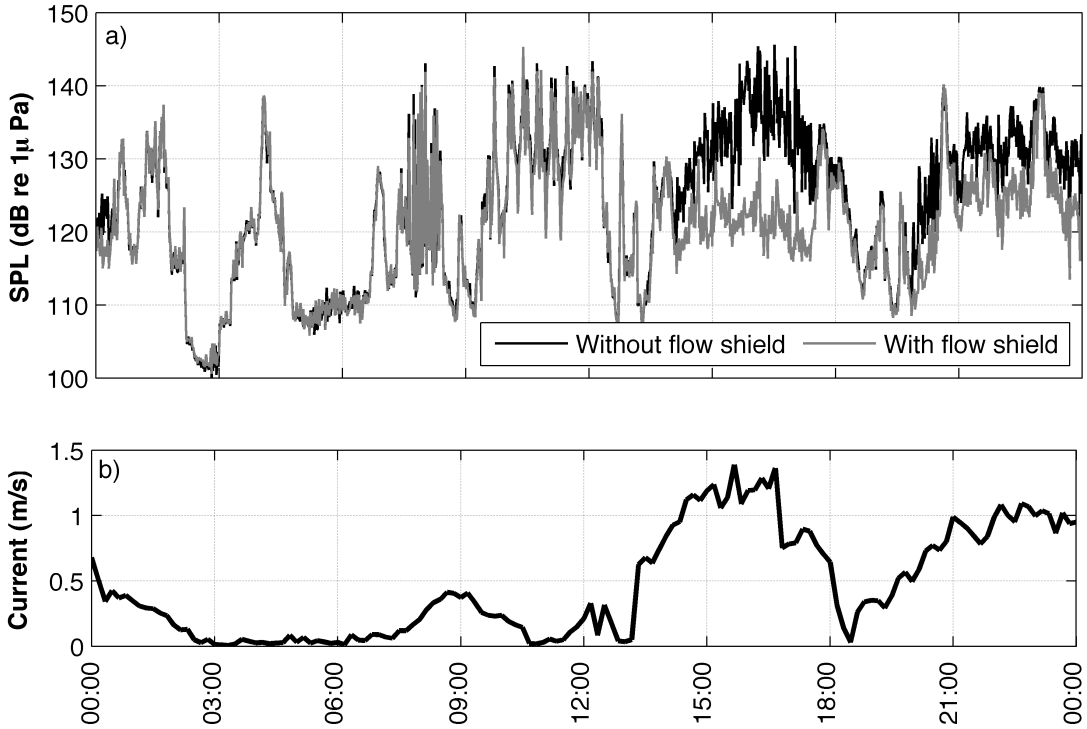

Figure B.7: Data from February 13, 2011. a) Time series of broadband sound pressure levels (0.02-30 kHz) for shielded and unshielded hydrophones. b) Time series of currents 1.05 m from the seabed. The broadband sound pressure levels agree during weak currents but that the shielded hydrophone records significantly lower ambient noise levels during strong tides by reducing flow-noise.

this threshold there are a number of frequencies at which the sound intensity measured by the shielded hydrophone sometimes exceed the unshielded hydrophone. These center frequencies of these differences are approximately 200 Hz, 400 Hz, and 800 Hz. The average difference between the hydrophones is less than 4 dB, but the difference is, at times, up to 10 dB. Good agreement between the hydrophones under low-current conditions suggests that the differences are related to the current velocities. Three hypotheses for the disagreement between the hydrophones are noise resulting for vortex shedding from the flow shield, acoustic resonance resulting from the geometry of the flow shield, and vibrations due the geometry and material properties of the flow shield.

As a fluid flows passed a blunt body an alternating series of vortices are shed from the downstream side of the body. A series of pressure fluctuations are also associated with the with the velocity fluctuations. The frequency of vortex shedding is related to the Strouhal number (St),

$$St = \frac{fd}{|\overline{u}|}, \tag{B.1}$$

where f is the frequency of vortex shedding, d is the diameter of the object from which vortices are shed, and $\overline{u}$ is the magnitude of the current velocity. Over a large range of Reynolds numbers the Strouhal number is approximately 0.2 [*Schewe*, 1983]. By solving the Strouhal number for the flow shield geometry over the range of near bed currents, the upper frequency limit for vortex shedding from the flow shield is 4 Hz. The same solution for the hydrophone ($d = 1.9\ cm$) yields an upper limit of 25 Hz. The upper frequency limit of vortex shedding for the hydrophone is an order of magnitude lower than the spectral peaks of concern and it is unlikely that the spectral peaks are a result of vortex shedding.

A second possible explanation for the disagreement between the shielded and unshielded hydrophones is that the shield acts as a Helmholtz resonator. In a Helmholtz resonator, external forcing increases the pressure in the cavity. The higher pressure within the cavity then forces the fluid to oscillate out of and back into the cavity. The frequency of sound created by this process is a function of the geometry of the cavity and the properties of the fluid. In the classical Helmholtz resonator, the solution for the fundamental frequency, or the "Helmholtz" frequency, and the harmonics is described by

$$\frac{l'A}{LS}kL = cot(kL), \tag{B.2}$$

where l' is the effective length of the orifice, A is the tube area, L is the total length, S is the orifice area, and k is the wavenumber. The effective length term accounts for end effects near the orifice where $l' = l + \Delta_o + \Delta_i$, l is the length of the orifice, and Δ_o and Δ_i are the correction factors for the inner and outer ends of the orifices. Because the orifice and inner radius of the flow shield are the same size only the outer correction factor is needed. The outer correction is given by

$$\Delta_o = \frac{8r_o}{3\pi}, \tag{B.3}$$

where r_o is the radius of the orifice [*Panton and Miller*, 1975]. By applying the geometry of the flow shield the classical solution for the Helmholtz resonator is obtained. The theoretical Helmholtz frequency the geometry, assuming rigid walls, is 2.7 kHz with a 5.5 kHz separation between standing wave modes. The fundamental frequency of the Helmholtz resonator solution is an order of magnitude above the disagreement between the hydrophones. Thus, the difference is not likely explained by acoustic resonance. This can be further justified based on the fact that the walls of the flow shield are not rigid. To act as a Helmholtz resonator the walls of the flow shield would need to be rigid enough to support pressure differences while the end cannot. In the case of the hydrophone, all exposed surfaces are constructed of the same materials. Given the disagreement between the observations and Helmholtz resonator solution, it is unlikely that acoustic resonance is responsible for the differences.

A third possible explanation for the disagreement between the hydrophones is that the vibrations of the flow shield at its natural frequency are the source of the noise. In order to investigate this possibility a complex model that couples the dynamic behavior of the flow shield to forces induced by currents and turbulence must be developed. A model was not developed for this study but future work could investigate this question in more detail.

B.4 Discussion

The flow shield developed for these studies significantly reduces the impact of turbulent pressure fluctuations on measured ambient noise spectra without significantly attenuating propagating ambient noise signals in the below 30 kHz. If the flow shield had trapped a significant number of air bubbles in the low-density foam, the performance of the shields could have been compromised. It is possible that in the case of deployments in less energetic environments, trapped bubbles could result in increased attenuation due to air bubbles. Tests have not been conducted to test this hypothesis.

At a limited number of frequencies the shielded hydrophone sometimes exceeded ambient noise levels measured by the unshielded hydrophone during periods of strong currents. Three possible explanations for the discrepancy were investigated: vortex shedding, structural vibrations associated with the excitation of the flow shield by the current, and the

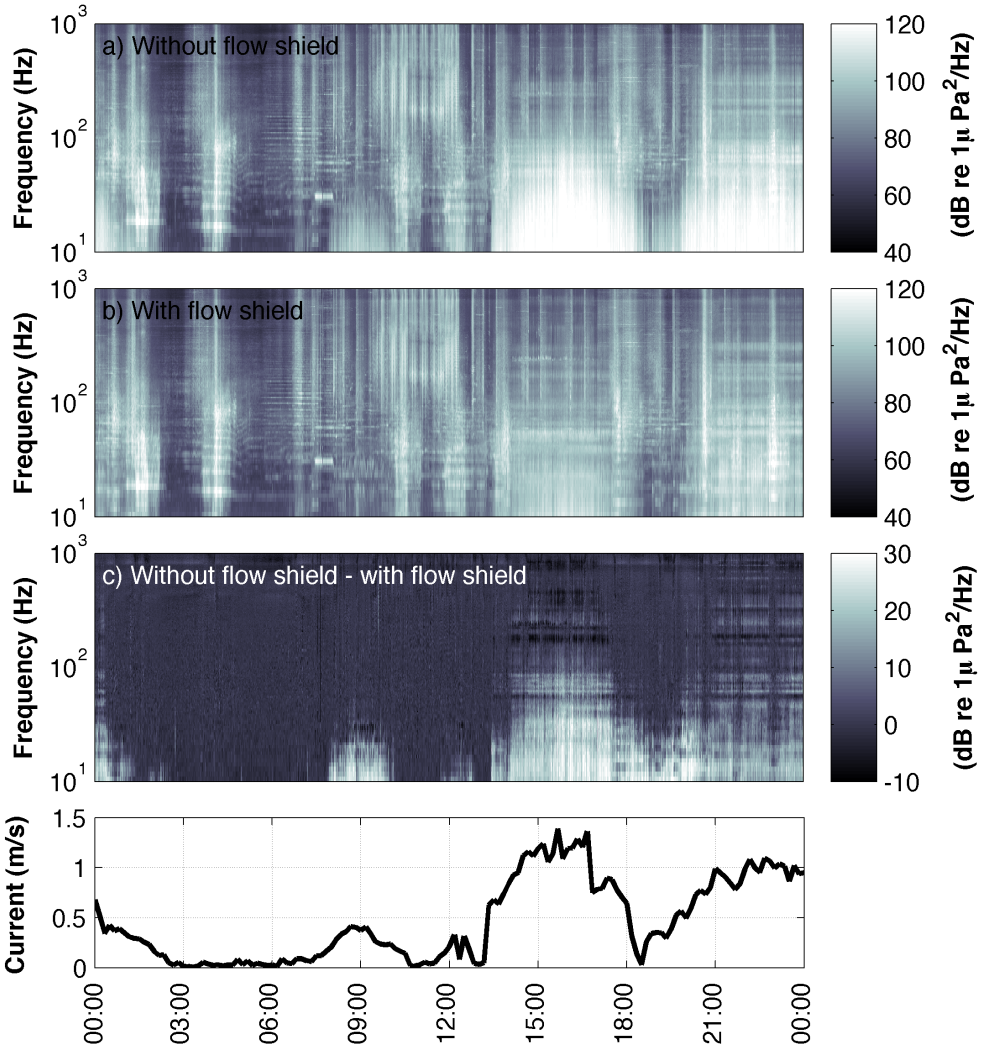

Figure B.8: Data from February 13, 2011. a). Spectrogram of hydrophone without a flow shield. b). Spectrogram of hydrophone with a flow shield. c) Difference between unshielded and shielded hydrophones. d). Time series of near-bed currents.

possibility of the shield acting as a Helmholtz resonator. None of these solutions yielded results suggesting it was the source of the discrepancy. As a result, if a similar method is to be employed in the future, the acoustic and structural resonance of a shield design should be considered. One final possibility is a difference self-noise from some component of the tripod. Special care should be given to removing any source of self-noise.

Over a series of three-month deployments, no significant biofouling was recorded on the flow shields. However, the open cell foam did trap a number of juvenile krill (*Euphausia pacifica*). Due to the small number and size of the krill relative size to the acoustic wavelengths under consideration, this alternative type of biofouling is not expected to have a significant attenuation of the flow shield. Given the sound speed and density of krill, which are similar to those of water [*Greenlaw*, 1979], krill scatter little energy at the frequencies under consideration.

To ensure proper quantification of ambient noise levels during measurements of tidal turbines, a combination of mechanical flow-noise reduction techniques and signal processing techniques is recommended for future study. Although the potential for fluid-filled elastic bodies to reduce flow-noise in highly turbulent environments is unclear, this approach may also warrant further consideration.

B.5 Conclusions

Flow-noise is likely to be a significant problem for stationary acoustic measurement platforms at sites suitable for tidal energy development. Measurements of ambient noise across all stages of the tide demonstrate that flow-noise can mask even very noisy sources including large commercial shipping vessels at a range of less than 2 km. During strong currents, flow-noise results in increased spectrum levels at frequencies up to 500 Hz with the most significant increases occurring below 100 Hz. Flow-noise was identified as the source of these increases by documenting insignificant coherence levels due to the stochastic nature of turbulence. Given that flow-noise is not a propagating noise source, it should not be included in an analysis of ambient noise and steps should be taken to reduce its impact on noise measurements. Furthermore, reducing flow-noise will be critical to the quantification of noise from tidal turbines.

To reduce measured flow-noise levels a flow-shield was constructed from a low solidity polymer mesh annulus filled with 1 inch think, 10-ppi foam. During low current periods ($\overline{u}$ <0.4 m/s) ambient noise levels obtained using a shielded and an unshielded hydrophone were in agreement across all frequencies included in the study (20 Hz - 30 kHz). When currents exceeded 0.4 m/s the shielded hydrophone resulted in lower ambient noise levels at frequencies affected by turbulent pressure fluctuations. During the strongest currents these reductions in spectrum levels exceeded 20 dB at 20 Hz. At a number of frequencies the shielded hydrophone regularly resulted in higher levels of ambient noise. Although the source of the discrepancy was not identified, it is not attributed to vortex shedding or the flow shield acting as a Helmholtz resonator. The proper implementation of a system to reduce flow-noise should consist of a mechanical device to reduce the impact of turbulent pressure fluctuations on noise measurements, while digital signal processing techniques can be used further reduce the received signals to only the propagating sound.

Appendix C

TRANSMISSION LOSS MODEL COMPARISON

C.1 Introduction

Chapters 7 and 8 both utilized simple sound propagation models in detection range analysis and chapter 4 utilized a simple sound propagation model to calculate transmission losses from vessels. In all of these cases, the models were used instead of range-dependent numerical modeling techniques due to their simplicity and transparency. In Chapter 4, a comparison was made between the Range-Dependent Parabolic Equation model [*Collins*, 1993] and single parameter model, sometimes referred to as "practical spreading." For the three modeled frequencies (50 Hz, 100 Hz, and 250 Hz), the models generally agreed well. Here, a comparison of the four models focuses on sound at 1.1 kHz, the lowest frequency included in the S1 vocalization in Chapter 8. In addition, a low-frequency (40 Hz) example is provided for one of the profiles in order to demonstrate the differences in transmission loss patterns attributable to the acoustic wavelength relative to the water depth.

Three range-dependent bathymetric profiles were identified for modeling. All three profiles begin at a point Admiralty Inlet and end at the site of the proposed tidal power project. These bathymetric profiles were also used in the vessel noise chapter (Sec. 4.6). With the exception of profiles near the shores, these profiles are representative of the variability across the sill in Admiralty Inlet. A map of Admiralty Inlet and the bathymetric profiles used in this analysis are included in Figure C.1. For the three profiles, a source depth of 10 meters and a source frequency

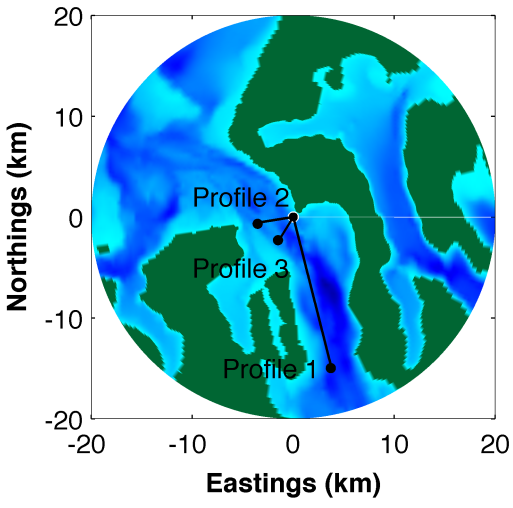

Figure C.1: A map of the bathymetric profiles for model comparison.

of 1.1 kHz were used. An additional simulation using one of the three bathymetric profiles was used with a source depth of 10 meters and a source frequency of 40 Hz in order to demonstrate the differences when the acoustic wavelength is a significant fraction of the depth of the water column. The depths at the start of the three bathymetric profiles were 112 m, 71 m, and 67 m, respectively. The following sections summarize the four models, provide a comparison between the output from the models, and comment on the differences between the models and how these outputs affect the interpretation of the results in particular applications.

C.2 Models

C.2.1 Cylindrical and Spherical Spreading

The first model, which was used to estimate in the detection range of operating tidal turbines in Chapters 7, combines the spherical and cylindrical spreading regimes to estimate transmission losses. The two regimes for spreading in the model are described by

$$TL = \begin{cases} 20\log_{10}(R) + \alpha(f)R, & \text{if} \quad R \leq R_s \\ 10\log_{10}(RR_s) + \alpha(f)R, & \text{if} \quad R > R_s, \end{cases} \tag{C.1}$$

where R is the total distance from the source, R_s is the distance between the source and the transition from spherical to cylindrical spreading, and α is the frequency-dependent attenuation coefficient. In all four other models the attenuation term is calculated according to *Francois and Garrison* [1982a, b]. For each bathymetric profile the transition to cylindrical spreading is modeled at one-half of the source depth.

C.2.2 Simplified Spreading

In the model described by Equation C.1, the spherical and cylindrical spreading regimes are modeled directly. An alternative to this approach, sometimes called "practical spreading," is described by

$$TL = 15\log_{10}(R) + \alpha(f)R, \tag{C.2}$$

where R is the distance between the source and the receiver and α is the frequency-dependent attenuation coefficient. This model further simplifies the combined spreading model by

assuming that the arithmetic mean of the two spreading regimes can be used to model transmission losses. While this approach has limited physical basis, it is sometimes effective at parameterizing propagation physics.

C.2.3 Marsh and Schulkin (1962)

Marsh and Schulkin [1962] is a more complicated, semi-empirical model, that expands on the spreading regimes described in Equation C.1. The model includes three transmission loss regimes: a spherical spreading regimes including a $20log_{10}(R)$ term, a mode stripping regime using a $15log_{10}(R)$ term, and a cylindrical spreading regimes using $10log_{10}(R)$ term. The transmission loss regime is determined by the distance from the source and the skip distance, $H = \left[\frac{1}{8}(R+L)^{\frac{1}{2}}\right]$, where R is the range to the source and L is the depth of the thermocline. The skip distance is the distance between successive interactions between a propagating wave and the seabed. H is calculated in kiloyards where R and L are in feet. The model is described by

$$TL = \begin{cases} 20\log_{10}(R) + \alpha R + 60 - k_L, & \text{if} \quad R < H \\ 15\log_{10}(R) + \alpha R + 60 + a_T(R/H - 1) & \\ \qquad + 5\log_{10}(H) + 60 - k_L, & \text{if} \quad H \leq R \leq 8H \\ 10\log_{10}(R) + \alpha R + a_T(R/H - 1) & \\ \qquad + 10\log_{10}(H) + 64.5 - k_L, & \text{if} \quad R > 8H, \end{cases} \tag{C.3}$$

where R is the distance from the source, k_L is the near-field anomaly, α is the frequency-dependent attenuation coefficient, and a_T is the loss coefficient for each interaction with the bed. Equation C.3 is calculated with the range in units of kilo-yards. The near-field anomaly term accounts for contributions to the sound field of bottom and surface reflections. The k_L and a_T terms, both of which are frequency dependent, are available in *Marsh and Schulkin* [1962]. The model accommodates two sediment types: sand and mud. Here, sand is used because the higher sound speed and density are closer to the known bed composition in Admiralty Inlet. A source frequency of 1.1 kHz was used and log-space interpolations of the tables in *Marsh and Schulkin* [1962] were used to determine k_L and a_T. Like the

previous two models, this approach does not account for range-dependent bathymetry.

C.2.4 Range-Dependent Parabolic Equation

The final model is the RAMGEO implementation of the Range-Dependent Parabolic Equation [*Collins*, 1993], also referred to as the PE model. The PE model is a finite element modeling approach that allows for range-dependent bathymetry, sound speed profiles, stratified seabed composition, a source depth, and a source frequency. The sediment used in the model was a coarse, gravely sand with a sound speed ratio of 1.25, a density ratio of 2.23, and an attenuation rate of 0.7 dB per wavelength [*APL-UW*, 1994]. For comparison the other models an average transmission loss was calculated for each range bin by averaging the transmission losses at depths from 5-35 meters.

C.3 Results

The PE model output and the bathymetry profiles are included in Figure C.2. In contrast to the other models, variability can occur throughout the water column due to constructive and destructive interference. In the two spreading models (Eqs. C.1 and C.2), the only variability that the models can capture is based on the distance from the source. When the range is much greater than the depth, this differences becomes negligible and the transmission loss is roughly equivalent throughout the water column. *Marsh and Schulkin* [1962] note in the development of the model that at the sound field is independent of the source and receiver depths when the acoustic wavelength is much smaller than the water depth.

Figure C.3 includes the transmission losses with range for all four models and the differences between the PE model and the other models for the three bathymetric profiles. Two clear patterns are present in these results: the two spreading models always predict lower losses than the PE model and at ranges greater than 1 km the Marsh and Schulkin model predicts higher losses than the PE model. The transmission losses calculated by the two spreading models are typically between 5-10 dB less than the PE model. The $15log_{10}$ model produces results in better agreement with the PE model, particularly as the range increases. Beyond ranges of 1 km, the Marsh and Schulkin model calculates transmission losses between 5-10 dB larger than the PE.

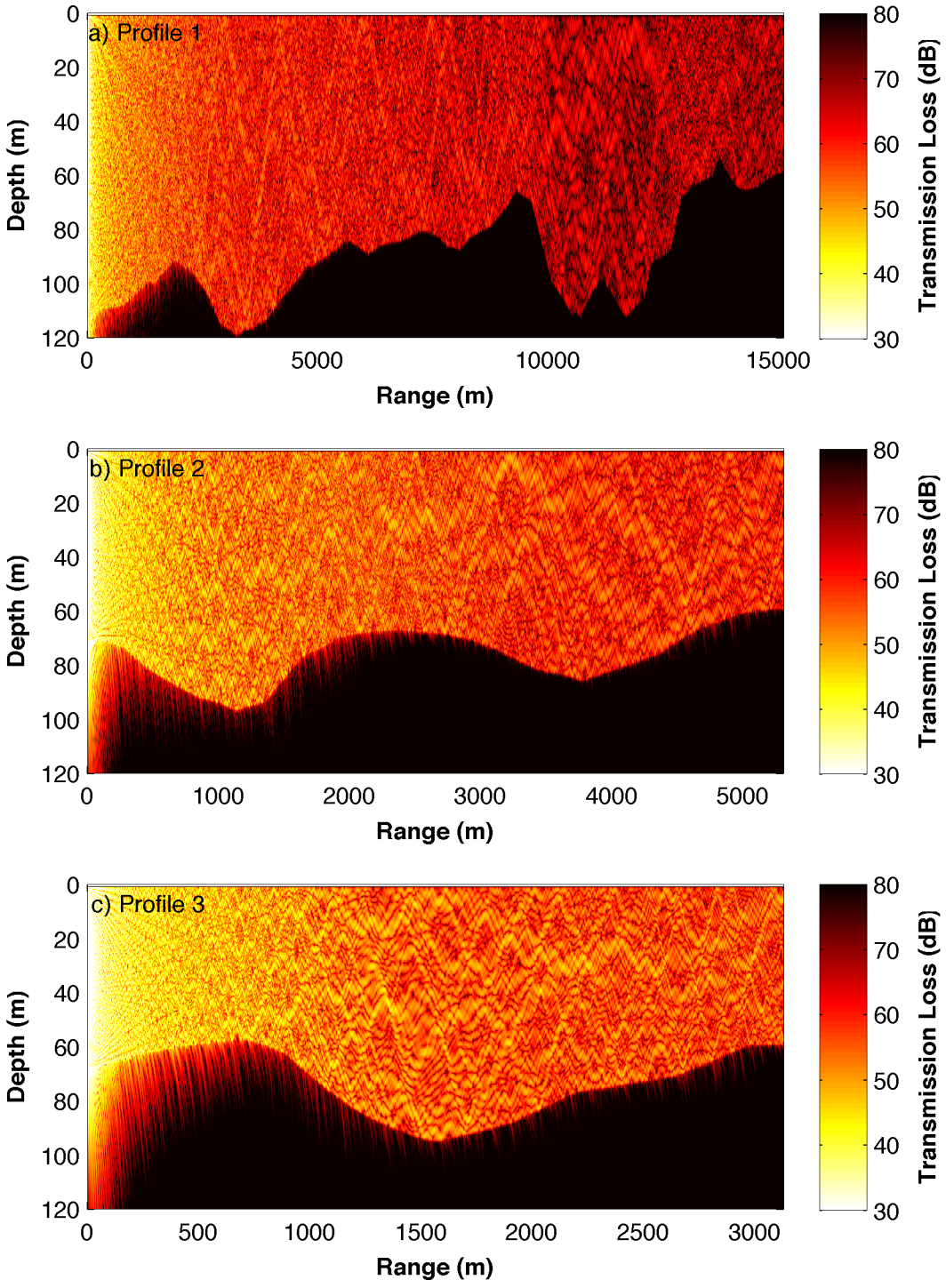

Figure C.2: PE model output for a 1.1 kHz source for three bathymetric profiles.

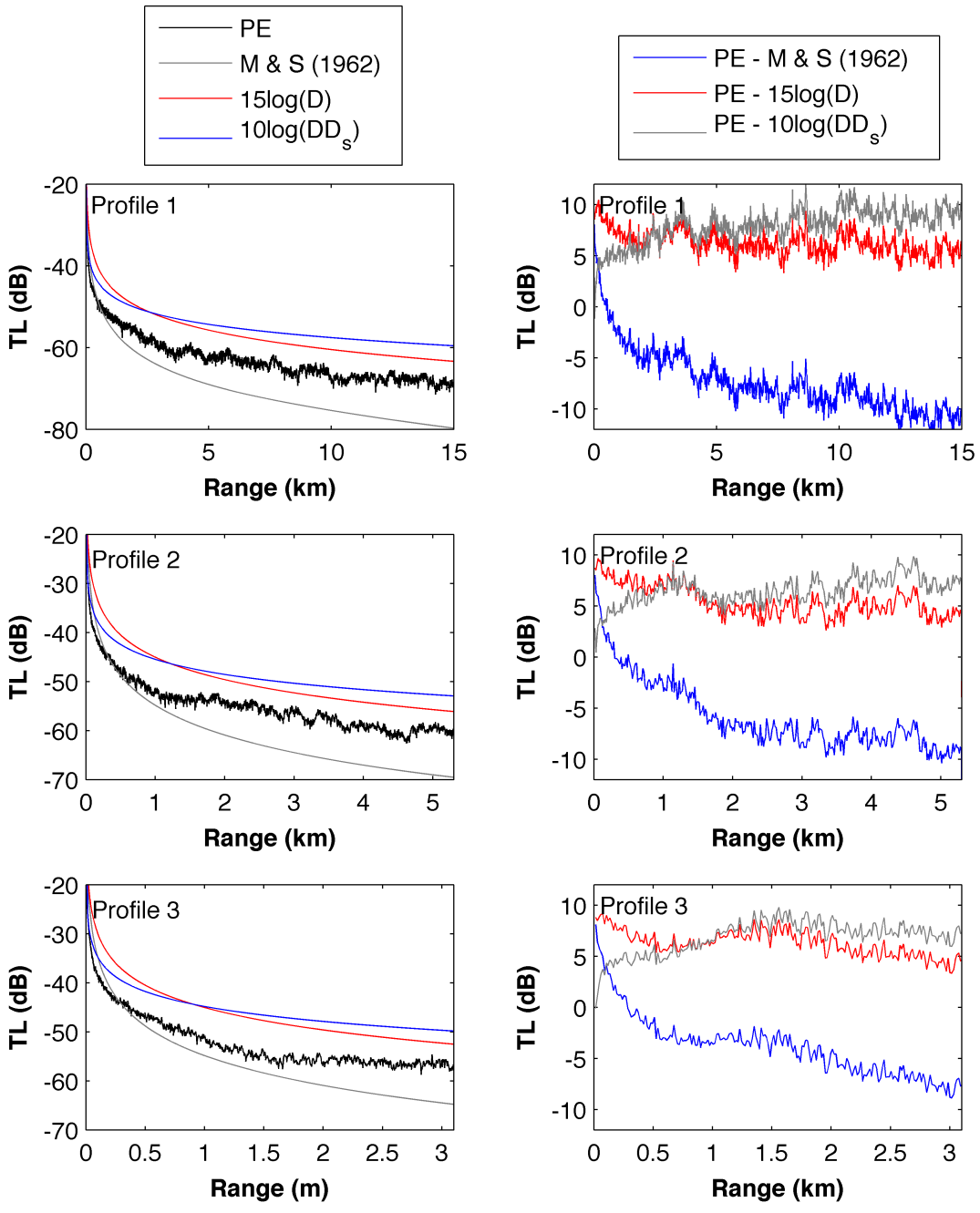

Figure C.3: A comparison between the output from the four models for three different bathymetric profiles in Admiralty Inlet.

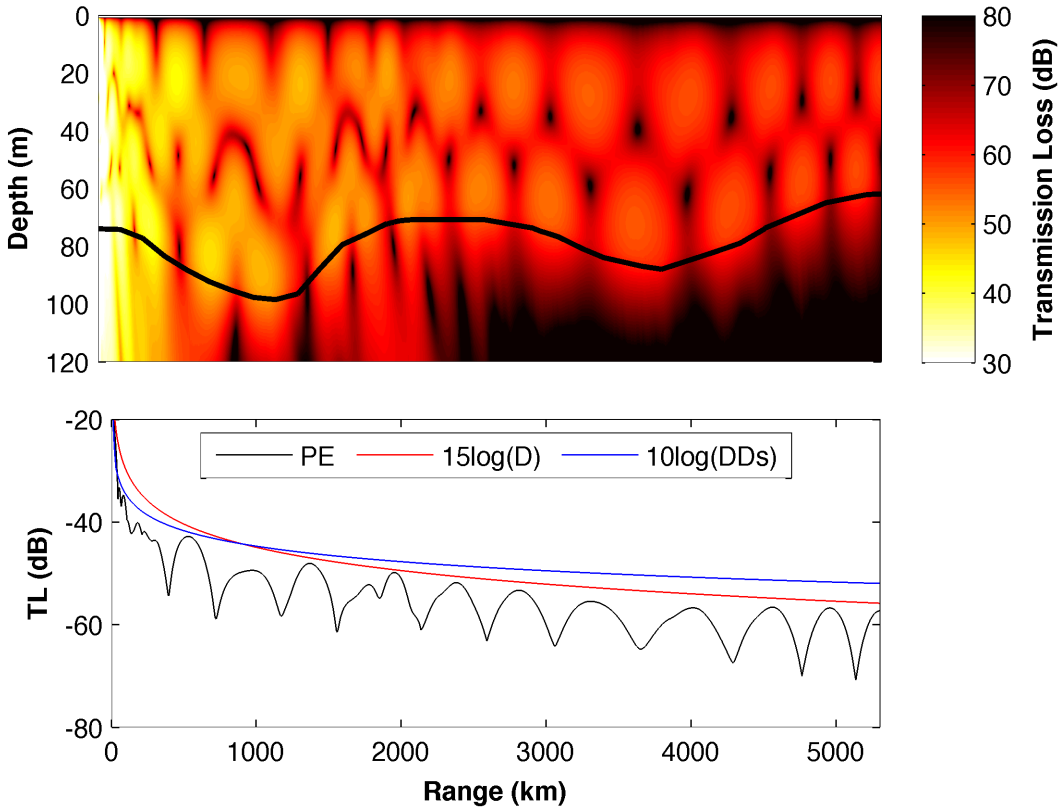

Figure C.4: a) PE model output with a source frequency of 40 Hz. The thick black line shows the depth of the seabed. b) Model comparisons for three models.

At the frequency modeled in Figures C.2 and C.3 (1.1 kHz), the acoustic wavelengths are only a small fraction of the water depth. At much lower frequencies ($f < 100$ Hz) the wavelengths are not small relative to the depth. As a result, the interpretation arrived at by modeling in the kHz range should not be considered as representative of low-frequency propagation. To demonstrate the differences between these regimes, an example model using the bathymetric profile in Figure C.2b using a source frequency of 40 Hz is included in Figure C.4. The figure also includes comparisons between the two spreading models and the PE output (the Marsh and Schulkin model is not included because the model is not suitable for the low-frequency source).

The transmission loss patterns shown in Figure C.4 are typical of low-frequency propagation in shallow water environments where the sound field is determined by the constructive and destructive interference of a limited number of propagating modes. As was the case

with the models at 1.1 kHz, the PE model calculates greater transmission losses than the spreading models. These differences, however, are less significant than in the models with a 1.1 kHz source.

C.4 Discussion

Given the significant differences shown between the results from the different models, it is worth considering the transmission losses calculated by the different models in the context of the applications for which they were applied. In the case of the detection of sound from operating tidal turbines by marine mammals (Ch. 7), the combined spreading model (Eq. C.1) was applied. This model produces the smallest transmission losses of the four models. Therefore, the application of this model provides an upper bound on the detection range of turbine sound, a precautionary result which is consistent with the objective of the study.

In the study of the detection range of SRKW vocalization the *Marsh and Schulkin* [1962] model was applied. Of the four models *Marsh and Schulkin* [1962] results in the largest transmission losses. Again, the application of this model is consistent with the objective of the study which was to estimate the range at which vocalizing Southern Resident killer whales could be detected under different ambient noise conditions. Due to the larger transmission losses associated with the application of the *Marsh and Schulkin* [1962] model, this again provides a conservative estimate for the range at which vocalizations might be detectable during periods of strong currents.